

5-1-2014

# Development of Novel Passive Control Techniques for More Uniform Temperature at Combustor Exit and Hybrid Les/Rans Modeling

Alka Gupta

*University of Wisconsin-Milwaukee*

Follow this and additional works at: <https://dc.uwm.edu/etd>



Part of the [Mechanical Engineering Commons](#)

---

## Recommended Citation

Gupta, Alka, "Development of Novel Passive Control Techniques for More Uniform Temperature at Combustor Exit and Hybrid Les/Rans Modeling" (2014). *Theses and Dissertations*. 461.  
<https://dc.uwm.edu/etd/461>

This Dissertation is brought to you for free and open access by UWM Digital Commons. It has been accepted for inclusion in Theses and Dissertations by an authorized administrator of UWM Digital Commons. For more information, please contact [open-access@uwm.edu](mailto:open-access@uwm.edu).

DEVELOPMENT OF NOVEL PASSIVE CONTROL TECHNIQUES FOR MORE  
UNIFORM TEMPERATURE AT COMBUSTOR EXIT AND  
HYBRID LES/RANS MODELING

by

Alka Gupta

A Dissertation Submitted in  
Partial Fulfillment of the  
Requirements for the Degree of

Doctor of Philosophy  
in Engineering

at

The University of Wisconsin – Milwaukee

May 2014

## ABSTRACT

### DEVELOPMENT OF NOVEL PASSIVE CONTROL TECHNIQUES FOR MORE UNIFORM TEMPERATURE AT COMBUSTOR EXIT AND HYBRID LES/RANS MODELING

by

Alka Gupta

The University of Wisconsin – Milwaukee, 2014  
Under the Supervision of Professor Ryoichi S. Amano

Gas turbines have become an important, widespread, and reliable device in the field of power generation. For any gas turbine system, the combustor is an integral part responsible for the combustion of the fuel. A number of studies have shown that the flow field exiting a combustor is highly non-uniform in pressure, velocity and, most importantly, temperature. Hot streaks amongst other non-uniformities cause varying thermal stresses on turbine blades and put pressure on the blade materials. In particular, these non-uniformities can have detrimental effects on the performance of the engine and cause a reduction in the expected life of critical components such as the turbine vanes. Due to the importance and severity of the problem, a large portion of the total combustor development effort is devoted to achieving better temperature uniformity. The present work is another attempt to develop novel passive control techniques to enhance mixing in a facility simulating the dilution zone of a typical gas turbine combustor and produce more uniform temperature at the combustor exit. Extensive experimentation was conducted to compare the proposed dilution techniques – staggered dilution holes, staggered dilution holes with streamlined body and staggered dilution holes with guide

vanes at various orientations ( $0^\circ$ ,  $30^\circ$ ,  $60^\circ$  and  $90^\circ$ ). A weighted parameter was defined called 'uniformity factor ( $\chi'$ )' to compare how close the mixture fraction is to the equilibrium value. For the majority of the flow conditions tested, the  $30^\circ$  guide vanes gave the most uniform temperature flow with just about 2% higher pressure loss as compared to the staggered dilution holes geometry. The fact that the use of  $30^\circ$  guide vanes can provide the turbine blade with 15% more uniform temperature flow than the staggered dilution holes design with merely 2% more pressure drop, has a very important implementation in order to reduce the damage of the turbine blades due to non-uniform temperature flow and extend its life-span. This would result in an overall reduction in the maintenance cost of the gas turbine systems which is quite significant. Furthermore, it was found that the introduction of the streamlined body not only improved the mixing in some cases but also helped decrease the pressure drop from inlet to exit of the experimental set-up. This is expected to increase the overall system efficiency and decrease the operating cost of a gas turbine system. Additionally, numerical modeling was used for various parametric studies to explore the effect of jet-to-mainstream momentum flux ratio on the exit temperature uniformity, variation of the cooling rate within the dilution zone, exergy analysis, etc.

The other significant part of this work comprised of development of an Algebraic Stress Model (ASM) in order to estimate the turbulence via Reynolds stresses prediction. The ASM model developed is validated for a simple two-dimensional turbulent flow over a flat plate and a complex three dimensional flow around Ahmed body. The developed model is capable of predicting Reynolds stresses for a variety of flow regimes. Based on these validation it can be concluded that adopting a hybrid approach which combines the

advantages of the ASM model with other turbulence models can be sought after for a more in-depth analysis of the flow structures and turbulent quantities both near-wall and away from the boundary for any fluid flow problem. The accurate prediction of the turbulent quantities plays a significant role in not just the fluid motion/transfer phenomenon rather it governs the heat exchange process as well especially in regions close to the wall.

© Copyright by Alka Gupta, 2014  
All rights reserved

Dedicated to my parents and my husband  
for their unconditional love, support and motivation

## **ACKNOWLEDGEMENTS**

First and foremost, I would like to express my sincere gratitude to my academic advisor - Professor Ryoichi S. Amano - for providing me with opportunity to pursue research under his guidance and for being an excellent academic mentor throughout my graduate program. This work would not have been possible without his generous support and guidance. His advice on research as well as my course study has been invaluable.

I would also like to thank the members of my PhD Committee - Dr. John R. Reisel, Dr. Chris Yuan, Dr. Woo-Jin Chang and Dr. Hans Volkmer - for taking out time to go through my work and for their insightful comments and suggestions.

I would like to acknowledge the support of my supervisor at work, Mr. Anthony Coffey, Technical Staff Engineer at Harley-Davidson Motor Company, for his motivation and encouragement during the course of this research. My sincere thanks goes to my colleague at work, Dr. Mojtaba Rajaei, Senior Project Engineer at Harley-Davidson Motor Company, for his valuable contributions and suggestions.

I would like to extend my appreciation to all the members of Dr. Amano's research group for sharing great camaraderie in the lab. The members of the group have contributed immensely to my professional and personal time at UWM. Special thanks to all the Senior Design Students for their constant assistance and help.

Above all, words cannot express how grateful I am to my parents who raised me with a love for science and supported me in all my pursuits, and for their unconditional love and care. Last but not least, I would like to thank my loving husband Deepak for his personal support, encouragement and great patience during the various stages of this PhD.



## TABLE OF CONTENTS

<b>Chapter 1 - Introduction.....</b>	<b>1</b>
1.1 Gas Turbine and its Components .....	1
1.1.1 Compressor .....	2
1.1.2 Combustor.....	2
1.1.3 Turbine.....	3
1.1.4 Diffuser/Nozzle.....	4
1.2 Combustor Requirements .....	4
1.3 Zones in a Combustor .....	6
1.4 Problem Realization .....	7
1.5 Organization of Material .....	10
 <b>Chapter 2 - Literature Review .....</b>	 <b>12</b>
2.1 Experimental Studies on Non-Reacting Flows .....	12
2.2 Computational Studies on Non-Reacting/Reacting Flows.....	24
2.3 Summary .....	33
 <b>Chapter 3 - Combustor Model Test Section Design.....</b>	 <b>35</b>
3.1 Design Process and Specifications of Experimental Set-up.....	36
3.2 Experimental Instrumentation and Measurement Techniques .....	41
3.2.1 Pressure and Velocity Measuring System.....	41
3.2.2 Temperature Measuring and Data Acquisition System .....	42
3.3 Description of Test Cases.....	45
3.3.1 Staggered Dilution Holes .....	46
3.3.2 Staggered Dilution Holes with Streamlined Body.....	47
3.3.3 Staggered Dilution Holes with Guide-vanes.....	49
3.4 Test Procedure.....	52
 <b>Chapter 4 - Computational Methodology .....</b>	 <b>54</b>
4.1 Meshing Procedure.....	55
4.2 Boundary Conditions.....	57
4.3 Governing Equations and Solution Methods .....	58
4.4 Initialization and Convergence Criteria .....	60
4.5 Turbulence Modeling and Near Wall Treatment .....	60

<b>Chapter 5 - Computational Results and Parametric Study .....</b>	<b>63</b>
5.1 Two-dimensional CFD Analysis.....	64
5.2 Three-dimensional CFD Analysis.....	67
5.2.1 Simulation Procedure.....	69
5.2.2 Grid Independence .....	70
5.2.3 Staggered versus In-line Dilution Holes .....	71
5.2.4 Effect of Adding Streamlined Body in the Dilution zone.....	73
5.3 Experimental Observation for Staggered Dilution Holes .....	77
5.4 Effect of Momentum flux Ratio on Temperature Uniformity.....	80
5.4.1 CFD Model Validation .....	80
5.4.2 Increasing Momentum Flux Ratio in Simulation.....	83
5.4.3 Data Analysis .....	84
5.5 Variation of Cooling Rate Number (CRN) .....	90
5.6 Exergy Destruction.....	92
5.7 Summary .....	93
 <b>Chapter 6 - Experimental Results and Discussion .....</b>	 <b>96</b>
6.1 Measure of Temperature Uniformity .....	97
6.2 Results and Discussion.....	97
6.3 Summary .....	104
 <b>Chapter 7 - Algebraic Stress Model (ASM) .....</b>	 <b>106</b>
7.1 Reynolds Stresses .....	107
7.2 Need for Higher-Order Turbulence Models.....	111
7.3 Motivation for Algebraic Stress Model (ASM) .....	114
7.4 Derivation of Algebraic Stress Model Equations.....	115
7.5 Summary .....	121
 <b>Chapter 8 - Turbulence Modeling Using ASM.....</b>	 <b>124</b>
8.1 Turbulence Modeling of Flow Over Flat Plate .....	125
8.2 Turbulence Modeling of Flow around Ahmed Body .....	135
8.2.1 Computational Set-up .....	136
8.2.2 Numerical Method .....	138
8.2.3 CFD Validation and Verification for Full-Scale Ahmed Body .....	139
8.2.4 Wind Tunnel Facility .....	143

8.2.4.1	Honeycomb and Screens .....	144
8.2.4.2	Settling and Contraction Chambers .....	145
8.2.4.3	Test-section.....	145
8.2.4.4	Diffuser and Fan .....	146
8.2.5	Hot-Wire Anemometry .....	147
8.2.5.1	Probe Specifications .....	148
8.2.5.2	Data Conversion .....	150
8.2.5.3	Data Acquisition .....	152
8.2.5.4	Hot-wire Calibration.....	153
8.2.5.5	Hot-wire Error Analysis .....	157
8.2.6	Flow Measurements .....	159
8.2.7	Mean Flow Validation for Scaled-down Ahmed Body .....	161
8.2.8	ASM Model Reynolds Stresses .....	169
8.3	Summary .....	187
<b>Chapter 9 - Conclusions and Future Research.....</b>		<b>191</b>
9.1	Conclusions .....	191
9.2	Recommendations .....	196
<b>References .....</b>		<b>198</b>
<b>Appendix .....</b>		<b>204</b>

## LIST OF FIGURES

<b>Figure 1.1</b> A modern land-based gas turbine (Langston and Opdyke, 1997). .....	2
<b>Figure 1.2</b> Diagram of a typical annular combustor (Pratt and Whitney, 1988) and the damage that can occur to a first stage turbine vane. ....	5
<b>Figure 1.3</b> Main zones of a conventional combustor (Lefebvre and Ballal, 2010). ....	7
<b>Figure 2.1</b> Schematic of plate hole with (a) external scoop, and (b) internal chute used by Norgren and Humenik (1968). ....	14
<b>Figure 2.2</b> Schematic of the experimental facility used by Wittig <i>et al.</i> (1984). ....	15
<b>Figure 2.3</b> Sketch of configuration, coordinate system and dimensions of the test section used by Liou <i>et al.</i> (1991). ....	16
<b>Figure 2.4</b> Orifice configurations tested by Holdeman (1993). ....	17
<b>Figure 2.5</b> Schematic of multiple jet mixing used by Doerr <i>et al.</i> (1997). ....	19
<b>Figure 2.6</b> Enlarged test section configuration used by Wang <i>et al.</i> (2000). ....	20
<b>Figure 2.7</b> Geometrical details of test section used by Barringer <i>et al.</i> (2002). ....	21
<b>Figure 2.8</b> Split and recombine micromixer used by Sheu <i>et al.</i> (2012). ....	22
<b>Figure 2.9</b> Schematic details of chutes with 10° and 20° angles of injection used by Ahmed <i>et al.</i> (2000). ....	23
<b>Figure 2.10</b> Schematic of the quick-mix section used by Talpallikar <i>et al.</i> (1992). ....	24
<b>Figure 2.11</b> Schematic of angled dilution jet concept used by Crocker & Smith (1995). ..	27
<b>Figure 2.12</b> Isometric three-dimensional view of computational grid for full five-cup sector modeling used by Gulati <i>et al.</i> (1995). ....	27
<b>Figure 2.13</b> Computational grid and dimensions (in cm) of a 22.5° sector of an annular combustor used by Su and Zhou (2000). ....	28
<b>Figure 2.14</b> Mean mixture fraction at several axial positions. Left: 60°-case, middle: 90°-case, right: 120°-case obtained by Wegner <i>et al.</i> (2004). ....	29
<b>Figure 2.15</b> Temperature contours for the non-optimized and optimized cases (Motsamai <i>et al.</i> , 2008). ....	31

<b>Figure 3.1</b> Schematic of the arrangement of the main components of the experimental set-up.....	37
<b>Figure 3.2</b> Detailed dimensions of the duct work. ....	39
<b>Figure 3.3</b> (a) Fan installed on the fixture, (b) Volume dam per, and (c) Heater. ....	40
<b>Figure 3.4</b> Control panel for all the heaters. ....	40
<b>Figure 3.5</b> Pressure and velocity measuring system. ....	42
<b>Figure 3.6</b> Temperature measuring system (a) K-type thermocouple, (b) Zip tied thermocouples, (c) Block to connect to DAQ, (d) LabView program window to record the temperatures. ....	44
<b>Figure 3.7</b> Dimensions of the test section and its Pro-E model. ....	45
<b>Figure 3.8</b> Staggered dilution holes (a) Detailed dimensions, and (b) Actual mounted in the test section.....	46
<b>Figure 3.9</b> Dilution holes with streamlined body (a) Detailed dimensions, and (b) Streamlined body 3-D model. ....	48
<b>Figure 3.10</b> Mounting system for the streamlined body. ....	48
<b>Figure 3.11</b> Streamlined body mounted in the test-section.....	49
<b>Figure 3.12</b> Schematic of the test section with guided vanes. ....	50
<b>Figure 3.13</b> Hollow steel hemispherical shell & completed guide vane cut at 45° angle.	51
<b>Figure 3.14</b> Guide vanes mounted inside the test-section.....	51
<b>Figure 3.15</b> Schematic of the four different guide vane orientations.....	52
<b>Figure 3.16</b> The constructed combustor simulator.....	53
<b>Figure 4.1</b> Geometry of the combustor simulator developed in the design modeler. ....	56
<b>Figure 4.2</b> Sample of the hybrid mesh generated with structured and unstructured elements. ....	57
<b>Figure 4.3</b> Schematic of the boundary conditions for the computational domain. ....	58
<b>Figure 5.1</b> Generated mesh for two-dimensional CFD analysis. ....	65

<b>Figure 5.2</b> Velocity vectors in the mixing section for (a) smaller dilution holes, and (b) larger dilution holes. ....	66
<b>Figure 5.3</b> Temperature contours in the mixing section for (a) smaller dilution holes, and (b) larger dilution holes.....	66
<b>Figure 5.4</b> Pressure contours in the mixing section for (a) smaller dilution holes, and (b) larger dilution holes. ....	67
<b>Figure 5.5</b> Test section with details of the in-line dilution holes pattern.....	68
<b>Figure 5.6</b> Test section with details of the streamlined body in the staggered dilution holes pattern. ....	69
<b>Figure 5.7</b> Radial temperature exit profiles for different mesh sizes for In-line dilution holes pattern. ....	71
<b>Figure 5.8</b> Deviation from equilibrium mixture fraction for in-line and staggered dilution holes patterns. ....	73
<b>Figure 5.9</b> Deviation from equilibrium mixture fraction for in-line, staggered, in-line with streamlined body and staggered with streamlined body dilution schemes. ....	75
<b>Figure 5.10</b> Position of the planes considered for plotting the velocity vectors for (a) In-line pattern, and (b) Staggered pattern.....	75
<b>Figure 5.11</b> Velocity vectors for (a) In-line dilution holes on plane 1, (b) In-line holes with streamline body on plane 1, (c) Staggered dilution holes on plane 1, (d) Staggered dilution holes on plane 2, (e) Staggered holes with streamlined body on plane 1, and (f) Staggered dilution holes with streamlined body on plane 2. ....	76
<b>Figure 5.12</b> Primary flow inlet profiles (a) Velocity, and (b) Temperature.....	78
<b>Figure 5.13</b> Exit flow profiles (a) Velocity, and (b) Temperature. ....	79
<b>Figure 5.14</b> Equivalent inlet condition points for the simulation. ....	81
<b>Figure 5.15</b> Comparison of experimental and simulation exit profiles (a) Velocity, and (b) Temperature. ....	82
<b>Figure 5.16</b> Variation of mixture fraction with momentum flux ratio.....	86
<b>Figure 5.17</b> Variation of pattern factor with momentum flux ratio. ....	86
<b>Figure 5.18</b> Variation of mixture uniformity with momentum flux ratio. ....	87

<b>Figure 5.19</b> Velocity vectors at Plane 1 for momentum flux ratio (a) 0.37, (b) 0.71, and (c) 0.85.....	88
<b>Figure 5.20</b> Variation of pressure loss with momentum flux ratio. ....	89
<b>Figure 5.21</b> Variation of cooling rate number with axial location at different radial distances for $I = 0.85$ .....	91
<b>Figure 5.22</b> Variation of cooling rate number (CRN) with axial location for different flux ratios.....	92
<b>Figure 5.23</b> Variation of the specific exergy destruction with momentum flux ratio.....	93
<b>Figure 6.1</b> Radial distribution of the normalized mixture fraction for Case A.....	101
<b>Figure 6.2</b> Radial distribution of the normalized mixture fraction for Case B. ....	101
<b>Figure 6.3</b> Radial distribution of the normalized mixture fraction for Case C. ....	102
<b>Figure 6.4</b> Radial distribution of the normalized mixture fraction for Case D.....	102
<b>Figure 6.5</b> Radial distribution of the normalized mixture fraction for Case E. ....	103
<b>Figure 7.1</b> Turbulence models. ....	111
<b>Figure 8.1</b> Schematic of boundary layer flow over a flat plate.....	125
<b>Figure 8.2</b> Computational domain with corresponding boundary conditions.....	126
<b>Figure 8.3</b> Generated mesh for the computational domain (Mesh size, $M = 64,000$ ). ..	127
<b>Figure 8.4</b> Velocity profile for various mesh sizes at $x = L$ .....	127
<b>Figure 8.5</b> Velocity vectors at inlet and outlet boundary.....	128
<b>Figure 8.6</b> Velocity profile along a line at $x = L$ .....	128
<b>Figure 8.7</b> Velocity profile at $x = L/2$ . ....	130
<b>Figure 8.8</b> Velocity profile at $x = L$ . ....	130
<b>Figure 8.9</b> Comparison of Reynolds stress $uu$ at $x = L$ computed using various ASM models with RST model.....	132
<b>Figure 8.10</b> Comparison of Reynolds stress $vv$ at $x = L$ computed using various ASM models with RST model.....	132

<b>Figure 8.11</b> Comparison of Reynolds stress $uv$ at $x = L$ computed using various ASM models with RST model.....	133
<b>Figure 8.12</b> Comparison of Reynolds stress $wv$ at $x = L$ computed using various ASM models with RST model.....	133
<b>Figure 8.13</b> Schematic of the original Ahmed body as studied by Ahmed <i>et al.</i> , 1984.	136
<b>Figure 8.14</b> Computational domain with boundary conditions.....	137
<b>Figure 8.15</b> Mesh around the Ahmed body.....	138
<b>Figure 8.16</b> Streamwise velocity profile along the front part of Ahmed body. ....	141
<b>Figure 8.17</b> Streamwise velocity profile along the rear part of Ahmed body.....	141
<b>Figure 8.18</b> Comparison of drag and lift coefficient for various turbulence models.....	142
<b>Figure 8.19</b> Schematic of the open circuit wind tunnel. ....	143
<b>Figure 8.20</b> Subsonic wind tunnel facility at University of Wisconsin - Milwaukee....	144
<b>Figure 8.21</b> Schematic of the X-Y-Z traverse system in the wind tunnel.....	146
<b>Figure 8.22</b> Miniature X-probe hot wire anemometer. ....	149
<b>Figure 8.23</b> Fixture on the traverse to mount the hot-wire sensor. ....	149
<b>Figure 8.24</b> Hot-wire calibrator manufactured by DANTEC Dynamics. ....	154
<b>Figure 8.25</b> Calibration connections for measurements.....	155
<b>Figure 8.26</b> Calibration curves for wire1 and wire2 of the X-probe sensor. ....	156
<b>Figure 8.27</b> Error curves for wire1 and wire2 of the X-probe sensor.....	156
<b>Figure 8.28</b> Ahmed body prototype mounted inside the wind tunnel.....	160
<b>Figure 8.29</b> Schematic of the vertical lines for hot-wire measurements.....	160
<b>Figure 8.30</b> Streamwise velocity profiles for line 1.....	164
<b>Figure 8.31</b> Streamwise velocity profiles for line 2.....	164
<b>Figure 8.32</b> Streamwise velocity profiles for line 3.....	165



<b>Figure 8.33</b> Streamwise velocity profiles for line 4.....	165
<b>Figure 8.34</b> Streamwise velocity profiles for line 5.....	166
<b>Figure 8.35</b> Streamwise velocity profiles for line 6.....	166
<b>Figure 8.36</b> Streamwise velocity profiles for line 7.....	167
<b>Figure 8.37</b> Streamwise velocity profiles for line 8.....	167
<b>Figure 8.38</b> Schematic of the flow in positive direction across the X-wire probes. ....	168
<b>Figure 8.39</b> Schematic of the flow in negative direction across the X-wire probes. ....	168
<b>Figure 8.40</b> Comparison of Reynolds stress $uu$ computed using various ASM models with RST model for line 3. ....	170
<b>Figure 8.41</b> Comparison of Reynolds stress $vv$ computed using various ASM models with RST model for line 3. ....	170
<b>Figure 8.42</b> Comparison of Reynolds stress $ww$ computed using various ASM models with RST model for line 3. ....	171
<b>Figure 8.43</b> Comparison of Reynolds stress $uv$ computed using various ASM models with RST model for line 3. ....	171
<b>Figure 8.44</b> Comparison of Reynolds stress $uw$ computed using various ASM models with RST model for line 3. ....	172
<b>Figure 8.45</b> Comparison of Reynolds stress $vw$ computed using various ASM models with RST model for line 3. ....	172
<b>Figure 8.46</b> Comparison of Reynolds stress $uu$ computed using various ASM models with RST model for line 5. ....	174
<b>Figure 8.47</b> Comparison of Reynolds stress $vv$ computed using various ASM models with RST model for line 5. ....	174
<b>Figure 8.48</b> Comparison of Reynolds stress $ww$ computed using various ASM models with RST model for line 5. ....	175
<b>Figure 8.49</b> Comparison of Reynolds stress $uv$ computed using various ASM models with RST model for line 5. ....	175
<b>Figure 8.50</b> Comparison of Reynolds stress $uw$ computed using various ASM models with RST model for line 5. ....	176

<b>Figure 8.51</b> Comparison of Reynolds stress $vw$ computed using various ASM models with RST model for line 5. ....	176
<b>Figure 8.52</b> Comparison of Reynolds stress $uu$ computed using various ASM models with RST model for line 6. ....	179
<b>Figure 8.53</b> Comparison of Reynolds stress $vv$ computed using various ASM models with RST model for line 6. ....	179
<b>Figure 8.54</b> Comparison of Reynolds stress $ww$ computed using various ASM models with RST model for line 6. ....	180
<b>Figure 8.55</b> Comparison of Reynolds stress $uv$ computed using various ASM models with RST model for line 6. ....	180
<b>Figure 8.56</b> Comparison of Reynolds stress $uw$ computed using various ASM models with RST model for line 6. ....	181
<b>Figure 8.57</b> Comparison of Reynolds stress $vw$ computed using various ASM models with RST model for line 6. ....	181
<b>Figure 8.58</b> Comparison of Reynolds stress $uu$ computed using various ASM models with RST model for line 7. ....	183
<b>Figure 8.59</b> Comparison of Reynolds stress $vv$ computed using various ASM models with RST model for line 7. ....	183
<b>Figure 8.60</b> Comparison of Reynolds stress $ww$ computed using various ASM models with RST model for line 7. ....	184
<b>Figure 8.61</b> Comparison of Reynolds stress $uv$ computed using various ASM models with RST model for line 7. ....	184
<b>Figure 8.62</b> Comparison of Reynolds stress $uw$ computed using various ASM models with RST model for line 7. ....	185
<b>Figure 8.63</b> Comparison of Reynolds stress $vw$ computed using various ASM models with RST model for line 7. ....	185
<b>Figure A.1</b> Streamwise velocity profile at various locations around scaled-down Ahmed body.....	205
<b>Figure A.2</b> Velocity profile for various mesh sizes of full-scale Ahmed body. ....	205

## LIST OF TABLES

<b>Table 3.1</b> Properties of Glass-wool. ....	38
<b>Table 5.1</b> Design details for combustor. ....	70
<b>Table 5.2</b> Mixture fraction values for uniform inlet conditions. ....	72
<b>Table 5.3</b> Cross-sectional areas of the ducts used. ....	77
<b>Table 5.4</b> Jet penetration angle for different flux ratio. ....	88
<b>Table 6.1</b> Inlet conditions for different experimental test cases. ....	96
<b>Table 6.2</b> Comparison of various dilution techniques. ....	99
<b>Table 6.3</b> Pressure loss data for various dilution techniques. ....	104
<b>Table 8.1</b> Properties of air. ....	139
<b>Table 8.2</b> Calibration transfer function coefficients. ....	155
<b>Table 8.3</b> Location of the vertical lines for hot-wire measurements. ....	161

## NOMENCLATURE

$A_{clad}$	Area of cross-section of cladding
$A_{holes}$	Total area of cross-section of the dilution holes
$A_{exit}$	Area of cross-section of exit section
$A_{inner}, A_{prim}$	Area of cross-section of inner duct for primary flow inlet
$A_{outer\ annular}$	Area of cross-section of outer annular duct
$A_{outer}$	Area of cross-section of outer duct
$A_{sec}$	Area of cross-section for the secondary inlet flow
$CRN$	Cooling rate number
$C_{p,air}$	Specific heat of air
$C_{\emptyset 1}$	Pressure strain coefficient (Value = 2.3)
$C_{\emptyset 2}$	Pressure strain coefficient (Value = 0.4)
$D_{ij}$	Diffusion
$E$	Heat addition required
$E_a$	Acquired CTA voltage
$E_{corr}$	Corrected CTA voltage
$e_d$	Specific exergy destruction
$f$	Mixture fraction
$\bar{f}$	Normalized mixture fraction
$f_{ave}$	Weighted average mixture fraction
$f_{equil}$	Equilibrium mixture fraction
$G_{ij}$	Production of Reynolds Stress

$G_k$	Production of turbulent kinetic energy
$h_m$	Specific enthalpy of mixed stream at the exit
$h_p$	Specific enthalpy of primary air
$h_s$	Specific enthalpy of secondary air
$I$	Jet-to-mainstream momentum flux ratio
$k^2$	Yaw coefficient of the X-probe wire
$M$	Mixture uniformity
$\dot{m}_{exit}, \dot{m}_m$	Mass flow rate of mixed stream at the exit
$\dot{m}_\infty, \dot{m}_{prim}, \dot{m}_p$	Main (or primary) stream mass-flow rate, before mixing
$\dot{m}_j, \dot{m}_{sec}, \dot{m}_s$	Dilution jet mass-flow rate
$n$	Number of data points
$p$	Pressure
$P_{exit}$	Total pressure at the exit
$P_{prim}$	Total pressure at the primary flow inlet section
$P_{sec}$	Total pressure at the secondary flow inlet section
$PF$	Pattern factor
$pf$	Profile factor
$Q_{primary}$	Primary (or main) stream flow rate
$R$	Radius of the duct at the exit section
$Re$	Reynolds number
$Re_{cr}$	Critical Reynolds number
$R_{20}$	Sensor resistance at 20°C
$R_L$	Lead resistance at 20°C

$R_S$	Support resistance at 20°C
$R_C$	Cable resistance at 20°C
$s_m$	Specific entropy of mixed stream at the exit
$s_p$	Specific entropy of primary air
$s_s$	Specific entropy of secondary air
$T_a$	Ambient temperature during data acquisition
$T_{adb}$	Adiabatic, ideal mixing temperature
$T_{exit}$	Average combustor exit temperature
$T_i$	Local temperature
$T_{inlet}$	Average combustor inlet temperature
$T_j$	Dilution jet temperature
$T_{max}$	Maximum spatial combustor exit temperature
$T_o$	Atmospheric temperature or Ambient reference temperature related to last overheat set-up of the hot-wire before calibration
$T_\infty$	Main (or primary) stream temperature, before mixing
$T_{sensor}$	Selected sensor operating temperature
$u_i, u_j, u_k$	Velocity in $i, j$ and $k$ directions, respectively
$\overline{u_i u_j}, \tau_{ij}$	Reynolds Stress
$\bar{U}$	Mean velocity
$U_{cal}$	Calibration velocity
$U_{effective-wire1}$	Effective cooling velocity of hot-wire probe 1
$U_{effective-wire2}$	Effective cooling velocity of hot-wire probe 2

$U_1, U_2$	Velocities in the wire-coordinate system (1,2)
$U, V$	Velocity components
$V_{ave\ exit}, V_m$	Average exit flow velocity of mixed stream
$V_{ave\ prim}$	Average primary inlet flow velocity
$V_{jet}$	Velocity of jet through the dilution holes
$V_{prim}, V_p$	Primary inlet flow velocity
$V_{sec}, V_s$	Secondary inlet flow velocity
$y$	Distance to the nearest wall
$u_*$	Friction velocity at the nearest wall
<b>Greek</b>	
$\alpha_{20}$	Temperature coefficient of resistance (TCR)
$\Gamma$	Effective diffusion coefficient
$\delta$	Boundary layer thickness
$\delta_{ij}$	Kroneker delta
$\partial$	Derivative
$\Delta T$	Temperature difference between primary and secondary air
$\Delta X$	Total length of the dilution zone (test-section)
$\varepsilon$	Rate of dissipation of turbulent kinetic energy
$\epsilon$	Overall mixing rate
$\epsilon_i$	Local mixing rate
$\mu$	Laminar fluid viscosity

$\mu_t$	Turbulent viscosity
$\Phi_{ij}$	Pressure-strain correlation
$\Phi_{ij1}$	Slow distortion part of pressure-strain correlation
$\Phi_{ij2}$	Rapid distortion part of pressure-strain correlation
$\Phi_{ijw}$	Wall-reflection part of pressure-strain correlation
$\nu$	Kinematic fluid viscosity
$\varphi$	Slant angle of the Ahmed body
$\rho_{air}$	Density of air
$\rho_{jet}$	Density of air at the secondary flow inlet temperature
$\rho_{prim}$	Density of air at the average primary flow inlet temperature
$\tau_w$	Wall shear stress
$\chi$	Uniformity factor
$\chi_{avg}$	Average uniformity factor



# Chapter 1 - Introduction

## 1.1 Gas Turbine and its Components

Gas turbines fall into a class of heat engines which use energy from fuel combustion to produce mechanical power. The produced power can be either a torque through a rotating shaft (industrial gas turbines) or a jet power in the form of velocity through an exhaust nozzle (aircraft jet engines). The products of combustions diluted with air act on a continuously rotating turbine to produce power. As compared to the reciprocating engines, gas turbines offer very high power-to-weight ratio; are smaller than most reciprocating engines of the same power rating; move in one direction only, with far less vibration than a reciprocating engine; has fewer moving parts. Also, gas turbines are known to provide greater reliability, particularly in applications where sustained high power output is required. The gas turbine has become an important, widespread, and reliable device in the field of power generation and other applications such as: petrochemical industry, in surface vehicles like ships, locomotives, helicopters, tanks and to a lesser extent, on cars, buses and motorcycles. Apart from the applications mentioned above, as a branch of gas turbine technology, micro gas turbines are becoming widespread. They range from hand held units producing less than a kilowatt, to commercial sized systems that can produce tens or hundreds of Megawatts.

Figure 1.1 shows a typical land-based gas turbine used for electrical power production and for mechanical drives. The compressor, combustor, turbine and power shaft form the main components of any gas turbine engine.

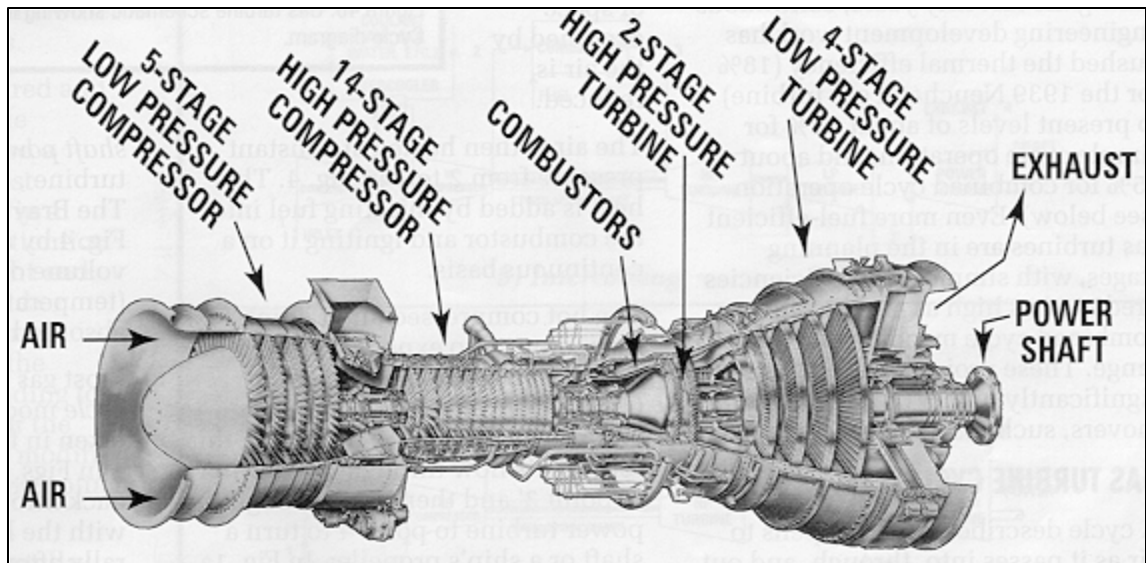


**Figure 1.1** A modern land-based gas turbine (Langston and Opdyke, 1997).

### 1.1.1 Compressor

Compressors are usually made up of several rows of alternating rotor vanes and stator blades, known as stages. By using multiple stages in tandem, the pressure of the air can be gradually increased by small increments, resulting in the most aerodynamically efficient process for achieving high overall pressure ratios. At the very highest of pressure ratios, the compressor is split into two or even three separate in-line compressors. Each is connected to its own shaft, nested one inside the other, and driven by individual turbines. The separate compressor and turbine set with its drive shaft is known as a spool.

### 1.1.2 Combustor

Also known as a burner, combustion chamber or flame holder, it is fed high pressure air by the compression system. The combustor then heats this air at constant

pressure. After heating, air passes from the combustor through the nozzle guide vanes to the turbine. Clean combustion products always come with efficient burning. Combustion stability and efficiency are achieved primarily by significantly reducing the air velocity from the relatively fast level, at which it leaves the compressor, to a very slow level with high turbulence. An increasing-area diffusion duct placed between the two components acts to reduce air velocity. At the end of the diffuser, atomizing fuel nozzles spray a fuel mist into the low-velocity airstream where a high temperature flame front is established. To feed the combustion zone with oxygen, metal liners, pierced by a succession of small holes, direct the air inward toward the center of the combustion chamber where the spray nozzles are located. The rest of the air, entering at the cooler compressor exit temperature around the outside of the combustion zone, is forced radially inward by another series of small liner holes designed for thermal mixing. The process of mixing cold with hot continues downstream until the overall gas temperature distribution is sufficiently devoid of hot peaks to enter the turbine.

### **1.1.3 Turbine**

Turbine operation is the reverse of that of compressors. Turbines are also composed of a series of stationary vane and rotating blade pairs, or stages, designed in the form of airfoils. However, the stationary turbine vanes act first to convert the thermal energy of the air into rotating swirl velocity as density decreases. The swirling air leaving the vanes impinges on the traveling airfoil blades and imparts a resisting torque to the vanes. The rotating airfoils change the swirl back to the axial direction while reducing air pressure in the process. Their torque travels through the discs holding the blades to the

connecting output shaft that is attached to the resisting, power-absorbing load on its other end.

#### **1.1.4 Diffuser/Nozzle**

Area-increase conduits, called diffusers, are integral gas turbine components. A diffuser is used to slow down the compressor air entering the combustor. In aircraft gas turbines a diffuser is also placed in front of the compressor to slow down the captured outside air from forward-flight velocity to a velocity that is aerodynamically compatible with the front compressor airfoils.

Area-reduction conduits are called nozzles. Nozzles in gas turbines find use in the exhaust section. The pressure level exiting the compressor drive turbine, expands through the engine exhaust nozzle down to ambient pressure while the jet velocity increases to provide jet propulsion.

### **1.2 Combustor Requirements**

A gas turbine combustor must satisfy a wide range of requirements whose relative importance varies among engines types. However, the basic requirements of all combustors may be listed as follow:

- i. High-combustion efficiency (i.e. fuel should be completely burned so that all its chemical energy is liberated as heat)
- ii. Reliable and smooth ignition
- iii. Wide stability limits (i.e. the flame should stay alight over wide ranges of pressure and air/fuel ratio)
- iv. Low pressure loss

- v. An outlet temperature distribution that is tailored to maximize the lives of the turbine blades and nozzle guide vanes
- vi. Low emissions of smoke and gaseous pollutant species
- vii. Design for minimum cost and ease of manufacturing
- viii. Maintainability and durability

A number of studies have shown that the flow field exiting a combustor is highly non-uniform in pressure, velocity and, most importantly, temperature. Hot streaks amongst other non-uniformities cause varying thermal stresses on turbine blades and put pressure on the blade materials. Blade cooling technologies, especially on the first stage of turbine turning vanes immediately downstream of the combustor exit is crucial. In particular, these non-uniformities can have detrimental effects on the performance of the engine and cause a reduction in the expected life of critical components such as the turbine vanes. Figure 1.2 shows a typical annular combustor and the damage that can occur to a first stage turbine blade.

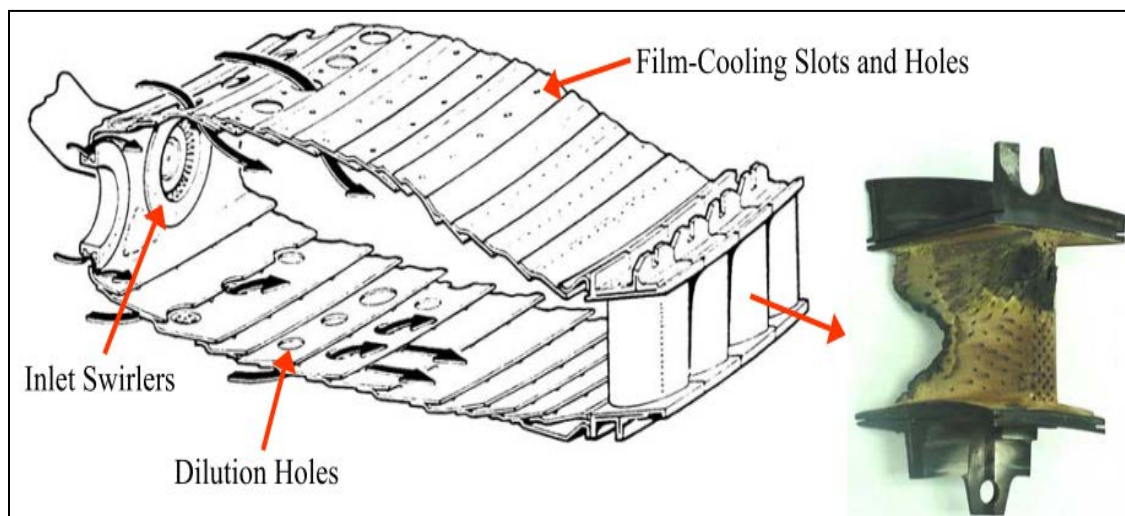


**Figure 1.2** Diagram of a typical annular combustor (Pratt and Whitney, 1988) and the damage that can occur to a first stage turbine vane.

### 1.3 Zones in a Combustor

A conventional combustor comprises of three basic zones - primary, intermediate and dilution (refer Fig. 1.3).

- **Primary Zone:** The main function of the primary zone is to anchor the flame and provide sufficient time, temperature and turbulence to achieve essentially complete combustion of the incoming fuel-air mixture. Many different types of flow patterns are employed, but one feature that is common to all is the creation of a toroidal flow reversal that entrains and re-circulates a portion of the hot combustion gases to provide continuous ignition to the incoming air and fuel. Some early combustors used air swirlers to create the toroidal flow pattern, whereas others had no swirler and relied solely on the air injected through holes drilled in the liner wall at the upstream end of the liner.
- **Intermediate Zone:** If the primary-zone temperature is higher than around 2000 K dissociation reactions will result in the appearance of significant concentration of carbon monoxide (CO) and hydrogen (H<sub>2</sub>) in the efflux gases. Should these gases pass directly to the dilution zone and be rapidly cooled by the addition of massive amounts of air, the gas composition would be "frozen", and CO, which is both a pollutant and a source of combustion inefficiency, would be discharged from the combustor unburned. Dropping the temperature to an intermediate level by the addition of small amounts of air encourages the burnout of soot and allows the combustion of CO and any other unburned hydrocarbons (UHC) to proceed to completion.

- Dilution Zone:** The role of dilution zone is to admit the air remaining after the combustion and wall-cooling requirements have been met, and to provide an outlet stream with a temperature distribution that is acceptable to the turbine. This temperature distribution is usually described in terms of "mixture fraction", a parameter defined in terms of the temperatures of the dilution and primary flow streams at the inlet and the exit plane of the combustor. The amount of air available for dilution is usually between 20 - 40% of the total combustor airflow. It is introduced into the hot gas stream through one or more rows of holes in the liner walls. The size and shape of these dilution holes are selected to optimize the penetration of the air jets and their subsequent mixing with the main stream.

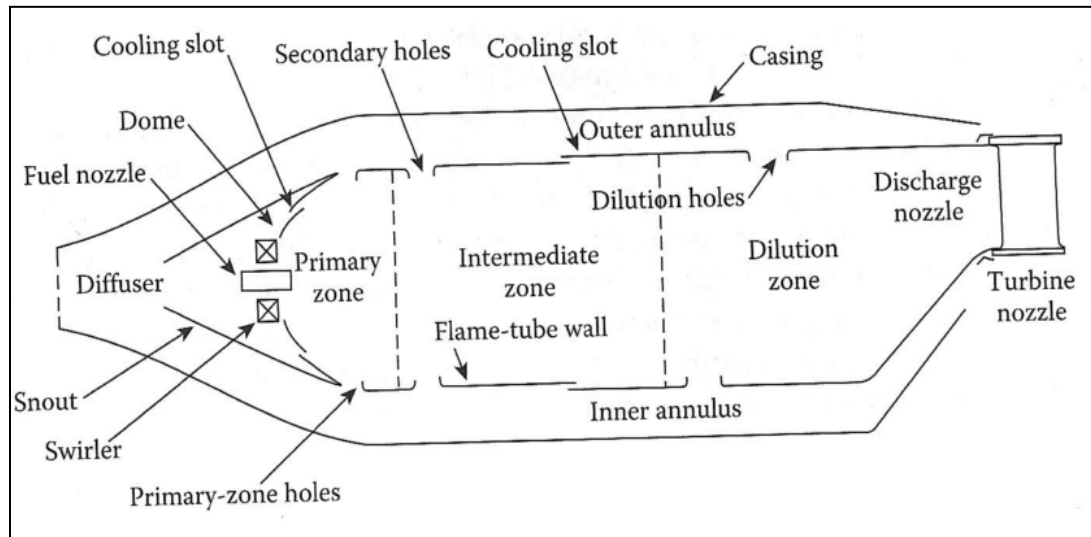


**Figure 1.3** Main zones of a conventional combustor (Lefebvre and Ballal, 2010).

## 1.4 Problem Realization

Increased turbine inlet temperatures and the resulting emphasis on the uniformity of the combustor exit temperature, stringent requirements on the pollutant emission such

as NO<sub>x</sub>, and the need for improved fuel efficiency have made mixing one of the most crucial processes in combustors. Regardless of the type of engine - low fuel consumption, long operating life and pollutant emissions are important factors. The damage to the downstream hot section components due to the highly non-uniform temperature distribution results in an increase in maintenance costs and operational down-time, both the factors being very crucial for any gas turbine industry. For instance, the cost of replacement of over 150 degraded nozzle guide vanes for the Canadian Forces fleet of T56-A-15 engines amounts to an annual material cost of over \$300,000. In addition to the material cost, highly skilled manpower is required for the maintenance which incurs extra cost (Kotzer, 2008). For the very high turbine entry temperature (around 2000 K) associated with modern high-performance engines, an ideal mixture fraction would be one that gives minimum temperature at the turbine blade root, where stresses are highest, and also at the turbine blade tip, to protect seal materials. Attainment of the desired temperature profile is paramount, owing to its major impact on the maximum allowable mean turbine entry temperature and hot-section durability. Due to the importance and severity of the problem, a large portion of the total combustor development effort is devoted to achieving the desired mixture fraction.

A uniform exit temperature distribution can be achieved with a long dilution zone. The additional space required for a long combustion chamber, coupled with the increased weight and pressure losses, limits the length to diameter ratio of the dilution zone between 1.5 to 1.8 for gas turbine engines (Lefebvre and Ballal, 2010). This criterion narrows down to the position of the dilution holes and geometry within the dilution zone as the only possible ways to control the exit temperature distribution. The present



research mainly focuses on the design changes within the dilution zone to improve the temperature uniformity at the combustor exit so as to extend the operating life of a gas turbine engine, which is ultimately determined by the material structural limits of its components.

Various methods have been developed and proposed to counter the challenges posed by the non-uniformities present in the exit flow from the combustor, which include both passive and active control techniques. Any geometrical modifications such as change in the combustor design or the way the cold air is introduced in the dilution zone, constitute the passive control techniques where as modification other than just the geometry like the use of pulsed air jet, synthetic jet actuators, etc. to improve mixing in the dilution zone come under the active control techniques. The present work is another attempt to develop techniques to enhance mixing in a facility, simulating the dilution zone in a typical gas turbine combustor. Here, only the passive control techniques are analyzed to achieve the objective of producing a more uniform temperature. Following are the techniques which were explored in the present work:

- i. Staggered dilution holes
- ii. Dilution holes with streamlined body
- iii. Dilution holes with guide vanes ( $0^\circ$ ,  $30^\circ$ ,  $60^\circ$  and  $90^\circ$ )

Both numerical and experimental analysis is taken up to investigate the effectiveness of the above mentioned techniques to produce a more uniform temperature flow at the exit of the combustor. It is to be noted at this point that only the mixing in the dilution zone is modeled and a non-reacting flow is considered. In the entire work, the terms dilution and mixing are used interchangeably. Although this study is motivated by

the application in dilution zone mixing in a combustor, the results can also be beneficial to many other applications involving cooling and/or drying process such as deicing, rapid drying of materials in the form of continuous sheets (e.g., tissue paper, photographic film, coated paper, textile webs, metal sheets, etc.).

## **1.5 Organization of Material**

Chapter 1 introduces the reader to a brief overview of the gas turbine system and the combustor requirements along with the identification of major challenges involved to improve the system efficiency as well as the life of the turbine blades, with emphasis on the improvement in the mixing process to produce a uniform temperature exit flow from the combustor.

Chapter 2 presents a broad overview of the existing literature and work done by researchers in the area of combustor simulators; to be more precise, in the field of dilution zone in the combustors. Both experimental and computational works are discussed in detail.

Chapter 3 gives an elaborate description of the experimental work taken up which include the design details of the experimental apparatus, dilution schemes and the procedure involved to test these schemes. The various measurement instruments and techniques used in this research are also described.

Chapter 4 deals with the three dimensional numerical simulations performed for parametric study. Details of the computational fluid dynamics (CFD) model - physical domain and mesh specifications; governing equations; turbulence model used; appropriate boundary conditions; etc., are also explained.

Chapter 5 discusses computational results and parametric study performed to take design decisions and study the effect of jet-to-mainstream momentum flux ratio on the exit temperature uniformity. Details of the variation of the cooling rate number (CRN) to predict the rapid cooling regions inside the dilution zone are presented. Lastly, the exergy analysis is included in the chapter to assess the amount of work lost with the increase in the jet-to-mainstream momentum flux ratio.

Chapter 6 presents the experimental results and comparison of the various passive dilution techniques to come up with the design which gives the most uniform temperature at the exit section. Details of the experimental cases considered and their findings are elaborated in this chapter, along with a couple of more definitions of the variables defined to illustrate the improvement in the mixing process with various dilution techniques.

Chapter 7 presents the formulation of Algebraic Stress Model for Reynolds stress determination. Motivation for the ASM model and limitations of the eddy viscosity models are discussed with a detailed derivation of the model and relevant assumptions made.

Chapter 8 deals with the validation of the ASM model developed in Chapter 7 for a simple two-dimensional flow over flat plate and a complex three dimensional flow around Ahmed body. Complete procedure of the numerical methodology and experimental data acquisition is provided in the chapter. A detailed description of the hot-wire anemometry and error analysis is also presented.

Finally, Chapter 9 presents some concluding remarks on this research. In addition, potential areas of future research on this topic are also identified.

## **Chapter 2 - Literature Review**

Over the years, numerous techniques have been developed to introduce the cooler air jets into the dilution zone in the combustor to mix with the incoming combustion gases and produce a temperature profile which is uniform enough to be handled by the first stage turbine blades without any detrimental effects. Still, the presence of hot streaks in the flow field at the combustor exit demands for improvement in the dilution zone mixing. A broad literature survey was conducted to compile the large amounts of data in existence and to highlight the importance of dilution zone mixing in producing a uniform temperature exit flow from the combustor. The first section of this chapter presents experimental studies conducted on non-reacting combustor simulators including the studies on mixing of confined jets, which closely resembles the mixing phenomenon in the dilution zone. The second section presents numerical/computational studies on reacting and non-reacting combustor simulators with experimental validation of results. This section is followed by a summary of all the literature discussed.

### **2.1 Experimental Studies on Non-Reacting Flows**

Experimental work plays a vital role to provide the ultimate check on any analysis and/or computation performed on any system. An experimental mixing study was undertaken by Norgren and Humenik (1968) to evaluate various dilution-jet entry schemes to achieve acceptable outlet-temperature profile for short-length combustors. Diluent and hot streams with a velocity ratio from 0.55 to 2.20 were introduced into a

rectangular configuration exhausting directly to the atmosphere. The mixed-stream exhaust temperature was in the order of 417 K to 542 K. Test conditions were representative to scaled-engine operation by geometric, velocity, and Reynolds number similarity. Outlet-temperature profiles were obtained for rectangular-slot configurations with (1) flush openings, (2) attached scoops immersed in the diluent-air stream, and (3) attached chutes immersed in the hot-air stream (refer Fig. 2.1). The geometry of the rectangular slots was further varied in four patterns. The four basic pattern variations used with rectangular slots consisted of two different slot spacings (One spacing was equivalent to the turbine blade height, and the other spacing to one-half of the turbine blade height) with the row of slots in the upper plate either in line or staggered with respect to the lower plate to allow reinforcement or interleaving of the jets. Marked differences in both the degree of mixing and the apparent nature of the mixing process were encountered. The configurations which provided the most uniform outlet temperature profiles included all three of the basic types of dilution-air entry apertures, flush holes, holes with external scoops, and holes with internal chutes. Hence, no clear superiority was indicated for any type of dilution aperture, and a good temperature profile can be obtained with any of the three basic apertures. Additionally, mixing was improved for flush holes of rectangular shape both with or without external scoops by enlarging the holes and increasing the hole spacing.

The mixing of multiple air jets with a subsonic heated cross-flow in a constant area duct was studied experimentally by Holdeman *et al.* (1973). The jet-to-mainstream momentum flux ratio was varied from 6 to 60. Temperature and pressure surveys were made at several downstream locations for orifice geometries with parametric variation of

orifice size and spacing. A mixing efficiency parameter was defined which characterized the effectiveness of the mixing over the range of conditions examined. It was found that for a given momentum flux ratio, there exists a ratio of orifice spacing to duct height which provides the best mixing. Furthermore, it was observed that the jet-to-mainstream momentum flux ratio is the most important operating variable influencing the mixing. The mixing efficiency was found to increase with increasing flux ratio. Also, for a given orifice diameter, the uniformity in the vertical temperature distribution was improved by increasing the spacing between orifices.

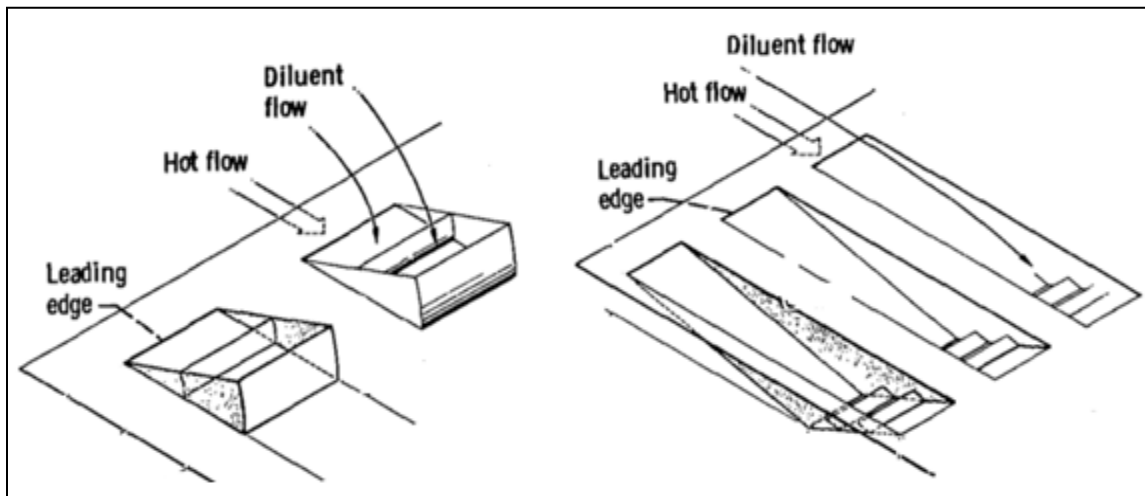


**Figure 2.1** Schematic of plate hole with (a) external scoop, and (b) internal chute used by Norgren and Humenik (1968).

Wittig *et al.* (1984) performed experimental and theoretical study of the mixing process between rows of jets and a hot confined cross-flow. Schematic of the experimental facility used in their study is shown in Fig. 2.2. Both single and opposite-wall injection with equal and different momentum flux ratios of each row of jets were investigated. The initial temperature difference between the primary and the mixing jet flow was generated by passing the primary air flow through an electric heater ( $\Delta T \cong$

350°C). With the aid of the experimental results of the temperature profile developed for the two cases, the applicability and limitations of the empirical multiple jet correlations for the case of double wall, directly opposite jets have been demonstrated. It was found that the geometry and momentum flux ratios are the dominant parameters. Also, large deviations were found between experiment and correlation for higher differences in the momentum flux ratios for opposite jet injection.

Stevens and Carrotte (1988) carried out an experimental investigation to study circumferential irregularities in the temperature distribution downstream of a row of 16 heated jets injected into a confined annular cross-flow at a momentum flux ratio of 4. Measurements of both temperature and velocity in planes parallel and perpendicular to the injection wall indicated the influence of the exit velocity profiles on the subsequent development of two jets. It was observed that the structure of a jet was modified by the exit velocity profile causing distortions of the temperature distribution about the hole center-plane. Further, since each jet has its own mixing characteristics an irregular temperature pattern around the dilution annulus was produced.

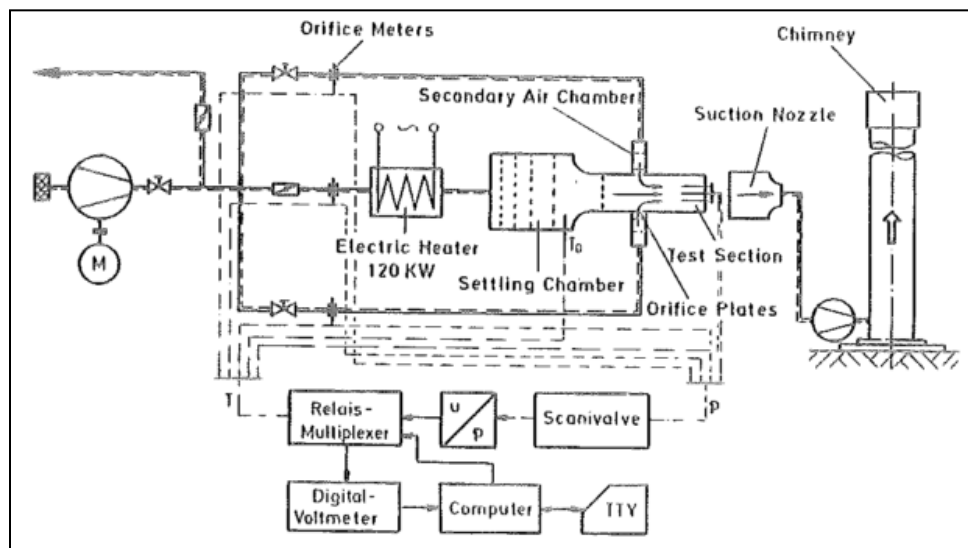


**Figure 2.2** Schematic of the experimental facility used by Wittig *et al.* (1984).

A study of turbulent mixing of two confined jets in a side-dump combustor was carried out by Liou *et al.* (1991). The sketch of configuration, coordinate system and dimensions of the test section used by them is shown in Fig. 2.3. The side-inlet angle was varied from  $15^\circ$  to  $135^\circ$ , air-to-fuel ratio from 1.8 to 6.4 and combustor Reynolds number from  $1.1 \times 10^4$  to  $5.9 \times 10^4$ , respectively, to investigate their effects on the flow and mixing patterns. From their study, it was concluded that the flow and mixing patterns in the side-dump combustor strongly depends on the side-inlet angle. There exists a critical side-inlet angle  $\theta = 45^\circ$ , below which the position of the large recirculating zone is shifted from the upper wall side to the bottom wall side and the number of re-circulating zones increased with decreasing  $\theta$ . In addition, it was found that at a given combustor Reynolds number and axial station, the uniformity of mixing increases with increasing A/F due to increasing strength of jet impingement. This observation strengthens the importance of the jet-to-mainstream momentum flux ratio, in line with earlier studies made by Holdeman *et al.* (1973) and Wittig *et al.* (1984).

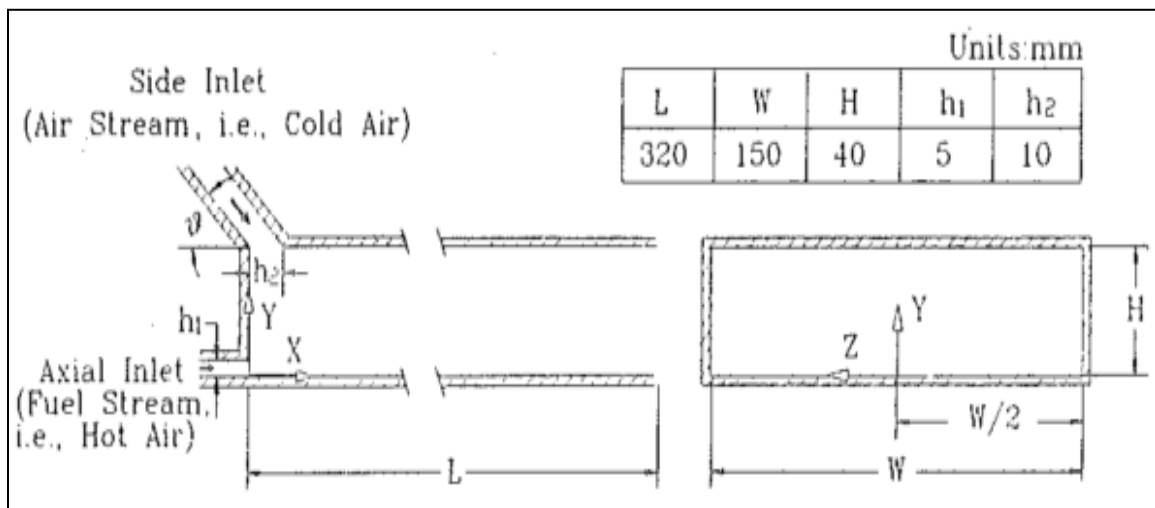


**Figure 2.3** Sketch of configuration, coordinate system and dimensions of the test section used by Liou *et al.* (1991).



To further his studies in the field of mixing of jets, Holdeman (1993) performed a series of experiments for single, double and opposed rows of jets with an isothermal or variable temperature mainstream in a confined subsonic cross-flow. The different orifice configurations studied are shown in Fig. 2.4. The principal observation from the experiments were that the momentum-flux ratio was the most significant flow variable and that temperature distribution were similar, independent of orifice diameter, when the orifice spacing and the square-root of the momentum-flux ratio were inversely proportional. For orifices that were symmetric with respect to the main flow direction, the effects of shape were significant only within the first few jet diameters downstream from the injection plane. Also, the penetration of slots slanted with respect to the main flow direction was less than for the circular holes or slots aligned with, or perpendicular to, the main flow. Furthermore, the exit temperature distributions for single-sided, single and double rows of jet injection were very similar indicating only slightly better mixing for the double row case (staggered, dissimilar and in-line). For the cases involving inline, opposed rows of jets, the two streams were mixed very rapidly. For opposed rows of staggered jets, optimum ratio of orifice spacing to duct height was twice the value for single-sided injection at the same momentum-flux ratio.

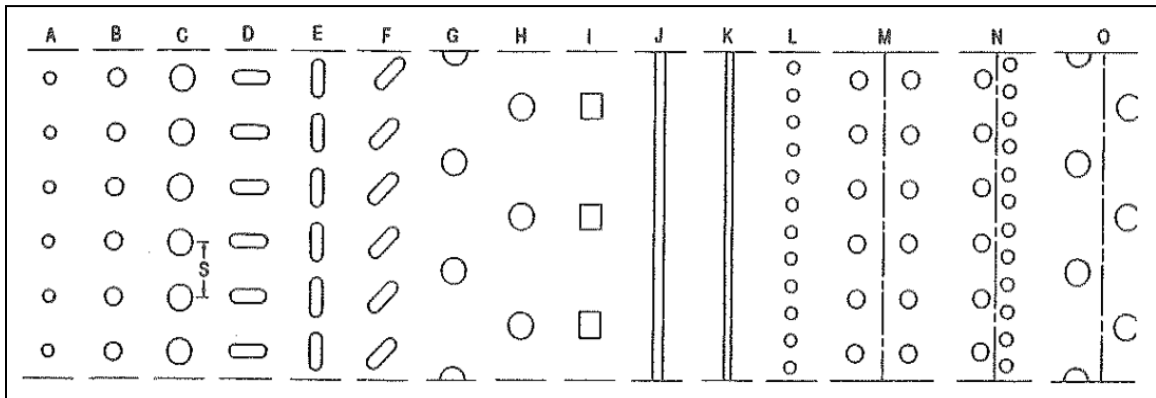


**Figure 2.4** Orifice configurations tested by Holdeman (1993).

Hatch *et al.* (1995) conducted experiments to study the geometry and flow influences on jet mixing in a cylindrical duct. To examine the mixing characteristics of jets in an axisymmetric can geometry, temperature measurements were obtained downstream of a row of cold jets injected into a heated cross stream. Results show that jet-to-mainstream momentum flux ratio and orifice geometry significantly impact the mixing characteristics of jets in a can geometry. Also, it was found that for a fixed number of orifices, the coupling between momentum-flux ratio and injector geometry determines (i) the degree of jet penetration at the injection plane, and (ii) the extent of circumferential mixing downstream of the injection plane. Additionally, for a fixed momentum-flux ratio, jet penetration was found to decrease with (i) an increase in slanted slot aspect ratio, and (ii) an increase in the angle of the slots with respect to the mainstream direction. Furthermore, they concluded that from an overall-mixing standpoint, moderate penetration to the center was desirable. Under-penetration forms a relatively unmixed core that persists at downstream locations. Over-penetration degrades circumferential mixing and forms unmixed regions along the walls.

Doerr *et al.* (1997) performed series of experiments to study the mixing of non-reacting multiple jets with a confined cross-flow. The jets were perpendicularly injected out of one opposed row of circular orifices into a rectangular duct (refer Fig. 2.5). Several mixing configurations were tested varying the momentum flux ratio and it was observed that mixing quality depends strongly on momentum flux ratio, hole size and spacing. For each geometry an optimum momentum flux ratio was determined using the mixing rate,  $\epsilon$  defined by Eqn. 2.1:

$$\epsilon = \frac{1}{n} \sum_{i=1}^n \epsilon_i \quad (2.1)$$

where,

$$\epsilon_i = \begin{cases} \frac{T_i - T_j}{T_{adb} - T_j} & \text{for } T_j < T_i < T_{adb} \\ \frac{T_i - T_\infty}{T_{adb} - T_\infty} & \text{for } T_{adb} < T_i < T_\infty \end{cases} \quad (2.2)$$

$$T_{adb} = \frac{\dot{m}_\infty T_\infty + \dot{m}_j T_j}{\dot{m}_\infty + \dot{m}_j} \quad (2.3)$$

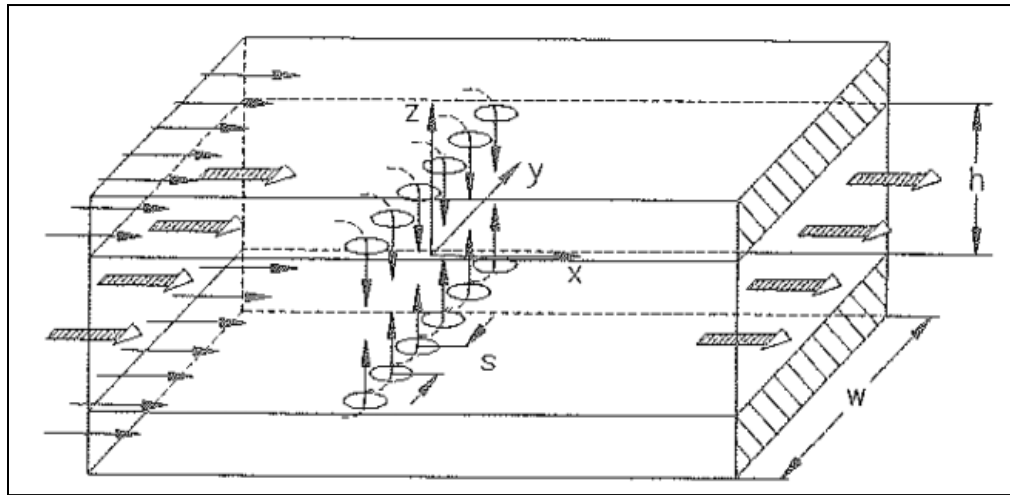


**Figure 2.5** Schematic of multiple jet mixing used by Doerr *et al.* (1997).

Wang *et al.* (2000) conducted an experimental program to focus on investigating the flow mixing behavior inside the slots. Contrary to the studies discussed so far, here, the temperature of the jet was greater than that of the primary flow by approximately 10°C ( $T_j \approx 50^\circ\text{C}$ ,  $T_\infty \approx 40^\circ\text{C}$ ). Figure 2.6 shows an enlarged view of the slot jet geometry used in their experiment. Various parameters including orientation angle, inclination angle, slot width, effect of primary flow and slot depth were systematically

examined to study its effect on the velocity and pressure uniformity of the exit flow. The results indicated that the flow distribution at the slot exit becomes more uniform as the orientation angle was increased from  $0^\circ$  to  $60^\circ$ . Wider slot width brought about high non-uniformity and was clearly undesirable.

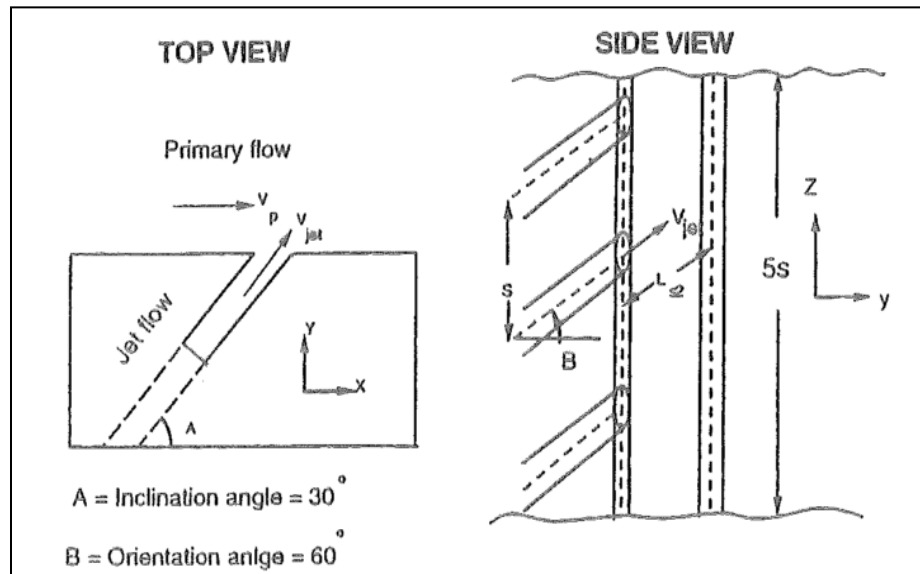


**Figure 2.6** Enlarged test section configuration used by Wang *et al.* (2000).

Barringer *et al.* (2002) performed experiments on a combustor simulator, to study the effects of dilution jets with regard to the downstream velocity and thermal flow fields. The geometrical details of the primary flow path used in the experiment is shown in Fig. 2.7. Flow and thermal field measurements made at the exit of the simulator put in question the accuracy in assuming either a constant total pressure field or a turbulent boundary layer approaching the turbine vane-endwall juncture. The thermal field contours suggested that the dilution jets increased the mixing of the coolant, provided by the upstream film-cooling panels, into the mainstream flow. The mixing implied a lack of available cooling along the downstream turbine vane endwall and verified the notion of dilution jets strongly affecting the various fields exiting the combustor.

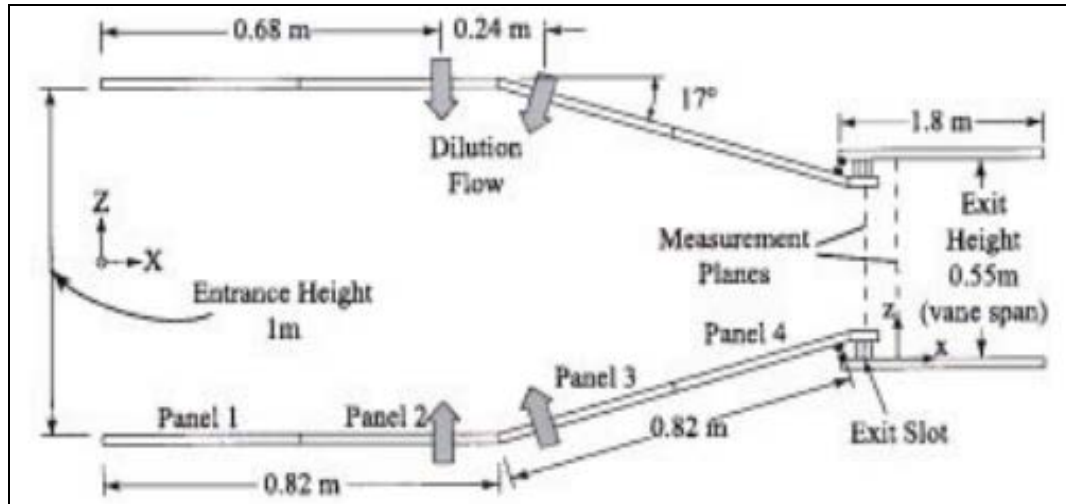


**Figure 2.7** Geometrical details of test section used by Barringer *et al.* (2002).

Vakil and Thole (2005) conducted experimental studies on the same combustor simulator as used by Barringer *et al.* (2002) to quantify the flow and thermal field conditions for a prototypical combustor design that is non-reacting. Their results indicate large penetration depths for the high momentum dilution jets, which result in a highly turbulent flow field. Downstream of the dilution jet injection, there was a large re-circulating region that transported warm fluid into the region just downstream of the injection.

Experimental study on combustor outlet temperature field of heavy-duty gas turbine on high-pressure test system was conducted by Liukai and Xuli (2012). Their experimental results indicate that the circumferential temperature distribution factor (OTDF) is sensitive to the diameter of the dilution holes and the radial temperature distribution factor (RTDF) is sensitive to location of dilution holes.

Another interesting study was performed by Sheu *et al.* (2012) on mixing of split and recombined micromixer with tapered curved microchannels. The authors designed a parallel laminar micromixer with two-dimensional curved rectangular channels to

investigate the mixing of two fluids. Figure 2.8 shows the micromixer used for their study. The centrifugal forces in curved channels cause fluids to produce vortex flows. The split and recombine (SAR) structures of the flow channels result in the reduction of the diffusion distance of two fluids. Furthermore, the impingement effects caused by the staggered configuration of the mixer increase the mixing strength when one fluid flowing along the tapered channel is injected into the other fluid. The authors concluded that the uneven split of the fluids inside the staggered curved channels with tapered structures can improve the mixing performance.

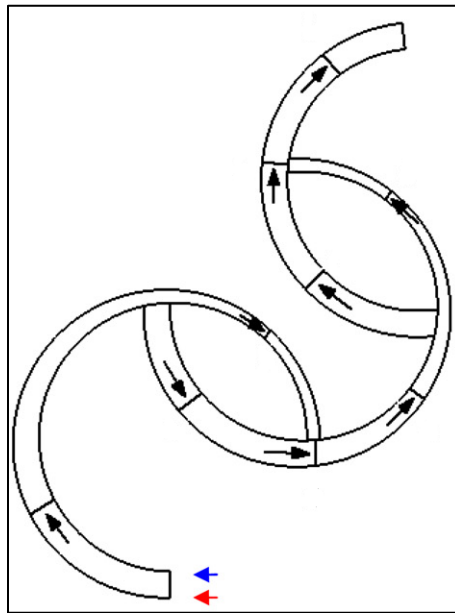


**Figure 2.8** Split and recombine micromixer used by Sheu *et al.* (2012).

Similar to the chute mixing concept utilized by Norgen and Humenik (1968), Ahmed *et al.* (2000) performed an experimental investigation on turbulent mixing enhancement in confined, co-axial jets using chute mixer configuration. The authors studied the influence of chute geometry on the turbulent mixing of two co-axial streams by using two chute mixer configuration having  $10^\circ$  and  $20^\circ$  angles of penetration of the

annular stream towards the core region at a velocity ratio of 1.8. Figure 2.9 shows the schematic details of the chutes used in their experiment. From the contours of mean velocity, streamwise and transverse turbulent intensities close to the injection points, it was found that the chutes improved the mixing. With the chute model having  $20^\circ$  angle of penetration, nearly complete mixing was achieved at a distance of 2.2 duct radii itself, suggesting feasibility of shortening of the duct by about 50%. However, a higher total pressure loss of about 1.7% was the penalty to be paid for enhanced mixing of the jets. The effect of use of  $20^\circ$  angle chute mixer was further investigated by Ahmed and Sharma (2006). The transverse turbulence component was found to be much stronger immediately downstream of the chute exit, causing rapid mixing in the transverse direction. The total turbulence generation was found to be more than twice with chutes compared to the case without chutes, which seemed to be the prime cause of enhanced mixing.

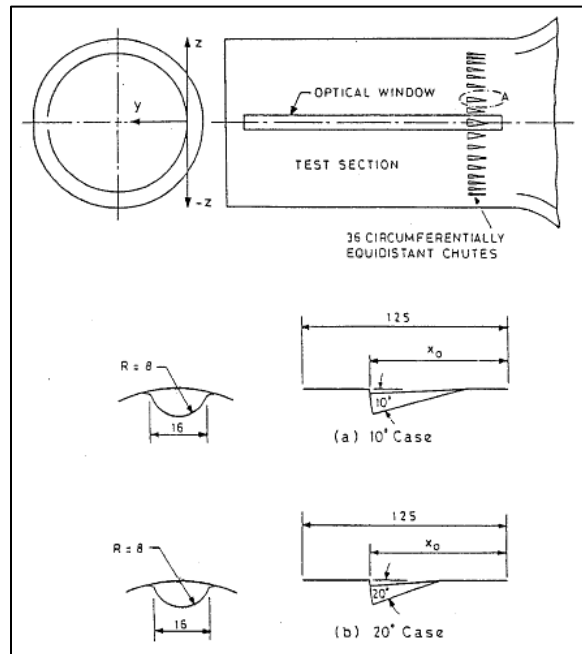


**Figure 2.9** Schematic details of chutes with  $10^\circ$  and  $20^\circ$  angles of injection used by Ahmed *et al.* (2000).

## 2.2 Computational Studies on Non-Reacting/Reacting Flows

The following studies concentrate on the results of computational simulations and experimental validations for non-reacting/reacting flows within combustor simulators. The findings support the notion that although computations are beneficial in providing general flow characteristics, the lack of a true turbulence model leaves the need for experiments to truly characterize the mixing and turbulence within a combustor.

Talpallikar *et al.* (1992) numerically studied the jet mixing in a cylindrical quick-mix section. Their study sought to investigate the influence of jet-to-mainstream momentum flux ratio and slot aspect ratio on mixing effectiveness in a RQL (Rich-burn/Quick-mix/Lean-burn) flame-tube combustor. Both reacting and non-reacting analyses were performed. Here, only the non-reacting results are discussed. The schematic of the quick-mix section used in their study is shown in Fig. 2.10. Twelve rectangular slots were located symmetrically around the perimeter of the quick-mix section. Due to geometric symmetry, only one slot was modeled with planes of symmetry set up halfway between adjacent slots. They used an advanced CFD code, REFLEQS for the computations. The problem was investigated using the standard  $k - \epsilon$  model with wall functions. For the non-reacting flow, as expected, increased jet penetration was observed for larger value of the momentum-flux ratio.

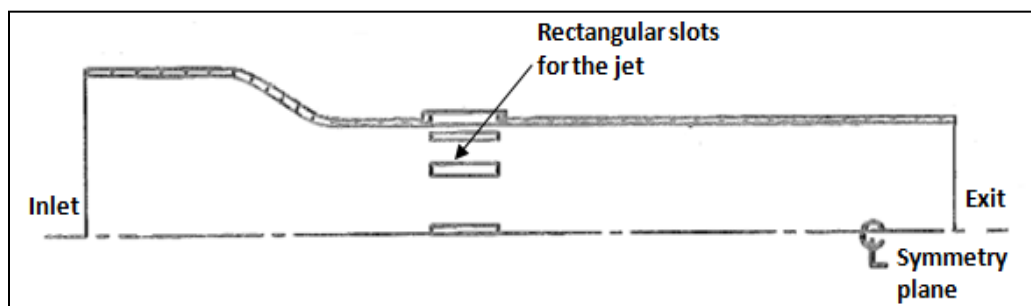


**Figure 2.10** Schematic of the quick-mix section used by Talpallikar *et al.* (1992).



Holdeman (1993) studied the mixing of multiple jets with a confined subsonic cross-flow by using the numerical scheme and the pressure-velocity solution algorithm adapted from the techniques described by Spalding (1972), Patankar and Spalding (1972) and Patankar (1980). The numerical model calculations made with approximately 20,000 nodes using the standard  $k - \epsilon$  model, although in qualitative agreement with their experimental data, showed temperature gradients that were too steep, especially in the transverse direction. The numerical calculations performed were shown to be grid sensitive and false diffusion was known to be present, which clearly questions the validity of the turbulence model used.

An advanced method for dilution zone mixing in a reverse flow gas turbine combustor was numerically investigated by Crocker and Smith (1995). Their advanced dilution hole concept (refer Fig. 2.11) consisted of injecting the dilution air jets angled to produce a high circumferential (swirl) velocity component. The jets on the outer liner were angled in one direction while the jets on the inner liner were angled in the opposite direction, thus enhancing turbulent shear at the expense of jet penetration. They used the code CFD-ACE by Owens (1992) to perform the computations for the reacting flow using the standard  $k - \epsilon$  model for turbulence and one-step reaction kinetics model for the primary zone with premixed fuel and air inlet. The results of the numerical tests showed that this concept has the potential for reducing the profile factor defined by Eqn. 2.4, as much 60% compared to the base-line dilution configuration.

$$pf = \frac{T_{max} - T_{exit}}{T_{exit} - T_{inlet}} \quad (2.4)$$

Gulati *et al.* (1995) studied the effect of dilution air on the scalar flow field at the combustor sector exit. They applied the Spontaneous Raman diagnostics to the exit plane of a full-scale 10-cup double annular research combustor sector to obtain the mean and rms of temperature and mole fractions of the major species for comparison with predictions of the code CONCERT-3D for the same geometry and operating conditions. CONCERT-3D represents a fully elliptical three-dimensional computational fluid dynamics code to predict flow fields in practical full-scale combustors. Turbulence was modeled using the standard  $k - \epsilon$  model. The combustion model utilized a conserved scalar variable for the fuel mixture fraction with assumed probability density function (PDF) and a fast chemistry approach for the turbulence/chemistry interaction (Shyy *et al.*, 1988). Figure 2.12 presents an isometric view of the generated grid mesh used in their model. The mean and rms temperature profiles and mean profiles of the major species were predicted quite well by the model. Dilution air was shown to have a significant impact on the mean and rms temperature profiles at the sector exit. The mean temperature profile was forced inbound by the outer dilution air, whereas the inner dilution air forced the temperature profile to be center-peaked with lower peak values.

Su and Zhou (2000) performed numerical modeling of gas turbine combustor integrated with diffuser. Their simulation was based on the solution of Navier-Stokes equations with phenomenological models of turbulence, sprays and chemical reactions. A single dome sector of  $22.5^\circ$  span of the combustor, which includes a swirler and a fuel nozzle (at the inlet of the liner) and a set of primary and secondary holes (on the outer and inner walls of the liner) was simulated. Figure 2.13 shows the computational grid generated for the sector under consideration, which was solved using the KIVA-3V CFD

code. Combustion efficiency and overall temperature distribution factor (OTDF) were predicted in a reasonable agreement with those from semi-empirical correlation. The effects of non-uniform profiles of inlet velocity on the overall temperature distribution factor were investigated and it was found that OTDF (defined same as the  $pf$ , refer Eqn. 2.4), increases with the non-uniformity of the velocity profiles at the inlet of diffuser. Also, the circumferential non-uniform profile has a strong influence on the exit temperature distribution.

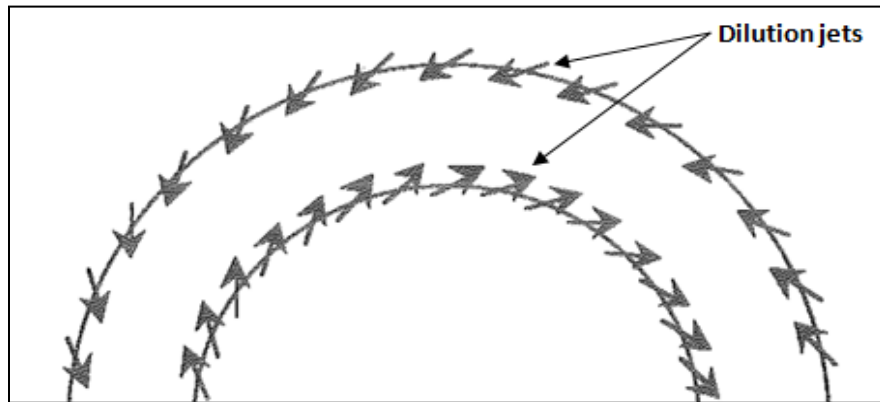


**Figure 2.11** Schematic of angled dilution jet concept used by Crocker & Smith (1995).

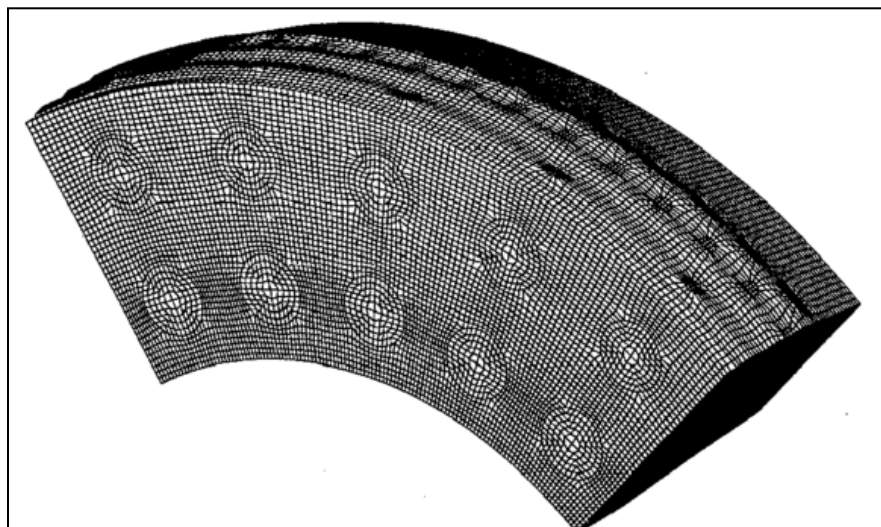


**Figure 2.12** Isometric three-dimensional view of computational grid for full five-cup sector modeling used by Gulati *et al.* (1995).

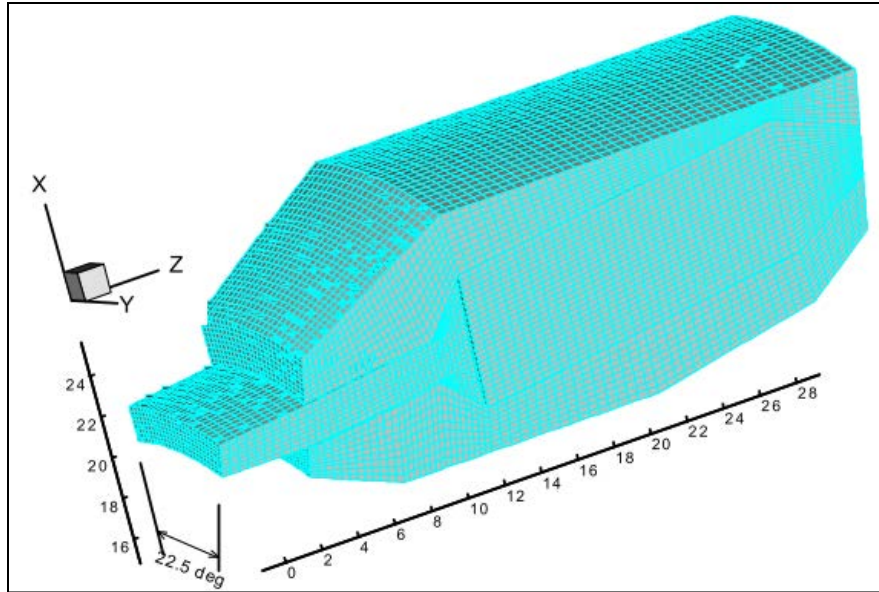


**Figure 2.13** Computational grid and dimensions (in cm) of a  $22.5^\circ$  sector of an annular combustor used by Su and Zhou (2000).

A row of jets discharging normally into a confined cylindrical cross-flow was numerically analyzed using the control-volume-based finite difference method by Tao *et al.* (2002). They presented a design procedure which can serve as an initial approach in configuration design. According to their procedure, for a given volume-flow ratio and number of nozzles, good mixing occurs when normalized penetration reaches values between 0.6 and 0.75. Further, for a given dynamic pressure ratio and number of nozzles, the jet penetrates deepest when nozzle spacing is between 2 and 5.

Wegner *et al.* (2004) used large eddy simulation (LES) methodology to investigate how turbulent mixing can be enhanced by varying the angle between the jet and the incoming crossflow. After validating the computations for  $90^\circ$  angle injection against measurements by Andreopoulos (1983) and Andreopoulos and Rodi (1984) to document the ability of the LES computations to precisely capture the flow and mixing phenomena in the investigated configuration, they analyzed qualitatively and

quantitatively the mixing process for three configuration with different angles ( $60^\circ$ ,  $90^\circ$  and  $120^\circ$ ). Their results showed that the inclination influences the characteristics of vortical structures and secondary motion which in turn have an effect on the mixing process. The time-averaged mixture fraction at several axial positions for all three cases is shown in Fig. 2.14. It can be directly observed that the fluid coming from the jet is spread fastest in the  $120^\circ$ -case where the jet is injected against the cross-flow direction and slowest in the  $60^\circ$ -case. Thus, from an engineering point of view it seems favorable to inject the jet at an angle inclined against the incoming main flow.

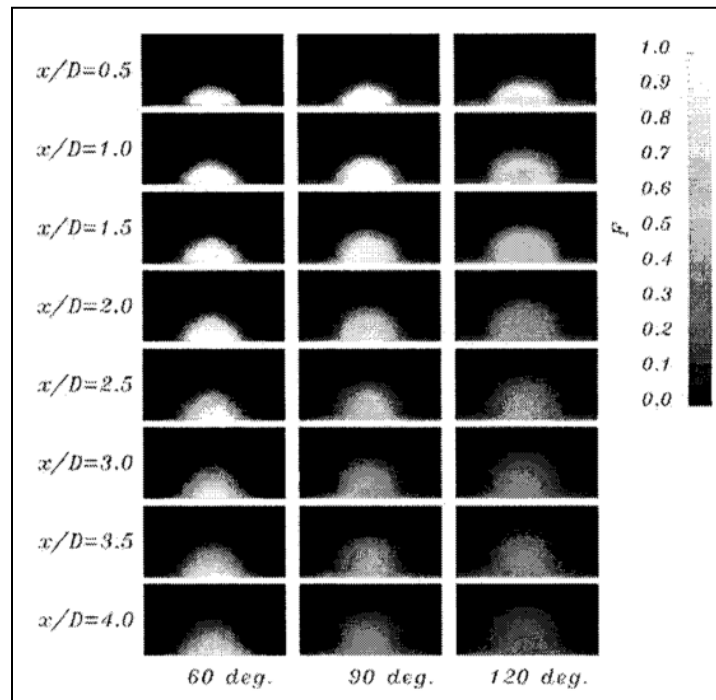


**Figure 2.14** Mean mixture fraction at several axial positions. Left:  $60^\circ$ -case, middle:  $90^\circ$ -case, right:  $120^\circ$ -case obtained by Wegner *et al.* (2004).

A small annular combustor of a micro gas turbine fuelled with methane was investigated numerically in order to improve the overall efficiency of the small engines by Iki *et al.* (2008). They used the general purpose CFD code SPIDER to model the turbulent reactive flow in the combustion chamber with a standard  $k - \epsilon$  model and the

EDC turbulent combustion model. Their numerical results matched to some extent with their experimental data at start-up, but at full-load large difference emerged between the computed and the measured temperatures. One possible explanation for the observed discrepancy can be found in the fact that at full-load conditions boundary layer effects become more important than at the start-up conditions due to increased fluid velocity throughout the combustor. The CFD model seems to be unable to correctly predict the temperature measured by the thermocouples that are placed very close to the combustor inner liner wall. Furthermore, the subsequent optimization analysis, conducted with respect to combustion efficiency (amount of UHC), pattern factor of the temperature profile at the combustor exit plane and combustor pressure loss, showed that a considerable improvement in engine operation could be achieved by inverting the air flow ratio between the inner and outer liner of the combustor.

Motsamai *et al.* (2008) presented a technique that entailed the use of computational fluid dynamics (CFD) and mathematical optimization to optimize the combustor exit temperature profile. They used the combustor parameters as the optimization variable since the optimum (uniform) combustor exit temperature profile mainly depends on the geometric parameters. The combustor investigated was an experimental liquid-fuelled atmospheric combustor with a turbulent diffusion flame. The CFD simulations used the FLUENT code with a standard  $k - \epsilon$  model. The optimization was carried out using the Dynamic-Q algorithm, which is specifically designed to handle constrained problems where the objective and constraint functions are expensive to evaluate. Design variables which directly affect the exit temperature profile, i.e., the number of holes and the radii of both the dilution and secondary holes were optimized,

using the combustor exit temperature profile approximated from the CFD results as the basis for optimization. The methodology was used to obtain a more uniform combustor exit temperature profile by optimizing the combustor with two dilution hole variables for Case 1 and four design variables (for dilution holes and secondary holes) for Case 2. Increasing the number of design variables from two (Case 1) to four (Case 2) provided an optimum which fell within acceptable limits of pressure loss. The optimization returns a significant improvement in the combustor exit temperature profile, in particular with respect to the pattern factor. Figure 2.15 shows the temperature contours at the combustor exit plane for both the non-optimized and the optimized cases. The temperature contours in Fig. 2.15 (b) are better than those in Fig. 2.15 (a). In Fig. 2.15 (a) there is a hot region in the centre and a cold region at mid-section, and a variation of cold and hot regions close to the combustor wall. This is caused by poor mixing because the number and diameter of dilution jets have not been optimized.

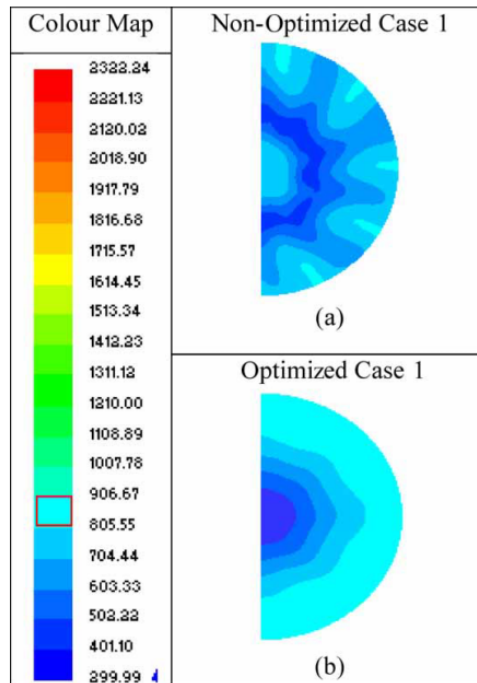


**Figure 2.15** Temperature contours for the non-optimized and optimized cases (Motsamai *et al.*, 2008).

Motsamai *et al.* (2010) validated their above discussed optimization methodology against the experimental results collected from Sayre *et al.* (1996), for an un-staged natural gas flame in a 200 kW industrial burner. A standard  $k - \epsilon$  model was investigated to assess its accuracy on reacting flows in a combustor. The agreement between the measurements and numerical results for velocity and temperature were found to be satisfactory. The curves for numerical predictions were in good consistency with the measurement in shape, but the accuracy in other locations was unsatisfactory.

Channwala and Kulshreshtha (2010) presented the design of tubular and annular combustion chamber followed by 3-D simulations with full film cooling to investigate the velocity profile, species concentration and temperature distribution within the liner. The SST  $k - \omega$  turbulence model and a combustion model comprising of an assumed probability density function flamelet concept is employed. An attempt has been made through CFD approach using CFX 12 to analyze the flow patterns within the combustion liner and through different air admission holes, namely, primary zone, intermediate zone, dilution zone and wall cooling, and from these the temperature distribution in the liner and at the walls as well as the temperature quality at the exit of the combustion chamber was obtained. High velocity from primary and dilution air admission holes of the order of 110 m/s was witnessed. Such high velocity from the air admission holes ensures high static pressure drop which is advantageous in mixing through air admission holes.

A numerical method using AUSMDV (advection upstream splitting method) scheme and  $k - \omega$  turbulence model with an explicit compressibility correction was developed and a 3-D numerical simulation of a supersonic flow field with a vertical sonic jet of hydrogen was performed by ZhenXun and ChunHian (2011). Good agreement



between numerical results and experimental data validated the reliability of the numerical method. Thereafter, two parameters, mass-weighted average total pressure and mixing efficiency, were defined to evaluate the mixing performance of different injection schemes. Comparison of slot injection and circular-hole injection reveals that, the latter cause comparable loss of total pressure with the slot injection, but can induce much higher mixing efficiency because of its 3-D flow characteristic. In addition, the variation of injection angle under circular-hole injection was found to affect the near-field mixing degree and among the five injection angles ( $30^\circ$ ,  $60^\circ$ ,  $90^\circ$ ,  $120^\circ$  and  $150^\circ$ ) studied in their work, angle  $120^\circ$  was the optimal one. Lilley (2011) studied the swirling flows and lateral jet injection for improved mixing and combustion. He found that the lateral jet velocities, flow rates and injection angles all affect the extent of mixing, turbulence levels and reaction rates in the combustor.

## 2.3 Summary

Though a lot of research has taken place in the field of dilution zone mixing in a combustor both experimental and computational, there are specific issues that need to be addressed with respect to temperature uniformity of the exit flow from the combustor. As discussed in Sec. 2.1 and 2.2, the factors which significantly affect the uniformity of the temperature are the jet-to-mainstream momentum flux ratio and the geometry (size, cross-section, spacing, etc.) of the dilution holes. Overall, it is generally accepted that the combustion process in a gas turbine engine is largely dependent on the mixing processes, with evaporation and chemical kinetics playing only minor roles (Lefevbre, 1984). The main factor which effects the combustor exit temperature distribution is the dilution zone

mixing followed by the temperature profile leaving the primary zone of the combustor. Although a number of methods have been proposed which mainly concentrates on the location of the dilution holes, shape of the holes, hole diameter, flush openings, attached scoops immersed in diluent air stream, use of synthetic jet actuators, angled dilution jets, etc. (Gobbato *et al.*, 2012, Liukai and Xuli, 2012, Chen *et al.*, 1999, Crocker and Smith, 1995, Hatch *et al.*, 1995, Holdeman, 1993) to improve the mixing in the dilution zone, there is scope of further research to make these methods perform better by introduction of streamlined body, guide vanes, etc. This work is an attempt to investigate these newer methods to enhance mixing in the dilution zone and produce a more uniform temperature flow at the combustor exit, which will reduce the detrimental effect the non-uniformities in flow have on the first stage turbine blades and increase their life span.

## **Chapter 3 - Combustor Model Test Section Design**

The main aim of this study is to improve the mixing process in the dilution zone of a combustor by exploring new techniques - use of streamlined body, guide vanes and understand the complex thermal and velocity fields within a combustor. To achieve these objectives, the first step is to design a non-reacting combustor test facility necessary to simulate the geometry and flow conditions of a realistic gas turbine engine combustor. A key to acquire accurate and representative data is to have a reliable and good measurement resolution supported by proper measurement apparatus and techniques. This chapter outlines the basic design process and instrumentation of the combustor simulator used in this research. The first section of this chapter deals with the design calculations and specifications of the experimental facility constructed as part of this work. Next, the various measurement equipments and methods used in this study are described in detail followed by details of the test cases designed for the different proposed dilution schemes. The last section of this chapter describes the test procedure followed.

The combustor which was simulated is typical of an annular combustor in a commercial gas turbine engine. The geometry is characterized by a dilution test section which consists of four rows of staggered dilution holes with different radii. The test section was modified according to the dilution scheme tested such as addition of streamlined body/guide vanes. The combustor has a constant cross-section until the test section where the cross-section converges and then leads into a constant area exit section.

### 3.1 Design Process and Specifications of Experimental Set-up

The purpose of this section is to describe the design process of constructing the non-reacting combustor model with specifications of its supportive instrumentation. Based on the details of the rectangular cross-section experimental set-up presented in Barringer *et al.* (2002), their design was modified into a circular cross-section case so as to relate the experimental set-up more closely to the real annular combustor which are used in industries. Figure 3.1 shows the schematic of the arrangement of the main components of the experimental set-up. The total flow was split into primary and dilution streams. The diluent air was directed through the dilution holes via the secondary duct into the test-section and the primary flow was directed through the primary passage via primary duct of the combustor simulator. The flow distribution was regulated with the help of volume dampers. The primary air was heated by passing it through an array of heaters and then it was diluted with cooler air entering through the dilution holes into the test section. The temperature difference between the primary and the dilution streams was controlled by choosing an appropriate number of heaters to operate at a particular time. Taking advantage of the symmetry of the cylindrical combustor simulator, data was recorded for temperature and velocity along a radial line at the combustor exit. At last the collected data was analyzed to check the effectiveness of the dilution scheme to produce a uniform temperature flow ready for entry to the turbine.

The duct sizing was chosen large enough to allow for good spatial measurement resolution, keeping in mind at the same time that the measurements should not be altered by the measuring devices itself. Taking this into consideration and the dimensions of Barringer *et al.* (2002), the exit section of the current experimental set-up was set to a

diameter of 0.3 m, the test section comprised of two portions - conical frustum which was 0.2 m long with  $17^\circ$  slant angle, and the straight cylindrical piece of 0.4 m diameter and 0.2 m in length.

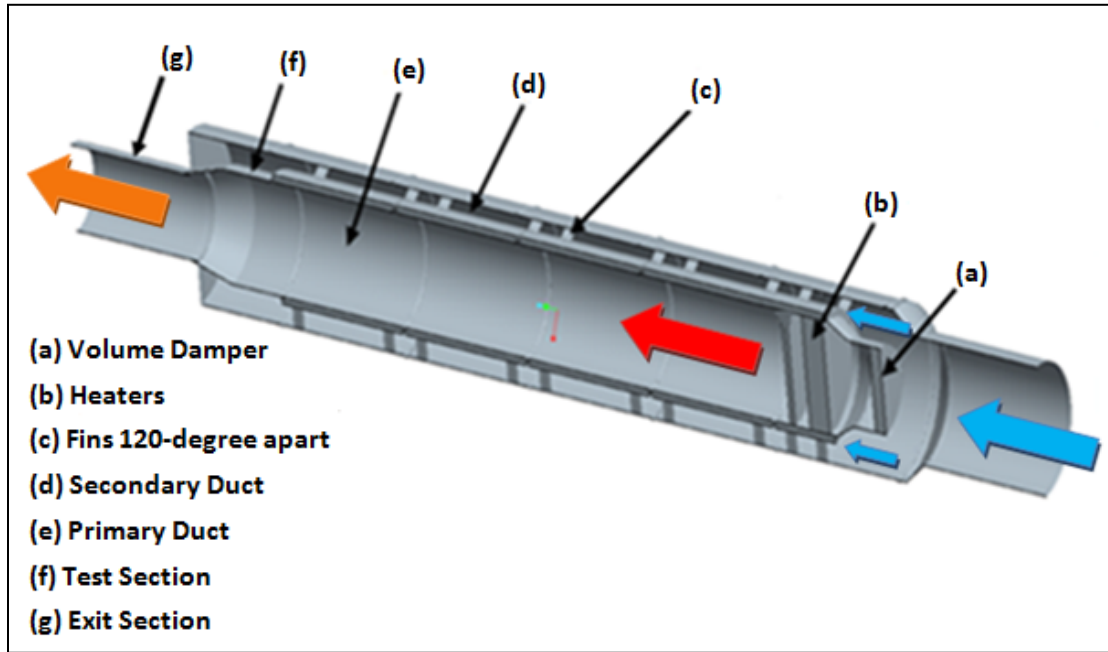


**Figure 3.1** Schematic of the arrangement of the main components of the experimental set-up.

With the primary (or inner) duct set to 0.4 m in diameter, the outer duct size was calculated for the same velocity as the primary air. The flow rate of the secondary (or dilution) air was kept at 55% of the total supplied flow rate, which is consistent with the general gas turbine applications; thus making the primary air flow rate equal to 45%. Assuming the same density and velocity for primary and secondary flow, the ratio between the inner cross-sectional area to the outer annular cross-sectional area was determined by Eqn. 3.1. From Eqn. 3.1, the diameter of the outer duct was calculated to be 0.6 m. Galvanized steel ducts with 18" gauge thickness were used in the set-up. A 2.5 cm thick glass wool cladding was introduced in between the two ducts after the heater section to insulate the primary heated flow to prevent any heat transfer prior to mixing in

the test section where the cooler dilution air enters through the dilution holes to lower the temperature of the primary heated air and obtain a uniform temperature flow at the exit of the combustor simulator. The properties of the glass wool insulation used are given in Table 3.1. Figure 3.2 shows the detailed dimensions of the duct work of the experimental set-up. The ducts are joined in parts to facilitate design changes for different dilution schemes and to provide easy access for maintenance purpose. The total length of the ducting from inlet to the exit section is approximately 4.675 m.

$$A_{outer\ annular} = \frac{0.55}{0.45} \times A_{inner} \quad (3.1)$$

**Table 3.1** Properties of Glass-wool.

<b>Density (kg/m<sup>3</sup>)</b>	<b>Specific Heat (J/kg-K)</b>	<b>Thermal Conductivity (W/m-K)</b>
40	670	0.04

The total air flow rate supplied by the fan was estimated to be 1.727 m<sup>3</sup>/s. Additionally the maximum total pressure drop for the critical path associated with the entire passage of the air starting from the fan right till the exit section was determined using an online software and equal to 124 Pa. With a factor of safety of 2, the fan was required to supply a pressure of 248 Pa at a 1.727 m<sup>3</sup>/s flow rate. Two volume dampers were installed in the set-up - one just after the fan and the other at the entrance to the primary duct to regulate the air supply in the two ducts. Figures 3.3 (a) - (c) show the axial fan blower installed on the fixture, the opposed blade volume damper used in the set-up and one of the larger heaters, respectively.

To get a relevant temperature profile at the combustor exit, the primary air temperature was raised by 20° above the secondary air by installing a bank of heaters in the primary air passage. Replicating the exact temperature distribution of the engine was not a priority, since the actual operation occurs at much higher combustion chamber inlet temperature and pressure conditions.

The required heat addition was determined using Eqn. 3.2 and heaters with combined capacity of 21 kW were mounted inside the inner duct in order to get the appropriate temperature difference at the desired flow rate. Four sets of smaller (1950 W, 240 V and 0.225 m radius) and larger (3700 W, 240 V and 0.368 m radius) circular fin-strip heating elements were connected together to provide approximately the required 21 kW of heat supply.

$$E = \dot{m}_{\infty} C_{p,air} \Delta T = \rho_{air} Q_{primary} C_{p,air} \Delta T \quad (3.2)$$

Each of these heaters can be manually controlled to regulate the temperature difference, if required. The manual control circuit comprised of a three position selector switch, an illuminated momentary push button and a contactor. Each of the six heater element contactor was electrically interlocked with the fan contactor to ensure that the heaters were not turned on without the air supply, thus to prevent the heaters from any accidental damage. Figure 3.4 shows the control panel used.

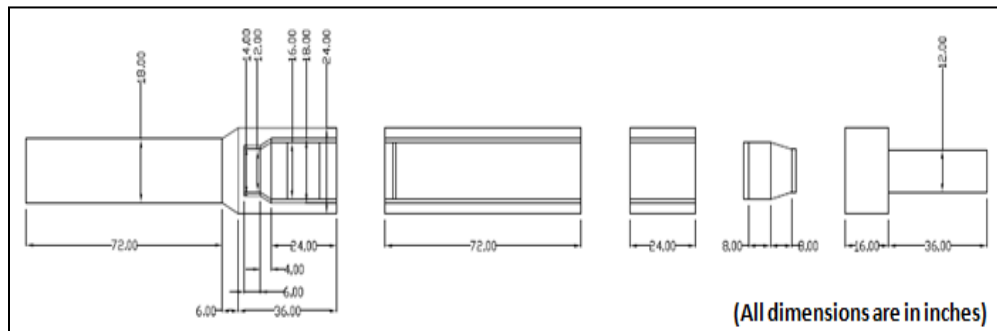


**Figure 3.2** Detailed dimensions of the duct work.



**Figure 3.3** (a) Fan installed on the fixture, (b) Volume damper, and (c) Heater.



**Figure 3.4** Control panel for all the heaters.



## **3.2 Experimental Instrumentation and Measurement**

### **Techniques**

This section focuses on describing the devices and techniques used for measurement of pressure, velocity and temperature at various points in the experimental set-up. Firstly, the details of the pressure and velocity measuring system used to set the proper flow within the combustor simulator are given. Next, the thermocouples and rakes used to make temperature measurements along with the data acquisition system and programs used to gather and process the temperature data are described in detail.

#### **3.2.1 Pressure and Velocity Measuring System**

A set of two pitot tubes were installed in the experimental facility - one at the entry to the test-section and the other in the exit section at 0.2 m distance away from the test-section outlet. These pitot tubes were connected to the transducer capable of giving the pressure as well as the velocity reading at a given point. All the necessary mass flow rates through the combustor simulator primary and secondary passages were set using the measured velocities and controlling the positions of the two volume dampers accordingly. Both the pressure and velocity was measured using a Dwyer Magnesense brand MS 121-LCD digital readout meter. The range of the pressure transducers employed in the experiment was 0-100 Pa. The setting of the same transducer can be modified to behave as a velocity transducer, by changing the position of the jumper in the circuit. The range of velocities that can be measured using this transducer varies from 0-28 m/s. The Dwyer transducers required 24 VDC supply which was provided by OTE DC Power Supply unit.

Figure 3.5 shows the pressure and velocity measuring system where the pitot tubes are mounted on a slider such that a single pitot tube can be used to measure the values for all the points along a radial line by sliding the pitot in or out accordingly. The transducers are secured on a wooden board to ensure a proper orientation.

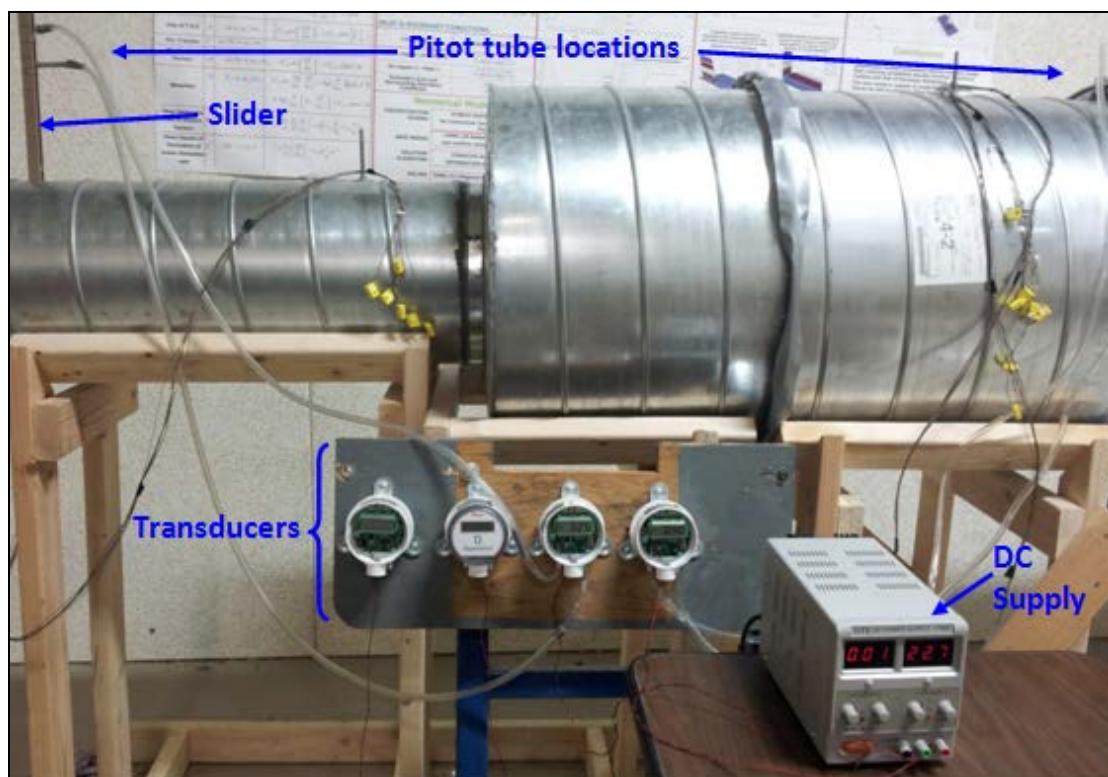


**Figure 3.5** Pressure and velocity measuring system.

### 3.2.2 Temperature Measuring and Data Acquisition System

Thermocouples were used to monitor temperatures in the primary (or mainstream) flow, secondary (or diluent) flow and in measuring the temperature field at the exit of the combustor simulator. The primary inlet temperature was measured using 6 thermocouples zip tied equally at a distance of 3.8 cm to a threaded rod to record the temperatures along

a radial line. One thermocouple was used in the annulus region to measure the inlet temperature of the diluent air. At the exit of the combustor simulator, 6 thermocouples zip tied equally at a distance of 2.5 cm to a threaded rod were utilized to collect the exit temperature data. All of the temperature measurements in this study were made using 30-gage type 'K' thermocouples provided by the Modine Manufacturing Company in Milwaukee. The thermocouple beads were made using a Tigtech argon-CO<sub>2</sub> thermocouple welder, which insured that no third metal was introduced. The use of a possible third metal could result in erroneous readings for it introduces another junction that was not accounted for in the calibration. Furthermore, by using a thermocouple welder, uniform and extremely small spherical beads are formed which results in a smaller thermal mass and minimal response time. These thermocouples were connected to the data acquisition box.

A data acquisition system manufactured by OMEGA was used in gathering all of the temperature data in this study. The system consisted of one terminal block, which served as the immediate connection for all the thermocouples and the DAQ card. On the user end, the software interface used to acquire and process all of the data was National Instruments LabView program. After recording the temperatures at the exit of the combustor simulator, the data is used to determine the temperature uniformity based on the mixture fraction of the exit flow. Figure 3.6 (a)-(d) shows the various components of the temperature measuring system used in the experiment.

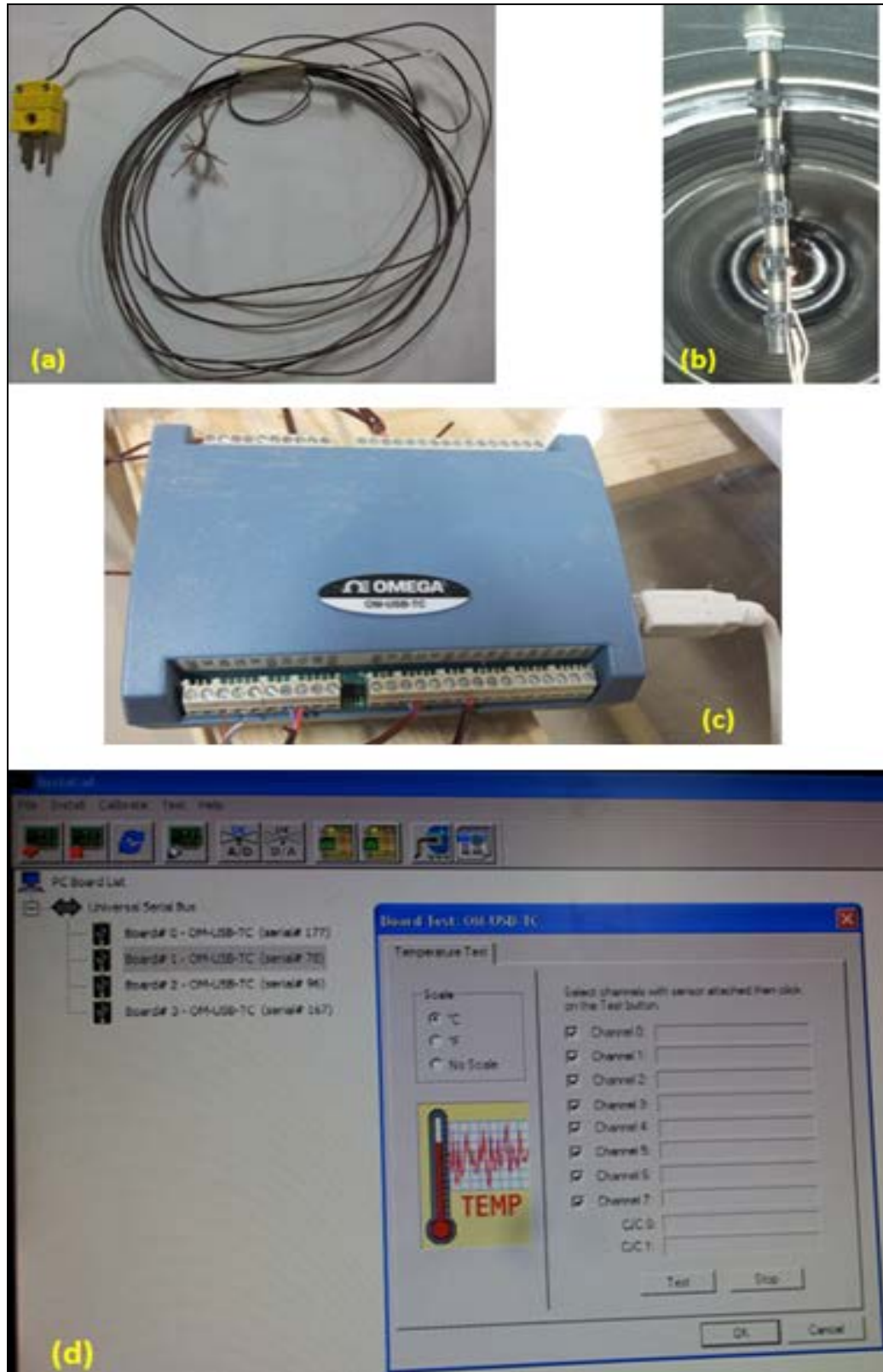


**Figure 3.6** Temperature measuring system (a) K-type thermocouple, (b) Zip tied thermocouples, (c) Block to connect to DAQ, (d) LabView program window to record the temperatures.

### 3.3 Description of Test Cases

A total of six test cases were modeled to determine the effect of the combustor geometry on the exit flow field. All the test cases were run on the same experimental facility with a design change within the test section to accommodate the dilution scheme being tested. These test cases were compared to come up with the most effective technique to produce a uniform temperature at the combustor exit. The following subsections focus on describing the details of the design modifications required in the test section for the corresponding scheme. Just to recall, the test section is a combination of cylindrical and conical frustum sections, each 0.2 m in length. The cylindrical section has the diameter of 0.4 m leading into a conical frustum with  $17^\circ$  slant angle. The test section is made of the same material as the rest of the ducting, which is galvanized steel. Figure 3.7 shows the dimensions of the test section and its Pro-E model.

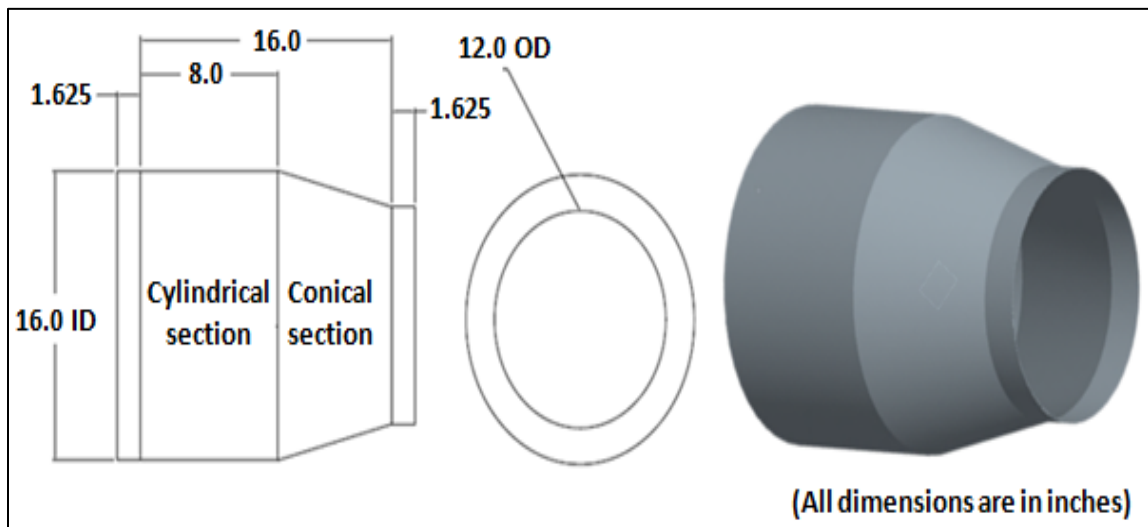


**Figure 3.7** Dimensions of the test section and its Pro-E model.

### 3.3.1 Staggered Dilution Holes

A lot of researchers have used the staggered holes pattern over the in-line holes pattern, as the former has the advantage of inter-leaving jets which leads to better mixing. Thus, in the current work, the staggered holes were tested. This dilution scheme forms the basis for comparison with the other schemes tested. Later, the same test section with staggered dilution holes was modified for the other proposed dilution techniques. Figure 3.8 (a) shows the detailed dimensions of the staggered dilution holes in the test section. Four rows of dilution holes were drilled in the test section with the help of a cutter. The two rows with larger holes of diameter 5 cm were located at 5 cm and 15 cm, respectively from the entrance to the cylindrical portion of the test section. While the rows of smaller holes with diameter of 2.5 cm were positioned at 5 cm and 10 cm, respectively from the entrance to the conical frustum portion. Each row consisted of 16 holes equally distributed circumferentially, thus making a total of 64 dilution holes in the test section. The second row was staggered with respect to the first one, as shown in Fig. 3.8. Figure 3.8 (b) shows the actual staggered dilution holes test section mounted in the experimental set-up.

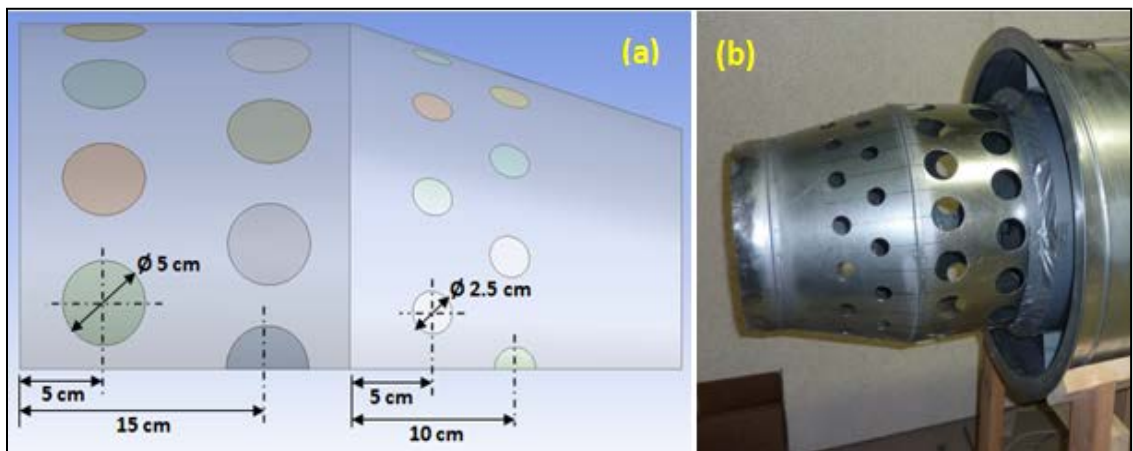


**Figure 3.8** Staggered dilution holes (a) Detailed dimensions, and (b) Actual mounted in the test section.

### 3.3.2 Staggered Dilution Holes with Streamlined Body

The use of streamlined body in the test section was based on the idea to push the primary hot air flow towards the cooler diluent air to enhance the mixing. The design utilized the concept of split and recombine (SAR) mixer of Sheu *et al.* (2012) which provided improved mixing as against the case of straight rectangular mixer. To achieve this deflection and SAR, the test section with staggered dilution holes was utilized and a streamlined body was installed in the middle of the test section. A streamlined body was chosen based on the aerodynamic advantage of its shape which offer minimal disturbance in the flow and keeps the flow attached and more defined around it. From Fig. 3.9 (b) it can be observed that the streamlined body is of prolate spheroid shape ("egg-shaped") with pointed ends which resembles the shape of an American football. Figure 3.9 (a) shows the details of the location and dimensions of the streamlined body designed. The length of the streamlined body was 30 cm with the largest radius 7.5 cm and radius of curvature 18.75 cm. The streamlined body was placed at a distance of 5 cm from the entrance to the test section. University of Wisconsin-Milwaukee CEAS rapid prototyping machine was used to make the streamlined body model. Since the temperature in the test section reach up to 60°C, the material used was ABS plastic which has high Melt Point of 108°C. The surface of the streamlined body was a pure plastic surface while the interior was sparsely filled (honey-comb) to save the material cost and reduce the weight as compared to a complete solid model. This type of construction reduced the overall cost and fabrication time of the prototype, yet allowed the model to remain rigid enough to withstand the airflow around it. In order to mount the streamlined body inside the test-section, a mounting system was devised based on the tensile strength of small-diameter

stainless steel wire. Two through holes were created within the streamlined body at  $90^\circ$  angles to each other at a distance of 1.5 cm from both front and back corners of the body. The diameter of these holes was kept at 2 cm to accommodate two runs of the stainless steel wires, which crossed each other at the center.

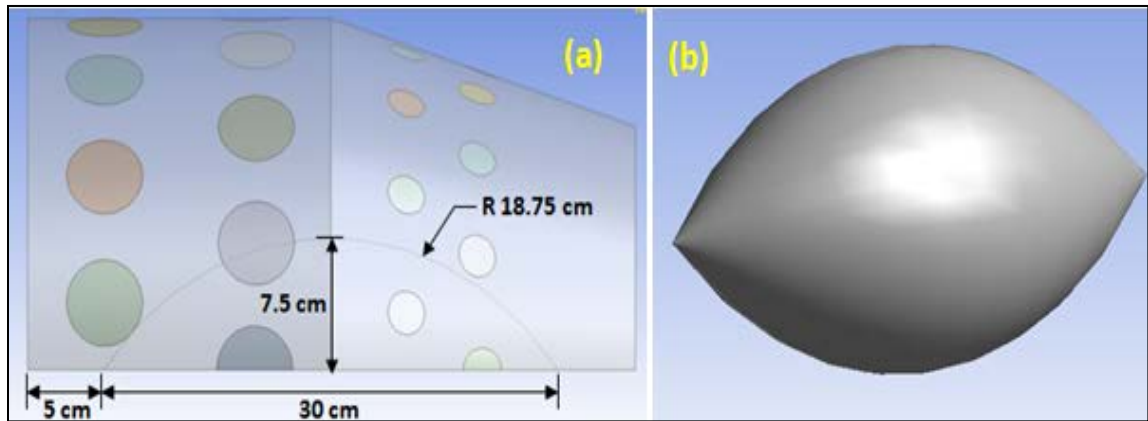


**Figure 3.9** Dilution holes with streamlined body (a) Detailed dimensions, and (b) Streamlined body 3-D model.

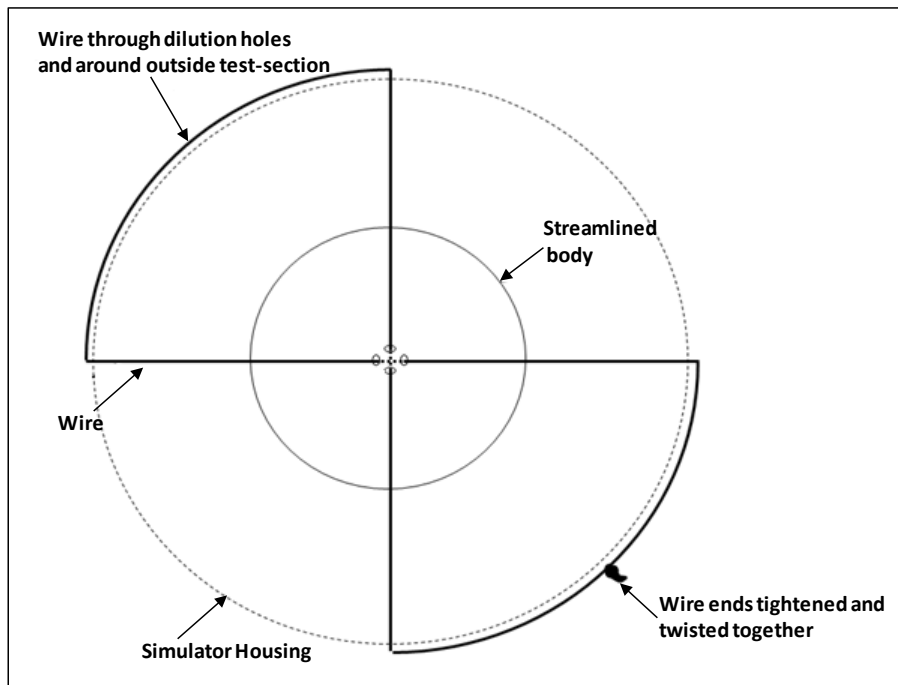


**Figure 3.10** Mounting system for the streamlined body.



Figure 3.10 shows the mounting system for the streamlined body in the test-section. Such a mounting design limited the amount of surface protrusions on the streamlined body with minimal disturbance to the flow around it. Furthermore, the design allowed for repositioning of the streamlined body forward and backward within the test-section by choosing the appropriate dilution holes for mounting, if required for additional testing. Figure 3.11 shows actual streamlined body mounted in the test-section.

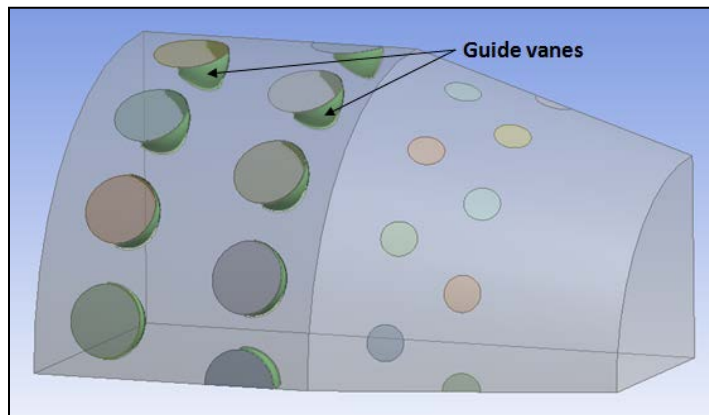


**Figure 3.11** Streamlined body mounted in the test-section.

### 3.3.3 Staggered Dilution Holes with Guide-vanes

Guide vanes have been used in a variety of applications to direct a flow. With the intention of forcing the diluent air into the primary hot air flow to improve mixing, guide vanes were used to direct the secondary flow in the test section. This directional push to the dilution jets would generate swirling motion in the flow which may lead to better mixing. This design makes use of the chute mixer concept of Ahmed *et al.* (2000), Ahmed and Sharma (2006), who demonstrated improved mixing with the use of  $20^\circ$  chutes for the entry of the jets into the mainstream flow. For this dilution scheme, the

same test section with staggered dilution holes was employed and guide vanes were attached to only two rows of larger holes, keeping in mind the associated pressure drop due to these guide vanes. Figure 3.12 shows the schematic of the test section with attached guide vanes. The diameter of the guide vane is same as the diameter of the holes, i.e., 5 cm with outer face surface area of  $1392 \text{ mm}^2$ . A total of 32 guide vanes were mounted in the test section. These guide vanes were created out of hollow steel hemispherical shells, 5 cm in diameter. Each shell was sliced at an angle of  $45^\circ$ .



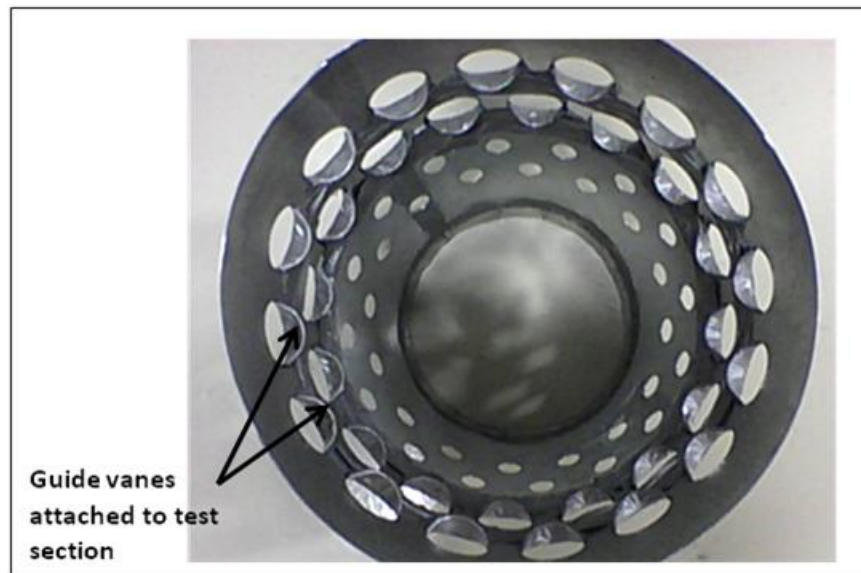
**Figure 3.12** Schematic of the test section with guided vanes.

Figure 3.13 shows the hemispherical shell and the completed guide vane cut at an angle of  $45^\circ$ . These guide vanes were attached to the dilution holes in the test-section with the help of duct tape as shown in Fig. 3.14. Here, it should be noted that the view in Fig. 3.14 is looking from the perspective of the primary flow entrance. The guide vanes are oriented in a manner directly opposing the flow of the primary air, such that the diluent air enters the test-section in a reversed direction against the primary hot air and mixing occurs. This orientation of the vanes is referred to as " $0^\circ$  guide vanes" position. Three additional orientations -  $30^\circ$ ,  $60^\circ$  and  $90^\circ$  were also tested to explore the mixing

effectiveness with different angle of injection of the dilution jet. The angle considered was with respect to the direction of the primary main flow. Figure 3.15 shows the different orientations of the guide vanes tested where the red arrows represent mainstream flow direction and black arrows represent normal direction to the guide vane surface.



**Figure 3.13** Hollow steel hemispherical shell & completed guide vane cut at 45° angle.



**Figure 3.14** Guide vanes mounted inside the test-section.

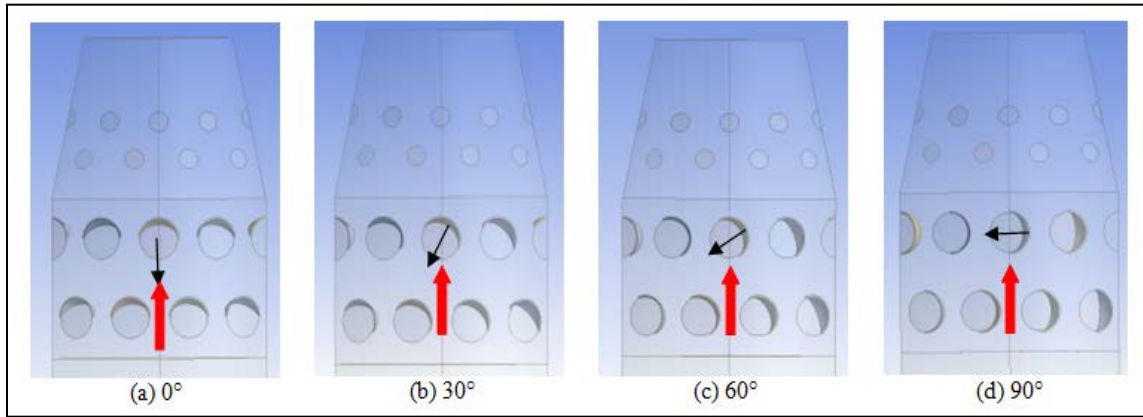


**Figure 3.15** Schematic of the four different guide vane orientations.

### 3.4 Test Procedure

To analyze the effectiveness of the proposed dilution schemes in producing a uniform temperature exit flow from the combustor simulator, a parameter is defined known as the mixture fraction which is given by Eqn. 3.3. This parameter gives a quantitative and qualitative measure of the uniformity of the exit temperature field. To judge how good the value of this mixture fraction is, the same is evaluated at the adiabatic or ideal mixing temperature, which is called the equilibrium mixture fraction and is defined by Eqn. 3.4. The closer the value of the mixture fraction to the equilibrium mixture fraction better is the uniformity of the temperature field. Thus, by gathering all the temperature data at the combustor simulator exit, an assessment can be done for the uniformity of the flow and efficiency of the proposed dilution schemes.

$$f = \frac{T_i - T_j}{T_\infty - T_j} \quad (3.3)$$

$$f_{equil} = \frac{T_{adb} - T_j}{T_\infty - T_j} \quad (3.4)$$

Figure 3.16 shows the constructed combustor simulator used for conducting the experiments. The figure depicts the main components of the experimental set-up - fan, control panel, heaters, dampers, test section mounted in the duct work and the measurement locations. The total flow from the fan is controlled with the help of the first damper where as the second damper regulates the flow distribution between the primary and the secondary ducts. The control panel is used to select the number of heaters to be operated depending on the primary air temperature required. The ambient air forms the secondary cooling air which is insulated from the hot primary air and flows into the test section through the dilution holes. The temperature and velocity measurements are done prior to the entrance to the test section and at the exit of the combustor simulator. All the data is recorded along a radial line which is a good representation of the conditions existing at that cross-section in the symmetrical combustor considered in the experiment. This data is recorded for different jet-to-mainstream momentum flux ratios for all the proposed dilution schemes. Additionally, the inlet data is used to define the boundary conditions in the numerical simulations of this combustor.

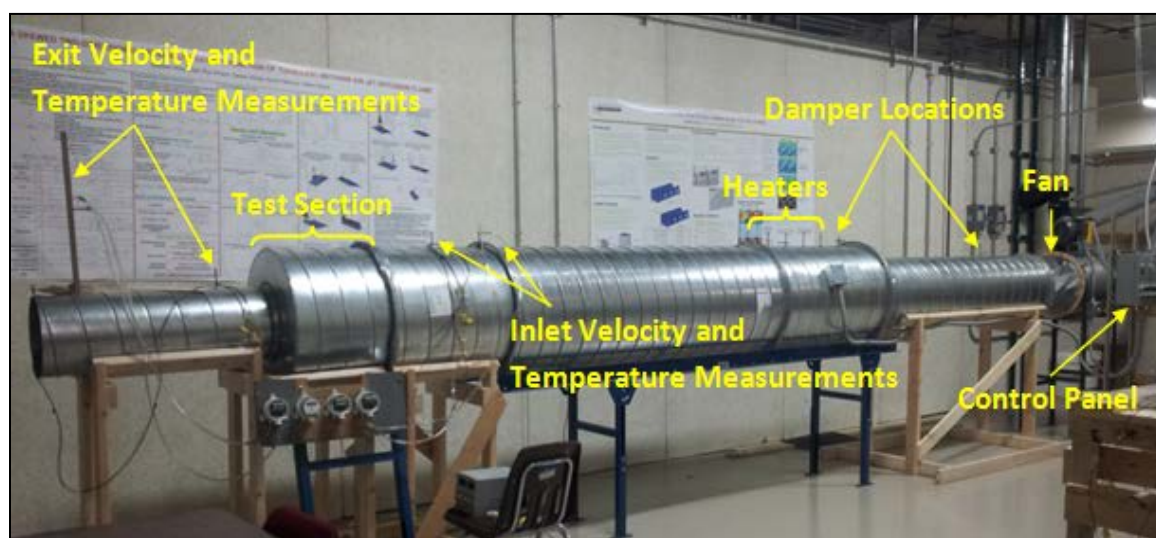


**Figure 3.16** The constructed combustor simulator.

## Chapter 4 - Computational Methodology

The rapid progress and implementation of Computational Fluid Dynamics (CFD) has contributed to substantial improvements in the performance and efficiency of gas turbine engine components through understanding of the complex viscous flow and heat transfer phenomena involved. For this reason CFD is currently one of the key technologies and invaluable tools used in the design and development of gas turbine engines. Validating a computational program with experimental data and using that program for design efforts, provides with capabilities to analyze a system in great depth for various parameters involved in the study. These computational methods can save significant amounts of both time and money - two of the major factors in creating a profitable product.

For this study all of the CFD simulations were done using a commercial code Ansys FLUENT, version 13.0. This general purpose CFD software is ideally suited for incompressible and mildly compressible flows. It utilizes pressure based flow solvers to model the mass, momentum and energy conservation equations using either structured or unstructured meshes. Additionally, it offers several turbulence models, which could be applied and compared with experimental results to determine the model that most accurately captures the specific flow field.

This chapter will outline the meshing procedure, details of the boundary conditions applied to mimic the experimental settings, the governing equations and solution methods involved in the computations, initialization and convergence criteria, turbulence model used with the associated wall treatment and lastly, the grid

independence done to enhance the confidence level that the solutions are converging to the correct solution.

## 4.1 Meshing Procedure

Mesh or grid generation is often quoted as the most important part of CFD analysis. The quality of the mesh has a direct and significant impact on the accuracy of the solution, regardless of the flow solver used. The staggered dilution holes combustor simulator model was meshed using Meshing program of the Ansys FLUENT software. The process of mesh generation required several steps, which will be outlined in detail in this section. To begin with, first the geometry of the combustor simulator was developed in the Design Modeler of FLUENT. The geometry developed was same as the experimental set-up described in Chapter 3 with the identical dimensions, except that the computational domain was created for the portion of the set-up beyond the heater section, which means that the flow through the fan and heaters was not modeled. For the combustor section under consideration, volumes were created corresponding to the primary flow and secondary flow passages, insulation cladding, dilution holes, etc. Using Boolean operations, these were combined to construct the complete combustor simulator geometry as shown in Fig. 4.1.

Once the basic geometry was developed, a hybrid mesh was generated with structured elements in the near wall region and unstructured elements elsewhere. Figure 4.2 depicts a sample of the generated mesh. The turbulence modeling for the near-wall region utilized the automatic near-wall treatment associated with the  $k - \omega SST$  turbulence model which will be discussed in detail later in this chapter. The automatic



near-wall treatment required a finer mesh near the wall which was achieved by adding inflation using the Pre Inflation Algorithm such that the wall  $y^+$  value defined by Eqn. 4.1 ranges between 1 and 5 in regions of high gradients, which is reasonably good enough for the  $k - \omega SST$  turbulence model employed in the simulations. The total number of cells or elements for the staggered dilution holes CFD model was approximately 2.4 million elements and for the case of streamlined body, the number of elements was around 2.5 million.

$$y^+ = \frac{u_* y}{\nu} \quad (4.1)$$

where,

$$u_* = \sqrt{\frac{\tau_w}{\rho}} \quad (4.2)$$

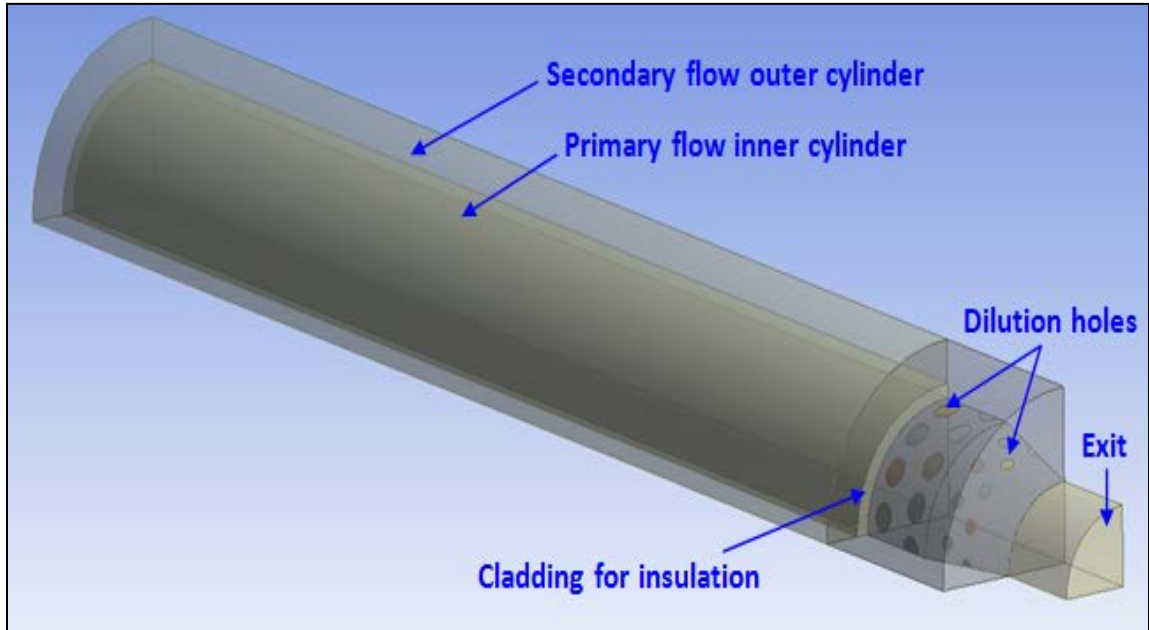


**Figure 4.1** Geometry of the combustor simulator developed in the design modeler.



Another important consideration during the meshing process was to ensure the quality of the generated mesh. The quality was determined by the cell skewness. The skewness gives the measure of how far a triangle or quadrilateral element (two-dimensional) or tetrahedron element (three-dimensional) is from its perfect form where perfect form means equilateral. A skew of zero is perfect and one is poor. For this model the cell volume skewness was kept below 0.80 with an average value of 0.47.

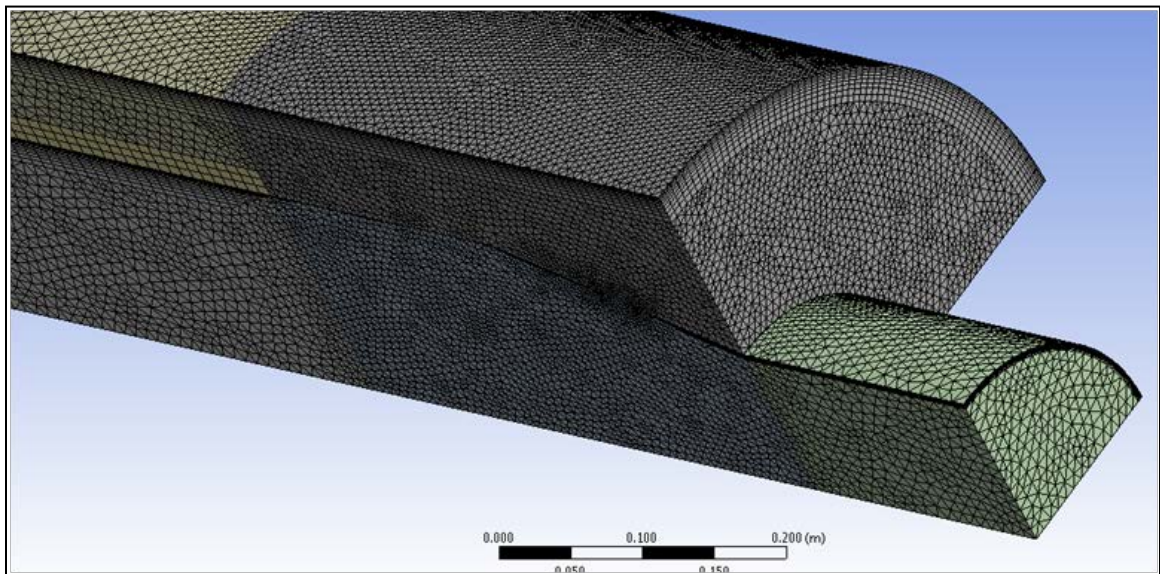


**Figure 4.2** Sample of the hybrid mesh generated with structured and unstructured elements.

## 4.2 Boundary Conditions

The boundary conditions were set to represent the conditions of the experimental set-up and are noted on the schematic in Fig. 4.3. Taking advantage of the symmetrical geometry of the combustor simulator, only a 90 degrees sector was considered for the computations which was confined by two symmetry planes - xz and xy planes (the vertical and horizontal planes as shown in Fig. 4.3). Symmetry conditions were applied at these two planes. This step reduced the size of the complete domain and hence the

computational efforts too. There were two velocity inlets at the entrance to the combustor simulator for the primary and secondary flow, respectively. The 'Velocity inlet 1' corresponds to the primary velocity inlet profile obtained from the experimental set-up and the temperature of the primary flow was set to match the experimental primary inlet temperature profile. The 'Velocity inlet 2' corresponds to the constant velocity inlet of the secondary flow that equals the value determined from the experiments using the exit velocity experimental data. The secondary flow enters the combustor simulator at a constant lower temperature equivalent to the temperature from the experiment. The outflow boundary condition was set at the combustor exit.

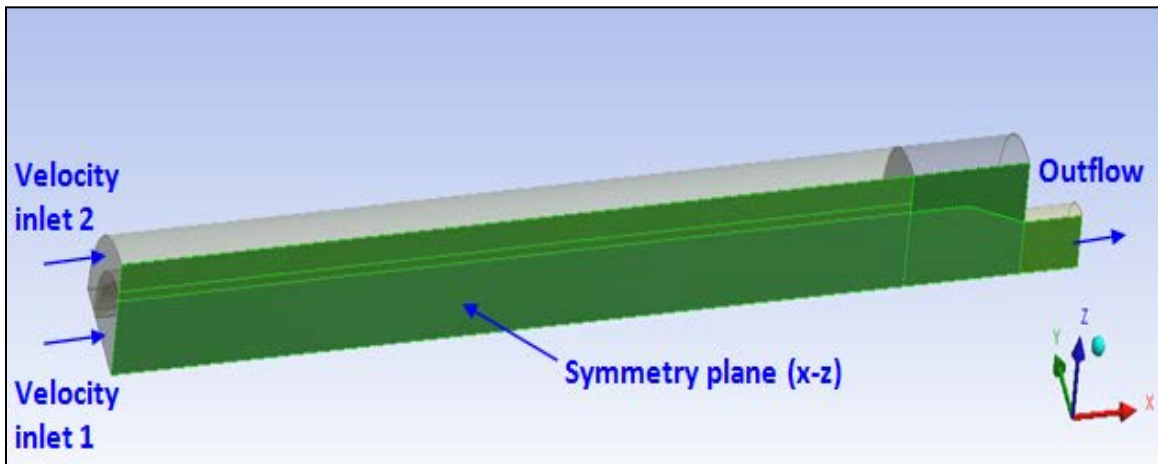


**Figure 4.3** Schematic of the boundary conditions for the computational domain.

### 4.3 Governing Equations and Solution Methods

The numerical method used in the solution was the pressure-based segregated algorithm. This pressure-based solver uses a solution algorithm where the governing equations (flow, energy and turbulence equations) were solved sequentially (i.e., segregated from one another). Because the governing equations were non-linear and coupled, the solution loop was carried out iteratively in order to obtain a converged

numerical solution. Thus, in the segregated algorithm, the individual governing equations for the solution variable (e.g.,  $u$ ,  $v$ ,  $w$ ,  $p$ ,  $T$ ,  $k$ ,  $\omega$ , etc.) were solved one after another. Each governing equation, while being solved, was 'decoupled' or 'segregated' from the other equations. The transient form of the three-dimensional conservation equations may be written in general for a conserved variable  $\phi$  (Wang *et al.*, 2011) given by Eq. 4.3 where  $\rho$  is the fluid density,  $\Gamma$  is the effective diffusion coefficient,  $U$  is the fluid velocity, and  $S$  is the source term which depends on the equation being considered. Continuity, momentum, energy, turbulence equations were solved with the dependent variable  $\phi$  representing 1, velocity, internal energy, turbulent kinetic energy ( $k$ ) and specific dissipation rate ( $\omega$ ), respectively.

$$\frac{\partial(\rho\phi)}{\partial t} + \nabla \cdot (\rho U \phi) = \nabla \cdot (\Gamma \nabla \phi) + S \quad (4.3)$$

With the segregated algorithm, each iteration consisted of the following steps:

- i. Fluid properties were updated based on the current (or initialized) solution.
- ii. The momentum equations were sequentially solved, using the recently updated values of pressure and face mass fluxes, to update the velocity field.
- iii. It should be noted here that the velocity field obtained in step ii may not satisfy the continuity equation locally; therefore a pressure correction equation was solved to obtain the necessary corrections to the pressure and velocity fields and face mass fluxes such that continuity equation was satisfied.
- iv. Equations for additional scalars such as turbulent quantities, energy, etc., were solved at this stage using the current values of the solution variables.
- v. Lastly, a convergence check was made until the convergence criteria were met.

This loop is continued until the convergence criteria, which are discussed next in Sec. 4.4, are met. The pressure and velocity were coupled using the Semi-Implicit Method for Pressure-Linked Equations (SIMPLE) algorithm. All the solutions were reached using the First Order Upwind discretization for momentum and turbulence equations.

#### **4.4 Initialization and Convergence Criteria**

To start iterating a solution, the entire computational domain was initialized to the velocity and temperature values prescribed at the primary flow inlet. These values were obtained from the experiments keeping in a range such that the flow was turbulent. In judging the convergence of the solution, the residuals of several quantities were monitored after each iteration. The FLUENT default settings require the residuals to decrease to  $10^{-3}$  for all the equations (continuity, momentum and turbulence equations) except energy, for which the criterion is  $10^{-6}$ . For all the simulations performed, the convergence criteria were further decreased to  $10^{-5}$  for all the equations except energy, for which it was reduced to  $10^{-8}$ . Each simulation was continued at least 100-200 iterations beyond convergence to insure that the residuals continued to decrease steadily and that the solution was actually converged. In addition to the residuals, the mean temperature at the combustor exit was also monitored to check for the convergence of the solution.

#### **4.5 Turbulence Modeling and Near Wall Treatment**

FLUENT offers a range of turbulence models to choose from which will solve a given problem as accurately as possible. Depending on the nature of the problem under

consideration, particular turbulence model is selected. Although many researches (Norihiko *et al.*, 2008, Wang *et al.*, 2011, Yehia *et al.*, 2011, Jaafar *et al.*, 2011), in the field of computational analysis of combustors have invariably used the  $k - \varepsilon$  model to capture the physics of turbulence, in the present simulation,  $k - \omega$  SST turbulence model was used. Through a well-designed blend function, the  $k - \omega$  SST model achieves that the  $k - \omega$  model was used in near-wall region and the standard  $k - \varepsilon$  model was used in far-wall region (ZhenXun, 2011). In the present work, the simulations for the staggered dilution holes geometry were first performed with the standard  $k - \varepsilon$  turbulence model and then repeated with the  $k - \omega$  SST model. It was found that the simulation results with the  $k - \omega$  SST turbulence model were in close proximity to the experimental measurements. Additionally, taking into account the kind of simulation required for the case of flow over streamlined body which involves flow separation and recirculation, the use of  $k - \omega$  SST model was better than  $k - \varepsilon$ . In comparison to  $k - \varepsilon$ ,  $k - \omega$  SST accounts for the transport of the turbulent shear stress and gives highly accurate predictions of the onset and the amount of flow separation (Channwala, 2010). Following are the transport equations for the  $k - \omega$  SST turbulence model solved by FLUENT:

$$\frac{\partial(\rho k)}{\partial t} + \frac{\partial(\rho k u_i)}{\partial x_i} = \frac{\partial}{\partial x_j} \left( \Gamma_k \frac{\partial k}{\partial x_j} \right) + \tilde{G}_k - Y_k \quad (4.4)$$

$$\frac{\partial(\rho \omega)}{\partial t} + \frac{\partial(\rho \omega u_i)}{\partial x_i} = \frac{\partial}{\partial x_j} \left( \Gamma_\omega \frac{\partial \omega}{\partial x_j} \right) + G_\omega - Y_\omega + D_\omega \quad (4.5)$$

In these equations,  $\tilde{G}_k$  represents the generation of turbulence kinetic energy due to mean velocity gradients,  $G_\omega$  is the generation of  $\omega$ ,  $\Gamma_k$  and  $\Gamma_\omega$  represents the effective

diffusivity of  $k$  and  $\omega$ , respectively.  $Y_k$  and  $Y_\omega$  are the dissipation of  $k$  and  $\omega$  due to turbulence.  $D_\omega$  represents the cross-diffusion term.

As mentioned earlier the  $k - \omega$  SST turbulence model is designed in such a way that it solves as a standard  $k - \omega$  model in near-wall region and the standard  $k - \varepsilon$  model in far-wall region. This automatic near-wall treatment requires a finer mesh near the wall as compared to rest of the domain. To achieve this the inflations on the wall are arranged such that the wall  $y^+$  value ranges between 1 and 5 in regions of high gradients, which is reasonably good enough for the  $k - \omega$  SST turbulence model employed in the simulations.

The above discussed computational methodology was followed for various parametric studies with the staggered holes dilution scheme being used in the test-section. The simulation results for temperature and velocity profile at the combustor exit were compared with the experimental measurements. This was followed by study of the effect of the jet-to-mainstream momentum flux ratio on the temperature uniformity, the variation of the cooling rate number (CRN) around the dilution holes inside the test-section, exergy destruction, etc. These parametric studies are discussed next in Chapter 5.

## **Chapter 5 - Computational Results and Parametric Study**

In this chapter, both two dimensional and three dimensional computational fluid dynamics analyses will be discussed along with the parametric studies performed to better understand the dilution process. The two dimensional CFD analysis was undertaken to make some basic design decisions and compare the alternatives of introducing the dilution air from smaller but large number of holes or larger but smaller number of holes. Later, this two dimensional analysis was advanced to a full three dimensional CFD analysis to weigh the advantage of using the staggered dilution holes over the in-line holes and study the effect of adding the streamlined body. Furthermore, the three dimensional computational results were analyzed for more in-depth investigation of the dilution process and factors affecting the exit temperature uniformity. The following are the research avenues explored in this chapter:

- Two-dimensional computational analysis to assess the option of introducing dilution air through smaller or larger holes.
- Three-dimensional computational analysis to evaluate the in-line, staggered pattern of dilution holes and the effect of adding the streamlined body in the dilution zone.
- Experimental observation for the staggered dilution holes scheme in the combustor simulator which forms the basis for the CFD model inlet conditions and validation.

- Numerical investigation to study the effect of jet-to-mainstream momentum flux ratio on the temperature uniformity at the combustor exit, variation of the cooling rate number (CRN) inside the dilution zone and exergy destruction associated with increasing jet-to-mainstream momentum flux ratio.

## 5.1 Two-dimensional CFD Analysis

During the early investigation of the dilution process for the combustor simulator, it was found that there are mainly two hole regimes that are practically used in combustion chamber manufacturing, the first one is introducing the dilution air from a large number of smaller holes while the second one by using concentrated larger holes. A two-dimensional computational analysis was carried out for both the regimes using the same ratio of primary to secondary air flow rates and same clear area. Figure 5.1 (a) shows the generated mesh for the whole domain, while Figs. 5.1 (b) and 5.1 (c), show the mesh close to the holes area for both small and large hole regimes. The mesh size was 100,000 nodes. Computations were made in ANSYS Fluent assuming a steady state flow with turbulence modeled using the realizable  $k - \varepsilon$  model with Standard Wall Functions. Based on the hydraulic diameter and velocity of the inlet section, the primary flow was set to be a constant velocity inlet of magnitude 5 m/s corresponding to a Reynolds number of  $1.4 \times 10^5$ . The secondary flow was set to be 55% of the total flow. SIMPLE method was used for the pressure-velocity coupling and the residuals were set to  $10^{-5}$  for all the flow field variables while the energy equation residuals were set to  $10^{-8}$ .

The velocity vectors for small and large holes are shown in Figs. 5.2 (a) - (b). It is clear that the larger holes pattern provides better penetration of the dilution air to shear



against the primary air flow and accordingly providing better mixing than the smaller holes pattern. Also, it was found that the dead zones at the top left corner were smaller in the larger holes pattern than the smaller dilution holes.

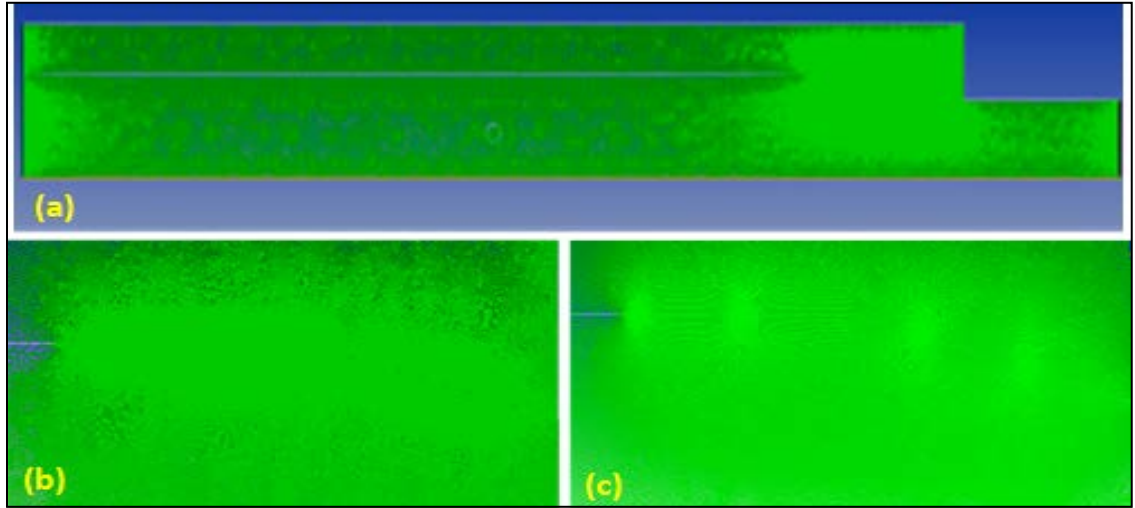


**Figure 5.1** Generated mesh for two-dimensional CFD analysis.

Figures 5.3 (a) - (b) show the numerical results for the temperature contours for smaller holes and larger dilution holes. A slight decrease in the hot area near the center was achieved by the larger dilution holes pattern than the corresponding smaller holes pattern near the mixing section. Additionally, from the pressure contours for the two different holes pattern as shown in Fig. 5.4 (a) - (b), a total pressure drop of 505 Pa was observed for smaller dilution holes as compared to only 134 Pa for the larger holes. It can be noticed that the smaller dilution holes pattern demanded almost four times more pressure than the larger holes pattern. Here, it is worth mentioning that any pressure drop will directly impact the performance of the turbine which will be placed downstream of the mixing section of the combustor. These two dimensional simulation results clearly indicate the effectiveness of the larger holes for better uniform exit temperature keeping in mind the pressure drop associated with the two holes configurations. This study has

been published in the proceedings of the ASME 2012 IDETC/CIE Conference (Ibrahim *et. al.*, 2012).

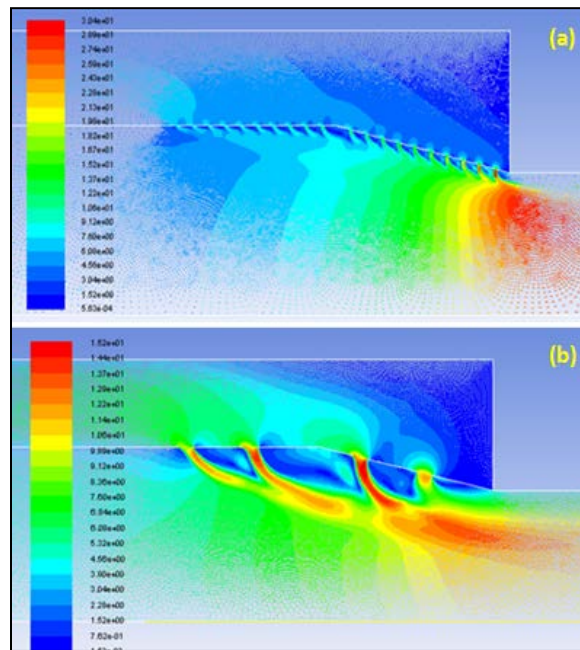


**Figure 5.2** Velocity vectors in the mixing section for (a) smaller dilution holes, and (b) larger dilution holes.

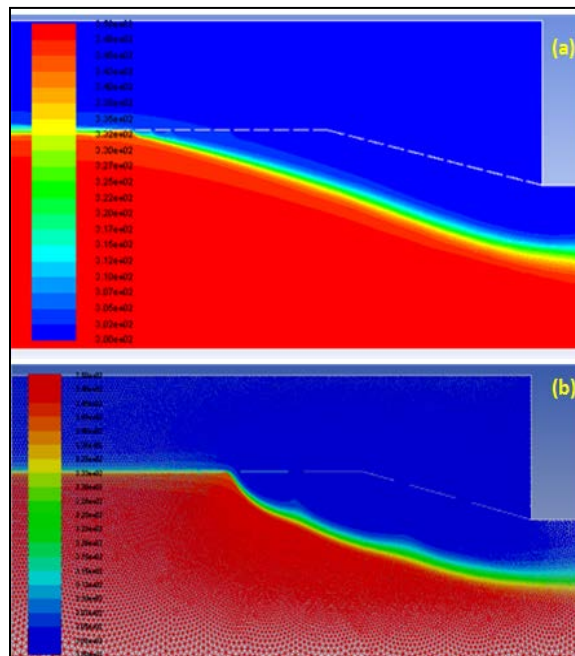


**Figure 5.3** Temperature contours in the mixing section for (a) smaller dilution holes, and (b) larger dilution holes.

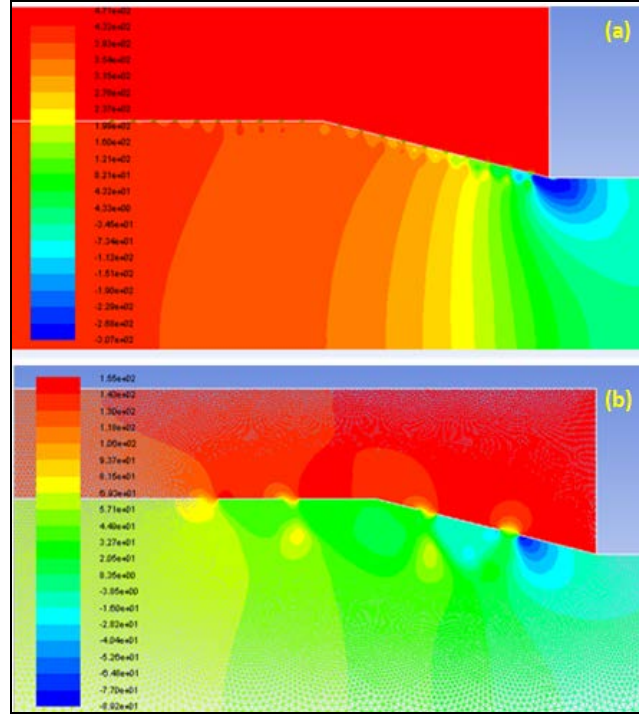


**Figure 5.4** Pressure contours in the mixing section for (a) smaller dilution holes, and (b) larger dilution holes.

## 5.2 Three-dimensional CFD Analysis

Based on the two-dimensional CFD analysis discussed in Sec. 5.1, a three dimensional computational analysis was performed to compare the effectiveness of the in-line and the staggered dilution holes pattern to give a better uniform exit temperature profile and study the effect of adding a streamlined body in the dilution zone. Due to the symmetric nature of the combustor simulator, only a quarter of the annular combustor was considered for the simulations to reduce the computational efforts involved. The four dilution holes patterns considered for these simulations are described below:

- **In-line dilution holes (ID):** In this scheme, the dilution jets entered the test-section from a total of 64 dilution holes. Figure 5.5 shows the details of the test section with the in-line dilution holes. Each row has 16 dilution holes equally

spaced circumferentially. Rows 1 and 2 have larger dilution holes than rows 3 and 4, with the holes in row 2 being in-line with holes in row 1 in the cylindrical portion and similarly, holes in row 4 are in-line with holes in row 3 in the conical portion of the test-section.

- **Staggered dilution holes (SD):** In this scheme, the number of holes, rows and sizes of the dilution holes were the same as in the in-line pattern, except that rows 2 and 4 were staggered with respect to rows 1 and 3, respectively, such that each hole in the staggered row was centrally located between the two corresponding holes of the reference row.
- **In-line dilution holes with streamlined body (IDS):** While keeping the same in-line dilution holes pattern, a streamlined body is introduced in the test-section which extends from the cylindrical portion to the conical portion.
- **Staggered dilution holes with streamlined body (SDS):** In this scheme, the same streamlined body as introduced in the previous scheme is combined with the earlier staggered dilution holes pattern. Figure 5.6 gives the details of the streamlined body in a staggered dilution holes pattern test-section.

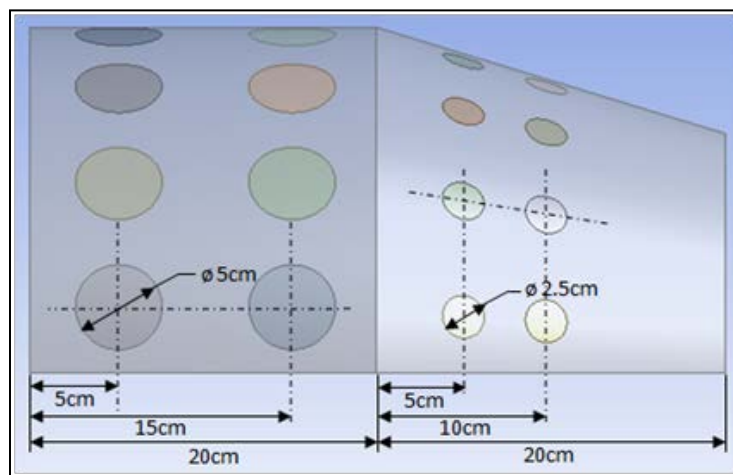


**Figure 5.5** Test section with details of the in-line dilution holes pattern.

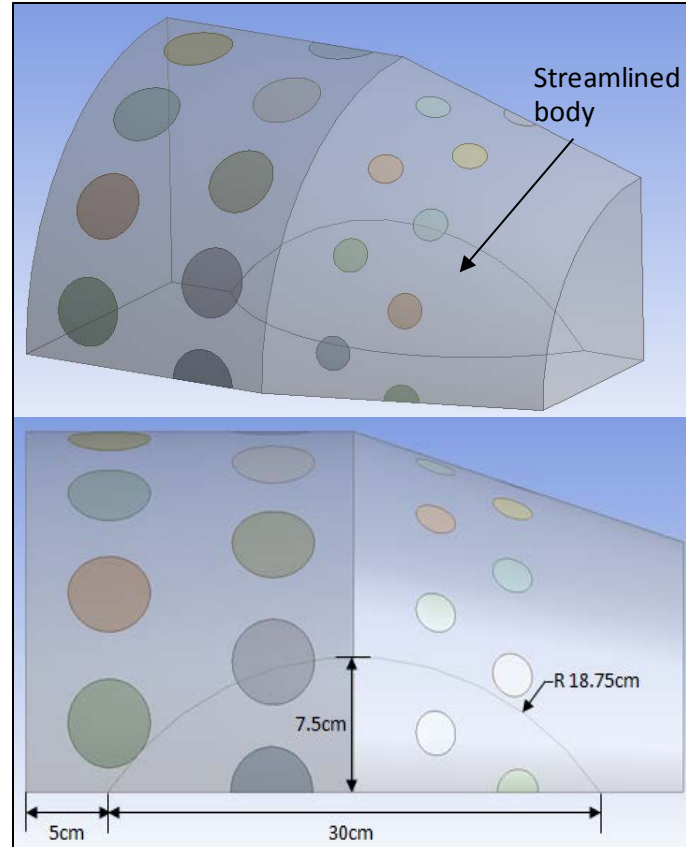


**Figure 5.6** Test section with details of the streamlined body in the staggered dilution holes pattern.

### 5.2.1 Simulation Procedure

The total flow was split into primary and secondary (or dilution) streams with nearly 40% of the flow directed through the dilution holes into the test-section and the remaining 60% of the flow was directed through the primary passage of the combustor simulator. Table 5.1 gives the details of the design data used for this simulation. The inlet conditions were considered to be uniform across the cross-section.

The unstructured mesh was refined near the walls by adding the inflation using the Pre Inflation Algorithm such that the  $y^+$  value of approximately 1 was achieved in regions of high gradients, which is reasonably good enough for the  $k - \omega$  SST turbulence model employed in the simulations. In all the simulations, a steady state pressure based

solver was used to solve the governing equations and Semi-Implicit Method for Pressure Linked Equations (SIMPLE) algorithm was used for pressure/velocity coupling. The boundary conditions used for the CFD model included the uniform inlet velocity and temperature for the primary and the dilution flow as 5 m/s, 350 K and 6 m/s, 300 K, respectively, the two planes which bound the quarter portion of the geometry were set as the symmetry planes while the exit boundary was defined as pressure outlet. Velocity components and turbulence quantities at the inlet were uniform. The same boundary conditions were used for all the simulations performed for the in-line dilution holes, staggered dilution holes, in-line dilution holes with streamlined body and staggered dilution holes with streamline body dilution schemes.

**Table 5.1** Design details for combustor.

	<b>Parameter</b>	<b>Value</b>
1	Mass flow rate of primary air	0.9378 kg/s
2	Mass flow rate of dilution jets	0.7295 kg/s
3	Inlet temperature of primary air	350 K
4	Inlet temperature of dilution jets	300 K

### 5.2.2 Grid Independence

Figure 5.7 shows the radial temperature distribution at the combustor exit for inline dilution holes for three different mesh sizes -  $1.0 \times 10^6$ ,  $2.5 \times 10^6$ ,  $3.0 \times 10^6$  elements. It can be observed from the figure that the radial temperature exit profile is approximately the same for  $2.5 \times 10^6$  and  $3.0 \times 10^6$  elements sized mesh, whereas for  $1.0$

$\times 10^6$  elements mesh size, the profile seems to be a little under-estimated. This was the reason why all the simulations were performed for mesh size of  $2.5 \times 10^6$  million elements.

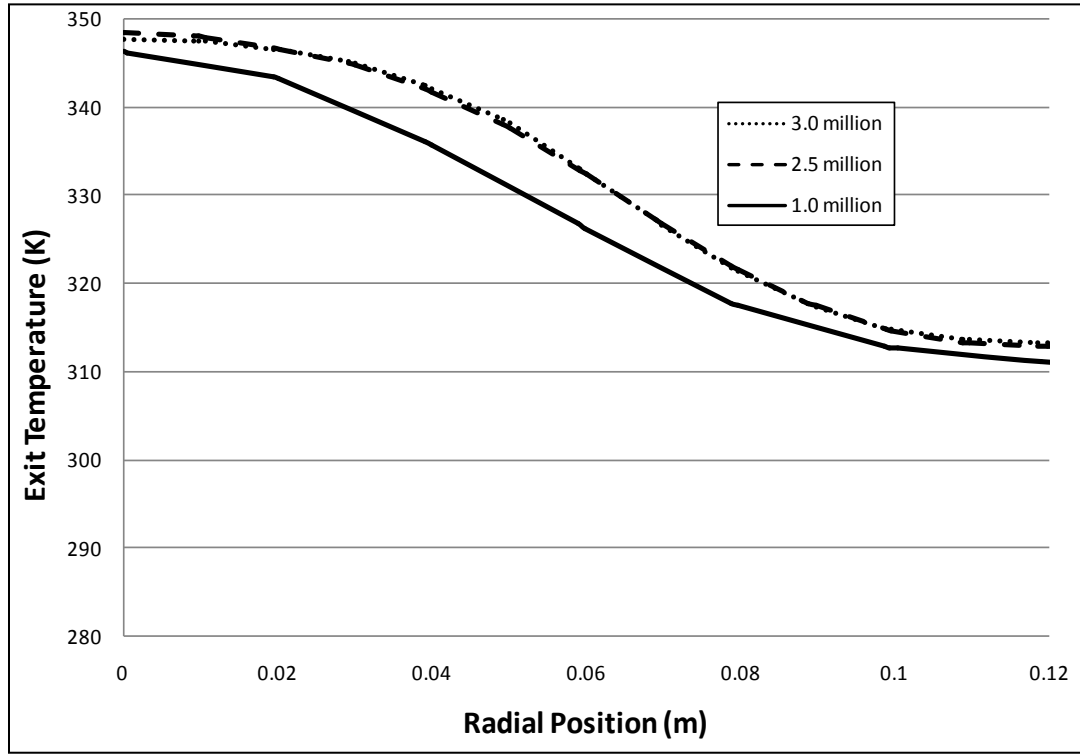


**Figure 5.7** Radial temperature exit profiles for different mesh sizes for In-line dilution holes pattern.

### 5.2.3 Staggered versus In-line Dilution Holes

To evaluate the effectiveness of the in-line and staggered hole patterns, the mixture fraction  $f$  as defined in Eqn. 3.3, at each point along a radial line on the exit plane of the combustor was compared with the equilibrium mixture fraction  $f_{equil}$  given by Eqn. 3.4. The equilibrium temperature for the given inlet conditions was determined to be 320 K, from the energy balance and the equilibrium mixture fraction was calculated to be 0.4. Based on the area-weighted average value of the mixture fraction  $f$ , it was found

that the staggered dilution holes has the mixture fraction closer to the equilibrium value 0.4. Table 5.2 gives the mixture fraction value for both the dilution holes patterns. A slight improvement about 84% closer to the equilibrium mixture fraction in the case of staggered holes can be observed over the case of in-line holes, which gives about 81% equilibrium mixture fraction. This 3% improvement with the staggered holes is attributed to the better distribution of the secondary air along the circumference of the mixing section allowing better homogeneity of the temperature at the exit section. Figure 5.8 shows the deviation of the mixture fraction from the equilibrium mixture fraction for in-line and staggered dilution holes patterns along the radial direction. From the figure it can be observed that the staggered dilution holes pattern has lesser slope than the in-line dilution holes pattern, which clearly suggests that the staggered dilution holes give better temperature uniformity than the in-line holes which is consistent with the results presented in Table 5.2. The three-dimensional CFD analysis discussion above justifies the decision of making staggered dilution holes instead of the in-line holes in the experimental set-up for the combustor simulator. This study has been published in the ASME 2012 IMECE Conference (Gupta *et. al.*, 2012).

**Table 5.2** Mixture fraction values for uniform inlet conditions.

	<b>Dilution Scheme</b>	<b>Mixture fraction value</b>
1	In-line dilution holes	0.3245
2	Staggered dilution holes	0.3364
3	In-line dilution holes with streamlined body	0.3546
4	Staggered dilution holes with streamlined body	0.3628



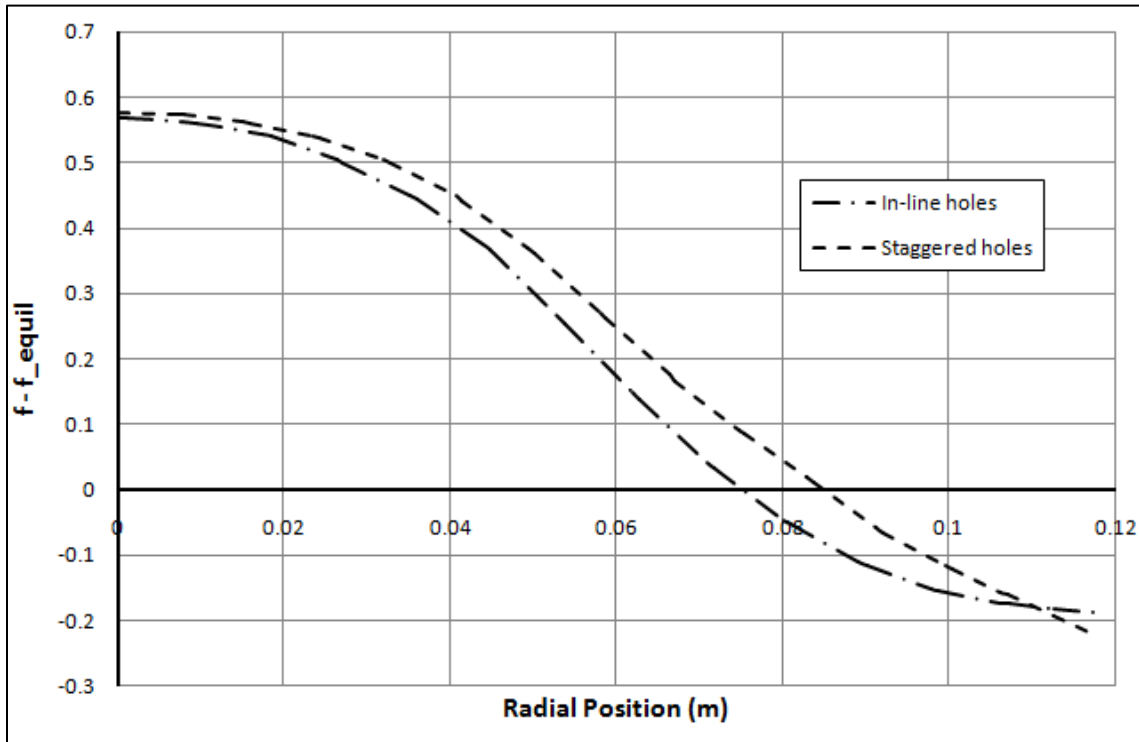


**Figure 5.8** Deviation from equilibrium mixture fraction for in-line and staggered dilution holes patterns.

#### 5.2.4 Effect of Adding Streamlined Body in the Dilution zone

To study the effect of adding a streamlined body in the dilution zone on the exit temperature uniformity, the same simulation procedure and the boundary conditions as used in Sec. 5.2.1 were used for this case. Two simulations were performed - one for the in-line dilution holes with the streamlined body and second for the case of staggered dilution holes with the streamlined body. The temperature and velocity data extracted from the simulation along the radial line at the exit plane was utilized to determine the mixture fraction  $f$  in the same manner as applied in Sec. 5.2.3.

The deviation of the mixture fraction from the equilibrium mixture fraction for all the four cases can be observed from the Fig. 5.9. The mixture fraction value for the case

of staggered dilution holes with streamlined body (0.3628) was found to be closest to the equilibrium mixture fraction (0.4) which was followed by the case of in-line dilution holes with streamlined body (0.3546). Almost 91% equilibrium mixture fraction value was achieved with the use of streamlined body in the staggered dilution holes set-up. Table 5.2 shows the values for the mixture fraction for the different schemes. This 7% improvement over just the staggered dilution holes pattern can be explained by the velocity vectors shown in Fig. 5.11, where the streamlined body is forcing the primary air to shear in the direction of secondary colder air. Figures 5.11 (a)-(f), show the velocity vectors and magnitudes for the different patterns. Introducing the streamlined body was meant to decrease the mixing area and promote the heat exchange between primary and secondary air. From the Figs. 5.11(a)-(f), it can be observed that the use of streamlined body resulted in higher velocities in the test-section section as compared with the schemes without it. Also, the magnitude of velocity for holes was found to be higher as we go closer to the exit, thus higher flow rates. This is because of the buildup of pressure in the annulus near its end where the velocities become very low. To overcome this, holes can be made smaller as we go towards the exit, increasing the mass fraction of primary air introduced from the beginning of mixing and allowing more residence time for heat exchange. This study has been published in the ASME 2012 IMECE Conference (Gupta *et. al.*, 2012).

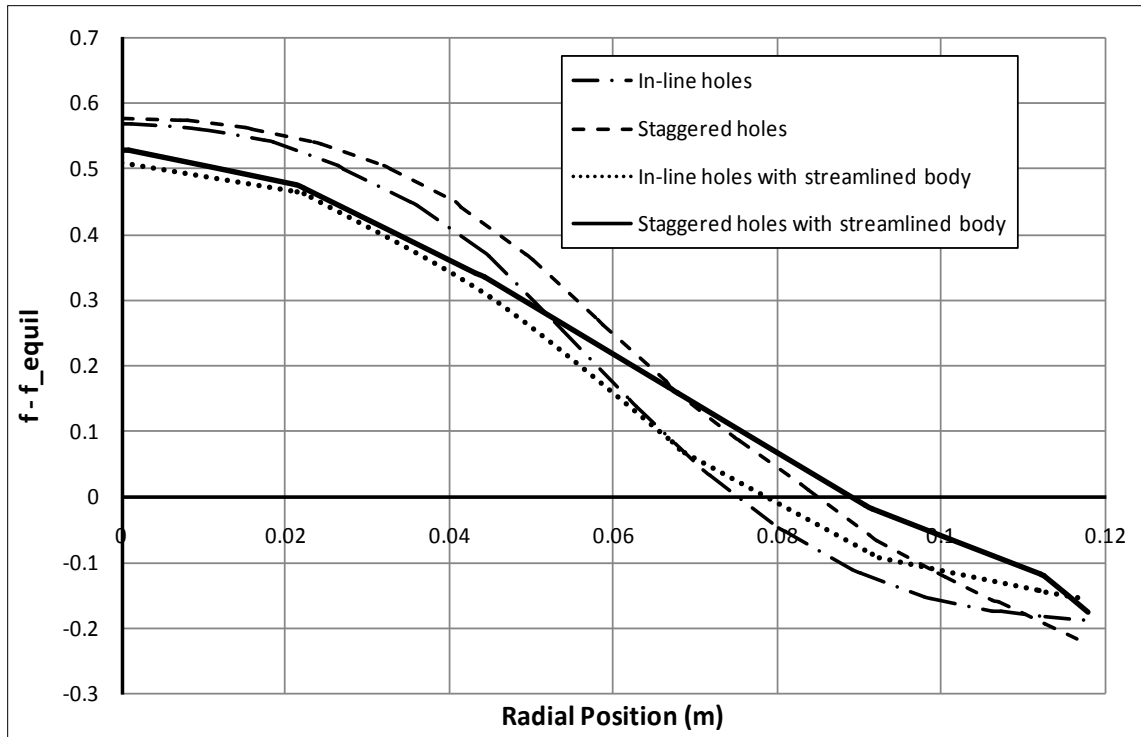


**Figure 5.9** Deviation from equilibrium mixture fraction for in-line, staggered, in-line with streamlined body and staggered with streamlined body dilution schemes.

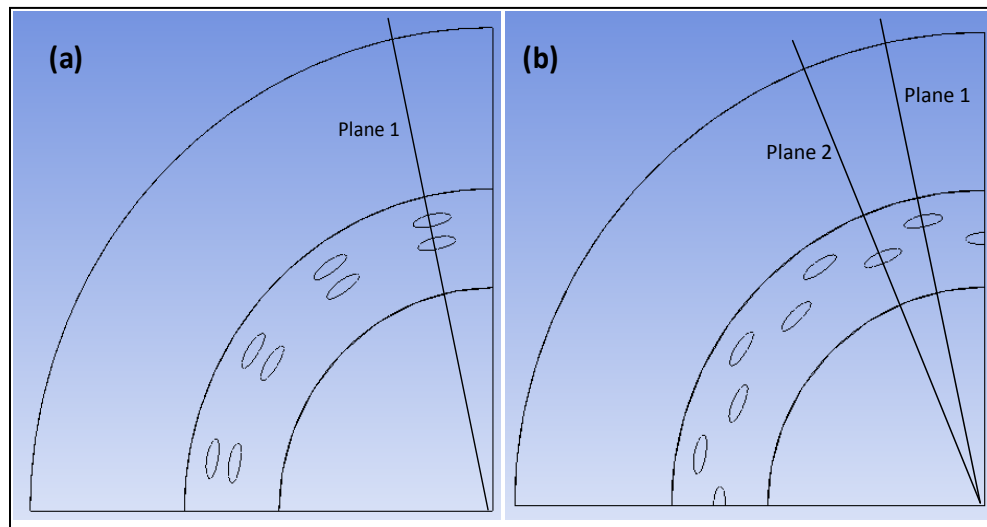


**Figure 5.10** Position of the planes considered for plotting the velocity vectors for (a) In-line pattern, and (b) Staggered pattern.

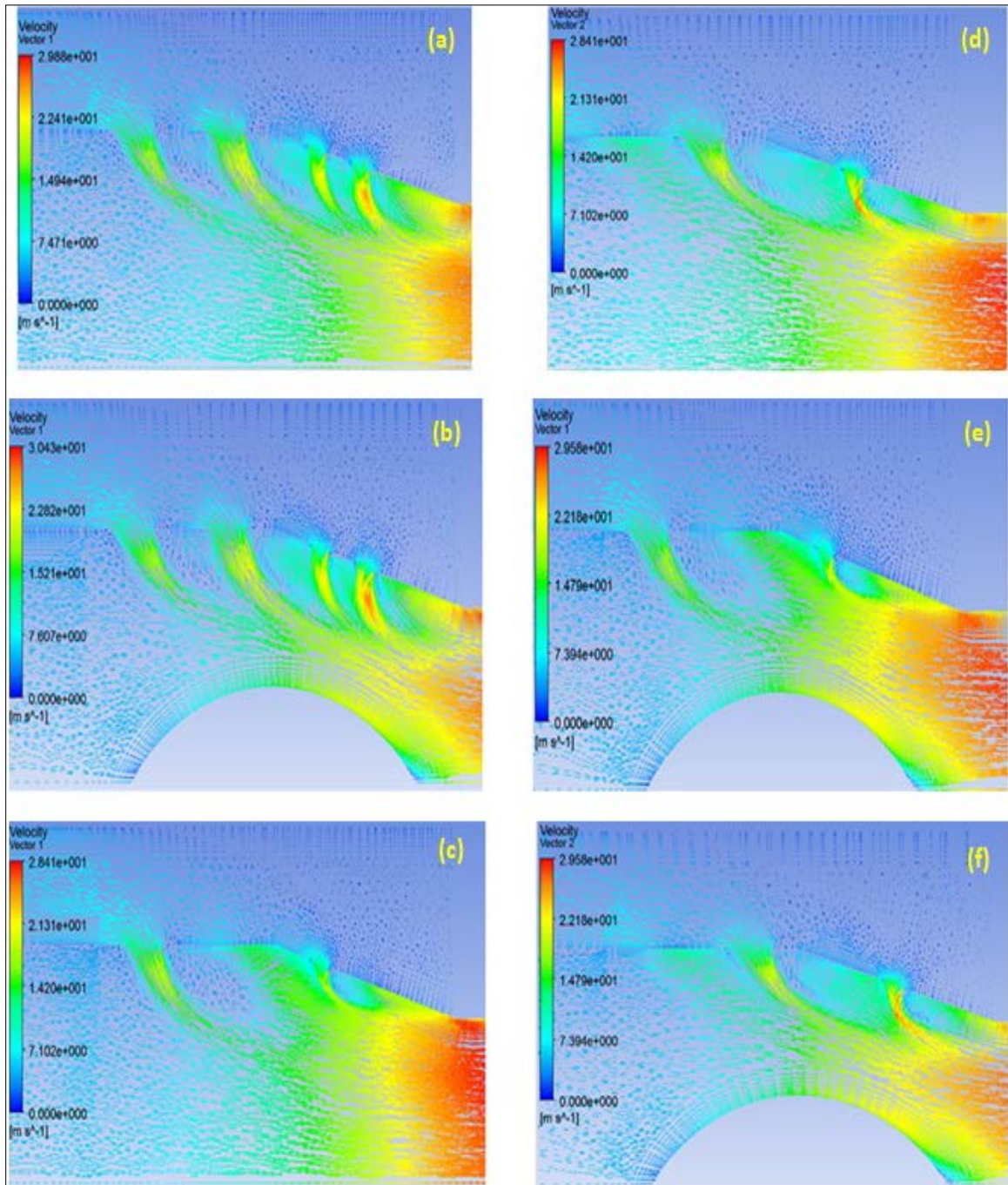


**Figure 5.11** Velocity vectors for (a) In-line dilution holes on plane 1, (b) In-line holes with streamline body on plane 1, (c) Staggered dilution holes on plane 1, (d) Staggered dilution holes on plane 2, (e) Staggered holes with streamlined body on plane 1, and (f) Staggered dilution holes with streamlined body on plane 2.

### 5.3 Experimental Observation for Staggered Dilution Holes

The experimental data were taken as per the detailed test procedure discussed in Chapter 3. At start-up, the combustor simulator was left to run for a few minutes providing enough time for the primary air to get heated and the flow field to stabilize. This was followed by velocity and temperature measurements at both inlet and exit plane as shown in Fig. 3.16. The primary flow inlet velocity and temperature profiles are illustrated in Figs. 5.12 (a) - (b). These profiles are used as the inlet boundary conditions for the primary flow in the numerical simulations. Based on the weighted average inlet primary flow velocity, the average exit flow velocity and the area of cross-sections, the inlet secondary flow velocity was determined. The dimensions and area of cross-section of the ducts, cladding and exit sections are given in Table 5.3. The secondary flow velocity is determined using Eqn. 5.1. The exit velocity and temperature profiles shown in Figs. 5.13 (a) - (b) are used to validate the numerical results. Later the validated simulations are used to study the effect of variation of momentum-flux ratio on the exit temperature uniformity.

**Table 5.3** Cross-sectional areas of the ducts used.

	<b>Diameter (m)</b>	<b>Area of cross-section (m<sup>2</sup>)</b>
<b>Inner duct</b>	0.4064	0.1297
<b>Cladding</b>	0.4572	0.1642
<b>Outer duct</b>	0.6096	0.2919
<b>Exit</b>	0.3048	0.0729

$$V_{sec} = \frac{(A_{exit} V_{ave\ exit} - A_{prim} V_{ave\ prim})}{A_{sec}} \quad (5.1)$$

where,

$$A_{sec} = A_{outer} - A_{clad} \quad (5.2)$$

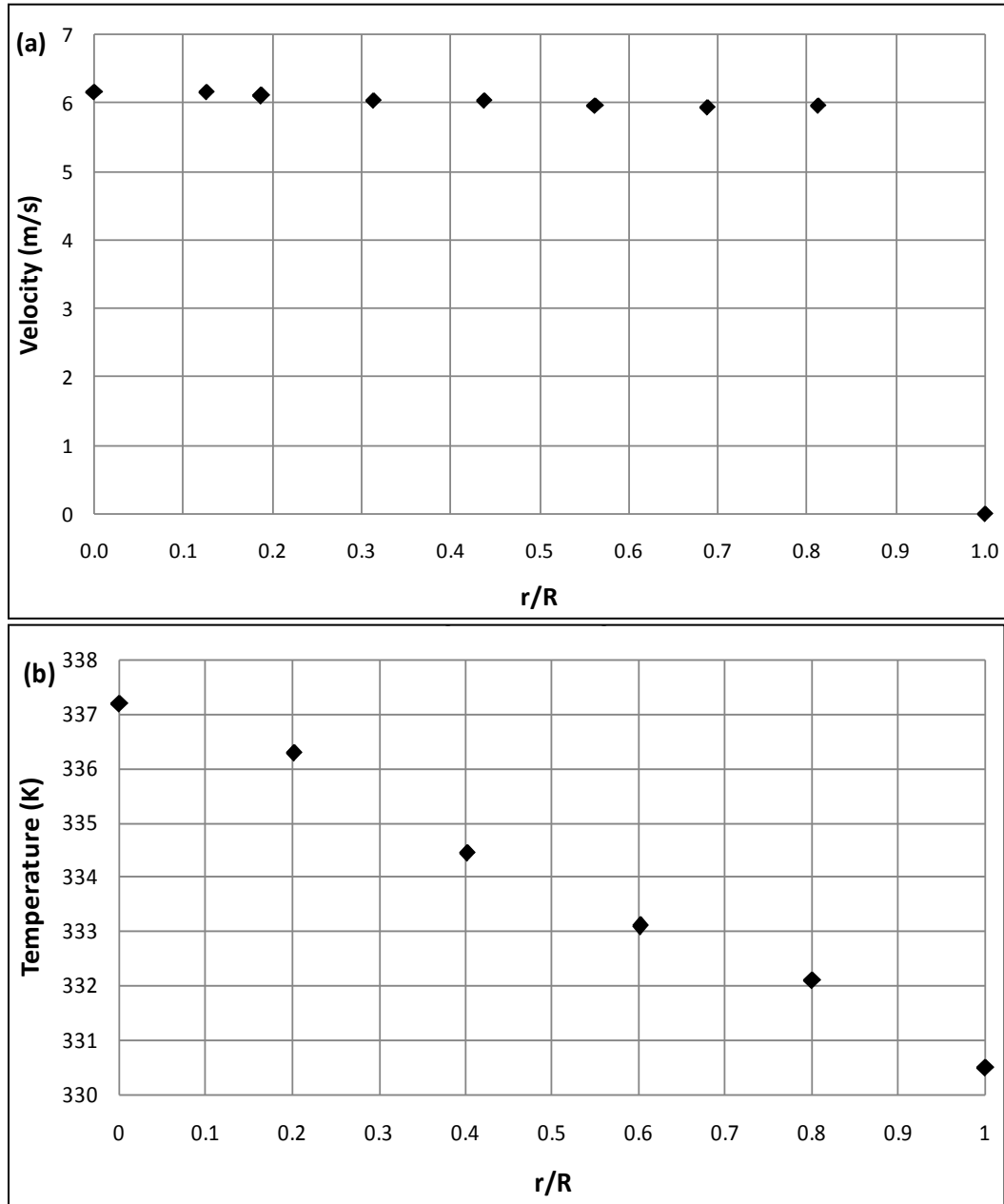


**Figure 5.12** Primary flow inlet profiles (a) Velocity, and (b) Temperature.

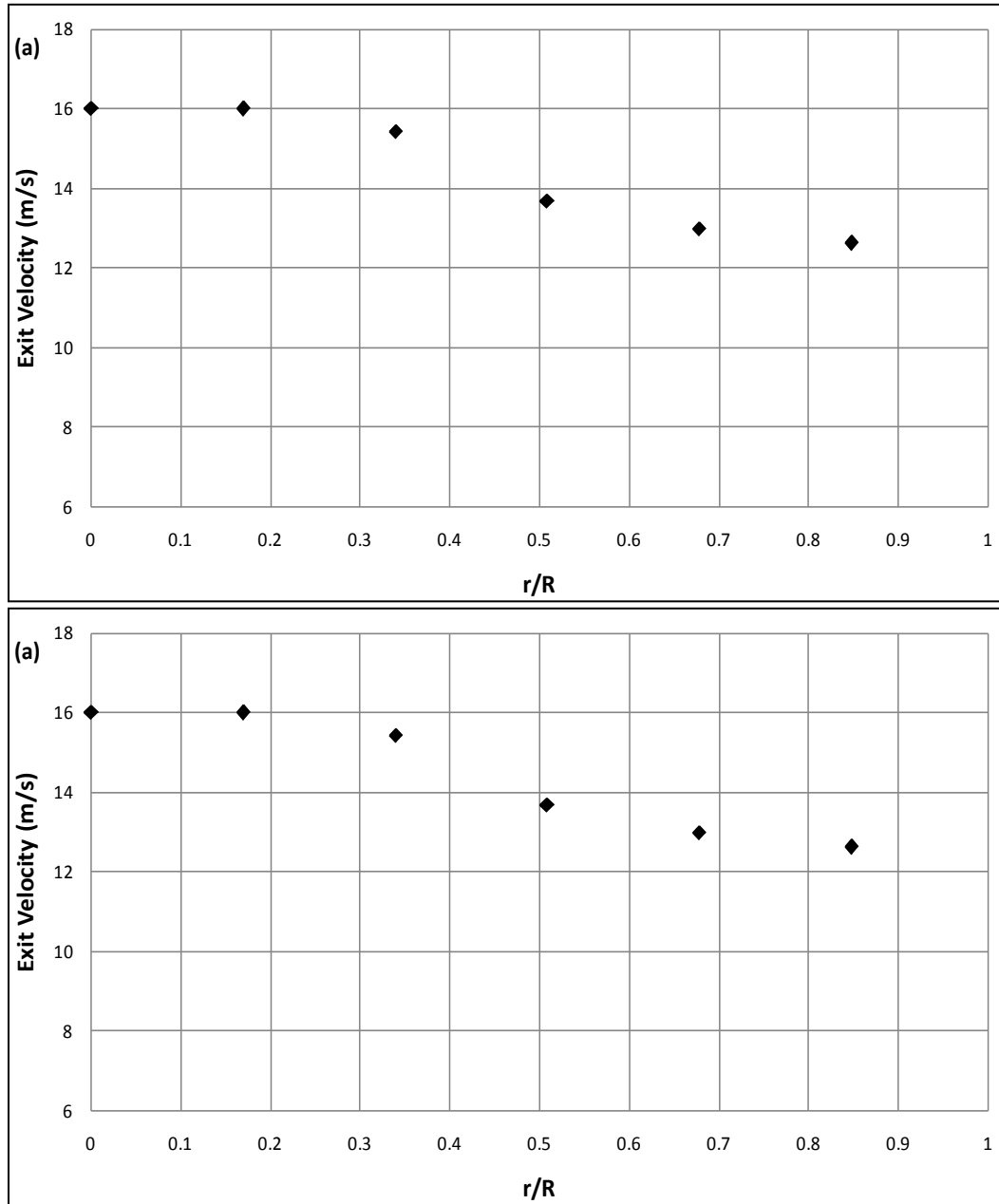


**Figure 5.13** Exit flow profiles (a) Velocity, and (b) Temperature.

## 5.4 Effect of Momentum flux Ratio on Temperature Uniformity

The jet-to-mainstream momentum flux ratio which is defined as the ratio of the momentum flux of the dilution jet to the momentum flux of the primary (or mainstream) flow is given by Eqn. 5.3. To study the effect of this momentum flux ratio on the uniformity of the temperature at the exit of the combustor simulator, three-dimensional computational analysis was performed with the inlet conditions as recorded in the experiment (refer Sec. 5.3). The details of the computational methodology followed for these simulations are given in Chapter 4. Numerical results were validated with the experimental findings for one of the simulations. This validated CFD model was subsequently utilized to individuate modifications of the combustor configuration such that the jet-to-mainstream momentum flux ratio was increased. Again, the simulations were performed for four different momentum flux ratio with the same inlet conditions and its effect on the temperature uniformity was analyzed.

$$I = \frac{\rho_{jet} V_{jet}^2}{\rho_{prim} V_{prim}^2} \quad (5.3)$$

where,

$$V_{jet} = \frac{V_{sec} A_{sec}}{A_{holes}} \quad (5.4)$$

### 5.4.1 CFD Model Validation

To compare the measured results with the computational predictions, temperature and flow field data were extracted from the numerical simulations performed for the same combustor simulator with the same inlet conditions as in the experiment. To



provide a better estimate of the inlet conditions for the simulations, the inlet data recorded along a single radial line were used to provide the inlet temperature and velocity profiles at different angles -  $0^\circ$ ,  $30^\circ$ ,  $45^\circ$ ,  $60^\circ$  and  $90^\circ$ , expanding on the entire inlet cross-sectional area as shown in Fig. 5.14. Each color in the figure represents the same temperature along that radius. The exit data were extracted for the same radial line along which the temperature and velocity values were measured experimentally.

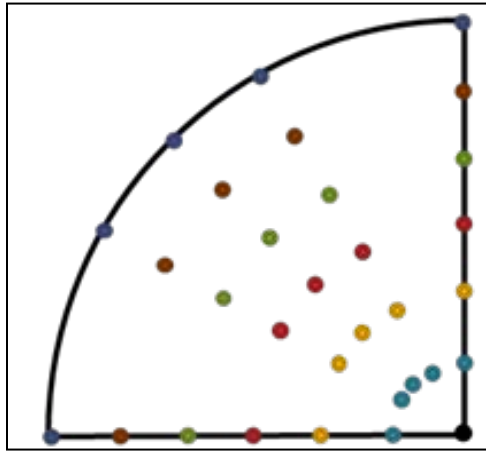


**Figure 5.14** Equivalent inlet condition points for the simulation.

Figures 5.15 (a) - (b) show a comparison of the exit temperature and velocity profiles for the simulation and experiment. Both the plots seem to exhibit the same characteristics with minor differences. The average percentage errors in the experimental and numerical values for the exit temperature and velocity were estimated to be approximately 3.0% and 8.5%, respectively. The possible reason for the temperature discrepancy could be the adiabatic wall condition considered for the simulation that overestimated the temperature values. Also, any heat loss to the surroundings in the experiments was not accounted for in the simulations, including the radiation and natural convection. Similarly, the lower experimental velocities may arise due to any loss of flow

that might occur at the joints in the set-up where as there was no flow loss in the simulations. Additionally, the uncertainty associated with measurements during the experiment may be a plausible reason for the differences in the experimental data and simulation predictions.

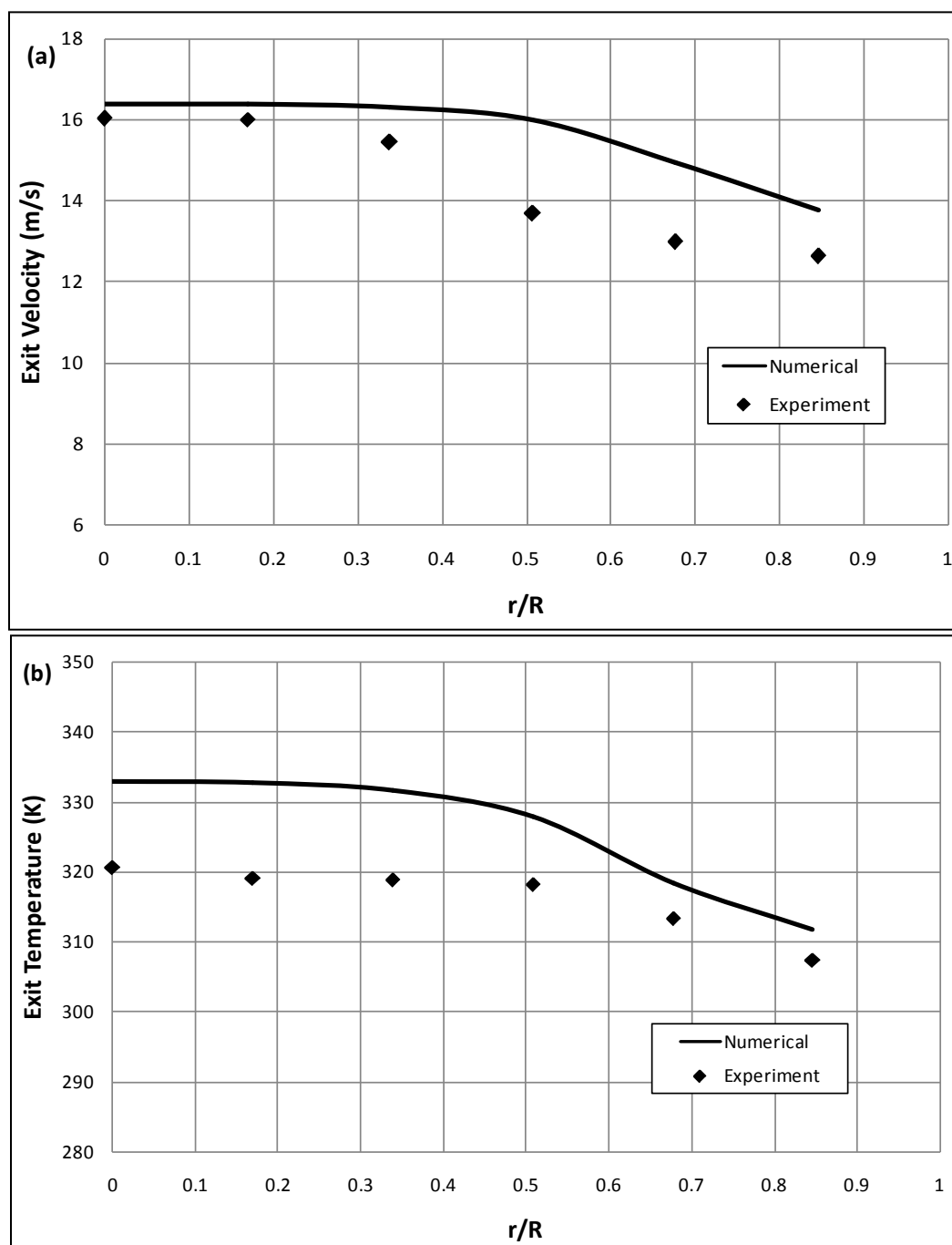


**Figure 5.15** Comparison of experimental and simulation exit profiles (a) Velocity, and (b) Temperature.

The uncertainty analysis performed for the experiment considered that the uncertainty of the temperature data was a combination of two different means of uncertainty — the repeatability, and the uncertainty of the laboratory equipment. The uncertainty of thermocouple wires was  $\pm 2.2^{\circ}\text{C}$  or 0.75% of the scale (in  $^{\circ}\text{C}$ ). For the repeatability of the test measurement, twenty readings were taken in nine seconds and variation from the mean was calculated. Then a combined uncertainty was calculated by taking the root of the sum of squares of the two uncertainties. And the maximum uncertainty was found to be  $\pm 3^{\circ}\text{C}$  for temperature. For velocity measurements, Pitot tubes connected to transducer were employed. The standard limit of error for this device was  $\pm 2\%$ , and was increased to  $\pm 4\%$  as a result of reducing the internal gain for the transducer to 0.5. Thus, the velocity measurements exhibited uncertainty values between the range of  $\pm 0.52$  to  $\pm 0.68$  m/s.

#### **5.4.2 Increasing Momentum Flux Ratio in Simulation**

From the Eqn. 5.3 it can be noted that the momentum flux ratio can be increased mainly in two ways, either by increasing the jet velocity or by reducing the primary flow velocity (assuming the air density will not vary much for the operating temperature range of the experiment). This increase can be achieved by varying the inlet velocities, but it would lead to different inlet conditions for the various simulations. Thus, a valid comparison cannot be made among the simulations performed with different inlet conditions. Therefore, to concentrate on the variation of just one parameter (momentum flux), the inlet flow rates were kept same for all the simulations. The area of the dilution holes was reduced to increase the jet velocity through these holes and therefore to

increase the momentum flux ratio. To reduce the cross-sectional area the diameter of the holes was decreased to get four different cases with an increasing momentum flux ratio. The same inlet conditions as used in the simulation which was validated with the experimental data were applied in these simulations. The simulation procedure followed the steps as discussed in Chapter 4. The temperature and velocity data were extracted along the same radial line at the exit section as was described in Sec. 5.4.1.

### 5.4.3 Data Analysis

For a qualitative and quantitative measure of the temperature uniformity from the data extracted from the simulation and the experiment, a number of parameters like the mixture fraction, mixture uniformity, pattern factor were determined for each simulation. Using the temperature data at each radial position from center of the exit section towards the wall, the mixture fraction was evaluated using Eqn. 3.3. An area-weighted average value for this mixture fraction was obtained by using the following Eqn. 5.5. The closer this value to the equilibrium mixture fraction  $f_{equil}$ , the better is the mixing and the more uniform the temperature profile.

$$f_{ave} = \frac{\int f \cdot ds}{A_{exit}} \quad (5.5)$$

Another parameter known as the pattern factor ( $PF$ ) defined by Eqn. 5.6 that relates the peak exit temperature and the average exit temperature was evaluated for each of the simulations. Higher values of the pattern factor correspond to a non-uniform temperature exit distribution and can lead to reduced turbine blade durability. For an ideal

case the value of this pattern factor should be equal to one, which would mean that the maximum temperature is same as the average temperature.

$$PF = \frac{T_{max} - T_j}{T_{exit} - T_j} \quad (5.6)$$

To quantify the mixing effectiveness of each module configuration, an area-weighted standard deviation parameter known as mixture uniformity ( $M$ ) given by Eqn. 5.7 was defined at the exit plane. A complete mixing is achieved when the mixture uniformity parameter across a given plane reaches zero.

$$M = \sqrt{\frac{1}{A_{exit}} \sum_{i=1}^n ds. (f - f_{equil})^2} \quad (5.7)$$

After determining the above parameters for all the simulations, plots were generated to analyze the variation of these parameters with the increase in the momentum flux ratio. Figure 5.16 shows the variation of the area-weighted average mixture fraction with the momentum flux ratio. It can be observed from the figure that as the momentum flux ratio is increased, the mixture fraction tends towards the equilibrium mixture fraction value that is equal to 0.71 for the given inlet conditions. Increasing the flux ratio from 0.6 to 0.85 improved the mixture fraction by approximately 7% and attained nearly 85% of the equilibrium value. This indicates that the exit temperature is nearing the adiabatic (or equilibrium) temperature at a higher momentum flux ratio.

The variation of pattern factor with the momentum flux ratio can be observed in Fig. 5.17. The pattern factor is found to improve with the increase in the momentum flux ratio as the value gets closer to one. This implies that the temperature uniformity is

improved as the maximum temperature approaches the average temperature at the combustor exit. From Fig. 5.18 which depicts the variation of mixture uniformity with the momentum flux ratio it can be noticed that the mixing improves at a higher momentum flux ratio as the value moves closer to zero.

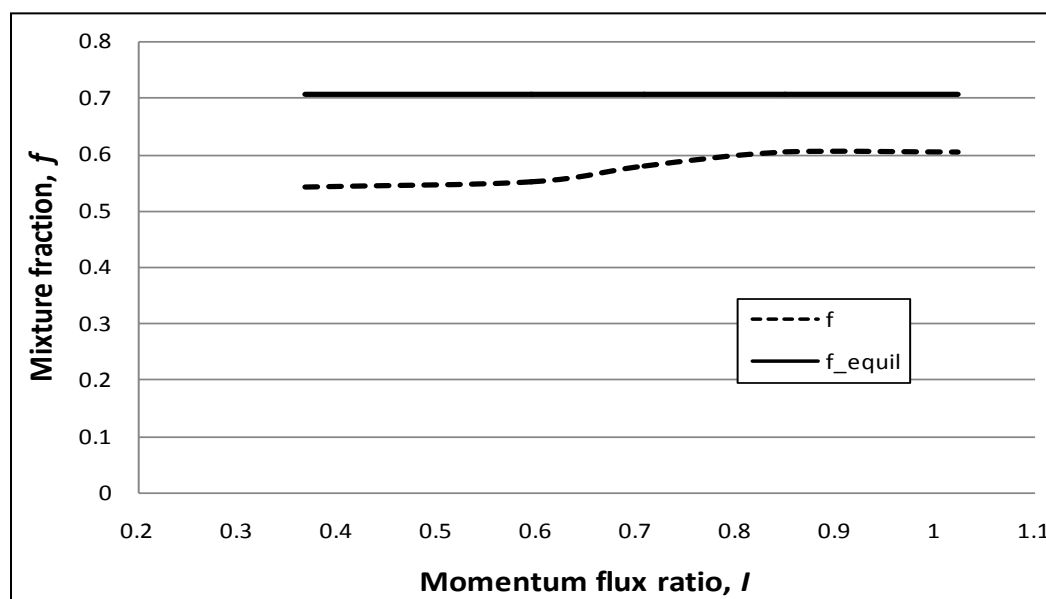


**Figure 5.16** Variation of mixture fraction with momentum flux ratio.

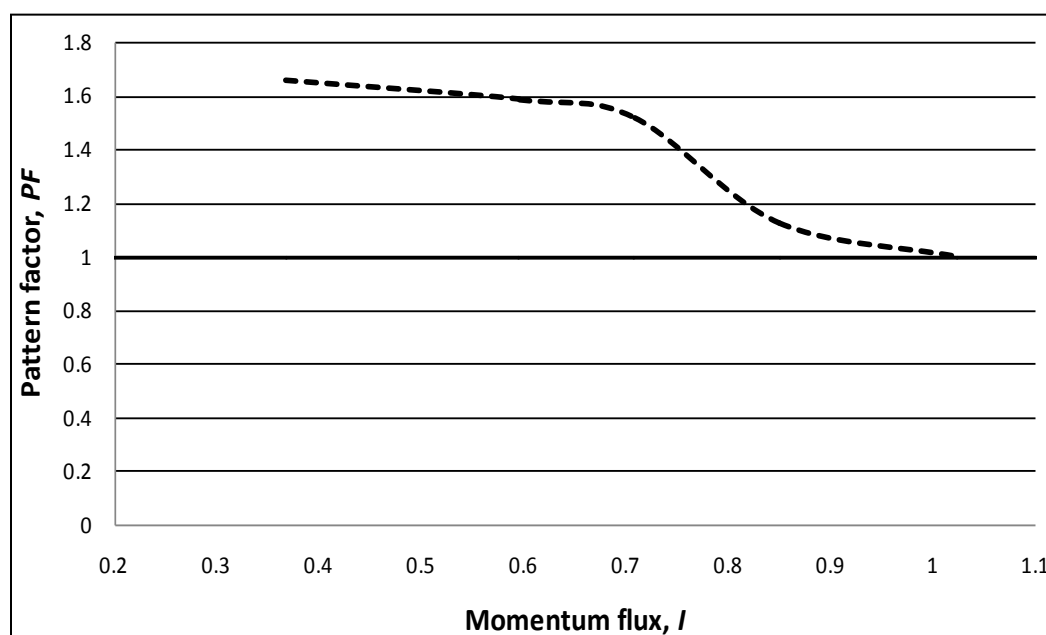


**Figure 5.17** Variation of pattern factor with momentum flux ratio.

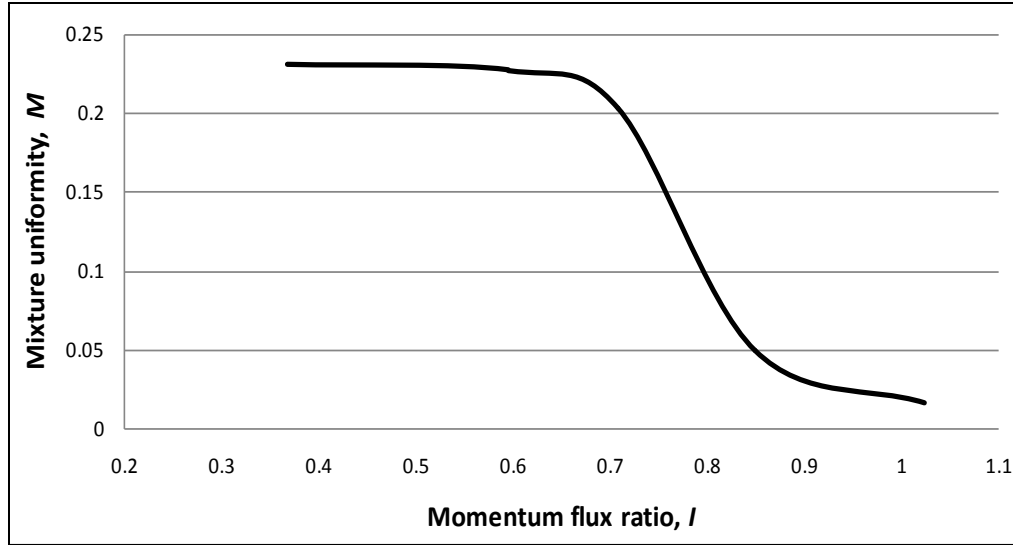


**Figure 5.18** Variation of mixture uniformity with momentum flux ratio.

The trends of the various parameters discussed above suggest that mixing is improved as the momentum flux ratio is increased. Also, improved mixing means a better uniform temperature profile at the combustor exit and lesser damage to the turbine blades as more uniform temperature flow hits the blades.

To explore further the reason for this improvement in temperature uniformity with the increase in the momentum flux ratio, velocity vectors were plotted at a plane passing through the dilution holes (refer to Plane 1 in Fig. 5.10). Figures 5.19 (a) - (c) show the velocity vectors near the dilution holes in the test section at Plane 1 for the momentum flux ratio of 0.37, 0.71 and 0.85. These figures suggest that the jets enter the mixing section with higher velocity at an increased momentum flux ratio and thus can penetrate deeper into the flow. By measuring the angle at which the dilution jet enters the test section, it was found that the penetration angle increased with the increase in the momentum flux ratio. Table 5.4 gives the jet penetration angle for different momentum flux ratios. This clearly indicates that the dilution jet penetrated deeper in the primary

flow at a higher momentum flux ratio, causing better mixing. The increased penetration angle means a larger penetration depth for the jet.

**Table 5.4** Jet penetration angle for different flux ratio.

	Momentum flux ratio	Jet penetration angle (degrees)
1	0.37	34
2	0.71	51
3	0.85	68

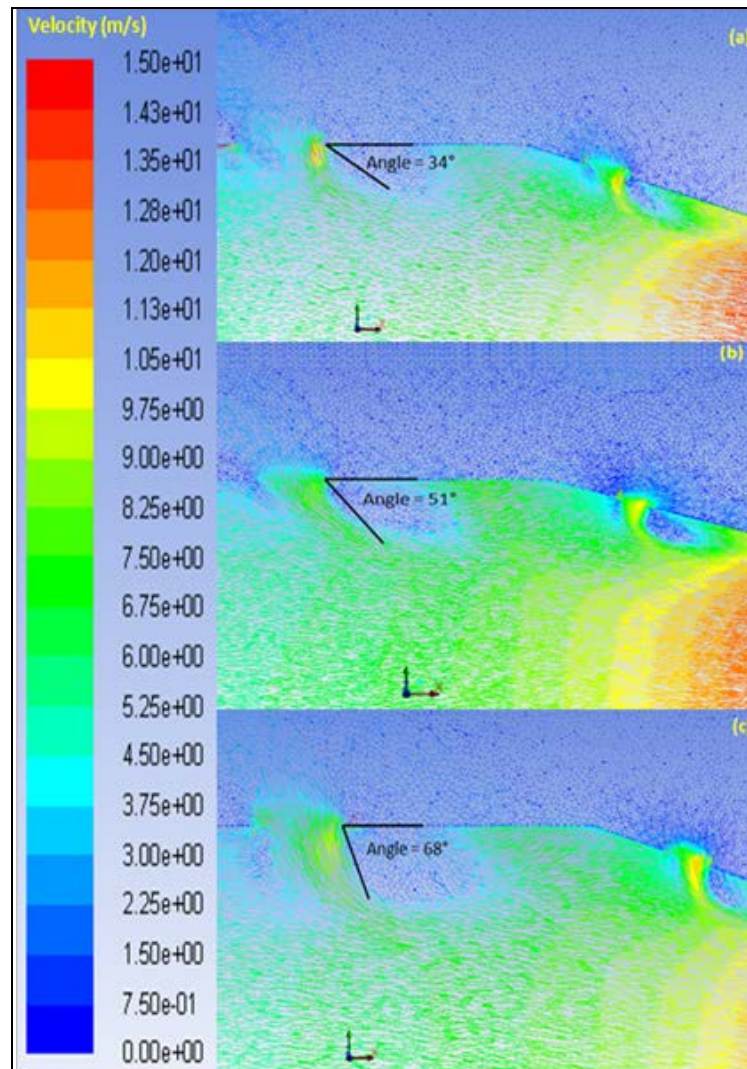


**Figure 5.19** Velocity vectors at Plane 1 for momentum flux ratio (a) 0.37, (b) 0.71, and (c) 0.85.



Although improved temperature homogeneity is obtained at a higher momentum flux ratio, it should be noted that a higher flux ratio would result in a higher pressure loss. Figure 5.20 shows the variation of the total pressure loss with the flux ratio, which was determined using the Eqn. 5.8. It can be noticed from the figure that the pressure loss is approximately 45 Pa at 0.85 jet-to-mainstream momentum flux ratio. This pressure loss from the inlet to the exit section was determined over the length of 3.34 m. Therefore, the choice to operate at a higher flux ratio should be made wisely, taking into consideration the associated pressure loss, which would eventually lead to a loss in the performance of the gas turbine engine. This study has been published in the 49<sup>th</sup> AIAA/ASME/SAE/ASEE Joint Propulsion Conference & Exhibit (Gupta *et. al.*, 2013).

$$\text{Pressure loss} = \frac{\dot{m}_{exit}P_{exit} - (\dot{m}_{prim}P_{prim} + \dot{m}_{sec}P_{sec})}{\dot{m}_{exit}} \quad (5.8)$$

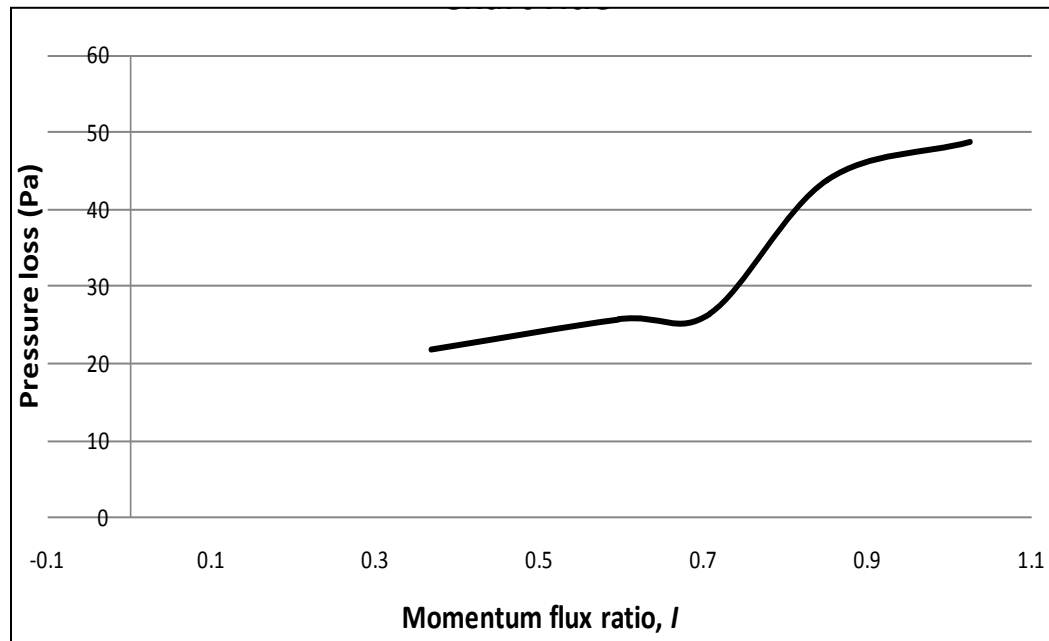


**Figure 5.20** Variation of pressure loss with momentum flux ratio.

## 5.5 Variation of Cooling Rate Number (CRN)

The primary hot stream should not be cooled rapidly since this would mean rapid cooling of the combustion products which may lead to a "frozen gas composition", discharging unburned CO in the exhaust. A parameter called the 'cooling rate number (CRN)' was defined given by Eqn. 5.9, to keep a check on any sudden fall in the dilution zone temperatures. This number basically represents the temperature gradient at various axial positions in the dilution zone.  $\Delta X$  in Eqn. 5.9 corresponds to the total length of the dilution zone (test-section) and  $dT$ ,  $dx$  are the difference in temperatures and axial distances, respectively.

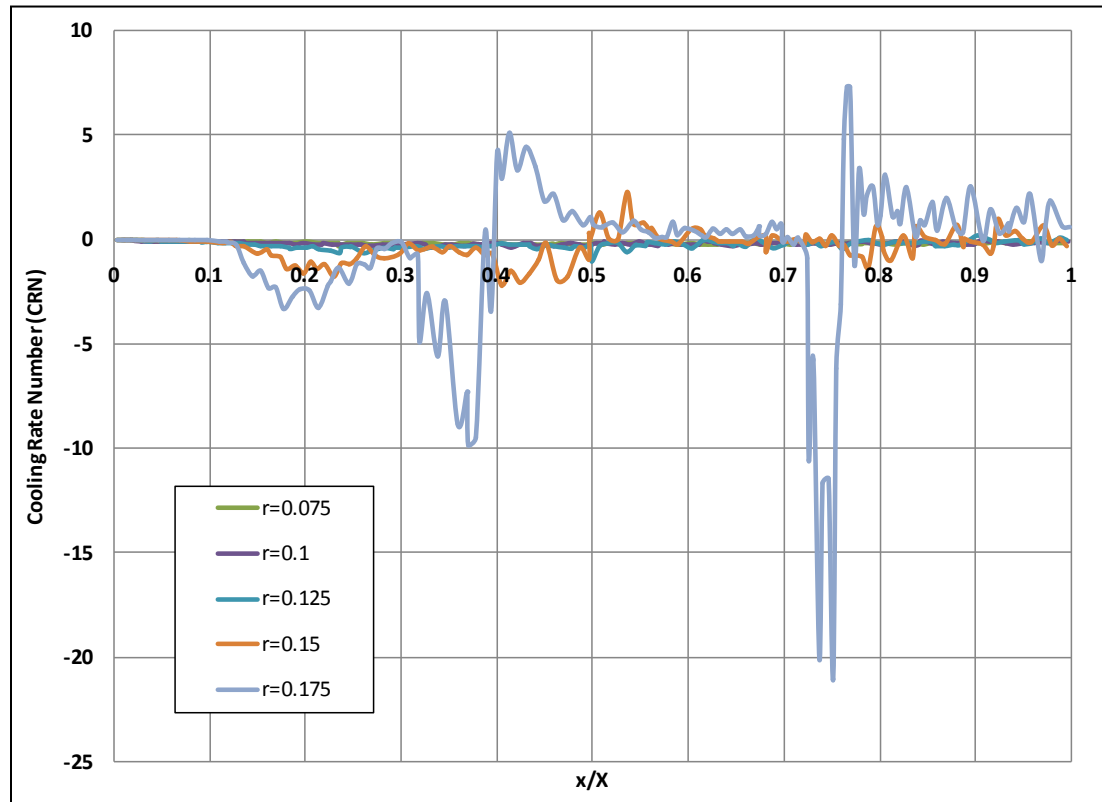
$$CRN = \frac{dT/\Delta T}{dx/\Delta X} \quad (5.9)$$

where,

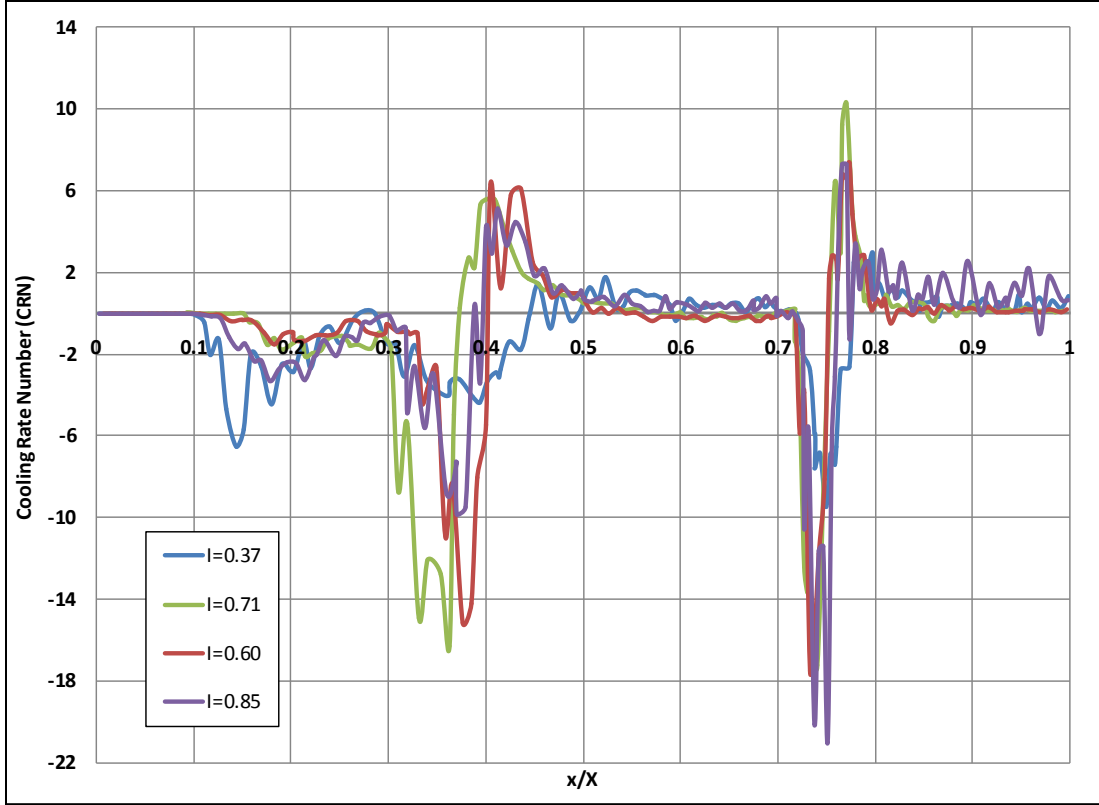
$$\Delta T = T_{\infty} - T_j \quad (5.10)$$

Figure 5.21 shows the variation of the cooling rate number with axial location at different radial distances for the case of momentum flux ratio  $I = 0.85$ . High cooling rate numbers (CRNs) can be observed at the two locations  $x/X = 0.375$  and  $x/X = 0.75$  which are the two holes cutting the calculation plane. The effect of holes at locations  $x/X = 0.125$  and  $x/X = 0.625$  is less as compared to in-plane holes. Still a minor effect can be noticed for larger diameter holes at  $x/X = 0.125$  as compared to smaller hole at  $x/X = 0.625$ . As we go closer to the dilution jets, rapid change in the CRNs can be noticed. A total variation of CRN from nearly -21 to 7 (28 units) can be noticed at  $x/X = 0.75$ , which means there are chances of rapid cooling of the combustion products

near these holes. While for the other radial distances a fairly uniform CRN was observed for the entire length of the dilution zone which leads to an even cooling of the two streams. Figure 5.21 also shows an increase in the CRN for  $r = 0.175$  m (closer to the dilution holes), just after the holes. This increase is due to the recirculation zones downstream the dilution holes as seen in Fig. 5.19. The recirculation area temperature is a mixture of the primary and secondary air rather than the cooler air at the hole where the secondary air is more dominant. A similar graph is plotted for various flux ratios for zone closest to the dilution jet entrance at  $r/R = 0.875$  as shown in Fig. 5.22, to examine the effect of increasing the momentum flux ratio on CRN at regions closer to the dilution holes. From the figure it can be noticed that  $I = 0.85$  has the maximum variation in CRN at  $x/X = 0.75$  and a fairly uniform cooling can be observed for  $I = 0.37$ .



**Figure 5.21** Variation of cooling rate number with axial location at different radial distances for  $I = 0.85$ .



**Figure 5.22** Variation of cooling rate number (CRN) with axial location for different flux ratios.

## 5.6 Exergy Destruction

Exergy represents the maximum amount of useful work that can be theoretically obtained from a system. Any exergy loss would mean reduced system efficiency. Thus, an exergy analysis was carried out to determine the amount of exergy destroyed in the process of mixing within the dilution zone. Equation 5.11 was used for the exergy destruction calculations.

$$e_d = \frac{\dot{m}_p \left[ (h_p - h_m) - T_o (s_p - s_m) + \frac{(v_p^2 - v_m^2)}{2} \right] + \dot{m}_s \left[ (h_s - h_m) - T_o (s_s - s_m) + \frac{(v_s^2 - v_m^2)}{2} \right]}{\dot{m}_m} \quad (5.11)$$

Figure 5.23 shows an exponential-wise increase in the specific exergy destruction with increase in the momentum flux ratio. More exergy (or useful work) is destroyed when the dilution jets enter the mixing section with higher velocities.

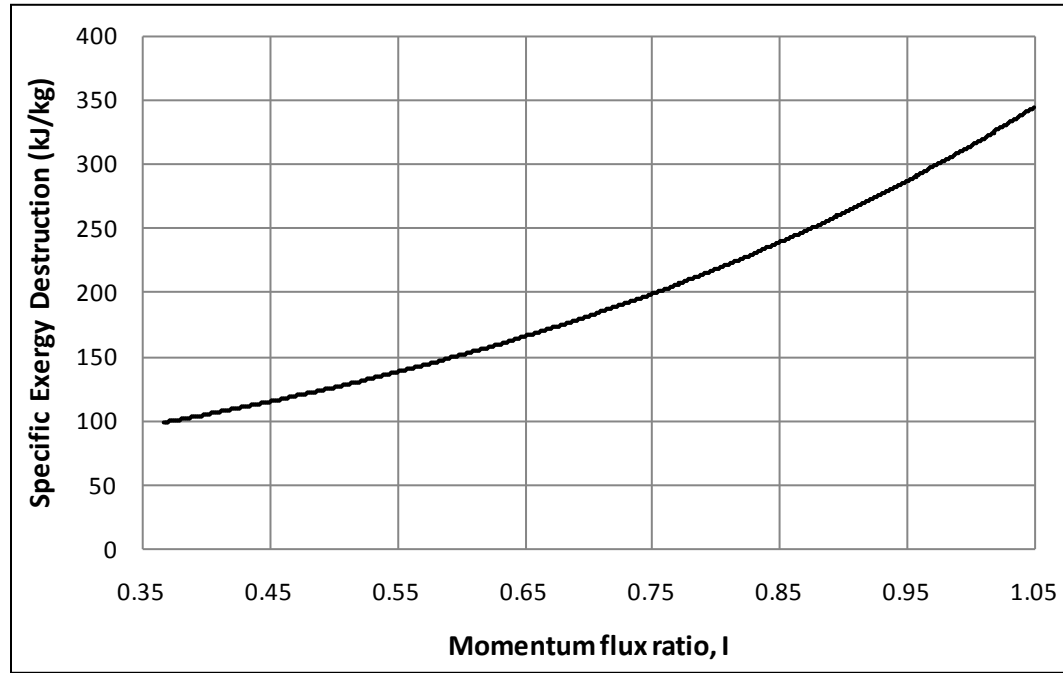


**Figure 5.23** Variation of the specific exergy destruction with momentum flux ratio.

## 5.7 Summary

In this chapter computational results are presented which forms the basis of design decisions and parametric studies. Based on the two-dimensional CFD analysis performed for in-line and staggered dilution holes pattern, it was proven that the introduction of the dilution cooling air through larger dilution holes results in better mixing and temperature uniformity with lower pressure loss as compared to the case of introduction of dilution air at the same flow rate from the same total surface area, but from smaller dilution holes.

From the three dimensional CFD analysis carried out for four different dilution zone configurations - in-line dilution holes, staggered dilution holes, in-line holes with streamlined body and staggered holes with streamlined body, it was found that the staggered dilution holes resulted in better mixing as compared to the in-line counter-part. Furthermore, the addition of a streamlined body improved the mixing of the primary and secondary air by pushing the primary air towards the cooler dilution air. Better mixing produced more uniform exit temperature profile. The staggered dilution holes with streamlined body performed the best amongst the different schemes being investigated and achieved almost 91% of the equilibrium mixture fraction value.

Numerical simulations were performed to investigate the effect of jet-to-mainstream momentum flux ratio on the exit temperature uniformity. To accomplish this, CFD model for staggered dilution holes scheme was first validate with the experimental observation. The numerical results showed good agreement with the experimental measurements. Later the validated model was used to generate various cases of momentum flux ratios. It was demonstrated that the dilution jets penetrated deeper into the flow at higher flux ratio causing enhanced mixing which improved the temperature uniformity. Almost 85% of the equilibrium mixture fraction was achieved at flux ratio of 0.85. Increasing the flux ratio further did not improve the uniformity beyond a certain threshold (mixture fraction,  $f = 0.6$ ).

A new parameter, 'Cooling Rate Number (CRN)', was defined to locate the regions of high temperature gradients which may result in cold regions. A higher variation in the cooling rate number (CRN) was observed at the vicinity of the dilution holes indicating presence of high temperature gradients in this region. Care should be

taken during the design of near holes region as the risk of rapid cooling of the gases is increased in these regions, which may result in more unburned CO being discharged in the exhaust. The exergy analysis taken up indicated exponential increase of the exergy with increasing momentum flux ratio.

## Chapter 6 - Experimental Results and Discussion

This chapter presents the experimental findings for all different types of the dilution techniques - staggered dilution holes, staggered dilution holes with streamlined body, staggered dilution holes with various configuration of the guide vanes orientation ( $0^\circ$ ,  $30^\circ$ ,  $60^\circ$  and  $90^\circ$ ). Results for three different Reynolds Number - 100,000, 80,000 and 30,000 are compared under different temperature conditions.

Extensive experimentation was performed for different inlet temperature and flow rate conditions following the same experimental procedure as outlined in Chapter 3. Following a consistent procedure, temperature, velocity and pressure data was collected for each dilution technique being tested. The data was recorded at the entrance to the test-section and after the mixing towards the exit of the combustor simulator. Five cases were run for each technique explored - three cases with different primary flow inlet temperature and two additional for different inlet flow rates. This makes a total of 30 experimental cases tested. The operating conditions for each test case are given in Table 6.1.

**Table 6.1** Inlet conditions for different experimental test cases.

Case	Inlet Conditions		
	Primary Flow Inlet Reynolds Number	Primary Flow Average Inlet Temperature (K)	Dilution Flow Average Inlet Temperature (K)
A	$1.0 \times 10^5$	323.94	296.85
B	$1.0 \times 10^5$	315.41	297.08
C	$1.0 \times 10^5$	310.67	293.1
D	$0.8 \times 10^5$	329.14	297.22
E	$0.3 \times 10^5$	363.07	298.17



## 6.1 Measure of Temperature Uniformity

For a qualitative and quantitative measure of the temperature uniformity from the data collected in the experiments, mixture fraction was determined for each case using the temperature data at each radial position from center of the exit section towards the wall using Eqn. 3.3 which is restated below for convenience purpose (Eqn. 6.1). Another weighted parameter was defined as ' $\chi$ ', called the 'uniformity factor', given by Eqn. 6.2 to compare how close the mixture fraction is to the equilibrium value. It can be defined as the area enclosed by the mixture fraction distribution and the equilibrium mixture fraction on the  $f - r/R$  diagram. The smaller the value of  $\chi$ , more uniform the temperature distribution. Based on the variation of the above two parameters, all the techniques were compared to come up with the design which gives the best temperature uniformity, keeping the pressure loss minimum during the mixing process, since any pressure loss would result in subsequent loss in the efficiency of the complete gas turbine system.

$$f = \frac{T_i - T_j}{T_\infty - T_j} \quad (6.1)$$

$$\chi = \frac{\sum |(f - f_{equil}) \cdot dr|}{R} \quad (6.2)$$

## 6.2 Results and Discussion

To compare the mixing performance of the dilution techniques and the resulting temperature uniformity, radial distribution of the normalized mixture fraction,  $\bar{f}$  given by Eqn. 6.3, at the combustor simulator exit for different dilution techniques - staggered dilution holes, staggered dilution holes with streamlined body, staggered dilution holes

with guide vanes - 0°, 30°, 60° and 90°, respectively are plotted and the  $\chi$  is determined for each case to get the deviation from the equilibrium condition.

$$\bar{f} = \frac{f - f_{equil}}{f_{equil}} \quad (6.3)$$

The greater the deviation of the mixture fraction from the equilibrium mixture fraction, the more is the non-uniformity in the temperature distribution. Figures 6.1 - 6.5 show the radial distribution of the normalized mixture fraction for various experimental cases tested. From the figures, it can be observed that the temperatures are higher at the centre of the duct and decrease towards the wall. A good mixing between the primary and the dilution streams would result in a flow condition that is more uniform throughout the radial direction. The introduction of the guide vanes forces the secondary air flow in a direction different from the basic staggered holes geometry. The 0° guide vanes should give maximum penetration of the fresh secondary (or dilution) flow into the primary flow while the 90° guide vanes should give the maximum swirl. Increasing the angle will decrease the depth while increasing the swirl. Both the depth and the swirl action are expected to give a positive effect to the mixing of primary and secondary flows and consequently increasing the temperature uniformity.

In Fig. 6.1, although all the dilution techniques give higher central core temperature, the 30° guide vanes provide a flow with closer equilibrium temperature at the centre of the duct. The values for ' $\chi$ ' shown in Table 6.2 were calculated using Eqn. 6.2 based on the experimental temperature data collected at the entrance and exit of the test-section. The best mixture uniformity is highlighted for each case. From Table 6.2, the  $\chi$  value for 30° guide vane, which is 0.23 for the case A with primary flow inlet Reynolds

number  $1 \times 10^5$  and  $\Delta T = 30^\circ$  approximately is an evidence for the uniformity improvement. Based on the  $\chi$  value, it can be found that the  $30^\circ$  guide vane gives about 8% more uniform flow as compared to the case of having just the staggered holes in the dilution zone. The  $60^\circ$  and  $90^\circ$  guide vanes provide the most non-uniform temperature flow with hotter central core.

**Table 6.2** Comparison of various dilution techniques.

Case $\longrightarrow$	A	B	C	D	E
$\downarrow$ Technique	$\chi$				
Staggered dilution holes	0.25	0.31	0.26	0.23	0.27
Streamlined body	0.28	0.26	0.29	0.28	0.19
$0^\circ$ Guide-vanes	0.26	0.27	0.23	0.22	0.18
$30^\circ$ Guide-vanes	0.23	0.27	0.23	0.20	0.14
$60^\circ$ Guide-vanes	0.31	0.28	0.27	0.29	0.12
$90^\circ$ Guide-vanes	0.32	0.30	0.42	0.29	0.15

For case B (refer Fig.6.2) with  $\Delta T = 20^\circ$  approximately and at same Reynolds number as case A, the most uniform flow is provided by the streamlined body with  $\chi = 0.26$  which is closely followed by  $0^\circ$  and  $30^\circ$  guide vanes. The streamlined body gives approximately 16% more uniform temperature flow than the staggered holes. All the guide vanes perform better than the staggered holes with  $0^\circ$  and  $30^\circ$  guide vanes giving approximately 13%,  $60^\circ$  giving 10% and  $90^\circ$  giving 3% more uniform temperature flow respectively.

In case C where  $\Delta T = 18^\circ$  approximately, the  $0^\circ$  and  $30^\circ$  guide vanes give the most uniform temperature flow with lowest  $\chi = 0.23$  and approximately 12% more uniform flow than staggered holes. From Fig. 6.3, it is clear that the  $90^\circ$  guide vanes seems to deviate the most from the equilibrium conditions. Although the central core with the staggered holes appear to be the closest to the equilibrium value, the overall normalized mixture fraction profile of the  $0^\circ$  and  $30^\circ$  guide vanes look more flatter and thus, radial distribution is more uniform.

Case D at 20% lesser flow conditions and  $\Delta T = 32^\circ$  approximately, the  $30^\circ$  guide vane provides 13% more uniform flow than the staggered holes, while the flow from rest of the techniques seems to deviate more from the equilibrium condition (refer Fig.6.4). For case E (refer Fig. 6.5) with 70% lesser flow and  $\Delta T = 65^\circ$  approximately, it is the  $60^\circ$  guide vanes which give the most uniform flow at  $\chi = 0.12$  which corresponds to approximately 56% more uniform flow than the staggered holes. All the other techniques also perform better than the staggered holes giving on an average 39% more uniform temperature flow.

From Table 6.2, it can also be observed that with decreasing the flow velocity, increasing the guide vane angle is more preferable. This is due to the decrease in the main flow inertia and the swirl flow from the guide vanes is more effective than increasing the depth to which the secondary flow is introduced.

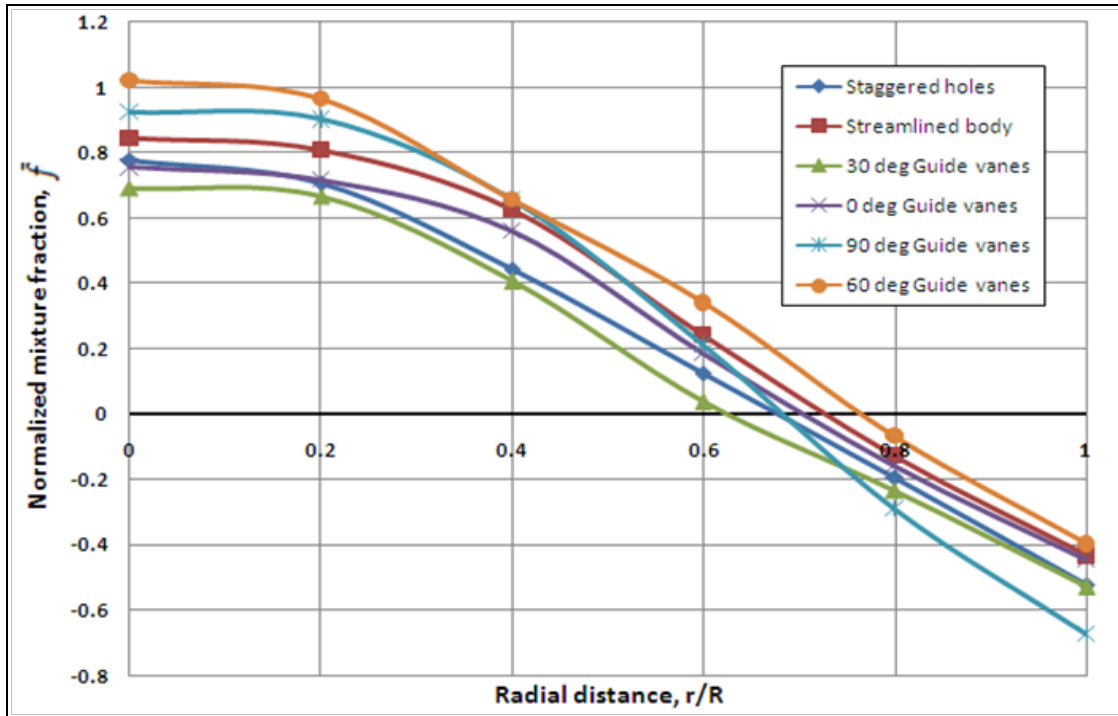


Figure 6.1 Radial distribution of the normalized mixture fraction for Case A.

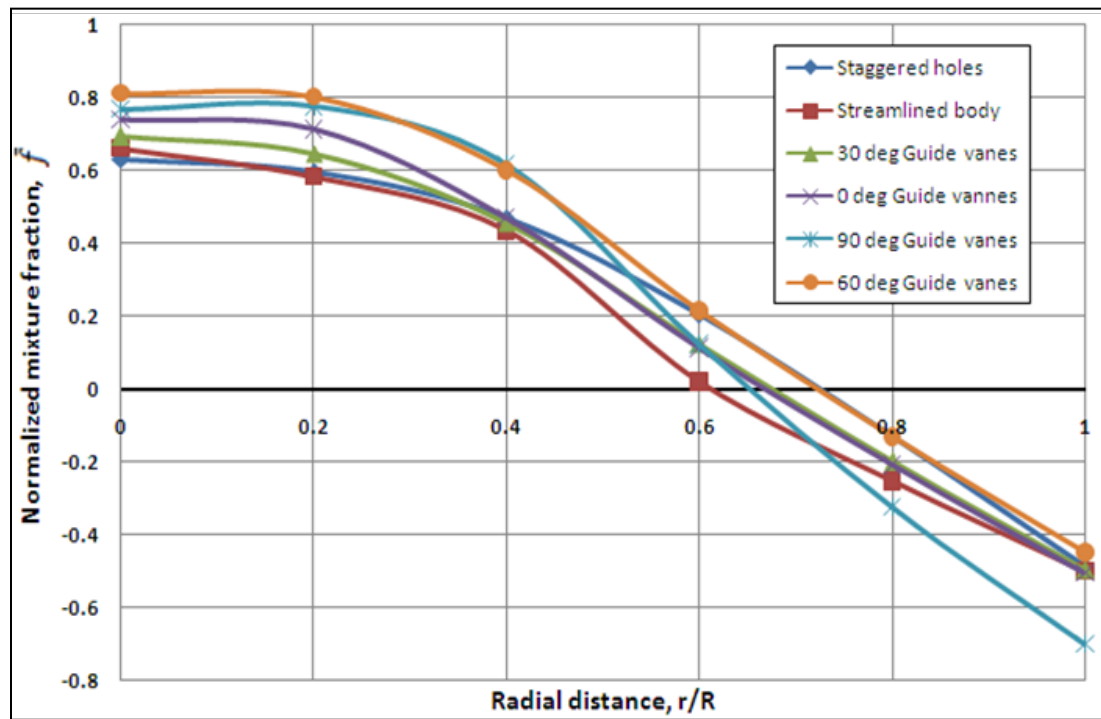


Figure 6.2 Radial distribution of the normalized mixture fraction for Case B.

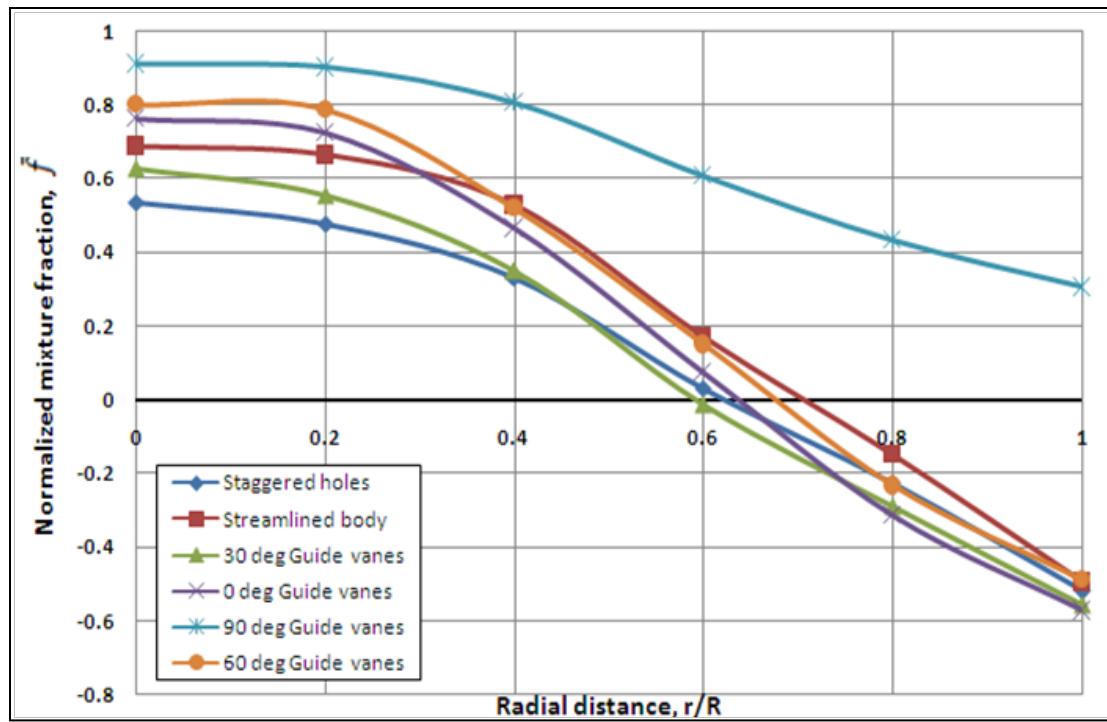


Figure 6.3 Radial distribution of the normalized mixture fraction for Case C.

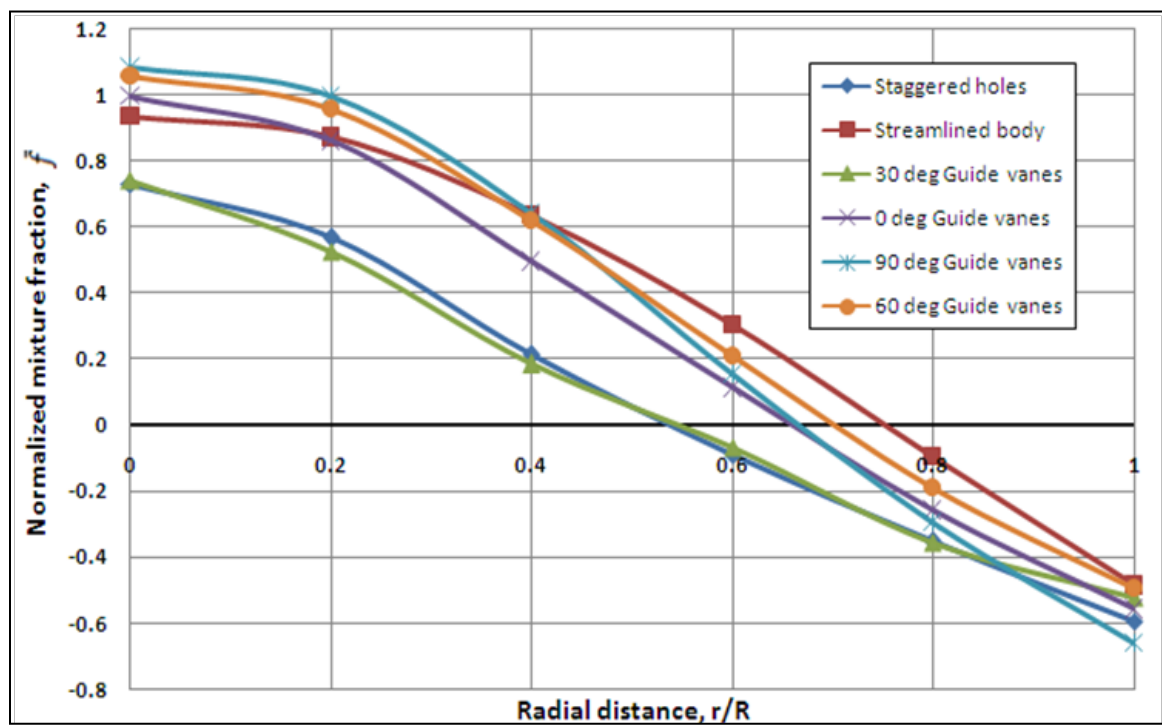
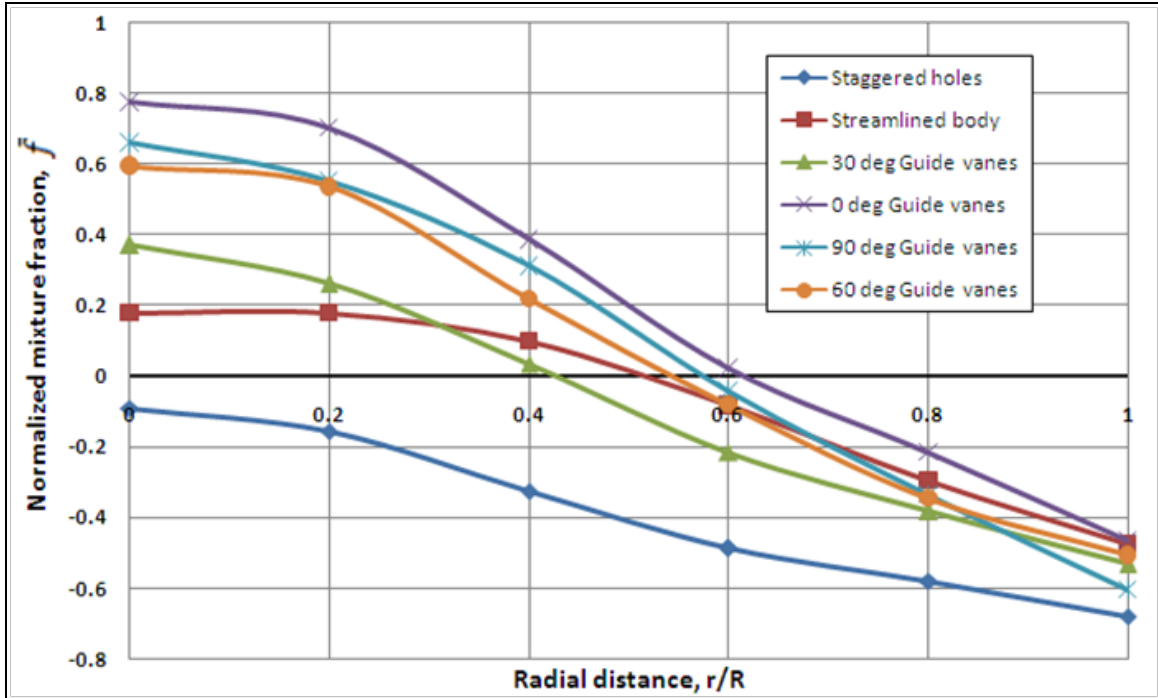


Figure 6.4 Radial distribution of the normalized mixture fraction for Case D.



**Figure 6.5** Radial distribution of the normalized mixture fraction for Case E.

The total pressure loss between the inlet and the outlet of the experimental set-up is given by Table 6.3 for three different flow conditions. The use of streamlined body in the dilution zone appears to be advantageous since it gives the minimum pressure loss which is about 4% lesser than the staggered dilution holes case. The plausible reason for this lesser pressure loss could be the basic geometry of the streamlined body, which not only forces the hotter primary flow towards the cooler dilution flow but at the same time makes the flow more directed and follow the shape of the streamlined body, thus, reducing the losses that used to happen with other geometries due to random motion of the fluid particles within the dilution zone. The 30° guide vanes give the maximum pressure loss. Although the pressure loss with the 30° guide vanes is the maximum, the mixing provided by these vanes seems to be the most uniform in majority of the flow cases considered.

**Table 6.3** Pressure loss data for various dilution techniques.

<b>Primary Flow Inlet Reynolds Number</b>	<b>Pressure loss (%)</b>					
	<b>Staggered holes</b>	<b>Streamlined body</b>	<b>0° Guide- vanes</b>	<b>30° Guide- vanes</b>	<b>60° Guide- vanes</b>	<b>90° Guide- vanes</b>
1.0 x 10 <sup>5</sup>	40.87	37.85	41.29	51.65	34.53	34.75
0.8 x 10 <sup>5</sup>	43.77	44.15	47.21	48.09	42.24	48.77
0.3 x 10 <sup>5</sup>	68.27	58.08	59.52	56.74	65.14	57.99
<b>Avg. Pressure loss (%)</b>	50.97	46.70	49.34	52.16	47.30	47.17

### 6.3 Summary

In this chapter experimental results are presented for all the proposed dilution techniques which include - staggered dilution holes, staggered dilution holes with streamlined body, staggered dilution holes with guide vanes at various orientation (0°, 30°, 60° and 90°). These guide vanes orientation were tested to evaluate the effect of varying the dilution jet injection angle on the temperature uniformity. Additionally, these experiments were conducted at three different Reynolds Number – 100,000, 80,000 and 30,000 to see the effect of Reynolds Number on the mixing. Based on the variation of the uniformity factor for various techniques at different Reynolds Number, it can be observed that the mixing improved at lower Reynolds Number in general. A plausible reason could be the more residence time available inside the dilution zone due to lower flow rate conditions, which provided sufficient time for the mixing of the primary hot air and the cooler dilution air, thus, resulting in better mixed flow and more uniform temperature distribution at the exit.



For three out of the five flow conditions, the 30° guide vanes gave the most uniform temperature flow with just about 1% higher pressure loss as compared to the staggered dilution holes geometry. If an average is taken for the  $\chi$  values for different flow conditions, the average uniformity factor for 30° guide vanes  $\chi_{\text{avg}} = 0.22$ , which is about 15% more uniform than the staggered holes ( $\chi_{\text{avg}} = 0.26$ ). The fact that the use of 30° guide vanes can provide the turbine blade with 15% more uniform temperature flow than the staggered dilution holes design with merely 2% more pressure drop, has a very important implementation in order to reduce the damage of the turbine blades due to non-uniform temperature flow and extend its life-span. This would result in an overall reduction in the maintenance cost of the gas turbine systems which is quite significant. Further, the introduction of the streamlined body not only improved the mixing in some cases but also helped decrease the pressure drop from inlet to exit of the experimental set-up. This is expected to increase the overall system efficiency and decrease the operating cost of a gas turbine system. Further investigation of the streamlined and guide vanes is required to optimize the geometry. Also, the applicability and feasibility of changing the gas turbine construction should be taken into consideration.

## Chapter 7 - Algebraic Stress Model (ASM)

Turbulence has a decisive influence on many physical phenomena which include but not limited to heat transfer, species transport, drag, vorticity distribution, separation and swirl flow. Separation and reattachment of turbulent shear layers in the presence of adverse pressure gradient can be seen in many practical, industrial and engineering applications, either in internal flow systems such as diffusers, combustors and channels with sudden expansion, or in external flows like those past bluff structures and buildings (El-Beheri and Hamed, 2009). Separations cause a loss in performance; this makes the study of turbulence which is mainly characterized by fluctuating velocity fields very vital and significant to gain more in-depth understanding of the above mentioned phenomena.

Apart from the novel passive control techniques for better temperature uniformity at the combustor exit developed with extensive experimentation described previously in this thesis, in order to address the need to better estimate the turbulence via Reynolds stresses prediction, development of an Algebraic Stress Model (ASM) is undertaken in this thesis. There exists class of turbulence flow problems which is mainly governed by the Reynolds stresses such as flow separation, recirculation, near-wall region flows, etc. Determination of the Reynolds stresses plays a significant role to accurately predict the turbulence level in these regions of interest. Better prediction of Reynolds stresses in the near-wall region would throw more light on the phenomenon of heat transfer near the wall which affects the mixing of fluids as the dilution jets enter the dilution zone. This chapter brings out the importance of the Reynolds stresses in turbulent flows, limitation of the Reynolds Averaged Navier-Stokes (RANS) turbulence models in predicting the

anisotropic nature of turbulence in real world, Reynolds Stress Modeling (RSM) with its relative merits and demerits, motivation for development of Algebraic Stress Model, derivation of the ASM model. The validation of the ASM model for a simple two-dimensional flow over flat plate and a complex three-dimensional flow around Ahmed body is demonstrated in Chapter 8.

## 7.1 Reynolds Stresses

In fluid dynamics, the Reynolds stress is the component of the total stress tensor in a fluid obtained from the averaging operation over the Navier-Stokes equations to account for turbulent fluctuations in fluid momentum. In taking an average of the Navier-Stokes equations for turbulent flow that is three-dimensional, unsteady, random, irregular, and rotational, detailed information about fluid motion is lost (Chen and Jaw, 1998). In order to recover the information lost during the averaging process, a turbulence model must be introduced. These turbulence model attempts to either model or solve the averaged equations with some other additional equation depending on the type of turbulence model.

For a Newtonian uniform density flow, the momentum transport equation may be written as:

$$\frac{\partial U_i}{\partial t} + U_j \frac{\partial U_i}{\partial x_j} = -\frac{1}{\rho} \frac{\partial P}{\partial x_i} + \frac{\partial}{\partial x_j} \left[ \vartheta \left( \frac{\partial U_i}{\partial x_j} + \frac{\partial U_j}{\partial x_i} \right) \right] \quad (7.1)$$

At any instant of time, the instantaneous velocity vector  $U_i$ , can be written as a summation of the mean velocity,  $\bar{U}_i$  and fluctuating (or turbulent) velocity,  $u_i$  as:

$$U_i = \bar{U}_i + u_i \quad (7.2)$$

Fluctuation in velocity will lead to fluctuation in pressure, thus the instantaneous value of pressure can be written as:

$$P = \bar{P} + p \quad (7.3)$$

On substituting Eqns. 7.2 - 7.3, in Eqn. 7.1 and averaging over time  $2T$  and rearranging the equation, the following transport equation can be obtained:

$$\frac{\partial \bar{U}_i}{\partial t} + \frac{\partial \bar{U}_i \bar{U}_j}{\partial x_j} = -\frac{1}{\rho} \frac{\partial \bar{P}}{\partial x_i} + \frac{\partial}{\partial x_j} \left[ \vartheta \left( \frac{\partial \bar{U}_i}{\partial x_j} + \frac{\partial \bar{U}_j}{\partial x_i} \right) - \overline{u_i u_j} \right] \quad (7.4)$$

The correlation  $\overline{u_i u_j}$  represents the Reynolds stress and will, in general, be non-zero. This term evidently arises from the non-linearity of the Navier-Stokes equations. It represents the additional rate of momentum transport due to the action of turbulence. These stresses cannot be represented uniquely in terms of mean quantities and the Eqn. 7.4 is not closed. Closure involves modeling the Reynolds stresses.

It is these Reynolds stresses that appear as unknowns in the momentum equations. Therefore, attention is given to the transport processes that determine the level of these correlations. A transport equation for the Reynolds stress is obtained from Eqn. 7.4 after some mathematical operations and manipulations as:

$$\begin{aligned} \frac{D \overline{u_i u_j}}{Dt} = & - \left[ \overline{u_i u_k} \frac{\partial \bar{U}_j}{\partial x_k} + \overline{u_j u_k} \frac{\partial \bar{U}_i}{\partial x_k} \right] - \vartheta \left( 2 \frac{\partial \overline{u_i u_j}}{\partial x_k \partial x_k} + \frac{\partial \overline{u_i u_k}}{\partial x_k} \frac{\partial \bar{U}_j}{\partial x_j} + \frac{\partial \overline{u_j u_k}}{\partial x_k} \frac{\partial \bar{U}_i}{\partial x_i} \right) \\ & + \frac{p}{\rho} \left( \frac{\partial \overline{u_i u_j}}{\partial x_j} + \frac{\partial \overline{u_j u_i}}{\partial x_i} \right) \\ & - \frac{\partial}{\partial x_k} \left[ \overline{u_i u_j u_k} + \frac{\overline{u_i p}}{\rho} \delta_{jk} + \frac{\overline{u_j p}}{\rho} \delta_{ik} - \vartheta \left( \frac{\partial \overline{u_i u_j}}{\partial x_k} + \overline{u_i} \frac{\partial \bar{U}_j}{\partial x_j} + \overline{u_j} \frac{\partial \bar{U}_i}{\partial x_i} \right) \right] \end{aligned} \quad (7.5)$$

where,  $\delta_{ij}$  is the Kronecker delta given by,

$$\delta_{ij} = \begin{cases} 0, & \text{if } i \neq j \\ 1, & \text{if } i = j \end{cases} \quad (7.6)$$

According to Eqn. 7.5, the Reynolds stress of a small fluid particle is a combination of an imbalance of the following processes:

- **Generation** of stresses by the working of components of the stresses against the mean strain tensor. This is represented by the first term on the RHS of Eqn. 7.5.
- **Dissipation** of stresses due to molecular viscous action on the small scale turbulent motion present. This is represented by the second term on the RHS of Eqn. 7.5.
- **Pressure-strain interaction** which acts both to promote a reversion towards isotropy of the stress-field and to smear out the effects of stress generation over the other components of the stress tensor (referred to as 'redistributive' action). This is represented by the third term on the RHS of Eqn. 7.5.
- **Diffusion** which arises by the act of velocity fluctuations, pressure fluctuations and molecular transport. This is represented by the last term on the RHS of Eqn. 7.5.

In high Reynolds number flows the second term of the dissipation becomes negligible. Also, the last two terms of the molecular transport in diffusion becomes very small. Thus, the final form of the Reynolds stress equation may be written as:

$$\frac{D\overline{u_i u_j}}{Dt} = G_{ij} - \varepsilon_{ij} + \phi_{ij} + D_{ij} \quad (7.7)$$

where,

$$G_{ij} = - \left[ \overline{u_i u_k} \frac{\partial \overline{U_j}}{\partial x_k} + \overline{u_j u_k} \frac{\partial \overline{U_i}}{\partial x_k} \right] \quad (7.8)$$

$$\varepsilon_{ij} = 2\nu \overline{\frac{\partial u_i}{\partial x_k} \frac{\partial u_j}{\partial x_k}} \quad (7.9)$$

$$\phi_{ij} = \frac{p}{\rho} \overline{\left( \frac{\partial u_i}{\partial x_j} + \frac{\partial u_j}{\partial x_i} \right)} \quad (7.10)$$

$$D_{ij} = - \frac{\partial}{\partial x_k} \left[ \overline{u_i u_j u_k} + \frac{\overline{u_i p}}{\rho} \delta_{jk} + \frac{\overline{u_j p}}{\rho} \delta_{ik} - \nu \frac{\partial \overline{u_i u_j}}{\partial x_k} \right] \quad (7.11)$$

Equation 7.7 can be read as:

- rate of change of Reynolds stress  $\overline{u_i u_j}$ , plus
- transport of  $\overline{u_i u_j}$  by convection, equals
- rate of generation  $G_{ij}$ , minus
- rate of dissipation  $\varepsilon_{ij}$ , plus
- transport due to turbulent pressure-strain interaction  $\phi_{ij}$ , plus
- transport by diffusion  $D_{ij}$

This equation describes six partial differential equations, one for the transport of each of the six independent Reynolds stresses.

## 7.2 Need for Higher-Order Turbulence Models

Over the years, several different types of turbulence models have been developed, Figure 7.1 shows the various types of turbulence models listed in the center in order of increasing sophistication i.e. increasing inclusion of more physics. Unfortunately, inclusion of more physics usually increases the computational cost.

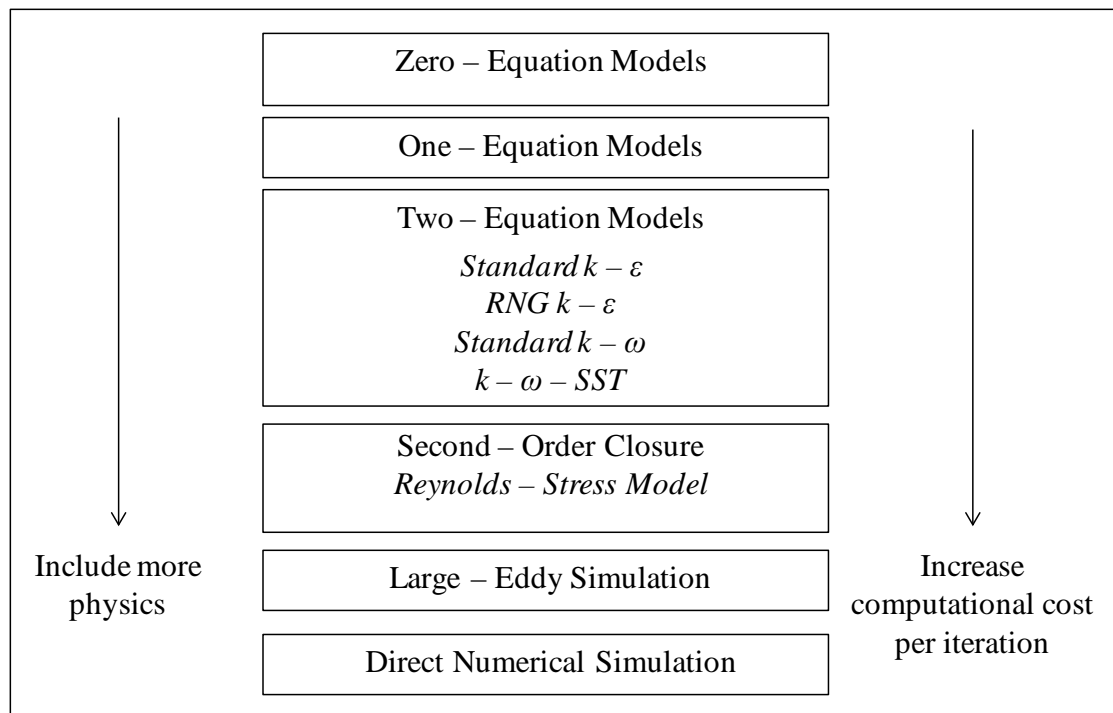


**Figure 7.1** Turbulence models.

Many turbulence models are based on the Boussinesq hypothesis, according to which the momentum transfer caused by turbulent eddies can be modeled with an eddy viscosity. This is in analogy with how the momentum transfer caused by the molecular motion in a gas can be described by a molecular viscosity. The Boussinesq assumption states that the Reynolds stresses are proportional to the mean strain rate and can be written as:

$$\tau_{ij} = -\rho \overline{u_i u_j} = \mu_t \left( \frac{\partial \bar{U}_i}{\partial x_j} + \frac{\partial \bar{U}_j}{\partial x_i} \right) \quad (7.12)$$

The turbulent viscosity  $\mu_t$ , is not a fluid property and it depends on the state of turbulence and must be determined by the turbulence model. Although two-equation models based on the eddy viscosity approximation provide excellent predictions for many flows of engineering interest, there are limitations to which this approximation can be valid. Applications for which the approximation is weak typically include flows with extra rate of strain (due to isotropic turbulent viscosity assumptions). Examples of such anisotropic turbulent flow conditions include:

- flows over boundaries with strong curvature
- flows in ducts with secondary motions
- flows with boundary layer separation
- flows in rotating and stratified fluid
- strongly three dimensional flows

Even though the turbulent viscosity is not homogeneous, i.e., it varies in space, these Eddy-viscosity models assume it to be isotropic in nature, this assumption limits the use of these models in flows where the turbulent transport or non-equilibrium effects are important. The eddy viscosity assumption is no longer valid in these cases and results of eddy viscosity models might be inaccurate. There are improvements done to the existing two-equations model like the *RNG*  $k - \varepsilon$  model is an improvement over the *Standard*  $k - \varepsilon$  for these classes of flow by incorporating the influence of additional strain rates, yet these are not able to fully resolve the anisotropic nature of turbulence.



The Second-order closure models include the effects of streamline curvature, sudden changes in the strain rate, secondary motions, etc. compared to turbulence models using the eddy viscosity approximation. This class of model is more complex and computationally more expensive than the RANS models. The Reynolds Stress Model (RSM) is a second-order closure model. Abandoning the isotropic eddy-viscosity hypothesis, the RSM closes the RANS equations by solving transport equations for Reynolds stresses, together with an equation of dissipation rate. This means that five additional transport equations are required in two-dimensional flows and seven additional transport equations must be solved in three dimensional fluid flow problems. The convective and generation/destruction terms are computed directly while the pressure-strain, potentially anisotropic dissipation and turbulent diffusion terms need to be modeled to provide closure.

Although Direct Numerical Simulation (DNS), which solves the Navier-Stokes equations together with the continuity equation without using any modeling and is capable of representing all the details of the complex turbulent flow could be the ultimate choice to solve any turbulent flow problem, it requires very large computational resource and time. Additionally, the number of grid points and the cost required increase roughly with  $Re^3$  (Pope, 2000). Also, the Larger Eddy Simulation (LES) which is a compromise for a full DNS, resolves large scales of the flow field solution allowing better fidelity than alternative approaches such as RANS methods and models the smallest scales of the solution, rather than resolving them as direct numerical simulation (DNS) does. Accordingly, LES can be used to calculate relatively high Reynolds number flows, but the proper resolution in the near-wall regions poses the problems, where a special near-

wall treatment has to be introduced (Rodi, 2006). These limitations of the above mentioned models brings back the focus to the RANS modeling with the second-moment correlations of fluctuating quantities appearing in the RANS equations.

### **7.3 Motivation for Algebraic Stress Model (ASM)**

While the two-equation linear eddy viscosity turbulence models still remain a popular choice for turbulence modeling in industries, their shortcomings as discussed in Sec. 7.2, cannot be disregarded. The incapability of these models to give satisfactory results especially for the turbulence quantities for complex flows compels to discard the Boussinesq approximation and look for alternative ways of treating the anisotropic nature of turbulence. One of the approaches to deal with this problem is to solve the transport equations for each Reynolds stress component in order to resolve fully the turbulence anisotropy. As mentioned earlier, the Reynolds Stress Model (RSM) solves six individual transport equations for each of the Reynolds stress component but the complexity and cost associated with this process is significant. Thus, the inherent inability of the eddy viscosity models to predict turbulence anisotropy and the complexity and computational cost of full Reynolds Stress Models (RSM) has lead to the development of Algebraic Stress Models. The need to incorporate the anisotropic nature of turbulence to tackle complex fluid flows and reduce the complexity of RSM model while retaining the features that allow the reproduction of dynamically important phenomena, such as the stress anisotropy, the near-wall blocking effect, etc gave impetus to the formulation of the Algebraic Stress Model (ASM). It is an economical way of accounting for the anisotropy of Reynolds stresses without going into full length of solving the Reynolds stress

transport equations. With the goal of establishing the capabilities and inadequacies of ASM model and application of the model to flows with increasing complexity which are of practical importance, an attempt is made in this thesis with the development of ASM model which is validated for a complex flow around Ahmed body.

## 7.4 Derivation of Algebraic Stress Model Equations

To close the Reynolds stress transport equation given by Eqn. 7.7, the generation term is solved while the other terms - dissipation, pressure-strain interaction and diffusion terms have to be modeled. Equation 7.7 which is restated below for quick reference is the starting point for the ASM formulation.

$$\frac{D\overline{u_i u_j}}{Dt} = G_{ij} - \varepsilon_{ij} + \phi_{ij} + D_{ij} \quad (7.13)$$

The pressure-strain interaction term  $\phi_{ij}$ , which is also known as the 'redistribution term', drives the turbulence towards isotropy. Modeling the  $\phi_{ij}$  term is perhaps the most controversial topic in the second-moment closure problems. This term is often represented as summation of three quantities as given by Eqn. 7.14.

$$\phi_{ij} = \phi_{ij1} + \phi_{ij2} + \phi_{ijw} \quad (7.14)$$

The  $\phi_{ij1}$  term involves only the fluctuating velocities and represents the interaction between the turbulent quantities only. It is also known as the 'slow distortion' or 'slow return to isotropic state'. The  $\phi_{ij2}$  term involves the mean velocity gradients and governs the interaction between the mean strain rate and turbulence fluctuations. It is also

known as the rapid distortion' or rapid return to isotropic state'. The last term in the Eqn. 7.14  $\phi_{ijw}$ , represents the wall-reflection term to model the near-wall phenomena in some models of the pressure-strain term. Here, only a simple version of the pressure-strain term is considered without the wall-reflection term. Nearly every researcher who has made closure approximation to the Reynolds stress transport equation (Eqn. 7.13) has adopted Rotta's (1951) proposal for  $\phi_{ij1}$  term, which is given by Eqn. 7.15 as:

$$\phi_{ij1} = -C_{\phi 1} \frac{\varepsilon}{k} \left( \overline{u_i u_j} - \frac{2}{3} \delta_{ij} k \right) \quad (7.15)$$

where,  $C_{\phi 1}$  is a constant and  $k$  and  $\varepsilon$  are the time-averaged turbulence kinetic energy and energy dissipation rate respectively. It has been found that the value of  $C_{\phi 1}$  differs from one flow to other but usually it is positive and it may vary between 1 and 3 (Hanjalic and Launder, 1972). The quotient  $k/\varepsilon$  thus represents a characteristic decay time of the turbulence (Launder *et al.*, 1975). This model proposed by Rotta (1951) is referred to as the 'linear model' because  $\phi_{ij1}$  is linearly proportional to  $\overline{u_i u_j}$ . The negative sign in the equation is an indication that when the difference  $\left( \overline{u_i u_j} - \frac{2}{3} \delta_{ij} k \right)$  is greater than zero, the  $\phi_{ij1}$  term promotes isotropy or return to isotropy (Chen and Jaw, 1998).

The  $\phi_{ij2}$  term is approximated as:

$$\begin{aligned} \phi_{ij2} = & -\frac{(C_2 + 8)}{11} \left\{ G_{ij} - \frac{2}{3} \delta_{ij} G_k \right\} - \frac{(30C_2 - 2)}{55} k \left\{ \frac{\partial \overline{U}_i}{\partial x_j} + \frac{\partial \overline{U}_j}{\partial x_i} \right\} \\ & - \frac{(8C_2 - 2)}{11} \left\{ H_{ij} - \frac{2}{3} \delta_{ij} G_k \right\} \end{aligned} \quad (7.16)$$

where,  $C_2$  is a constant,  $G_{ij}$  is the generation of Reynolds stresses given by Eqn.

7.8.  $G_k$  is the rate of production of turbulent kinetic energy and is given by Eqn. 7.17 as:

$$G_k = -\overline{u_i u_j} \frac{\partial \overline{U}_i}{\partial x_j} \quad (7.17)$$

$$H_{ij} = -\left[ \overline{u_i u_k} \frac{\partial \overline{U}_k}{\partial x_j} + \overline{u_j u_k} \frac{\partial \overline{U}_k}{\partial x_i} \right] \quad (7.18)$$

Launder *et al.*, 1975, also pointed out that the first group on the RHS of Eqn. 7.16 turns out to be the dominant one. Moreover, because each of the three groups vanishes under contraction, one may retain simply the first group without causing any loss to the essential redistributive nature of the approximation. Thus, the simplified equation for  $\phi_{ij2}$  becomes:

$$\phi_{ij2} = -C_{\phi 2} \left\{ G_{ij} - \frac{2}{3} \delta_{ij} G_k \right\} \quad (7.19)$$

where,  $C_{\phi 2}$  is a constant and is assigned a value different than  $C_{\phi 1}$  to compensate for the neglected terms. Therefore, the complete equation for the pressure-strain term is given as:

$$\phi_{ij} = \overline{\frac{p}{\rho} \left( \frac{\partial u_i}{\partial x_j} + \frac{\partial u_j}{\partial x_i} \right)} = -C_{\phi 1} \frac{\varepsilon}{k} \left( \overline{u_i u_j} - \frac{2}{3} \delta_{ij} k \right) - C_{\phi 2} \left\{ G_{ij} - \frac{2}{3} \delta_{ij} G_k \right\} \quad (7.20)$$

There are three contributions in Eqn. 7.7 to the diffusive transport of the Reynolds stresses. Of these, only diffusion by turbulent velocity fluctuations is retained in the model. Neglect of transport by molecular interaction is permissible since, for the flows considered, the Reynolds number of the energy-containing motions is large. Neglect of

pressure-induced diffusion follows the practice of most other researchers (Launder *et al.*, 1975). Daly and Harlow, 1970 proposed a simple form for the triple-velocity fluctuations  $(\overline{u_l u_j u_k})$  as:

$$\overline{u_l u_j u_k} = -C'_s \frac{k}{\varepsilon} \overline{u_k u_l} \frac{\partial \overline{u_i u_j}}{\partial x_l} \quad (7.21)$$

Here, the coefficient  $C'_s$  is recommended to be equal to 0.25. Thus, the diffusion term  $D_{ij}$ , given by Eqn. 7.11 reduces to:

$$D_{ij} = -\frac{\partial}{\partial x_k} \left( -C'_s \frac{k}{\varepsilon} \overline{u_k u_l} \frac{\partial \overline{u_i u_j}}{\partial x_l} \right) \quad (7.22)$$

For the dissipation term  $\varepsilon_{ij}$ , in the Reynolds stress transport equation (Eqn. 7.7), the dissipation rate of turbulent kinetic energy,  $\varepsilon$ , is defined as:

$$\varepsilon = \vartheta \overline{\left( \frac{\partial u_l}{\partial x_k} \right)^2} \quad (7.23)$$

The dissipation term  $\varepsilon_{ij}$ , is modeled according to the postulation (Chen and Jaw, 1998) that small turbulent eddies are isotropic. This is also known as the 'isotropic dissipation model'. As a result of this postulation, Eqn. 7.9 can be written as:

$$\varepsilon_{ij} = 2\vartheta \overline{\frac{\partial u_l}{\partial x_k} \frac{\partial u_j}{\partial x_k}} = \frac{2}{3} \delta_{ij} \varepsilon \quad (7.24)$$

The equations for  $k$  and  $\varepsilon$  define the dynamics of turbulent kinetic energy and illustrate the major physical mechanisms in a turbulent flow within the framework of Reynolds-averaging approach.

The exact  $k$  equation is derived by taking the half of the trace of Eqn. 7.7:

$$\frac{Dk}{Dt} = G_k - \varepsilon + D_k \quad (7.25)$$

where, the turbulent kinetic energy  $k = \frac{1}{2}\overline{u_i u_i}$ . The terms on the RHS of Eqn. 7.25  $G_k$ ,  $\varepsilon$  and  $D_k$ , can be interpreted as production of turbulent kinetic energy  $k$ , dissipation rate of  $k$  and lastly, diffusion transport of  $k$  respectively, which are given as (Hanjalic, 2005):

$G_k$  is same as given by Eqn. 7.17. The recommended range for coefficient  $C_k$  is between 0.09 - 0.11.

$$D_k = \frac{\partial}{\partial x_k} \left( C_k \frac{k}{\varepsilon} \frac{\partial k}{\partial x_l} \right) \quad (7.26)$$

So far, each term of the Reynolds stress transport equation and the exact  $k$  equation has been modeled. To derive the Algebraic Stress Model, the local-equilibrium assumption is invoked. The general local-equilibrium condition (Rodi 1972, 1976) states that for flows when turbulent convection and diffusion are small (high shear flows) or convection and diffusion are approximately equal, then the Reynolds stress transport equation may be approximated by dropping the convection and diffusion terms. Thus, Eqn. 7.7 reduces to:

$$G_{ij} - \varepsilon_{ij} + \phi_{ij} = 0 \quad (7.27)$$

Assuming  $\overline{u_i u_j} \sim k$ , with some mathematical manipulation it can be shown that:

$$\frac{D\overline{u_i u_j}}{Dt} - D_{ij} = \frac{\overline{u_i u_j}}{k} \left( \frac{Dk}{Dt} - D_k \right) \quad (7.28)$$

Combining Eqns. 7.7, 7.25, 7.27 and 7.28, leads to:

$$G_{ij} - \varepsilon_{ij} + \phi_{ij} = \frac{\overline{u_i u_j}}{k} (G_k - \varepsilon) \quad (7.29)$$

On substituting the expressions for  $G_{ij}$  (Eqn. 7.8),  $G_k$  (Eqn. 7.17),  $\phi_{ij}$  (Eqn. 7.20) and  $\varepsilon_{ij}$  (Eqn. 7.24), in Eqn. 7.29 and some rearrangement of terms the following equation can be obtained:

$$\frac{\overline{u_i u_j}}{k} = \lambda_1 \frac{G_{ij}}{\varepsilon} - \lambda_2 \frac{2}{3} \delta_{ij} \quad (7.30)$$

where,  $\lambda_1$  and  $\lambda_2$  represents the constant coefficient given by:

$$\lambda_1 = \frac{1 - C_{\phi 2}}{\frac{G_k}{\varepsilon} - 1 + C_{\phi 1}} \quad (7.31)$$

$$\lambda_2 = \frac{1 - C_{\phi 1} - C_{\phi 2}}{\frac{G_k}{\varepsilon} - 1 + C_{\phi 1}} \quad (7.32)$$

Equation 7.30 is an algebraic equation involving no differential terms like the Reynolds stress transport equation. It represents the Algebraic Stress Model that retains some effects of the convection - diffusion and is simpler to solve than the six complex transport equations of the Reynolds Stress Model. From Eqn. 7.30, the corresponding algebraic equations for each Reynolds stress component can be written as follows:



$$\overline{uu} = \left[ \lambda_1 \left( \frac{G_{11}}{\epsilon} \right) + \lambda_2 \frac{2}{3} \right] k \quad (7.33)$$

$$\overline{uv} = \left[ \lambda \left( \frac{P_{12}}{\epsilon} \right) \right] k \quad (7.34)$$

$$\overline{uw} = \left[ \lambda \left( \frac{P_{13}}{\epsilon} \right) \right] k \quad (7.35)$$

$$\overline{vv} = \left[ \lambda \left( \frac{P_{22}}{\epsilon} - \frac{2}{3} \right) + \frac{2}{3} \right] k \quad (7.36)$$

$$\overline{vw} = \left[ \lambda \left( \frac{P_{23}}{\epsilon} \right) \right] k \quad (7.37)$$

$$\overline{ww} = \left[ \lambda \left( \frac{P_{33}}{\epsilon} - \frac{2}{3} \right) + \frac{2}{3} \right] k \quad (7.38)$$

## 7.5 Summary

Turbulence is a flow regime characterized by chaotic and stochastic property changes. This includes low momentum diffusion, high momentum convection, and rapid variation of pressure and velocity in space and time. When the flow is turbulent, the fluid particles exhibit additional transverse motion which enhances the rate of energy and momentum exchange between them, thus increasing the heat transfer and the friction coefficient. The accurate prediction of the turbulent quantities plays a significant role in not just the fluid motion/transfer phenomenon rather it governs the heat exchange process

as well especially in regions close to the wall. This requires precise values for the Reynolds stresses which are the additional unknowns that appear in the averaged Navier-Stokes equations. There are various approaches to acquire these stresses - some include modeling while other includes solving independent equations for the six Reynolds stress components or a combination of both modeling and solving.

The drawback of the eddy viscosity models based on the Boussinesq approximation in accurately predicting the turbulent quantities in anisotropic turbulent flows which encounter flow separation, recirculation or the near-wall region flows; restricts the use of these models in such flow scenarios and a more sophisticated model is required which can solve for six individual components of Reynolds Stresses. From the detailed discussion on the Reynolds stresses, its importance in the turbulent flows and limitations of the Boussinesq approximation, the need for higher-order turbulence modeling is strongly realized. Although the Direct Numerical Simulation (DNS) and Large Eddy Simulation (LES) are capable of giving closer insight to the turbulence structures in a fluid flow, their use is still restricted to primarily simpler problems due to the high computational resource, time and grid resolution requirements. Thus, the focus is brought back to the Reynolds Stress Model (RSM) which resolves all the components of the Reynolds stress tensor at lesser resource requirements than the DNS and LES. To further reduce the task of solving the complex transport equations for Reynolds stresses, algebraic approach is adopted. The Reynolds stress transport equation is converted into simpler algebraic form by a combination of solving and/or modeling the contributor to the Reynolds stress transport process which include - generation of stresses, dissipation of stresses due to molecular viscous action, pressure-strain interaction and lastly,

diffusion of stresses due to velocity fluctuations, pressure fluctuations and molecular transport. The derivation of the complete Algebraic Stress Model equations followed by algebraic equations for each of the six Reynolds stress component is performed. The derived Algebraic Stress Model is later verified for two flow scenarios ranging from simple two-dimensional flow over flat plate to a complex three-dimensional flow around the Ahmed body, which is discussed next in Chapter 8.

## Chapter 8 - Turbulence Modeling Using ASM

This chapter examines the validity of the Algebraic Stress Model (ASM) derived in Chapter 7 for predicting the Reynolds stresses in order to gain more insight into the turbulent structures found in a fluid flow at high Reynolds number. Two fluid flow problems are discussed in this chapter - two dimensional turbulent flow over a flat plate and three dimensional flow around Ahmed body.

Section 8.1 gives complete detail of the flow over the flat plate which includes - problem description, flow specifications, geometry, mesh details, boundary conditions used, turbulence model used, validation of the simulation model with theoretical solution, use of the ASM model to obtain the Reynolds stresses and lastly, comparison of the ASM Reynolds stresses with the stresses from the Reynolds Stress Model (RST) to validate the predictions of the ASM model.

Section 8.2 describes the problem of flow around Ahmed body. To analyze the flow around Ahmed body, firstly the simulation were carried on a full-scale Ahmed body model and compared with other experimental data to verify the CFD methodology, next the same methodology was used on a scaled-down Ahmed body model which was tested in the Wind Tunnel Facility of University of Wisconsin - Milwaukee. Once the simulations were verified with the mean flow data acquired in the wind tunnel, it was employed to obtain the ASM Reynolds stresses and lastly, these stresses were compared with the stresses from the RST model. Section 8.2 gives full detail of each step followed to examine the validity of the ASM model for three dimensional flow around Ahmed body.

## 8.1 Turbulence Modeling of Flow Over Flat Plate

The first study for determining the Reynolds stresses using the ASM model was carried on for a flow over flat plate with zero pressure gradient. The study of a flat plate boundary layer is quite popular owing to its geometric simplicity and available theoretical solutions. Though a flat plate boundary-layer does not separate, it undergoes transition to become turbulent. Figure 8.1 shows the schematic of boundary layer flow over a flat plate. The boundary layer thickness  $\delta$ , grows continuously from the start of the fluid-surface contact i.e. the leading edge. It is a function of the distance from the leading edge  $x$ , not a constant. The flow will generally be laminar at the starting from  $x = 0$  and undergo laminar to turbulent transition if the stream-wise dimension is greater than a critical distance which corresponds to the location of the transition Reynolds number,  $Re_{cr}$  and finally turn into turbulent flow beyond the transition region as shown in Fig. 8.1. Outside the boundary layer region, free stream conditions exist where velocity gradients and therefore, viscous effects are typically negligible. Transition from laminar to turbulent flow typically occurs at the local transition Reynolds number, which for a flat plate boundary layer flows can be in the range of  $3 \times 10^5 \leq Re_{cr} \leq 5 \times 10^5$ .

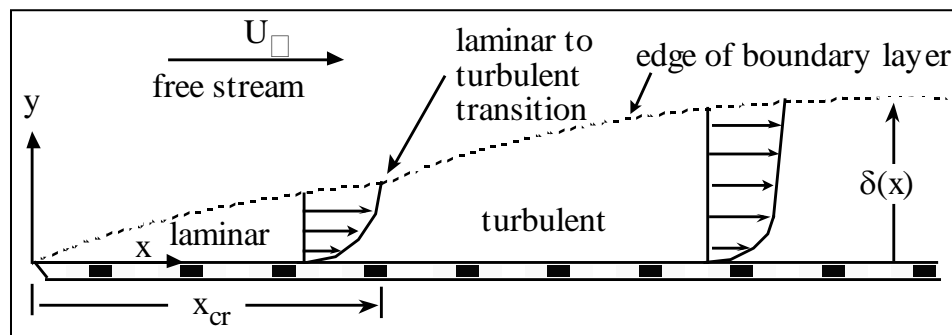


**Figure 8.1** Schematic of boundary layer flow over a flat plate.

Consider a two dimensional fluid flow over a flat plate of length  $L = 10$  cm with free stream velocity  $U_{\infty} = 10$  m/s. The fluid medium is water with density,  $\rho = 997.56$  kg/m<sup>3</sup> and dynamic viscosity,  $\mu = 8.8871 \times 10^{-4}$  Pa-s. The flow was modeled using the commercial CFD software STARCCM+. The two dimensional computational domain considered for this problem is shown in Fig. 8.2 with the boundary conditions and Fig. 8.3 shows the mesh generated for the computational domain. A very fine structured grid was obtained with the element size of 0.25 mm and total number of elements 64,000. A grid independent study was performed using a 0.04 and 4 times the mesh size,  $M = 64000$ . Figure 8.4 shows the normalized velocity profile obtained at  $x = L$  for the three mesh sizes being tested. It can be observed from the figure that coarse mesh has not adequately captured the flow near the plate surface. On the other hand, no significant advantage was observed by using a mesh size of four times rather it took more computational time to solve. Therefore, the intermediate mesh of size 64,000 elements was selected for further investigation. Based on the length of the plate using Eqn. 8.1, the Reynolds number was found to be  $11.22 \times 10^5$ , clearly indicating the flow is turbulent in nature. This turbulence was modeled using the realizable  $k - \varepsilon$  model.

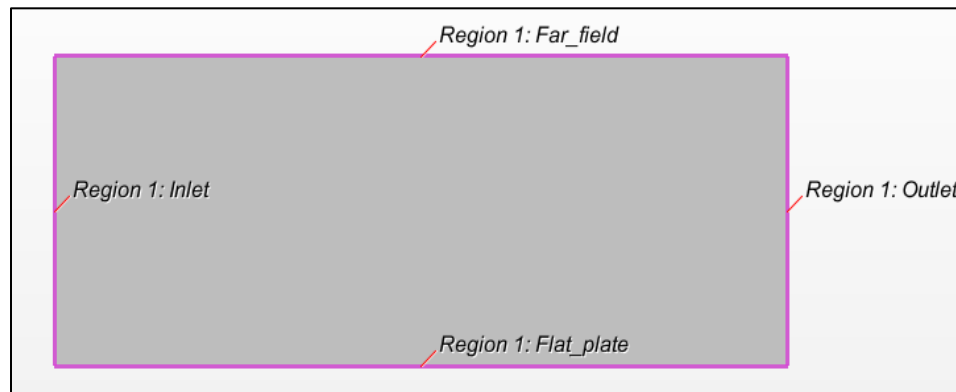


**Figure 8.2** Computational domain with corresponding boundary conditions.

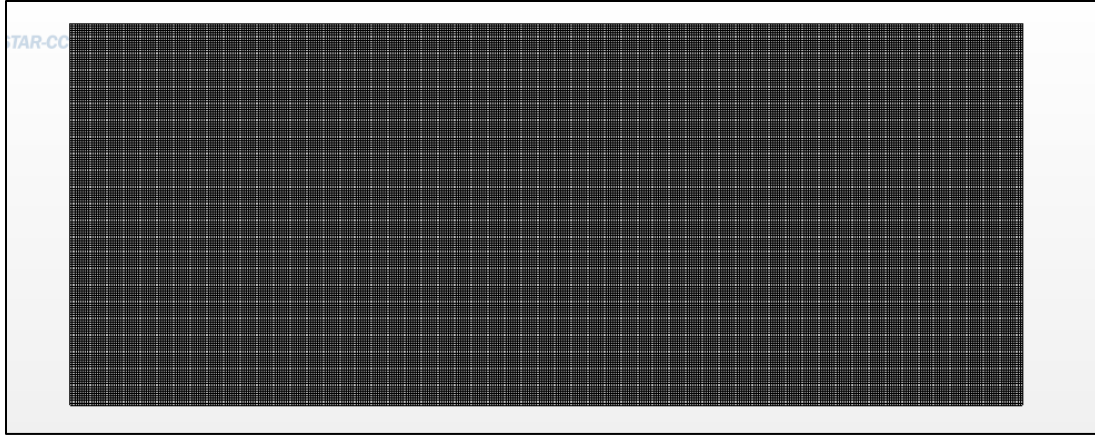


**Figure 8.3** Generated mesh for the computational domain (Mesh size,  $M = 64,000$ ).

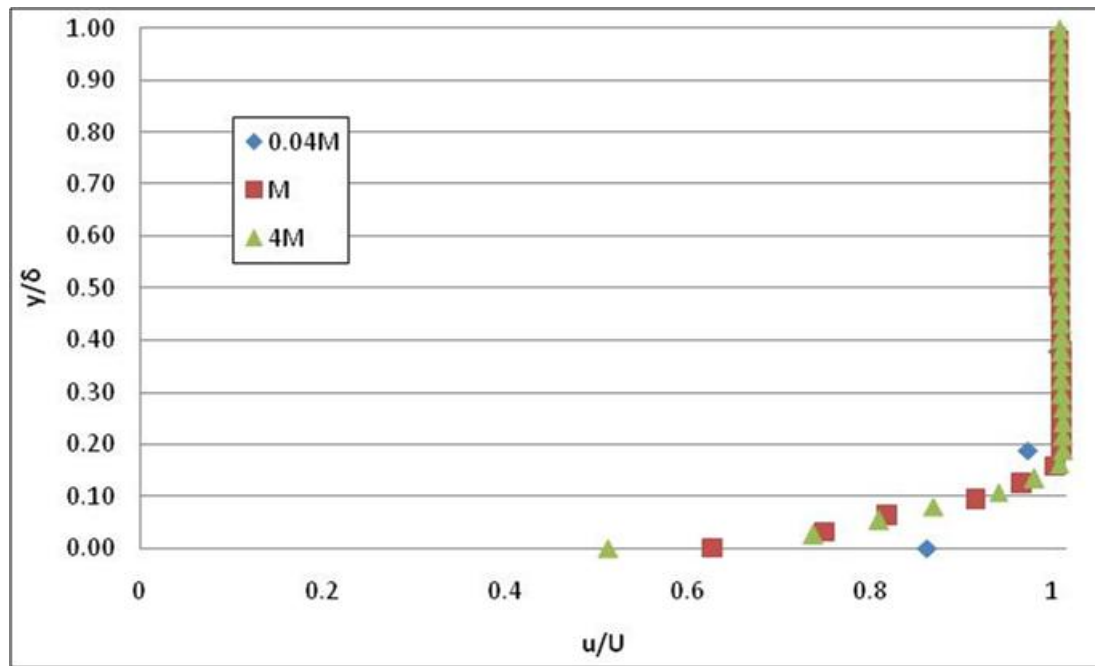
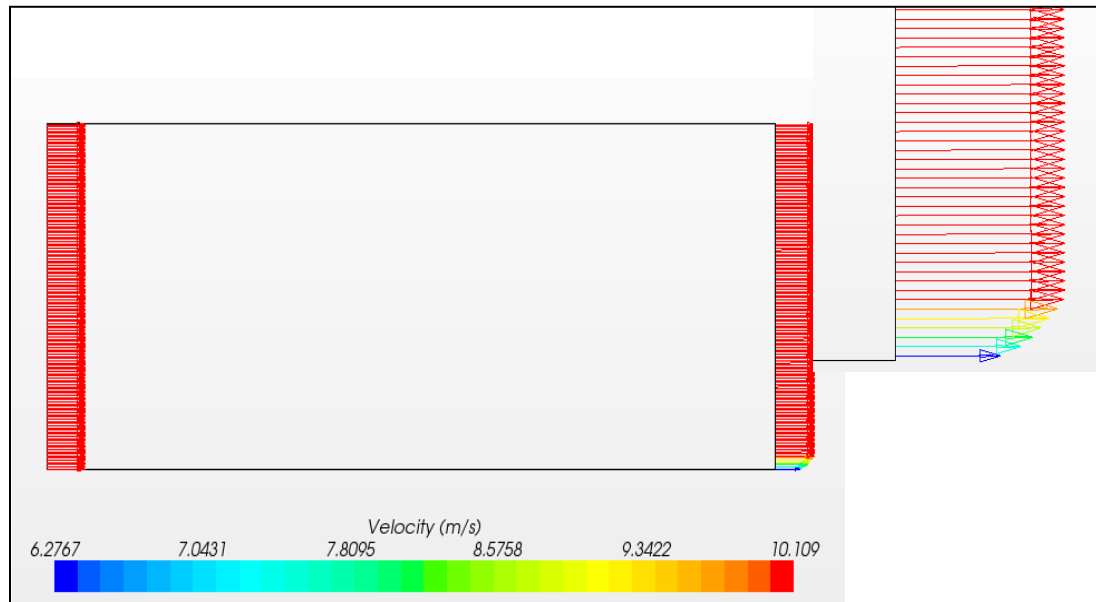


**Figure 8.4** Velocity profile for various mesh sizes at  $x = L$ .

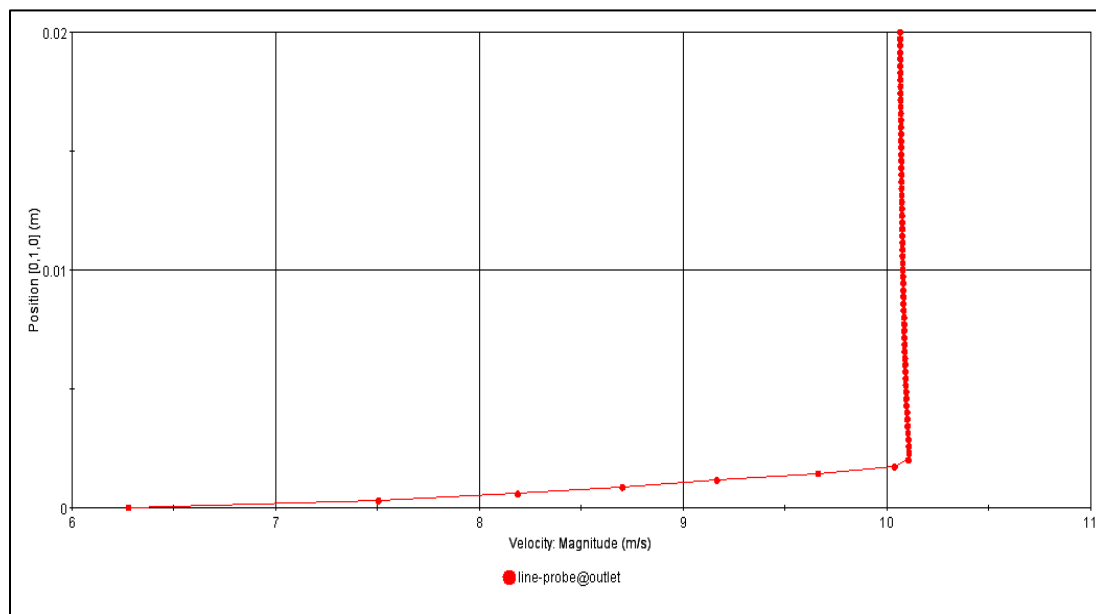
$$Re = \frac{\rho U_{\infty} x}{\mu} \quad (8.1)$$

Figure 8.5 shows the velocity vectors obtained at the inlet and outlet boundaries. The flow starts with a constant velocity and turns into turbulent flow as it passes over the length of the plate. Figure 8.6 shows the velocity profile near the plate surface along a

line at the edge of the plate length. This velocity profile is typical for a turbulent flow over a flat plate.



**Figure 8.5** Velocity vectors at inlet and outlet boundary.



**Figure 8.6** Velocity profile along a line at  $x = L$ .



In order to get an insight into the turbulence near the plate surface, it is important to know the Reynolds stresses in the near-wall region. Since the  $k - \varepsilon$  model is incapable of providing the Reynolds Stresses, the same flow scenario was modeled using the Reynolds Stress Turbulence (RST) model. Similar velocity profile as shown in Fig. 8.6 was obtained with the RST model as well.

The simulations were validated with the theoretical solution for a turbulent boundary layer flow over a flat plate. Two velocity profiles at mid-length of the plate,  $x = L/2$  and at the end of the plate length,  $x = L$  were considered for comparison of the simulation and theoretical data. For the theoretical solution one-seventh-power law was used to obtain the turbulent flow velocity profile which is given by Eqn. 8.2 (White, 2009).

$$\frac{u}{U_{\infty}} = \left(\frac{y}{\delta}\right)^{1/7} \quad (8.2)$$

where,

$$\frac{\delta}{x} = \frac{0.371}{Re_x^{0.2}} \quad (8.3)$$

Figures 8.7 and 8.8 show the velocity profile obtained from simulations and Eqn. 8.2. Good agreement can be observed between the simulation and the theoretical data with the two turbulence model -  $k - \varepsilon$  and RST giving similar profiles. This step completes the entire data requirement for calculation of the Reynolds stresses using the ASM model. The properties and flow data required to use the ASM model equations given in Chapter 7 include - turbulent quantities ( $k, \varepsilon, G_k$ ), velocity gradients, Reynolds stresses ( $u_i u_j$ ).

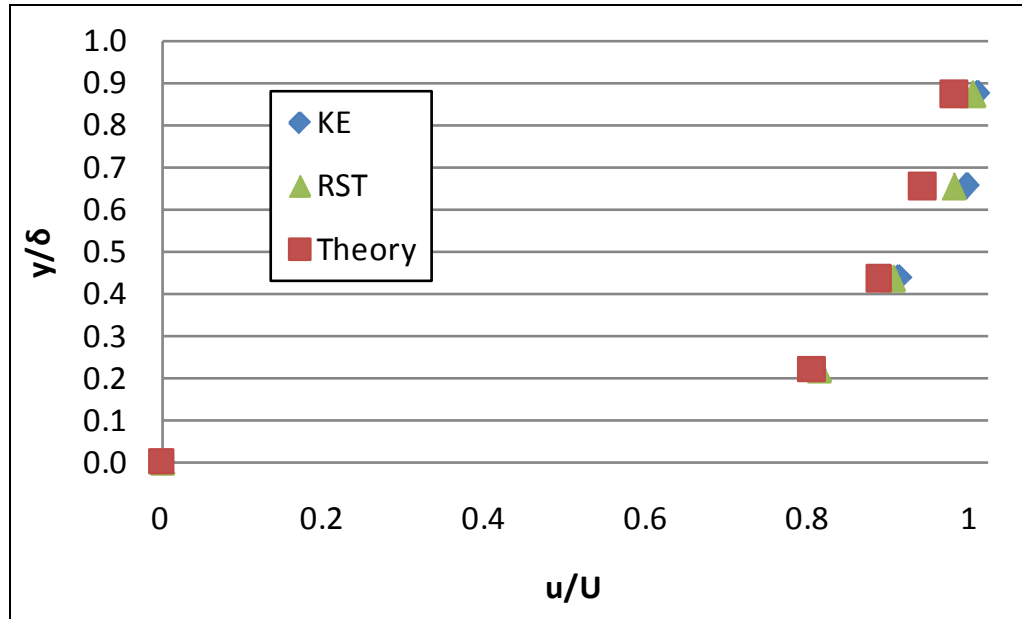


**Figure 8.7** Velocity profile at  $x = L/2$ .

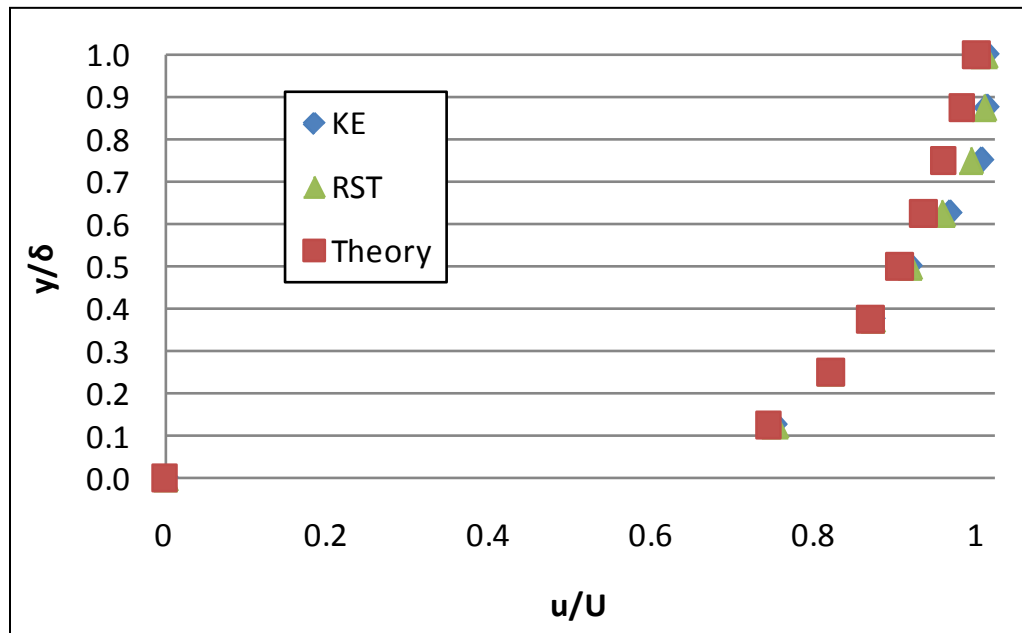


**Figure 8.8** Velocity profile at  $x = L$ .

For the Hybrid RANS/RSM modeling with ASM to determine the Reynolds stresses, the following steps were involved:

1. All the velocity gradient terms were obtained from  $k - \varepsilon$  model.
2. Turbulent quantities -  $k, \varepsilon$ , were obtained from  $k - \varepsilon$  model.
3. Reynolds stresses  $\overline{u_i u_j}$ , were obtained from RST model.
4. Using the Reynolds stresses and the velocity gradients, the production of turbulent kinetic energy  $G_k$ , was calculated using Eqn. 7.17.
5. Modified Reynolds stresses were obtained using the ASM equations.

Figures 8.9 - 8.12 show the comparison of the Reynolds stresses at  $x = L$ , for different models used. The stresses from the ASM Eqn. 7.30 which is re-written below as Eqn. 8.4, is represented as 'M2ASM'. Assuming  $G_k \sim \varepsilon$  in the near-wall region, a simplified ASM model was obtained as given by Eqn. 8.5. Another reference ASM model was included for the comparison purpose which is represented as 'SASM' and is given by Eqn. 8.6 (Kumar, 2012).

$$\mathbf{M2ASM:} \quad \frac{\overline{u_i u_j}}{k} = \lambda_1 \frac{G_{ij}}{\varepsilon} - \lambda_2 \frac{2}{3} \delta_{ij} \quad (8.4)$$

$$\mathbf{M1ASM:} \quad \frac{\overline{u_i u_j}}{k} - \frac{2}{3} \delta_{ij} = \lambda_1 \left( \frac{G_{ij}}{\varepsilon} - \frac{2}{3} \delta_{ij} \right) \quad (8.5)$$

$$\mathbf{SASM:} \quad \frac{\overline{u_i u_j}}{k} - \frac{2}{3} \delta_{ij} = \lambda \left( \frac{G_{ij}}{\varepsilon} - \frac{2}{3} \delta_{ij} \right) \quad (8.6)$$

where,

$$\lambda = \frac{1 - C_{\emptyset 2}}{C_{\emptyset 1} - 1} \quad (8.7)$$

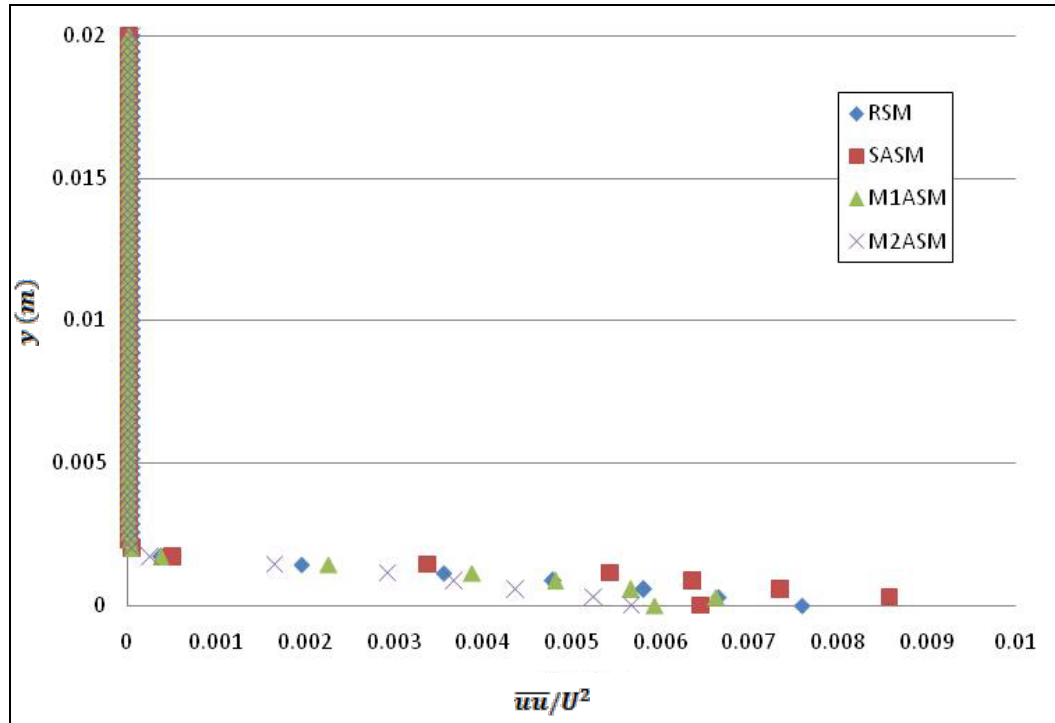


**Figure 8.9** Comparison of Reynolds stress  $\overline{uu}$  at  $x = L$  computed using various ASM models with RST model.

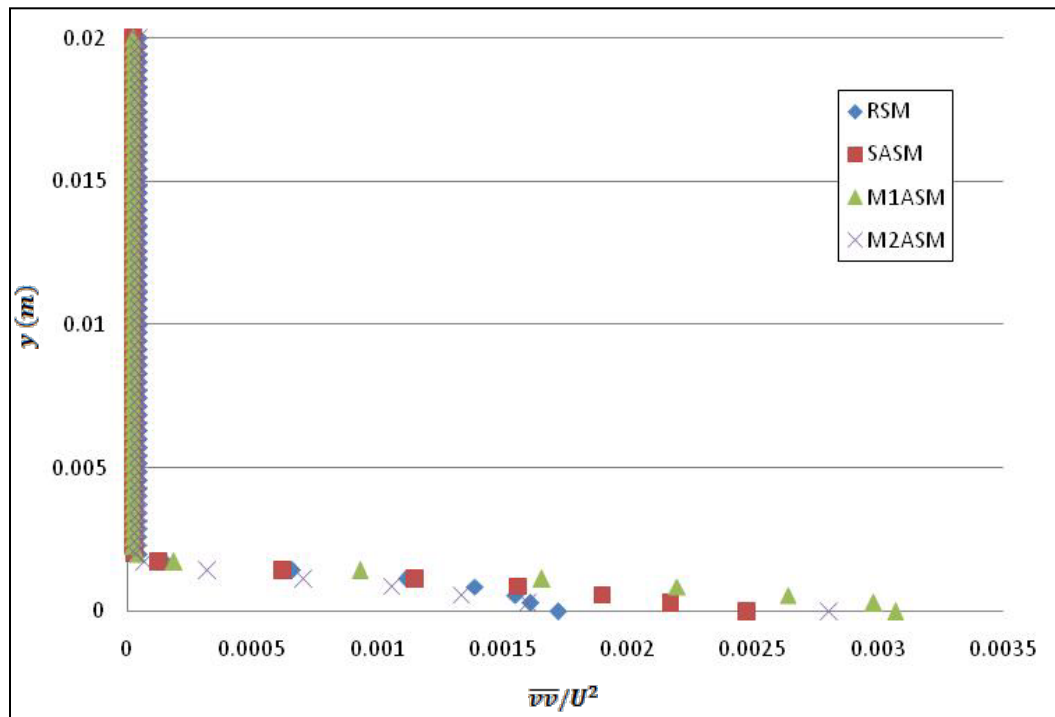


**Figure 8.10** Comparison of Reynolds stress  $\overline{vv}$  at  $x = L$  computed using various ASM models with RST model.

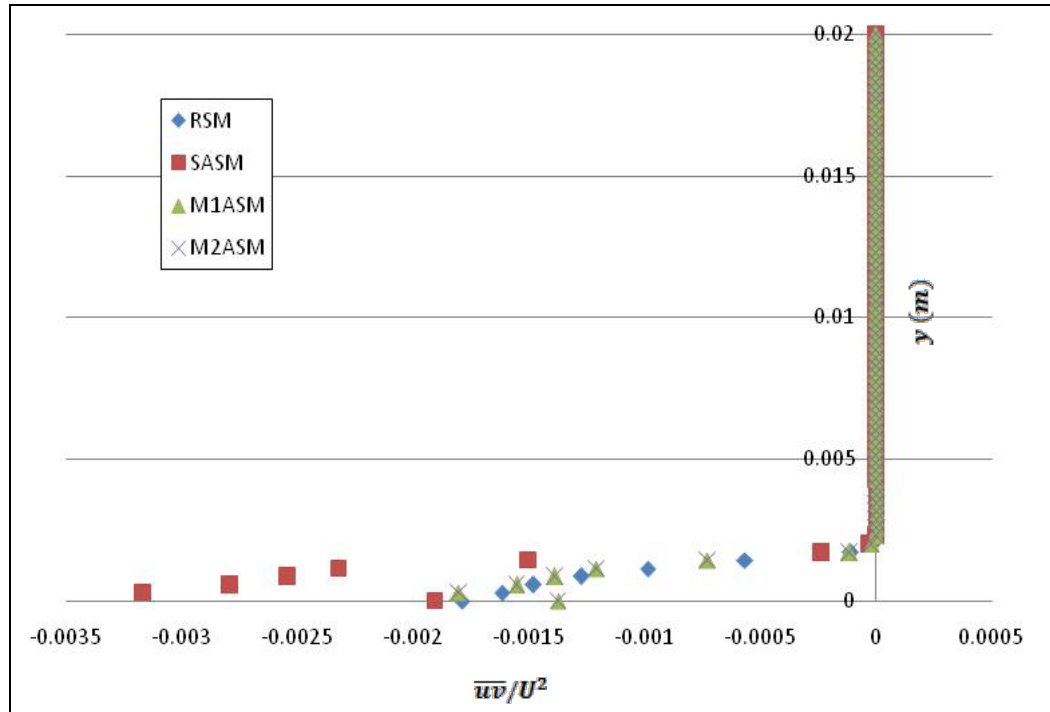


**Figure 8.11** Comparison of Reynolds stress  $\overline{uv}$  at  $x = L$  computed using various ASM models with RST model.

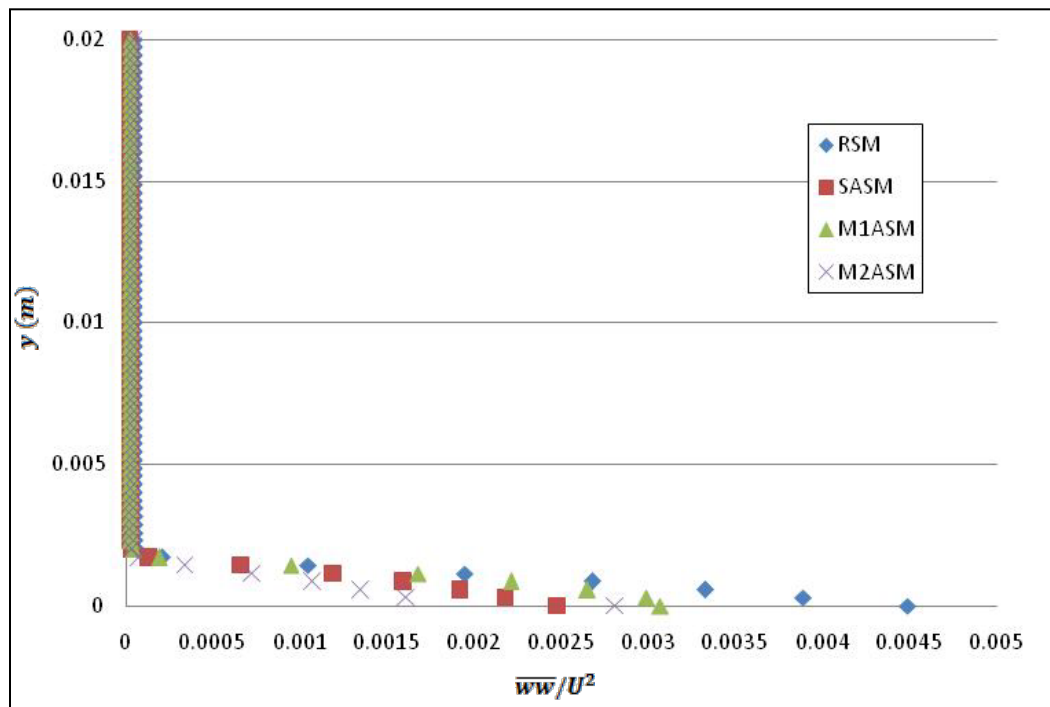


**Figure 8.12** Comparison of Reynolds stress  $\overline{ww}$  at  $x = L$  computed using various ASM models with RST model.

From Fig. 8.9, it can be observed that although all the ASM models (SASM, M1ASM and M2ASM) give reasonable results as compared to the stresses from the RST model, the models M1ASM and M2ASM give better agreement with the RST model than the SASM model which over-predicts the  $\overline{uu}$  stresses closer to the plate surface.

Figure 8.10 shows the comparison of the  $\overline{vv}$  stresses for various models. It can be noted from the figure that both the SASM and M1ASM model over-predicts the stress  $\overline{vv}$  which acts normal to the plate surface, close to the wall surface. In general, the M2ASM agrees well with the RST stress distribution.

The Reynolds shear stress  $\overline{uv}$  distribution is shown in Fig. 8.11 for different models. Both M1ASM and M2ASM models show good agreement with stresses from the RST model even for the region close to the wall, where as the SASM model over-predicts the shear stress values.

Lastly, the  $\overline{ww}$  stresses are compared for the different models considered as shown in Fig. 8.12. From the figure it can be observed that all the three models - SASM, M1ASM and M2ASM under-predicts the distribution of the  $\overline{ww}$  stresses as compared with the RST model stresses in the region close to the plate surface with M1ASM and M2ASM models somewhat giving closer results than the SASM model.

Thus, the capability of Reynolds stress prediction for the various ASM models for a flow over flat plate can be summarized based on the stress distribution figures Figs. 8.9 - 8.12. In general, the M1ASM and M2ASM performed better than the SASM model and predicted stresses which showed good agreement with the RST model stresses. The plausible reason for this better performance can be attributed to the extra terms considered in these models than the SASM model as can be noted from the models

equations Eqns. 8.4 - 8.6. Additionally, the production of turbulent kinetic energy ( $G_k$ ) term was neglected in the SASM model where as both the M1ASM and M2ASM model considered this term. This term plays a very crucial role in the near wall turbulence and contributes significantly to the Reynolds stress distribution and should not be neglected when evaluating the Reynolds stresses.

## 8.2 Turbulence Modeling of Flow around Ahmed Body

After the successful application of the ASM model for the case of a simple two dimensional flow over a flat plate, an attempt was made to test the validity of the ASM model for a complex three dimensional flow around the Ahmed body. The Ahmed reference model is a generic car-type bluff body with a slant back, which is frequently used as a benchmark test-case for the numerical simulation of flow around ground vehicles (Krastev *et al.*, 2011). The Ahmed body model as shown in Fig. 8.13 was first defined and its characteristics were described in the experimental work of Ahmed *et al.*, 1984. The authors concluded that most of the drag of the body is due to the pressure drag generated at the rear end. The structure of the wake is very complex, with a separation zone and counter-rotating vortices coining on the slant side edges of the body. More recently, Lienhart *et al.*, 2002 performed some additional experiments on the same body, although at a somewhat lower stream-wise wind velocity. The authors measured the mean and fluctuating velocity components by means of LDA and obtained surface oil-flow pictures for two rear vehicles body slant angles ( $\alpha = 25^\circ$  and  $\alpha = 35^\circ$ ). Their experimental data is used to verify the CFD methodology followed for the investigation of the flow around Ahmed body.

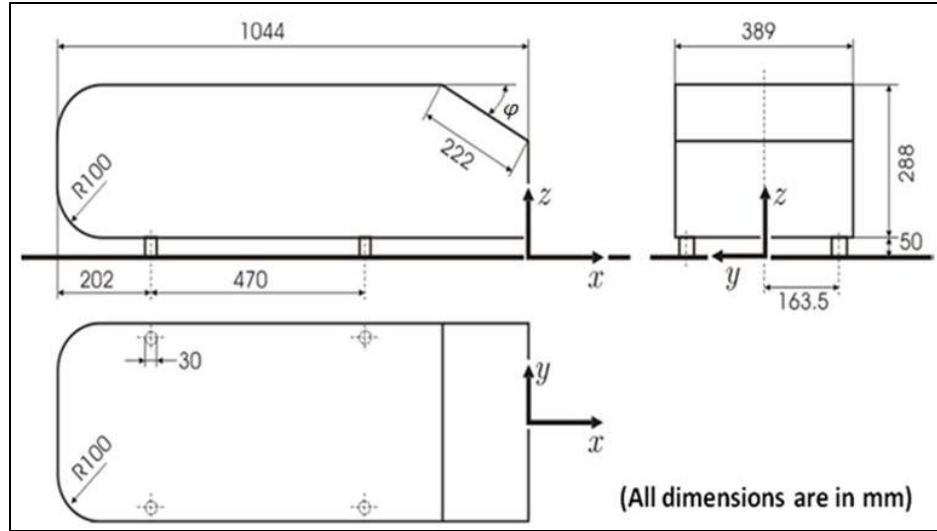


**Figure 8.13** Schematic of the original Ahmed body as studied by Ahmed *et al.*, 1984.

### 8.2.1 Computational Set-up

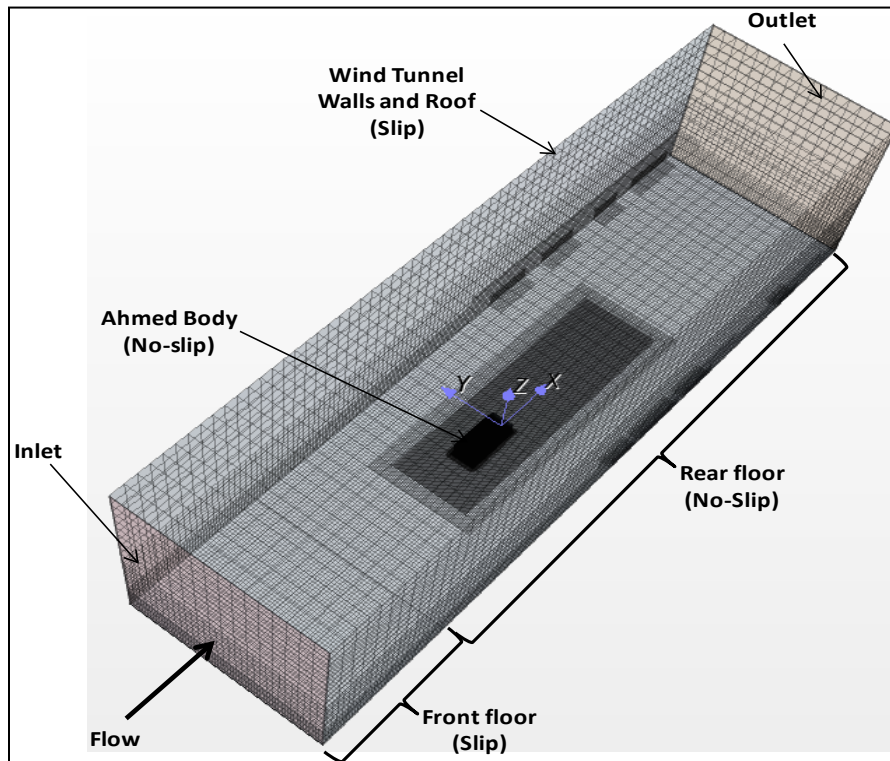
The present configuration has been specifically chosen to match the experiment of Lienhart *et al.*, 2002. The same dimensions were used for the Ahmed body as shown in Fig. 8.13. The bulk velocity was 40 m/s. Based on the length of the body  $L = 1.044$  m, the Reynolds number was determined as  $Re = 2.8 \times 10^6$ , which is of the same order of magnitude but somewhat lower as the one in the original experiment of Ahmed *et al.*, 1984, which was  $Re = 4.3 \times 10^6$ . A  $25^\circ$  slant angle was considered for the simulations.

Figure 8.14 shows the computational domain with the boundary conditions considered for the numerical analysis of the flow. The entrance to the numerical wind tunnel was defined as a velocity-inlet boundary. The condition was set as a uniform normal velocity of 40 m/s in x-direction. At the wind tunnel exit, a pressure outlet boundary condition was set. The upstream region was chosen very long in order to avoid any feedback from the model to the inlet boundary. The correct no-slip condition would then yield a too thick boundary layer at the model location. For this reason, i.e. to adjust



the boundary layer thickness, a slip condition was applied throughout the first part of the test section floor (marked as 'Floor front') followed by No-slip boundary condition on the Ahmed body and the remaining portion of the wind tunnel floor (marked as 'Rear floor'). The boundaries were about  $\pm 6L$  upstream and downstream,  $4L$  high, and  $\pm 1.8L$  from the wind tunnel walls with reference to the co-ordinate axes located at back of the Ahmed body along the symmetry plane as shown in Fig. 8.14.

A structured mesh was generated for the computational domain with a total of 12,966,113 mesh elements. A finer mesh was obtained with prism layers on the surfaces of Ahmed body to capture the flow physics more accurately close to the surfaces as shown in Fig. 8.15. An element size of  $\leq 1$  mm was used in regions adjacent to the Ahmed body surfaces with prism layer stretching 1.1 and thickness of 3 mm.



**Figure 8.14** Computational domain with boundary conditions.

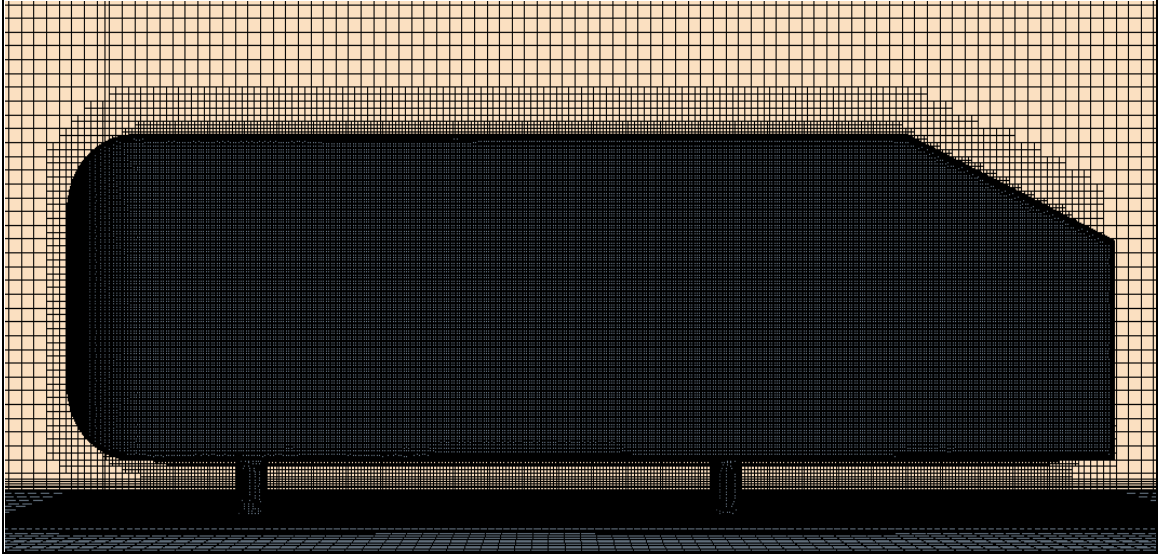


**Figure 8.15** Mesh around the Ahmed body.

### 8.2.2 Numerical Method

Both steady and unsteady incompressible flow simulations were performed to analyze the flow around Ahmed body. Different turbulence model ( $k - \varepsilon$ ,  $k - \omega$  -  $SST$ ,  $LES$ ) were used to compare their performance to predict the flow velocity profile. A segregated solver was used with bounded-central differencing and under-relaxation factor of 0.7 for velocity and 0.3 for pressure. A second-order temporal scheme was employed for the implicit unsteady calculations with a time-step of 0.01 s and number of inner iterations 20. All  $y^+$  wall treatment was used for the simulations, which is a hybrid treatment that attempts to emulate the wall-function-type approach for coarse meshes assuming that the near-wall cell lies within the logarithmic region of the boundary layer and low  $y^+$  wall treatment for fine meshes, assuming that the viscous sublayer is properly resolved. For Large Eddy Simulations, Wall Adapting Local Eddy Viscosity (WALE) model was adopted for the sub grid-scale (SGS) modeling for the small scale eddies. This

sub grid-scale model was preferred over the Smagorinsky-Lilly model since the WALE model returns a zero turbulent viscosity for laminar shear flows. This allows for the correct treatment of the laminar zones in the domain unlike in the Smagorinsky-Lilly model which produces non-zero turbulent viscosity. Plots of the residuals from the governing equations, as well as plots of both drag and lift coefficients were monitored to ascertain the convergence of the solution. The computation was terminated when the force coefficients had stopped fluctuating. Air is the fluid medium in the simulations whose properties are given in Table 8.1.

**Table 8.1** Properties of air.

Property	Value
Density	1.184 kg/m <sup>3</sup>
Dynamic viscosity	1.855e-5 Pa-s

### 8.2.3 CFD Validation and Verification for Full-Scale Ahmed Body

To evaluate the performance of the turbulence model to simulate the flow around Ahmed body, the streamwise mean velocities at 16 locations were compared with the experimental data from Lienhart *et al.*, 2002. Figures 8.15 and 8.16, show the velocity profile obtained from various turbulence model for front and back regions of the Ahmed body at various x-positions in the symmetry plane ( $y = 0$ ). The corresponding coordinate system is depicted in Fig. 8.14. Since the *LES* model is unsteady solver, the force coefficient fluctuating pattern was observed to determine the averaging time. It was noted

from the changing pattern of the coefficients that 0.05 s is the typical duration of the fluctuating cycle, so the velocity profile of *LES* was averaged of 10 samples in 0.1 s.

The data in Figs. 8.16 and 8.17 correspond to the coordinates  $x = -1463, -1263, -1062, -963, -863, -563, -363, -222, -162, -103, -42, -2, 14, 37.4, 88.1, 200.2$  (all values in mm). From Fig. 8.16, it can be observed that the experimental data in upstream of the Ahmed body and in the freestream above it is well reproduced by all the three turbulence models. This is because in this region the level of turbulence is so low that the flow is nearly potential flow.

In Fig. 8.17, the mean streamwise velocity profiles are compared with the experimental data in the rear body part and the near wake (in the symmetry plane). The general agreement with the experiment is reasonably good. The complex unsteady flow on the slant back leads to high fluctuation intensities which are very difficult to predict. However, it can be noticed from the figure that *LES* turbulence model gives better results as compared to the steady  $k - \varepsilon$  and  $k - \omega - SST$  models. Even in the wake, the results of the simulations agree quite well with the experiment, with only minor deviations. Good agreement of the experimental data for the flow between the wind tunnel floor and the under body of the model can be seen from these figures. Figure 8.18 shows the comparison of lift and drag coefficient for various turbulence model with the experimental data. From the figure it can be observed that although the drag coefficient was predicted quite well by all the three turbulence models -  $k - \varepsilon$  and  $k - \omega - SST$  and *LES*, within 7% error, the lift coefficient was predicted closest by the *LES* model with only 1.3% error. On an average, the error with *LES* model was approximately 4% for the force coefficient measurements which is lower than the other model errors.

From the above discussion, it can be concluded that the choice of turbulence model has influence on the simulated flow field data and *LES* results turn out to be closest to the experimental data.

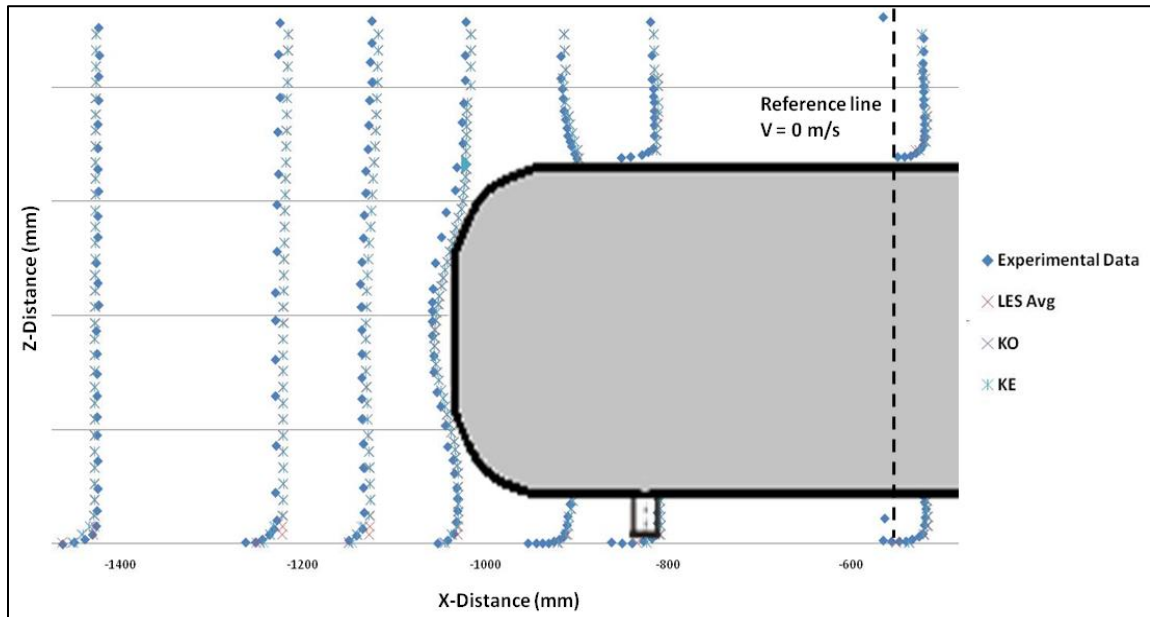


**Figure 8.16** Streamwise velocity profile along the front part of Ahmed body.

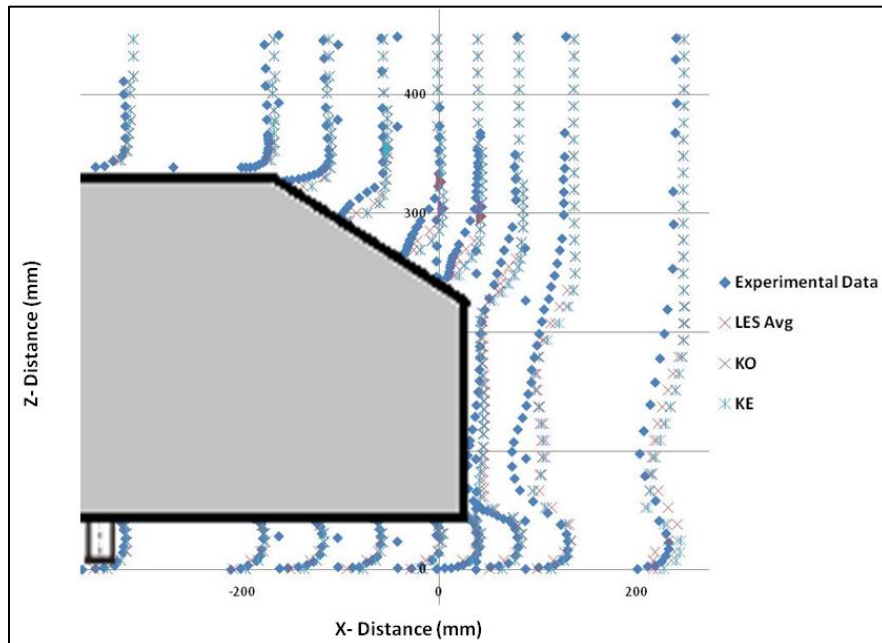


**Figure 8.17** Streamwise velocity profile along the rear part of Ahmed body.

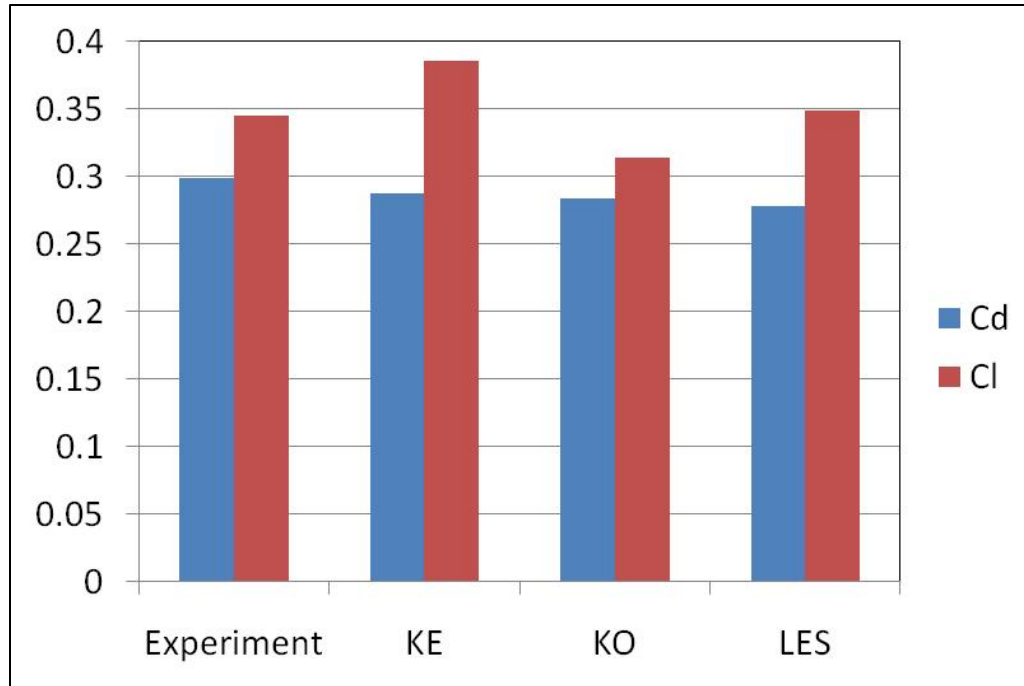


**Figure 8.18** Comparison of drag and lift coefficient for various turbulence models.

Once the CFD methodology validation and verification was successfully achieved, the same methodology was used for a one-third-scaled down model which was tested in the Wind Tunnel Facility at University of Wisconsin to get the mean flow experimental data. In view of the fact that *LES* model represented the closest mean flow results to the experimental data, the same model was used on the scaled-down model. The inlet conditions used in the simulations for a scaled down model differed from the full-scale model based on the flow measurements in the wind tunnel. The free-stream inlet velocity of 12 m/s with a turbulence intensity of 0.01% and a smaller time-step size of 0.001 s was used. In addition to the *LES* model, since it is incapable of providing the Reynolds stress data, the simulations were also performed with *RST* model to get the values of the Reynolds stresses for later use in the ASM model.

### 8.2.4 Wind Tunnel Facility

An open circuit low turbulence wind tunnel was used to provide the air for the flow analysis around the Ahmed body. A low turbulence wind tunnel eliminates the twist in the incoming air and significantly reduces the scale of turbulence entering the test-section. The open circuit wind tunnel has the advantage over the re-circulating wind tunnel as the former require significantly lesser space than the re-circulating wind tunnel. Additionally, for the open circuit wind tunnel the heat generated gets dissipated to the room air leading to much steadier flow temperatures. Steady temperatures are very important for any hot-wire measurements. The main components of the wind tunnel as depicted in Fig. 8.19 from inlet to outlet, include - honeycomb, screens, settling and contraction chambers, test-section, diffuser and fan. Figure 8.20 shows the actual subsonic wind tunnel facility employed for testing.

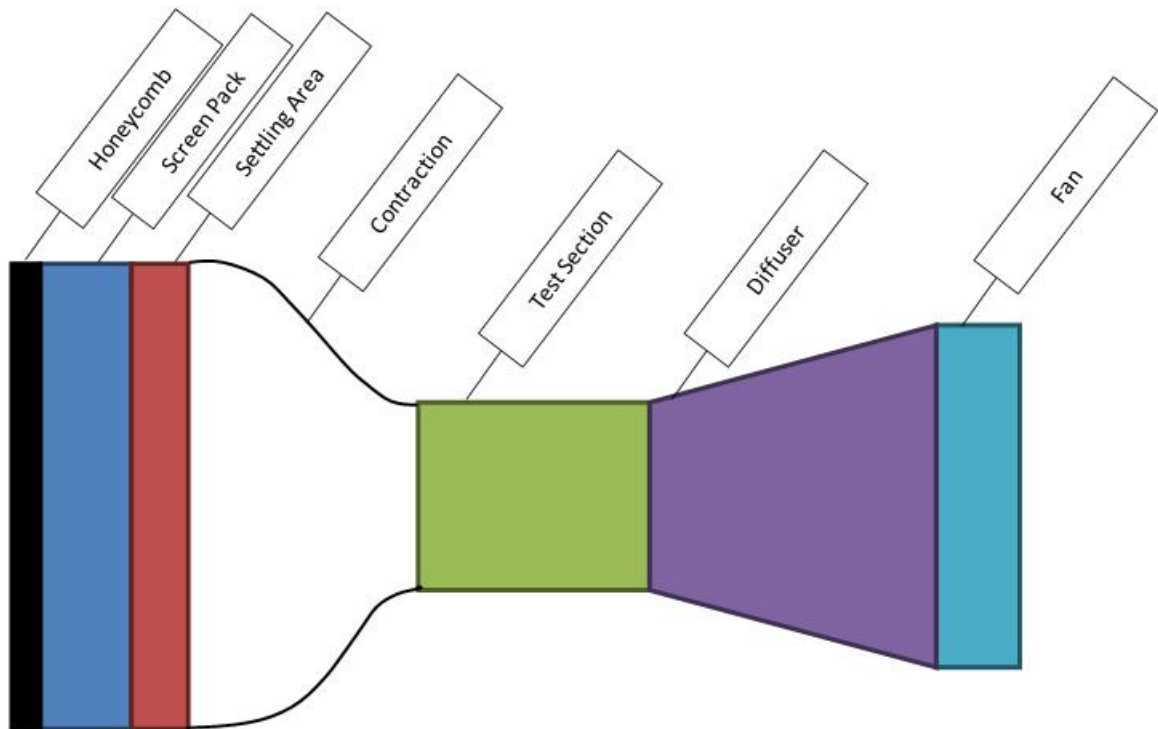


**Figure 8.19** Schematic of the open circuit wind tunnel.



**Figure 8.20** Subsonic wind tunnel facility at University of Wisconsin - Milwaukee.

#### **8.2.4.1 Honeycomb and Screens**

The flow enters the wind tunnel through the honeycomb. Both honeycomb and screens along with the settling chamber form the flow conditioning section of the wind tunnel entrance. The honeycomb and screens are located in the lower velocity region of the wind tunnel. The main purpose of the honeycomb is to reduce the large scale turbulence in the flow, remove twist from the incoming air and straighten the flow. Screens further break the large eddies and reduce the turbulence level in the flow. A combination of one honeycomb and six screens of varied mesh size at different streamwise locations were used at the inlet of the wind tunnel.



#### **8.2.4.2 Settling and Contraction Chambers**

Settling and contraction chambers are designed to laminarize the flow and reduce the turbulence level in the flow before it enters the test-section. The settling chamber which follows the screen section, allows for the flow stabilization before it gets accelerated in the contraction section. If unstable flow enters the contraction section, it may lead to flow separation and additional turbulence in the test-section.

For the contraction section, it is desirable to minimize the length as additional length increases the boundary layer. However, if a high contraction ratio is used over too short distance, it will result in flow separation. Also, more power is required for high contraction ratio. As stated in Bradshaw and Pankhurst, 1964, the ideal contraction ratio minimizing boundary layer growth and maximizing the air velocity is between 6 and 9. The contraction ratio of this wind tunnel based on the inlet area of  $3.05 \text{ m}^2$  and the test-section area of  $1.19 \text{ m}^2$  was 6.2. A fifth order polynomial was used for the contraction section.

#### **8.2.4.3 Test-section**

The test-section has polycarbonate transparent walls (side walls, top and bottom surfaces) for better visualization. The test-section has a cross-sectional area of  $1.19 \text{ m}^2$  and 2.42 m in length. The test section is equipped with a X-Y-Z traverse system (schematic shown in Fig. 8.21) which has a fixture to mount the hot-wire assembly and move it inside the wind tunnel. The traverse system is computer controlled via LabView program and is programmed to capture both horizontal and vertical planes, covering the entire test-section length. The bottom surface of the test-section has a slot to mount the Ahmed body in the wind tunnel.

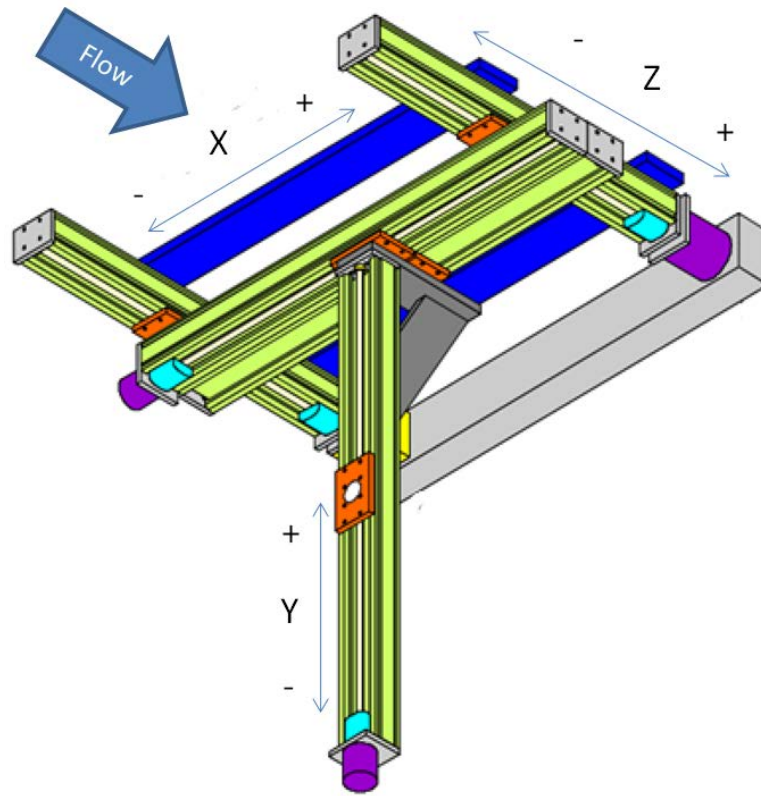


**Figure 8.21** Schematic of the X-Y-Z traverse system in the wind tunnel.

#### 8.2.4.4 Diffuser and Fan

The test-section is followed by a diffuser section which smoothly transitions the flow to the fan diameter. Flow separation in the diffuser can cause pressure fluctuations and turbulence in the test-section. To prevent the flow separation, the diffuser area ratio should not exceed 2.5. The ratio for this wind tunnel is 2.25. The diffuser has a cross-sectional area of  $1.22 \text{ m}^2$  at the test-section and ends as an octagon roughly matching the 1.83 m diameter of the fan.

The fan pulls the air through the wind tunnel. It has a constant speed driving motor. The speed of the fan can be controlled by setting the frequency as per flow

velocity required through a main control board. The maximum flow velocity that can be achieved with this fan is approximately 25 m/s. A rubber coupling connects the diffuser to the fan and prevents any fan vibrations from spreading to rest of the wind tunnel and causing turbulence. The fan rests on four vibration reducing rubber mounts which connects the fan to its stand, which is also mounted on rubber pads to further reduce the fan vibrations from spreading to the floor.

### **8.2.5 Hot-Wire Anemometry**

Hot wire anemometry is used to measure the mean and fluctuating instantaneous fluid velocity of turbulent flows and provide measurement of turbulent intensities and shear stresses. The flow measurements for this thesis were conducted using Constant Temperature Anemometry (CTA). In constant temperature anemometry, the controlling circuit tries to maintain a constant resistance and temperature in the wire, whilst the variation of current is measured. Typically the probe wires can be heated to temperatures of 300°C. By passing current through the wire its resistance causes electrical energy to be converted to thermal energy. When the probe is placed in the fluid flow, where its temperature is elevated above that of the fluid, heat transfer from the wire to the fluid occurs by forced convection. The fluid effectively has a cooling effect on the probe and the rate of convective heat transfer is therefore, a function of the velocity of the fluid and the proportional difference between the fluid and probe temperatures. In equilibrium conditions (voltage difference across the wire is zero), there is a balance between the electrical circuit keeping the resistance constant (and so its temperature) and the heat loss to the fluid. As the flow velocity increases, the wire cools down, its resistance decreases and this results in bridge imbalance. This imbalance is represented by the voltage signal

across the Wheatstone bridge. To balance the bridge, the current in the circuit is increased, the sensor wire heats up and the resistance is increased until the circuit is balanced. The system allows for rapid response to the changes in the flow and so the sensor temperature and resistance can be maintained constant with the changes in the flow velocity. The voltage drop across the bridge can be used to represent the probe current.

#### 8.2.5.1 Probe Specifications

The two-component velocity measurements were made using a miniature X-probe hot-wire anemometry. The miniature X-probe as shown in Fig. 8.22, used for the measurements was manufactured by DANTEC Dynamics. It is a platinum-plated tungsten wire  $5\ \mu\text{m}$  in diameter and  $1.25\ \text{mm}$  long. The sensors are arranged in X-arrays, where they form an angle of  $90^\circ$  with one another. The probe body is a  $2.3\ \text{mm}$  diameter ceramic tube, equipped with gold-plated connect to the probe supports by means of plug-and-socket arrangements. The probe support has a diameter of  $6\ \text{mm}$ . The probe is attached to the fixture on the traverse system (shown in Fig. 8.23), which is driven by a computer-controlled stepper motor with a minimum resolution of  $0.00635\ \text{mm}$ . The probe mounts with the probe axis perpendicular to the main flow and rotated, so that the predominant flow vector attacks the two wires under  $45^\circ$ . The sensor resistance  $R_{20} \cong 3.5\ \Omega$  with the temperature coefficient of resistance (TCR),  $\alpha_{20} = 0.36\%/^\circ\text{C}$ . The sensor lead resistance,  $R_L = 0.5\ \Omega$ , support resistance,  $R_S = 0.4\ \Omega$  and the cable resistance,  $R_C = 0.6\ \Omega$ . The maximum sensor temperature is  $300^\circ\text{C}$ . The operating sensor resistance  $R$ , can be calculated from the amount of overheat chosen for the sensor using Eqn. 8.8. The operating sensor resistance is the probe hot resistance inclusive of lead

resistance in the probe body and in fixed mounted cable. The sensor operating temperature  $T_{sensor}$ , is the temperature selected higher than the air flow temperature.

$$R = R_{tot} + \alpha_{20} R_{20} (T_{sensor} - T_o) \quad (8.8)$$

where,

$$R_{tot} = R_{20} + R_L + R_S + R_C \quad (8.9)$$

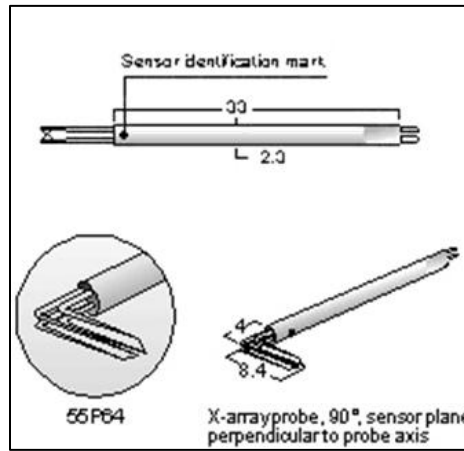


**Figure 8.22** Miniature X-probe hot wire anemometer.

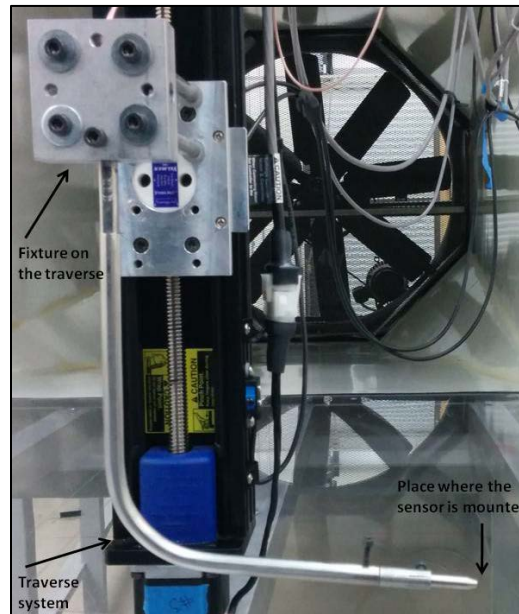


**Figure 8.23** Fixture on the traverse to mount the hot-wire sensor.

### 8.2.5.2 Data Conversion

Data conversion transforms the CTA voltages into calibration velocities in m/s by means of the calibration transfer function. Multi-sensor probes are further decomposed into velocity components in the probe coordinate system. If it differs from the laboratory coordinate system, the velocity components are finally transformed into the laboratory coordinate system. Data conversion consists of the following processes:

- Re-scaling of acquired CTA output voltages (raw data) - Only if signal conditioning gain and offset have been applied.
- Temperature correction - Only if sensor temperature has been kept constant during the experiment (no over heat adjustment).
- Linearization - Only if data reduction in amplitude domain is required.
- Decomposition into velocity components - Only for X-probes and Tri-axial probes.

The CTA signal was not subjected to any DC-offset and amplification between overheat set-up and calibration, thus there was no need of rescaling the raw data. However, the overheat ratio was not adjusted prior to the data acquisition, thus requiring that the CTA voltages ( $E_a$ ) must be corrected ( $E_{corr}$ ) for possible temperature variations before conversion to velocities. The fluid temperature needs to be recorded along with the CTA voltages to determine the corrected voltages using Eqn. 8.10. The sensor hot temperatures ( $T_w$ ) for the X-probe used were 240°C and 220°C for wire1 and wire 2, respectively. The ambient reference temperature ( $T_o$ ) related to the last overheat set-up before calibration was 22.1°C and the ambient temperature ( $T_a$ ) was recorded during data acquisition.

$$E_{corr} = \left( \frac{T_w - T_o}{T_w - T_a} \right)^{0.5} \cdot E_a \quad (8.10)$$

The linearization or conversion of voltages to calibration velocities is achieved by inserting the acquired voltages into the calibration transfer functions after re-scaling and temperature corrections, if applicable. The simplest and most accurate transfer function is the polynomial, at least in the case of a wide dynamic velocity range. The velocities are calculated as if the velocity attacked the probe under the same angle during measurement as during calibration. The linearized or calibrated velocity  $U_{cal}$ , is obtained using Eqn. 8.11.

$$U_{cal} = C_o + C_1 E_{corr} + C_2 E_{corr}^2 + C_3 E_{corr}^3 + C_4 E_{corr}^4 \quad (8.11)$$

where,  $C_o$  to  $C_4$  are the calibration constants which are obtained from best-fit curve on the calibration data which consists of a set of known velocities and the corresponding CTA output voltages.

In two-dimensional flows measured with X-probes, the calibrated velocities together with the yaw coefficient  $k^2$  are used as intermediate results to calculate the velocity components  $U$  and  $V$  in the probe coordinate system. The yaw coefficients for the two sensors may be the manufacture's default values, or if higher accuracy is required they are determined by directional calibration of the individual sensor. The default yaw coefficients for the miniature wire probe sensors used are  $k_1^2 = k_2^2 = 0.04$ . The velocities ( $U_1$  and  $U_2$ ) in the wire-coordinate system (1,2) is given by Eqns. 8.12 and 8.13.

$$U_1 = \frac{\sqrt{2}}{2} \cdot \sqrt{(1 + k_2^2) \cdot U_{cal2}^2 - k_2^2 \cdot U_{cal1}^2} \quad (8.12)$$

$$U_2 = \frac{\sqrt{2}}{2} \cdot \sqrt{(1 + k_1^2) \cdot U_{cal1}^2 - k_1^2 \cdot U_{cal2}^2} \quad (8.13)$$

Finally these velocities ( $U_1$  and  $U_2$ ) are converted to velocity components ( $U$  and  $V$ ) using Eqn. 8.14 and 8.15.

$$U = \frac{\sqrt{2}}{2} \cdot U_1 + \frac{\sqrt{2}}{2} \cdot U_2 \quad (8.14)$$

$$V = \frac{\sqrt{2}}{2} \cdot U_1 - \frac{\sqrt{2}}{2} \cdot U_2 \quad (8.15)$$

### 8.2.5.3 Data Acquisition

The CTA signal is a continuous analogue voltage. In order to process it digitally it has to be sampled as a time series consisting of discrete values digitized by an analogue-to-digital converter (A/D board). The parameters defining the data acquisition are the 'sampling rate',  $SR$  and the 'number of samples',  $N$ . Together they determine the 'sampling time' as  $T = N/SR$ . The values for  $SR$  and  $N$  depend primarily on the specific experiment, the required data analysis (time-averaged or spectral analysis), the available computer memory and the acceptable level of uncertainty. For the time-averaged analysis involved in the flow measurements, a sampling rate of 2000 and number of samples 20000 was used which gives the sampling time as 10 s.



#### 8.2.5.4 Hot-wire Calibration

Calibration is an inevitable step for any experimental study. The process of hot-wire calibration aims to establish a relationship between the CTA bridge output voltage and the flow velocity. As described in the earlier sections, the hot-wire anemometer measures the flow characteristics in terms of voltages which are then converted into velocities (m/s). Thus, to calibrate the output from the hot-wire, it needs to be placed in a flow whose velocity is known. This was achieved with the help of DANTEC Dynamics Hot-Wire Calibrator shown in Fig. 8.24. It is a simple but accurate, device for 2-point calibration of most of hot-wire probes used with constant temperature anemometers. The calibrator produces a free jet, where the probe is placed during calibration. It requires a normal pressurized air supply and is able to set velocities from 0.5 m/s to 60 m/s.

For the calibration procedure, the calibrator is placed inside the wind tunnel and the hot wire is mounted in the fixture on the traverse system such that the tip of the hot-wire is exposed to the free jet from the calibrator. The compressed air supply is connected to the 'Air Inlet' port to provide the free jet. A digital multi-meter is connected to the port marked 'Temperature' to measure the wire resistance in Ohms. An airflow meter is connected to the 'Pressure' port of the calibrator to record the differential pressure. The reference pressure port on the airflow meter is left open to the atmosphere and the barometric pressure of the surrounding room is monitored with the help of a digital barometer. Figure 8.25 shows all the connections for the calibration when the calibrator is outside the wind tunnel. A LabView program is initiated to record the data when the air supply is varied. The user inputs required for the program are - differential pressure, wire resistance, ambient temperature, barometric pressure and flow angle (which is set to

zero). Once all the user inputs are provided the program is run to give the voltages for the two wires. The program outputs all the data in a calibration text file, which includes - voltages from the two wires (in V), differential pressure (in Pa), barometric pressure (kPa), wire resistance ( $\Omega$ ), flow angle ( $^\circ$ ) and ambient temperature ( $^\circ\text{C}$ ). A total of 15 set of data is recorded by varying the air supply. Based on the pressure applied across the calibrator pressure ports, the calibration velocity range was 2 m/s to 26 m/s.

Next, a MATLAB program is used to compute the calibration coefficients ( $C_0$  to  $C_4$ ) using the calibration text file data. A forth order polynomial is used to fit a curve through the calibration data. Figure 8.26 shows the calibration curve and Fig. 8.27 shows the error curve obtained for the two wires. Error between the calibration and best-fit velocity for the range of velocity being tested was within  $\pm 0.5\%$ , which is acceptable. Table 8.2 gives the computed coefficients for the forth order polynomial to be used as calibration transfer function given by Eqn. 8.11. These two sets of coefficients are used to convert the corrected voltages to velocities which are further processed to get the required U and V velocity components.



**Figure 8.24** Hot-wire calibrator manufactured by DANTEC Dynamics.

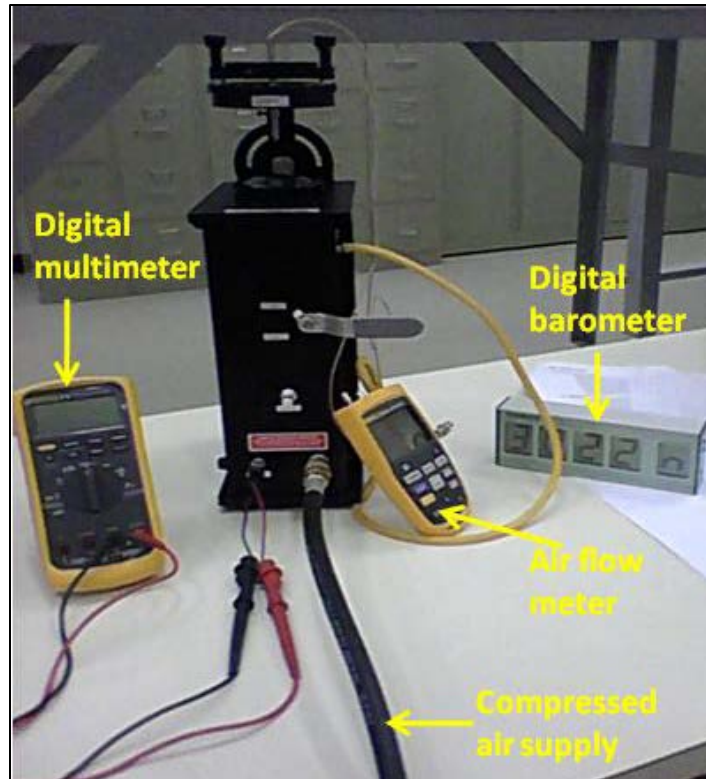


**Figure 8.25** Calibration connections for measurements.

**Table 8.2** Calibration transfer function coefficients.

Coefficient	Wire1	Wire2
$C_0$	587.8	631.2
$C_1$	-1311.6	-1407.4
$C_2$	1102.0	1182.9
$C_3$	-418.5	-450.0
$C_4$	62.0	66.9

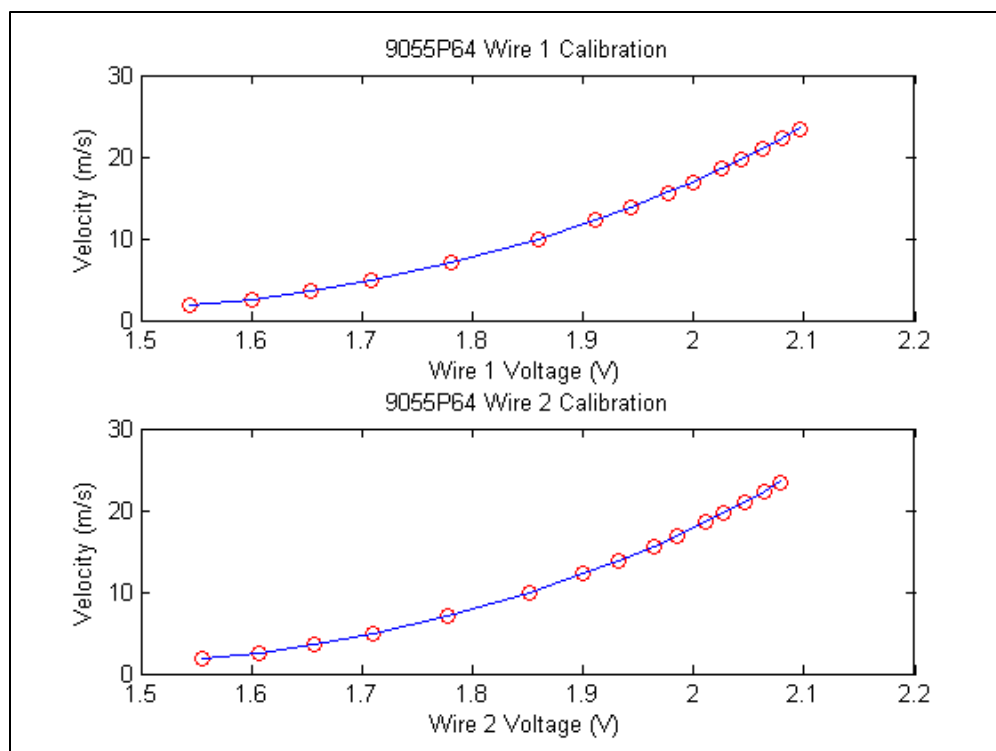


**Figure 8.26** Calibration curves for wire1 and wire2 of the X-probe sensor.

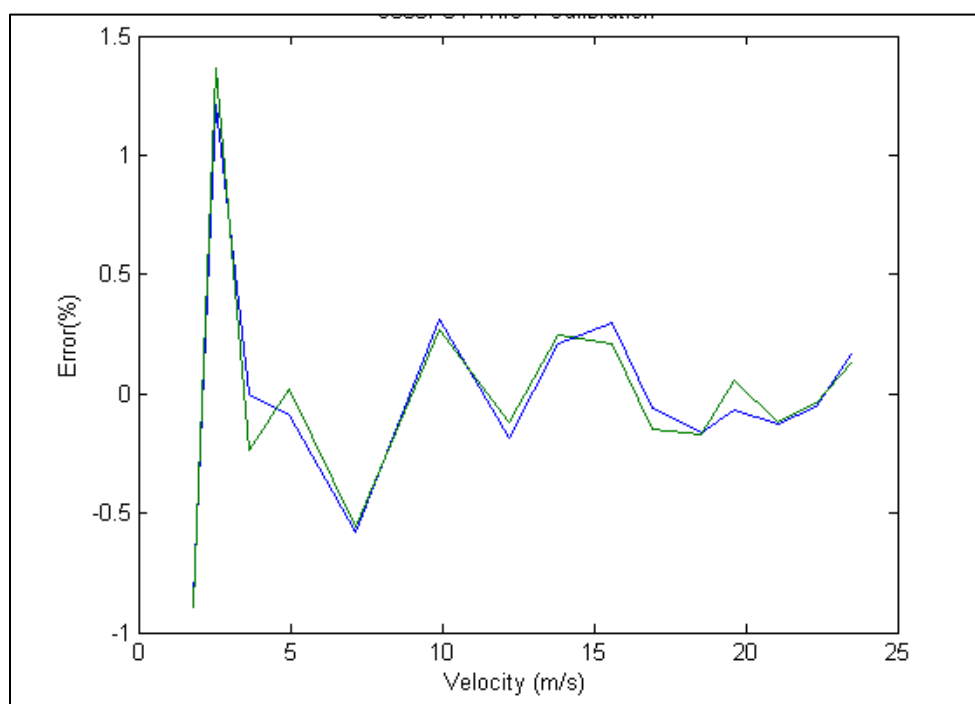


**Figure 8.27** Error curves for wire1 and wire2 of the X-probe sensor.

### 8.2.5.5 Hot-wire Error Analysis

The A/D resolution of the data acquisition (DAQ) system is a source of error in flow measurements. The A/D resolution for the employed DAQ system was 0.01 mV. Using Eqn. 8.11, the transfer function for the two velocities can be written as:

$$U_{cal1} = C_o + C_1 E_{corr1} + C_2 E_{corr1}^2 + C_3 E_{corr1}^3 + C_4 E_{corr1}^4 \quad (8.16)$$

$$U_{cal2} = C_o + C_1 E_{corr2} + C_2 E_{corr2}^2 + C_3 E_{corr2}^3 + C_4 E_{corr2}^4 \quad (8.17)$$

where,  $C_o$  to  $C_4$  are the calibration constants for Wire1 and Wire 2 respectively from Table 8.2 and  $E_{corr1}$  &  $E_{corr2}$  are the corresponding corrected voltages. The error estimate for  $U_{cal1}$  can be derived by differentiating Eqn. 8.16 as:

$$\Delta U_{cal1} = C_1 \Delta E_{corr1} + 2C_2 E_{corr1} \Delta E_{corr1} + 3C_3 E_{corr1}^2 \Delta E_{corr1} + 4C_4 E_{corr1}^3 \Delta E_{corr1} \quad (8.18)$$

Similarly, for the second calibrated velocity  $U_{cal2}$ , the error equation becomes:

$$\Delta U_{cal2} = C_1 \Delta E_{corr2} + 2C_2 E_{corr2} \Delta E_{corr2} + 3C_3 E_{corr2}^2 \Delta E_{corr2} + 4C_4 E_{corr2}^3 \Delta E_{corr2} \quad (8.19)$$

Substituting the calibration coefficients from Table 8.2, the estimated error for the velocity measurements due to 0.01 mV A/D resolution is at most  $\Delta u = \pm 0.00041 \text{ m/s}$  and  $\Delta v = \pm 0.00044 \text{ m/s}$  for the velocity components  $U$  and  $V$  respectively.

Other flow related disturbing effects which influence the measurements with hot-wire anemometers include temperature, pressure variations, composition, etc. Temperature variations are normally the most important error source, as the heat transfer

is directly proportional to the temperature difference between the sensor and the fluid. For a wire probe operated under normal conditions, the error in measured velocity is approximately 2% per 1°C change in temperature. The measured velocity decreases with increasing ambient temperature.

Different precautions can be taken in order to avoid systematic conversion errors when probe voltages are converted to velocities. One solution is to readjust the overheat resistor to the changed temperature, so that overheat ratio is kept constant from calibration to measurement. Another solution is to leave the overheat resistor constant, measure the temperature and correct the probe voltage. In the present flow measurements, to compensate for any change in the temperature from calibration to measurements, a corrected voltage was determined using Eqn. 8.10.

Pressure variations enter directly into the heat transfer equation, as the probe in fact measures the mass flux. Normally probes are calibrated against velocity only. As pressure variations from calibration to experiment are normally small, the pressure influence in the CTA measurements is normally neglected. In most cases, the fluid composition remains constant during calibration and experiment, and it is of no importance. In air one normally experiences variation in water vapor content (humidity). The influence is very small, less than 1% and is almost always neglected.

Sensor conditions like contamination, sensor orientation, etc. also influence the flow measurements. Particles contamination reduces the heat transfer resulting in a downward drift in the calibration. The influence of particle contamination increases with decreasing sensor surface. However, the wire probes with 5  $\mu m$  sensors can be used

without problems in normal laboratory air, if they are recalibrated at regular intervals. Contamination is a much bigger problem in liquid flows than in gas flows.

The effect of sensor orientation is negligible as long as the sensor is placed identically with respect to the flow during calibration and measurement. The misalignment is normally so small that it may be neglected as an error source.

### 8.2.6 Flow Measurements

Flow measurements were conducted inside the open loop suction type wind tunnel facility described in Sec. 8.2.4. The tunnel was run at a velocity of 12 m/s with the turbulence intensity of 0.01%. The Reynolds number based on the Ahmed body scaled down prototype length was  $3.3 \times 10^5$ . The hot-wire measurements were performed at the mid-plane ( $y = 0$ ) along 8 vertical lines capturing the flow in front and behind the Ahmed body. Figure 8.28 shows the Ahmed body prototype mounted inside the wind tunnel. The traverse system is operated with the help of LabView program such that the hot-wire moves in the z-direction along the vertical lines which are depicted in Figure 8.29. The locations of the vertical lines with respect to the back of the Ahmed body in the negative x-direction are given in Table 8.3. For the lines 1 to 5, the closest the hot-wire could be positioned to the wind tunnel floor was 8 mm, where as for the lines behind the Ahmed body this distance was nearly 13 mm above the wind tunnel floor. The measurements were taken with 1 mm vertical position resolution for lines 1 and 2 and with 2 mm resolution for rest of the lines over a range of z-coordinates (30 to 200 mm) for different vertical lines.

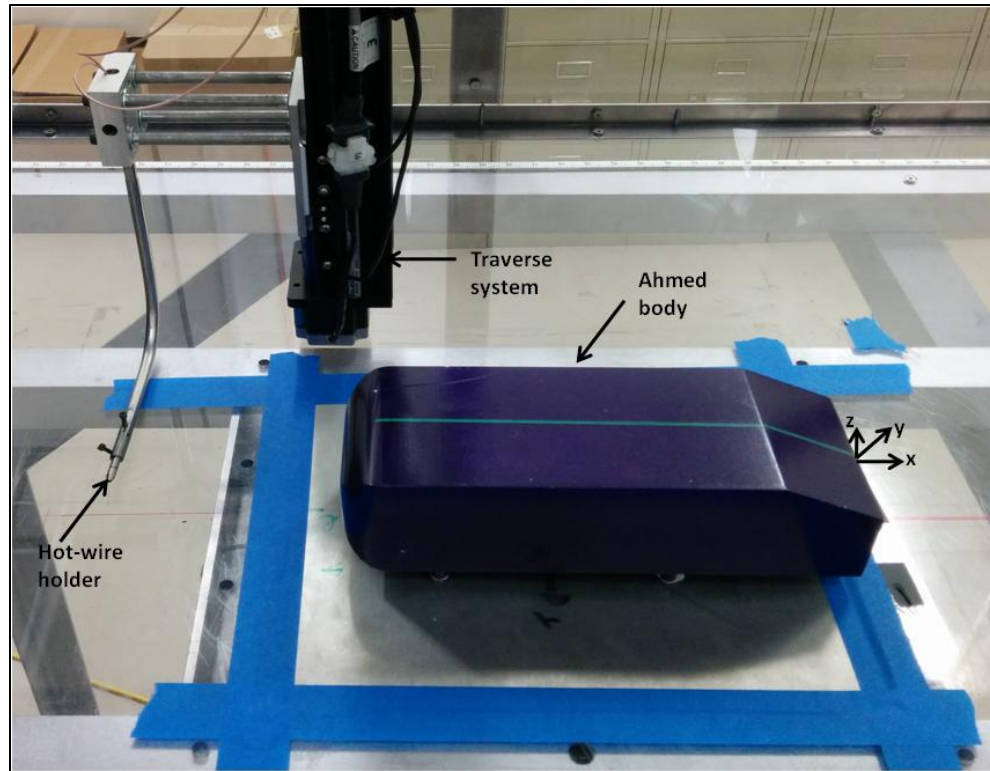


**Figure 8.28** Ahmed body prototype mounted inside the wind tunnel.

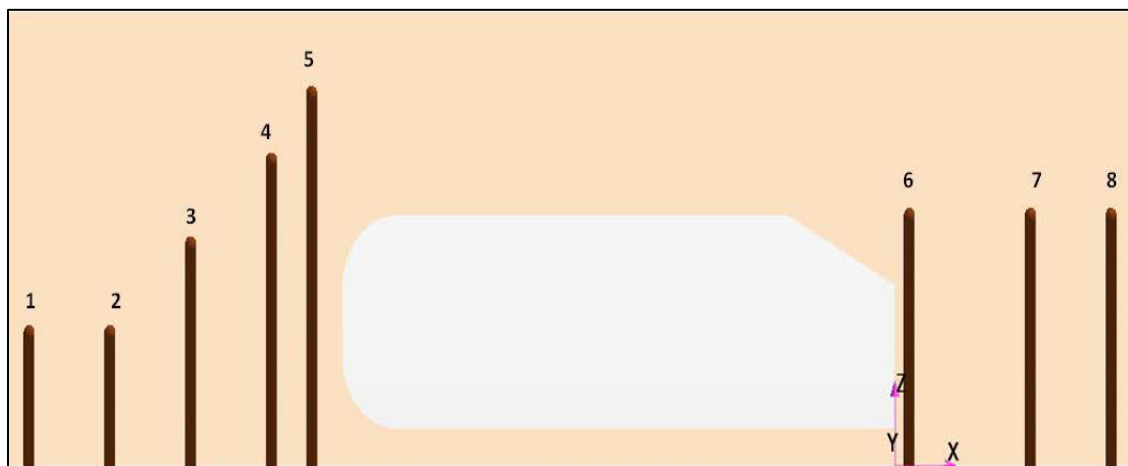


**Figure 8.29** Schematic of the vertical lines for hot-wire measurements.



**Table 8.3** Location of the vertical lines for hot-wire measurements.

Line-Probe	Position from back of the Ahmed body x/L
1	-1.57
2	-1.42
3	-1.27
4	-1.13
5	-1.05
6	0.03
7	0.24
8	0.39

### 8.2.7 Mean Flow Validation for Scaled-down Ahmed Body

Both *LES* and *RST* simulations were run at a Reynolds number of  $3.3 \times 10^5$ , which is the same as inside the wind tunnel corresponding to 12 m/s inlet velocity. The mean velocity profiles obtained in experiments were measured by a miniature X-probe with the axis of the probe perpendicular to the main flow direction. Figures 8.30 - 8.34 compare the normalized streamwise velocity profiles obtained from experiment and simulations at various x-locations in front of the Ahmed body prototype. It can be observed from Figs. 8.30 - 8.32 that the velocity profile is quite similar to a simple boundary layer flow for lines 1, 2, 3 and the presence of the Ahmed body cannot be noticed. The velocity profiles for lines 4 and 5 as shown in Figs. 8.33 and 8.34, clearly demonstrate the effect of presence of the Ahmed body with the flow right in front of the

Ahmed body getting obstructed resulting in slower velocities. Once again both *LES* and *RST* simulations follow the experimental velocity profile very closely.

Figures 8.35 - 8.37 compare the normalized streamwise velocity profiles for the measurements behind the Ahmed body, in the wake region. Measurements in the wake region which experienced recirculation in the flow proved unreliable, as errors in the streamwise velocity were caused by the large crossflow velocities. Also, the velocity range of hot-wire calibration 2 m/s - 26 m/s subjected the measurement of velocities below 2 m/s in the experiments to more errors, where as both *LES* and *RST* simulations clearly show velocities below 2 m/s including the flow reversal which is indicated by the negative velocities obtained in simulations. The negative simulation velocities verify the presence of a recirculation zone behind the Ahmed body which is missed out completely in the experimental measurements. Also, due to the limited probe traverse close to the wind tunnel floor, measurements below 13 mm were not recorded. In regions close to the wall both *LES* and *RST* simulations give similar velocity profiles.

Other than the restricted velocity range of the hot-wire, the main reason for the experimental measurements not showing the flow reversal in the wake is the incapability of the hot-wire sensor to measure recirculation and resolve flow direction, as well as potential probe interference. If the sensor has infinite length, then the effective cooling velocity that the sensor experiences is that which is perpendicular to the longitudinal axis of the sensor; the parallel component has no effect. Figures 8.37 and 8.38 show the schematic of the flow across the X-wire probes for positive and negative flow directions. From the figures, the effective cooling velocity component for the two wire probes under positive and reversed flow conditions can be written as:

For positive flow direction (refer Fig. 8.38),

$$U_{effective-wire1} = U\sin45^\circ + V\cos45^\circ \quad (8.20)$$

$$U_{effective-wire2} = U\cos45^\circ - V\sin45^\circ \quad (8.21)$$

For negative flow direction (refer Fig. 8.39),

$$U_{effective-wire1} = U\sin45^\circ + V\sin45^\circ \quad (8.22)$$

$$U_{effective-wire2} = U\cos45^\circ - V\cos45^\circ \quad (8.23)$$

Since sine and cosine of  $45^\circ$  is the same, the effective cooling velocity across the hot-wire probes under both the flow conditions - positive and negative - are the same. Thus, the hot-wire is incapable of distinguishing the positive and negative flow direction and results in erroneous measurements in the recirculation zone.

In addition to the above possible reasons for discrepancy in the velocities in the wake of the Ahmed body could be the potential interference between the thermal wakes of the two sensors. Both the sensors on a X-wire are basically heating devices and when submerged in a moving stream, have a wake of heated fluid trailing behind them. If the third velocity component not being measured is very large, or the flow is very turbulent, it is possible for the thermal wake of one sensor to be directed over the other sensor, contaminating its signal. When this happens, the contaminated sensor sees a warmer fluid which reduces its cooling rate and results in a lower velocity reading for that sensor than what actually exists. Because of this, not only is the  $u$ -velocity measurement incorrect (which is the sum of the two wire voltages), the other velocity measurement, be it  $v$  or  $w$  (which is the difference of the two wire voltages) is also incorrect (Greiner, 1990).

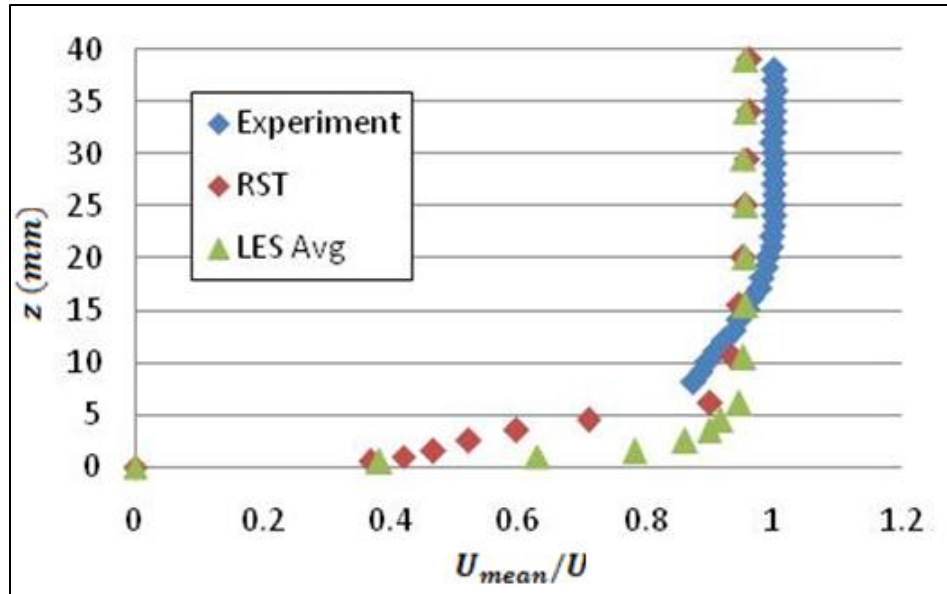


Figure 8.30 Streamwise velocity profiles for line 1.

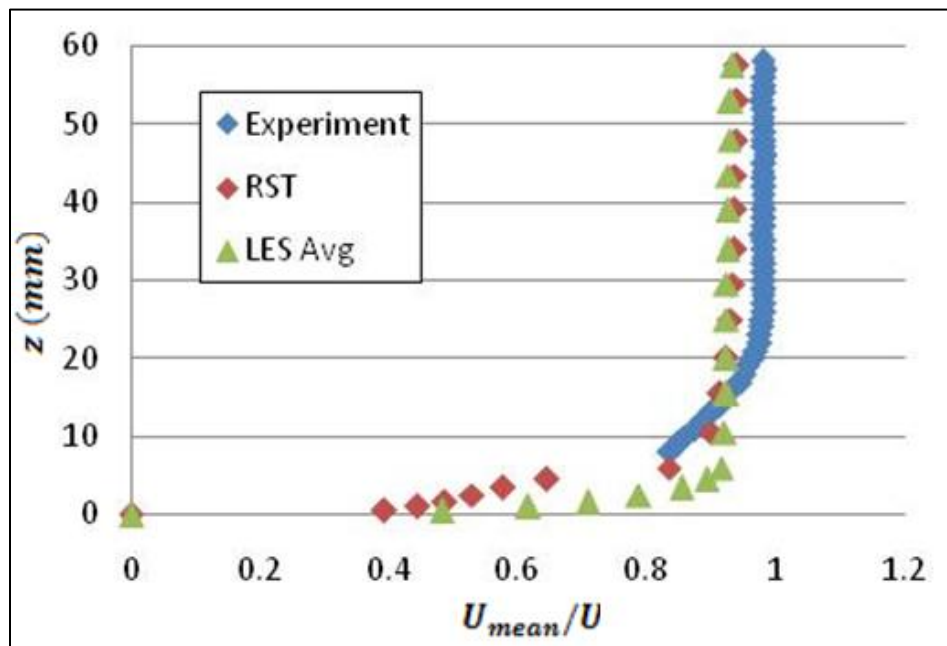


Figure 8.31 Streamwise velocity profiles for line 2.

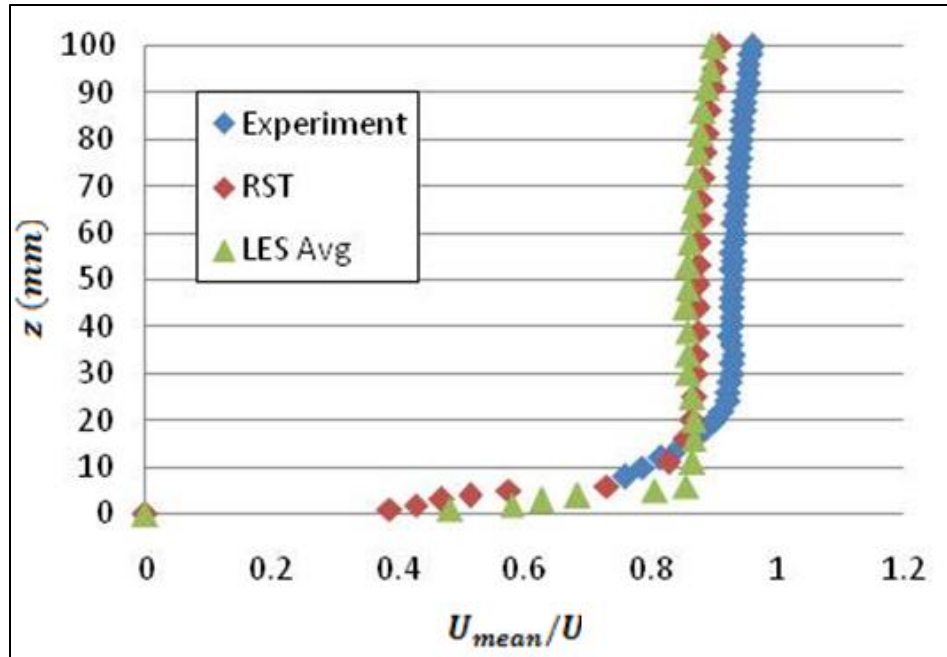


Figure 8.32 Streamwise velocity profiles for line 3.

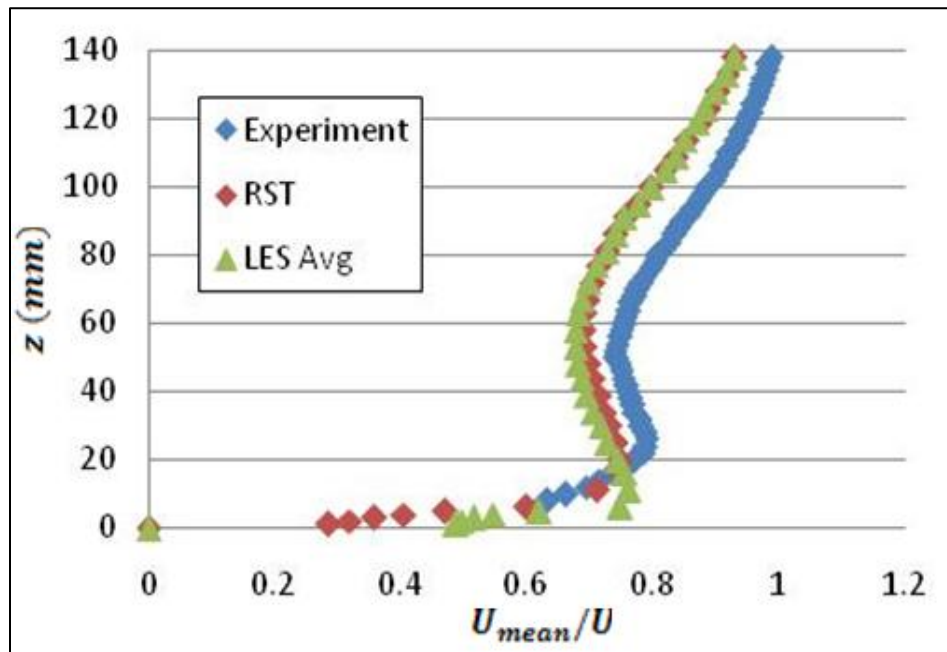


Figure 8.33 Streamwise velocity profiles for line 4.

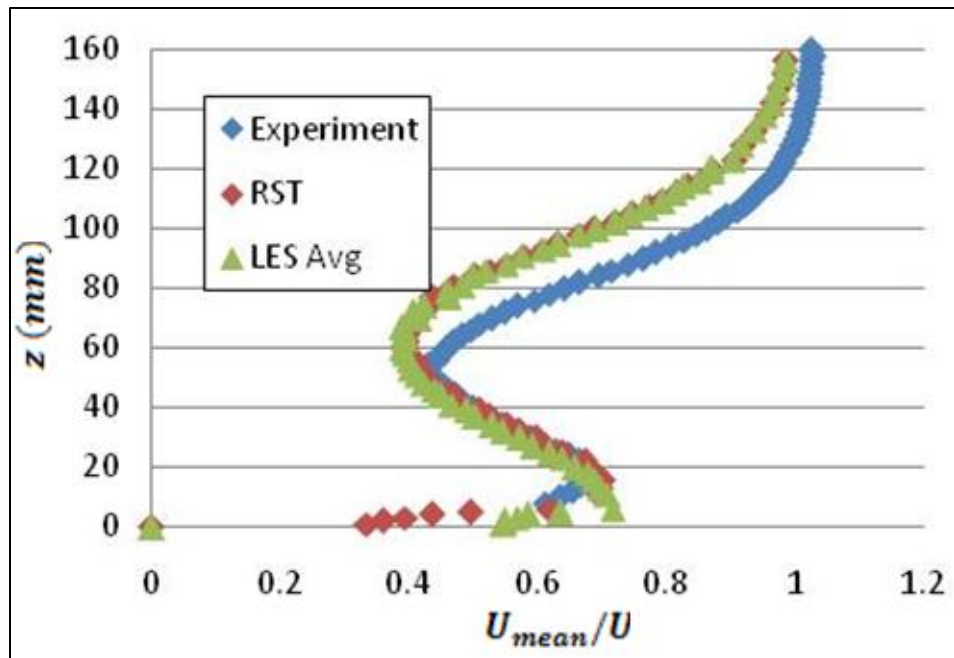


Figure 8.34 Streamwise velocity profiles for line 5.

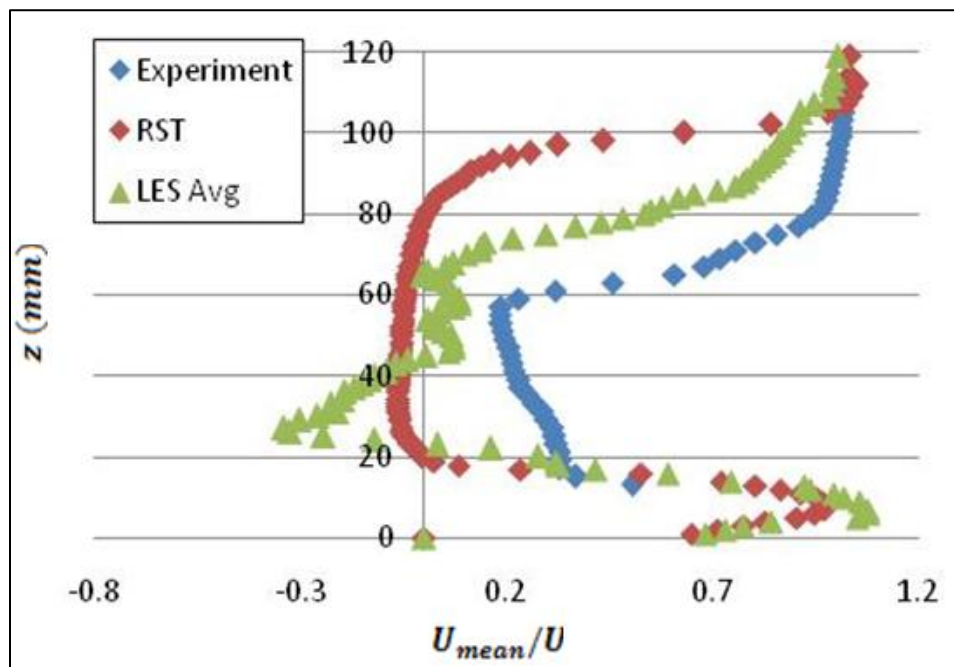


Figure 8.35 Streamwise velocity profiles for line 6.

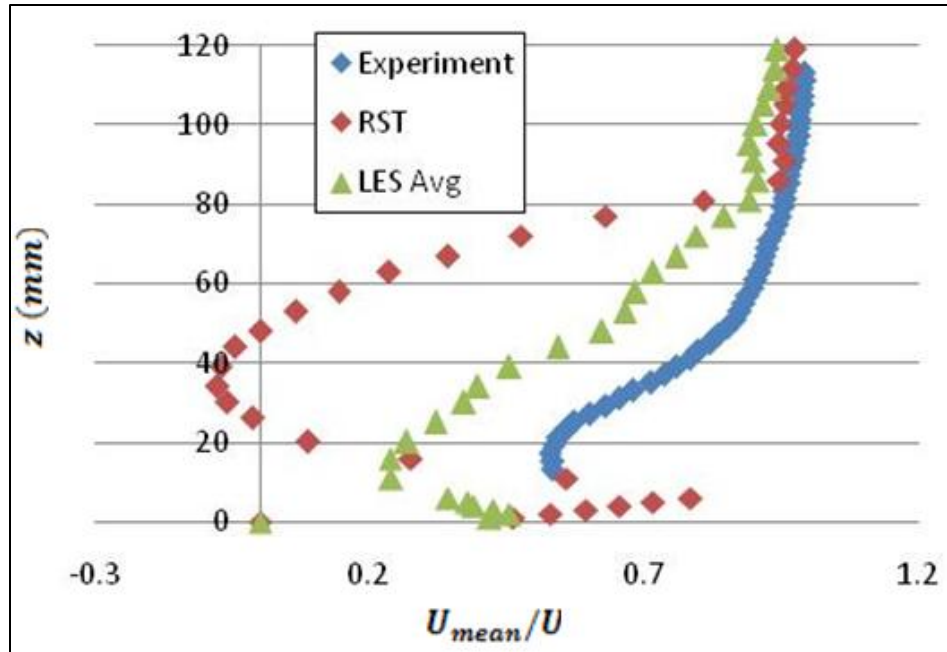


Figure 8.36 Streamwise velocity profiles for line 7.

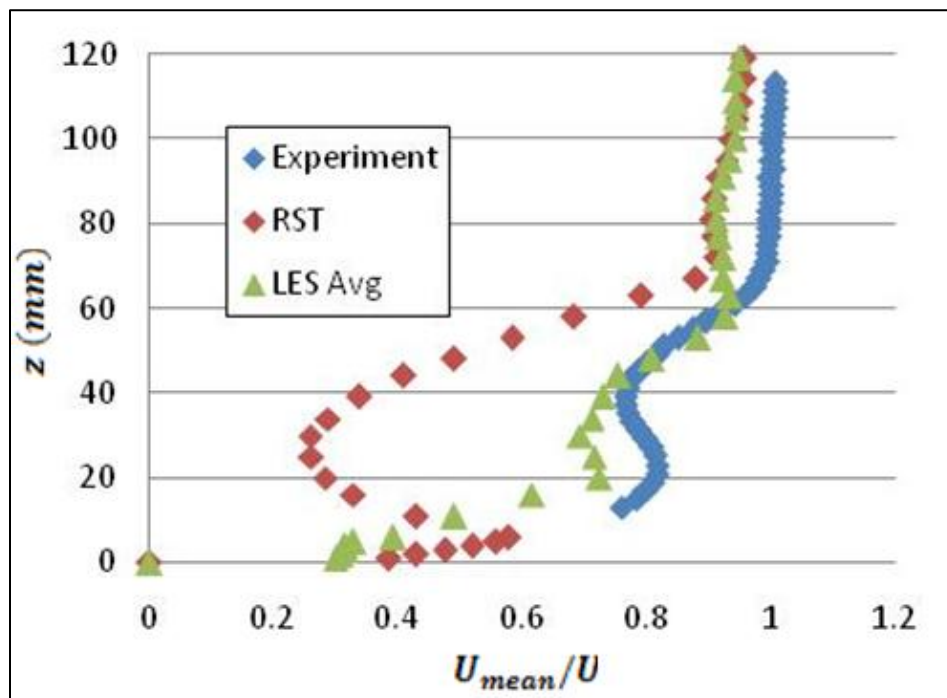
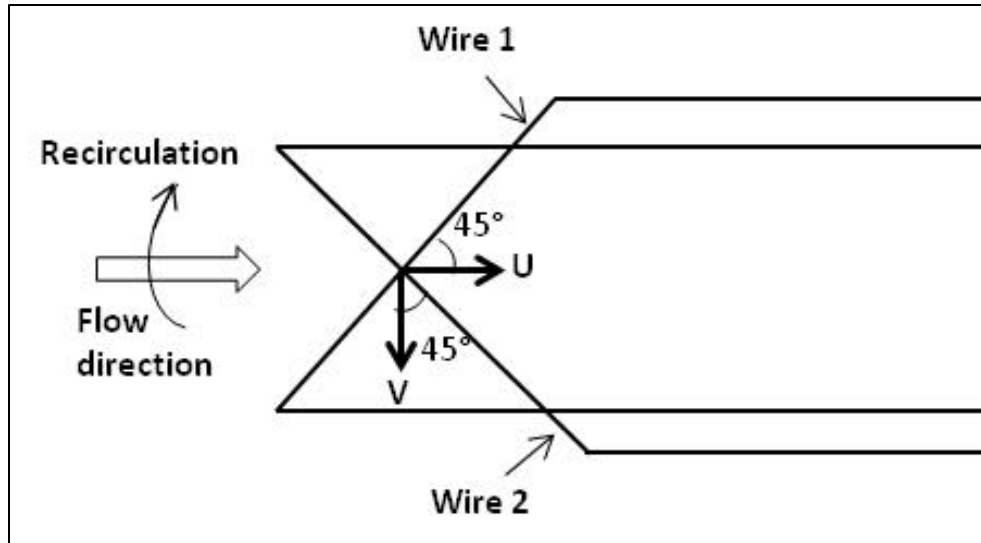
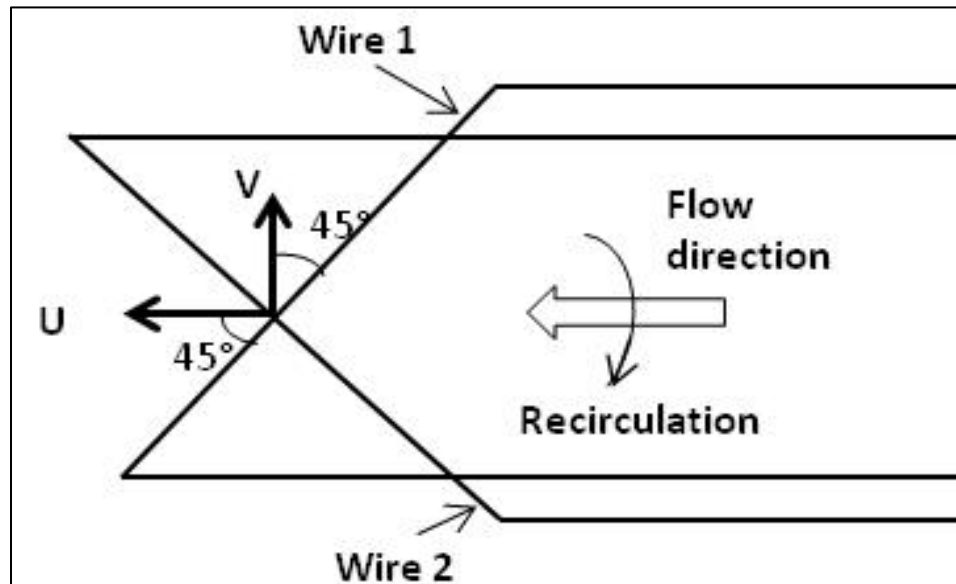


Figure 8.37 Streamwise velocity profiles for line 8.



**Figure 8.38** Schematic of the flow in positive direction across the X-wire probes.



**Figure 8.39** Schematic of the flow in negative direction across the X-wire probes.



### 8.2.8 ASM Model Reynolds Stresses

From the mean flow validation discussed in the previous section, it can be concluded that both *LES* and *RST* simulations give similar results for the flow in front of the Ahmed body but for the flow in the wake of the Ahmed body, the *LES* model seems to give better results in the region away from the wall. The main reason for this good prediction of the flow in regions away from the wall with *LES* model being, it actually solves for the large eddies in these regions instead of modeling, thus performing better than the *RST* model whose velocities seems to be a little under-predicted in regions away from the wall. For regions close to wall where the Reynolds stresses are more prominent, the use of *RST* model is recommended since it takes care of the anisotropy present in the near-wall turbulence regions unlike the *LES* model which uses wall functions in regions close to wall. Thus, to determine Reynolds stresses in the near-wall regions using the ASM model, all the flow properties, velocity gradients, turbulent quantities and Reynolds stresses were collected from the *RST* model and used in ASM model equations.

For upstream flow around the Ahmed body, the streamwise mean velocity profiles were very similar for lines 1, 2, 3 and 4, so only line 3 was chosen for comparison of the modified Reynolds stresses obtained using the ASM model with the Reynolds stresses from the *RST* model. In addition to line 3, line 5 was also selected for comparison since from the velocity profile it can be noticed that this location clearly demonstrates the presence of the Ahmed body. These two locations would enable to test the ASM model for both boundary layer flow as well as flow near an obstruction. Figures 8.40 - 8.51 show the comparison of Reynolds stresses obtained using various ASM models with the stresses from *RST* model for lines 3 and 5.

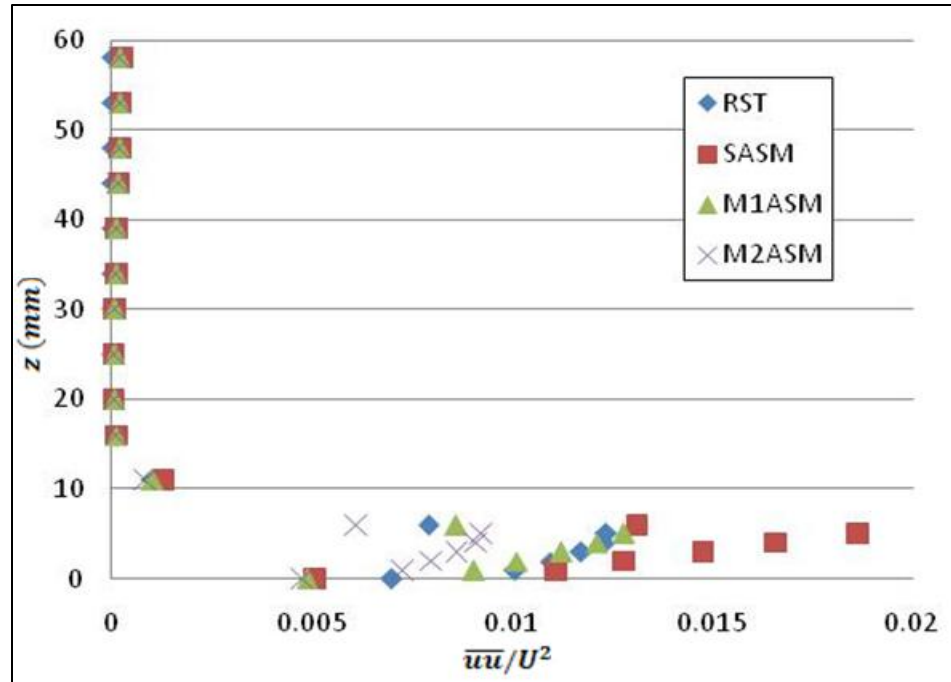


**Figure 8.40** Comparison of Reynolds stress  $\overline{uu}$  computed using various ASM models with RST model for line 3.

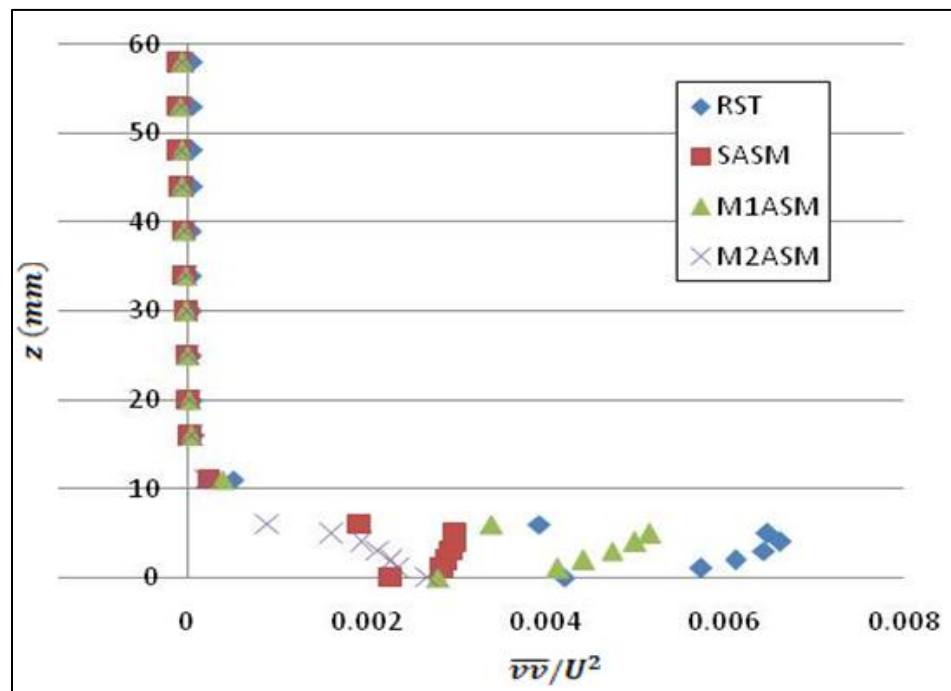


**Figure 8.41** Comparison of Reynolds stress  $\overline{vv}$  computed using various ASM models with RST model for line 3.

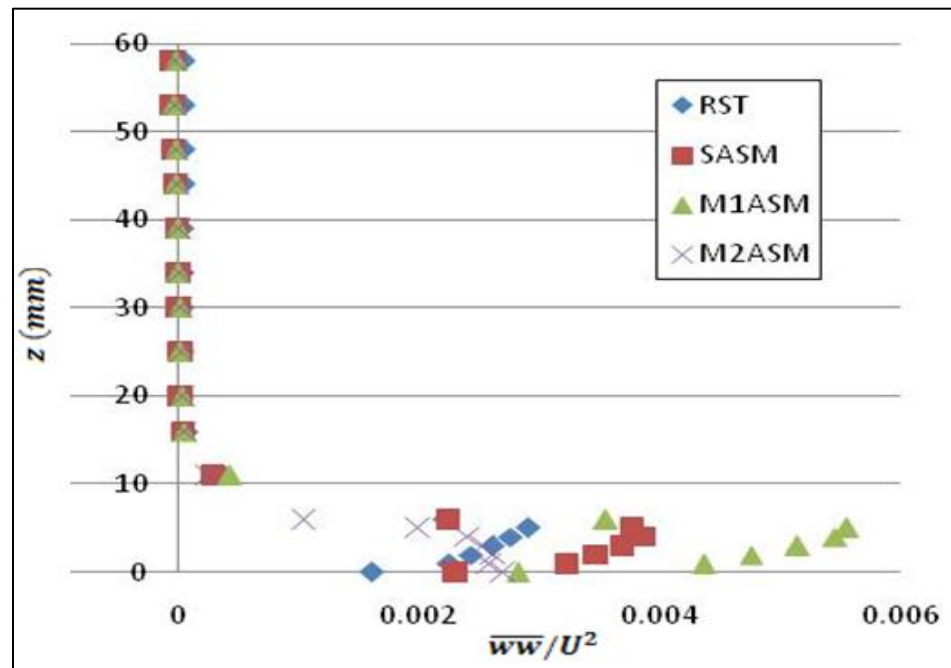


**Figure 8.42** Comparison of Reynolds stress  $\overline{w}w$  computed using various ASM models with RST model for line 3.

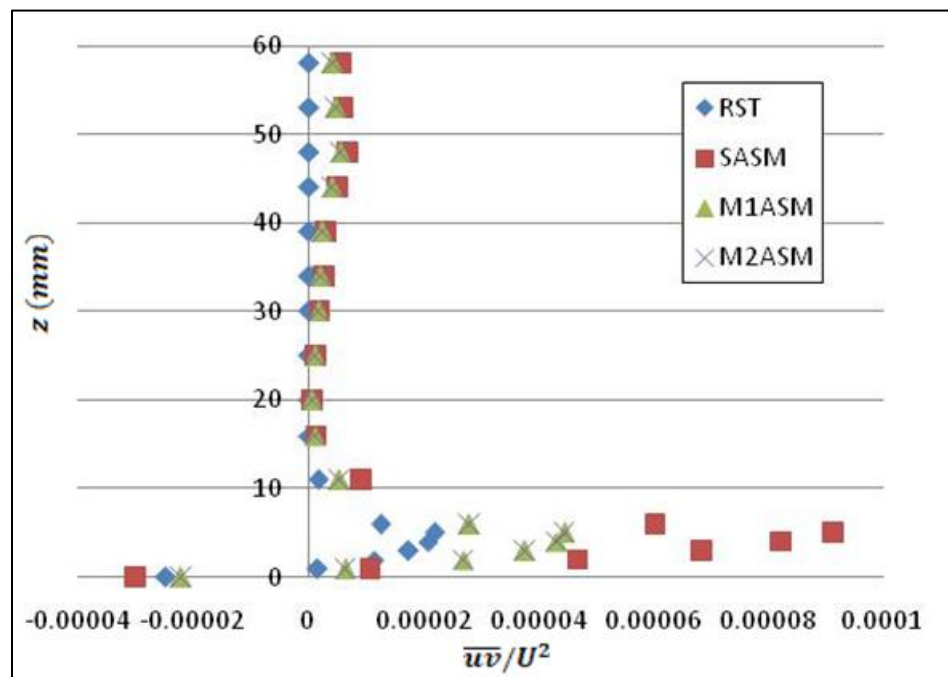


**Figure 8.43** Comparison of Reynolds stress  $\overline{u}v$  computed using various ASM models with RST model for line 3.

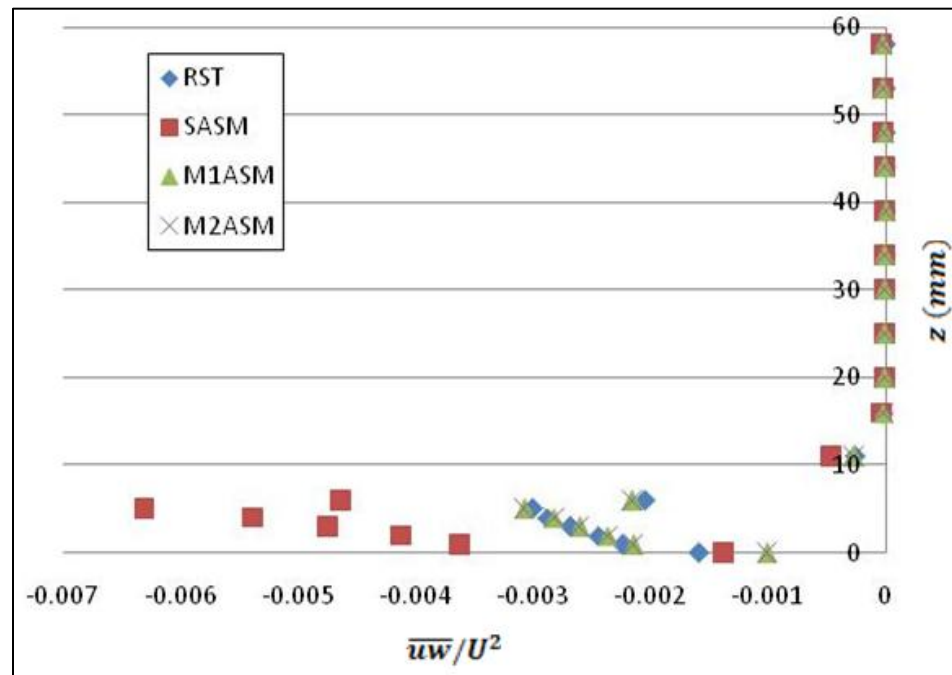


**Figure 8.44** Comparison of Reynolds stress  $\overline{uw}$  computed using various ASM models with RST model for line 3.

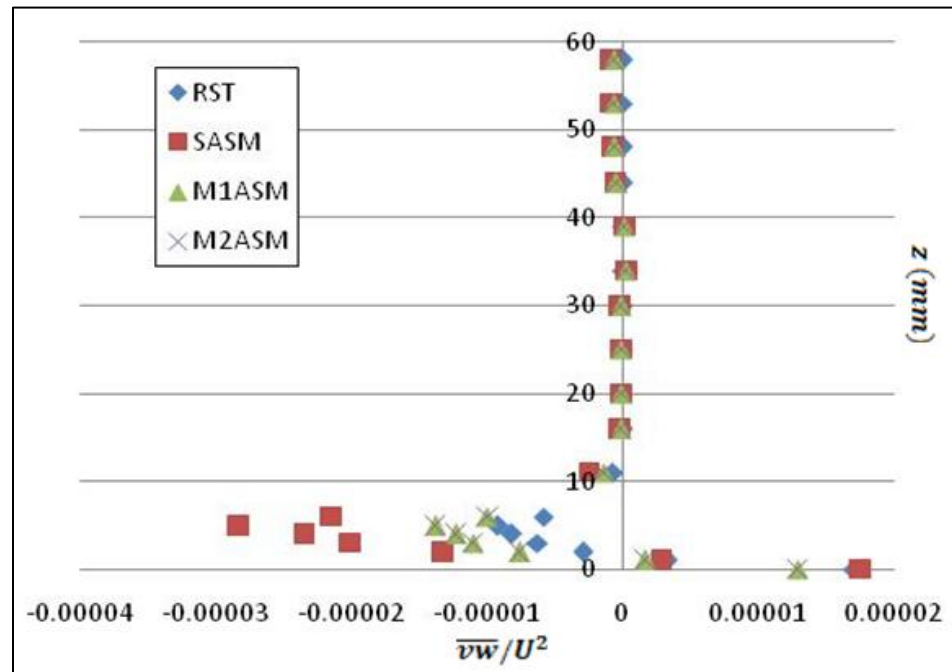


**Figure 8.45** Comparison of Reynolds stress  $\overline{vw}$  computed using various ASM models with RST model for line 3.

From Figs. 8.40 and 8.41, it can be observed that for the location represented by line 3 which is essentially a region of simple boundary layer flow, the Reynolds stresses  $\overline{uu}$  and  $\overline{vv}$  obtained using ASM model M1ASM show good agreement with the stresses from the RST model. The SASM model over-predicts the  $\overline{uu}$  stresses and under-predicts the  $\overline{vv}$  stresses whereas, the M2ASM model under-predicts both  $\overline{uu}$  and  $\overline{vv}$  stresses. For distance more than 10 mm away from the wall, all the ASM models give good agreement with the RST model.

Figure 8.42 show the comparison of the  $\overline{ww}$  stresses which act normal to the wall which represents the blocking effect of the wall. All the ASM models agree well with the RST model for distance above 10 mm from the wall. For near-wall regions, the M2ASM and SASM model give better prediction of the  $\overline{ww}$  stress than M1ASM model.

The Reynolds shear stress  $\overline{uv}$  distribution along line 3 is shown in Fig. 8.43 for different models. It can be noticed from the figure that both M1ASM and M2ASM model stresses are closer to the RST stresses where as the SASM model over-predicts these stresses. Same is observed for the near-wall  $\overline{uw}$  stresses as can be seen in Fig. 8.44. The  $\overline{uw}$  stresses from both M1ASM and M2ASM are in very good agreement with the RST stresses while SASM model over-predicts these stresses.

Again for the  $\overline{vw}$  stresses in the near-wall region, M1ASM and M2ASM models performs better than the SASM model giving stresses that are in good agreement with the stresses from the RST model (refer Fig. 8.45). Thus in general for location marked by line 3 away from the Ahmed body, the M1ASM and M2ASM model performed better than the SASM model and predicted stresses which showed good agreement with the stresses from the RST model.

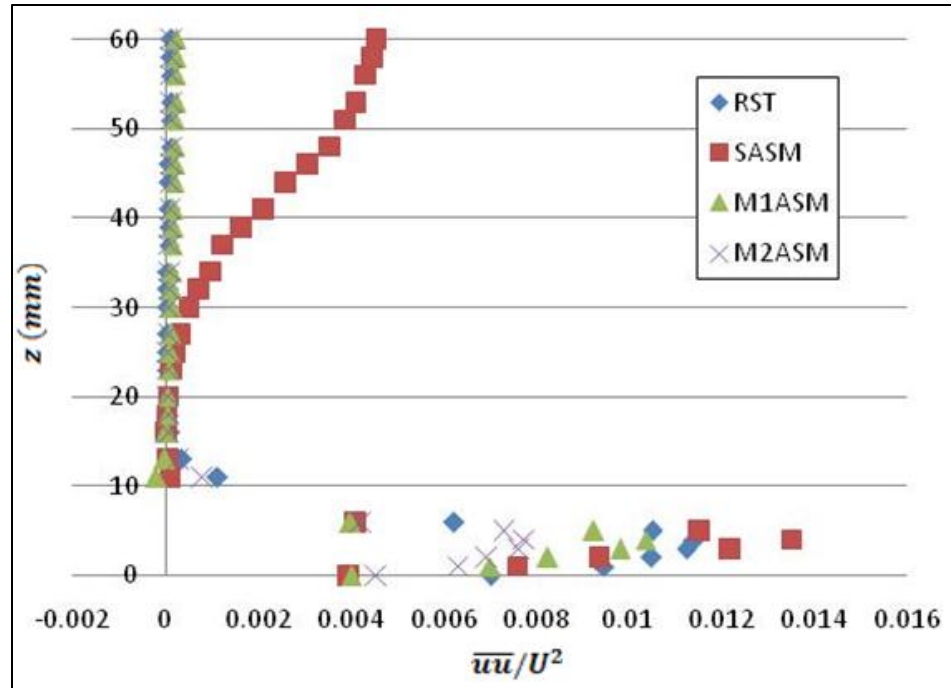


**Figure 8.46** Comparison of Reynolds stress  $\overline{uu}$  computed using various ASM models with RST model for line 5.

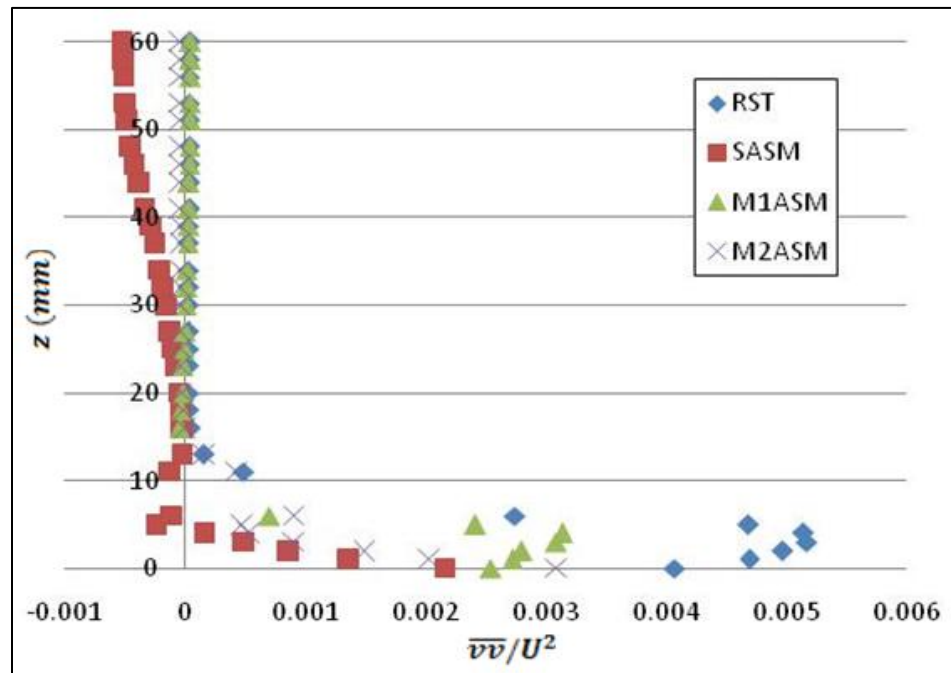


**Figure 8.47** Comparison of Reynolds stress  $\overline{vv}$  computed using various ASM models with RST model for line 5.

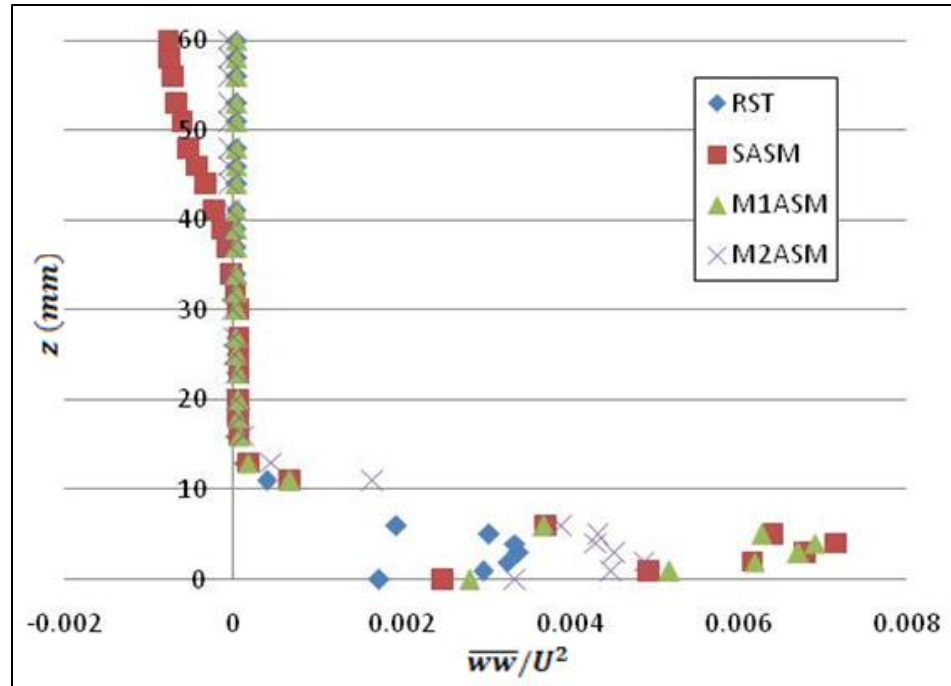


**Figure 8.48** Comparison of Reynolds stress  $\overline{w'w'}$  computed using various ASM models with RST model for line 5.

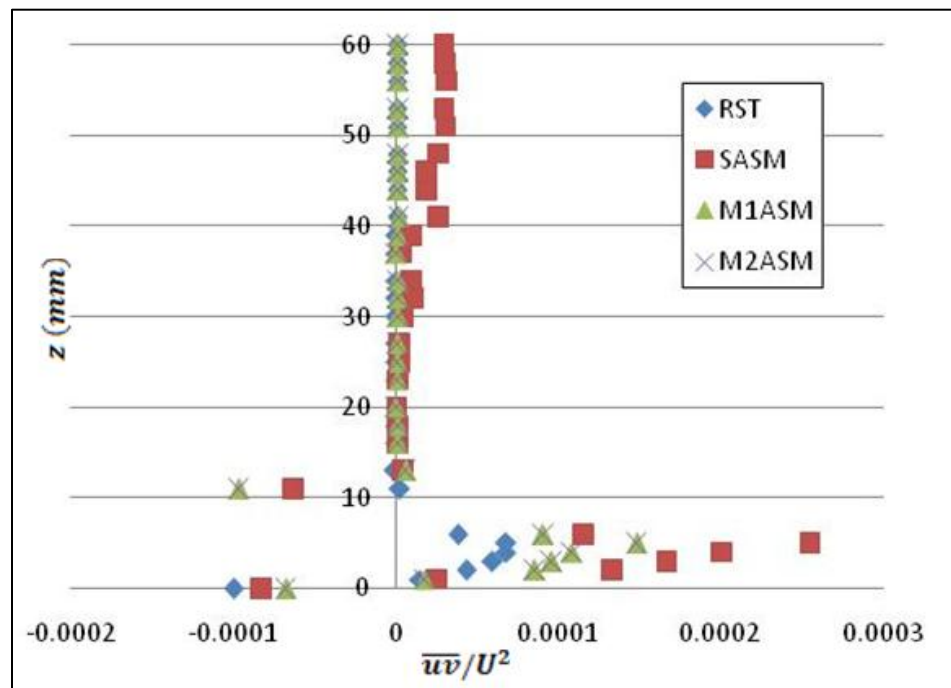


**Figure 8.49** Comparison of Reynolds stress  $\overline{u'v'}$  computed using various ASM models with RST model for line 5.

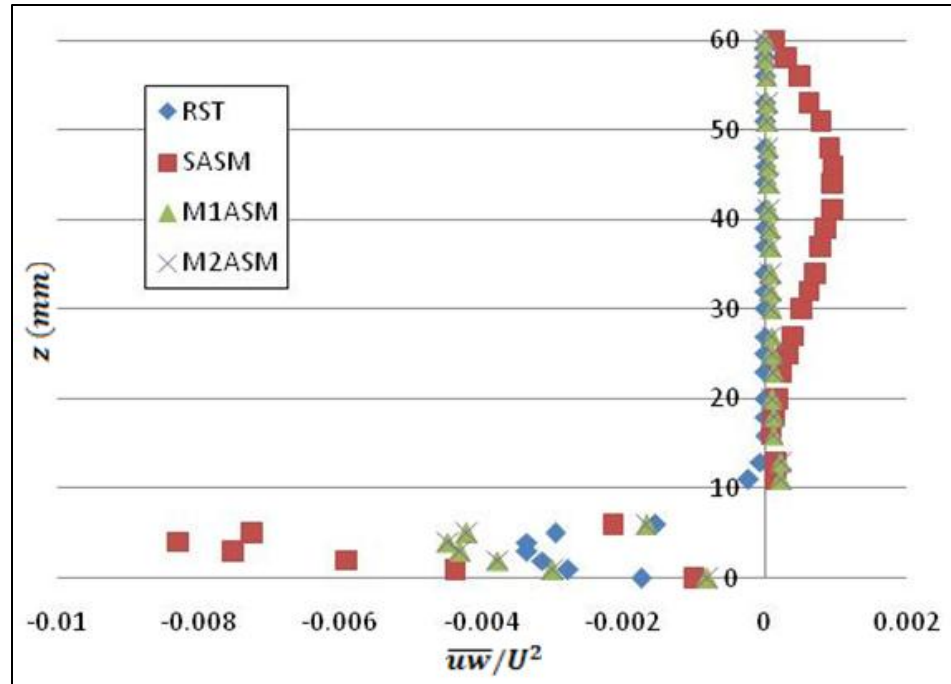


**Figure 8.50** Comparison of Reynolds stress  $\overline{uw}$  computed using various ASM models with RST model for line 5.

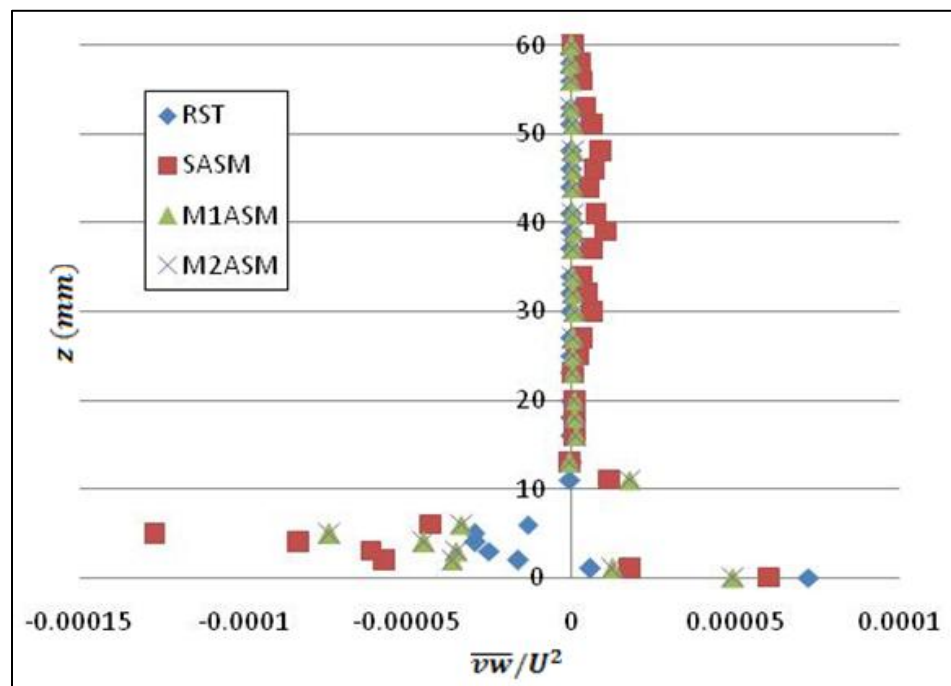


**Figure 8.51** Comparison of Reynolds stress  $\overline{vw}$  computed using various ASM models with RST model for line 5.



The validation of the ASM models in region right in front of the Ahmed body is quite crucial because of the fact that the presence of an obstruction disturbs the oncoming flow. After a successful validation of the ASM model for the simple boundary layer region at location marked by line 3, the testing of the ASM model in obstructed flow region is the next important step towards validating the model.

From Figs. 8.46 and 8.47 it can be observed that the Reynolds stresses  $\overline{uu}$  and  $\overline{vv}$  obtained using ASM model M1ASM show best agreement with the stresses from the RST model as compared to SASM and M2ASM. The SASM model over-predicts the  $\overline{uu}$  stresses and under-predicts the  $\overline{vv}$  stresses whereas, the M2ASM model under-predicts both  $\overline{uu}$  and  $\overline{vv}$  stresses. For distance more than 20 mm away from the wall, the SASM model performs poorly while the M1ASM and M2ASM model stresses are in excellent agreement with the  $\overline{uu}$  and  $\overline{vv}$  stresses from the RST model.

For  $\overline{ww}$  stresses (refer Fig. 8.48) which is normal to the wall the M2ASM model stresses are in better agreement with the RST model stresses than the SASM and M1ASM models, which over-predict the stresses for regions within 10 mm distance from the wall. Here again for distance more than 30 mm from the wall the SASM model performs poorly where as the stresses from M1ASM and M2ASM are still in good agreement with the RST stresses.

For Reynolds shear stresses  $\overline{uv}$ ,  $\overline{uw}$  and  $\overline{vw}$ , it can be observed from Figs. 8.49 - 8.51 that the prediction of shear stresses using models M1ASM and M2ASM are in close agreement with the RST model stresses as compared with the stresses from the SASM model which suffers from over-prediction of the shear stresses in all the three cases. Thus, in general the performance of the M1ASM and M2ASM model is found to be

better than the SASM model for region where the flow field is affected by the presence of an obstruction (Ahmed body).

For the comparison of stresses from various ASM models in the wake of the Ahmed body lines 6 and 7 are chosen which captures the flow closest to the Ahmed body back and far from it as well. Figures 8.52 - 8.63 show the variation of stresses obtained using various ASM models and RST models for the wake region.

For the  $\overline{uu}$  stresses right behind the Ahmed body, the predictions using the M2ASM model are the closest to the stresses from the RST model as can be seen in Fig. 8.52. The M1ASM model stresses are in reasonable agreement with the RST model stresses where as the SASM model over-predicts the stresses in regions 20 mm away from the wall.

From Fig. 8.53 it can be observed that the  $\overline{vv}$  stresses are predicted reasonably well using the M1ASM model as compared to M2ASM and SASM models which under-predict these stresses. Similarly, for the  $\overline{ww}$  stresses normal to the wall (refer Fig. 8.54), the agreement between the stresses from M1ASM model and RST model stresses is quite good where as both M2ASM and SASM models under-predict these stresses.

For the Reynolds shear stresses  $\overline{uv}$ ,  $\overline{uw}$  and  $\overline{vw}$  right behind the Ahmed body (refer Figs. 8.55 - 8.57) the stresses using the M1ASM and M2ASM model are in very good agreement with the RST model stresses where as stresses from the SASM model are over-predicted for region between 10 mm to 20 mm away from the wall. Therefore, in general, the performance of the M1ASM and M2ASM model is found better than the SASM model for region right behind the Ahmed body where recirculation is observed as evident in the streamwise velocity profile for line 6 (refer Fig. 8.35).

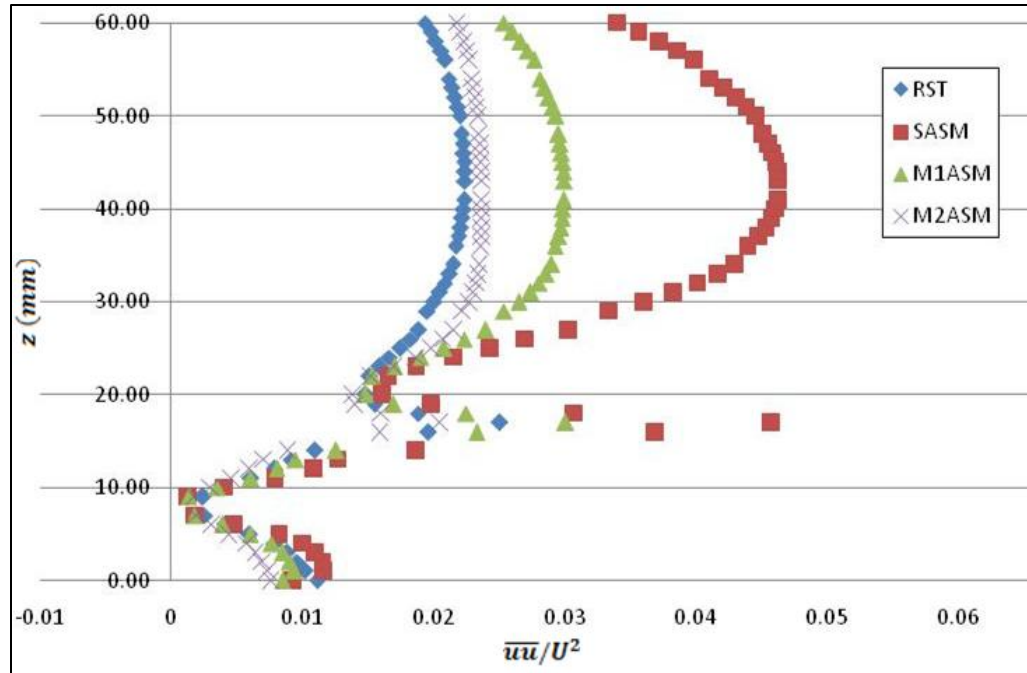


**Figure 8.52** Comparison of Reynolds stress  $\bar{u}u$  computed using various ASM models with RST model for line 6.

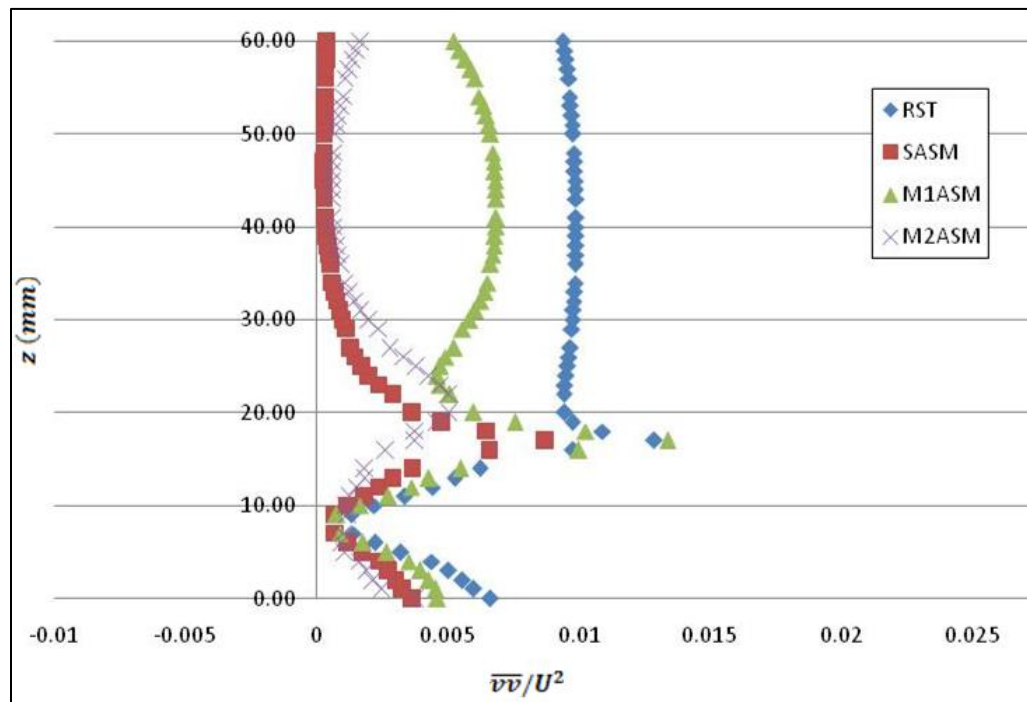


**Figure 8.53** Comparison of Reynolds stress  $\bar{v}v$  computed using various ASM models with RST model for line 6.

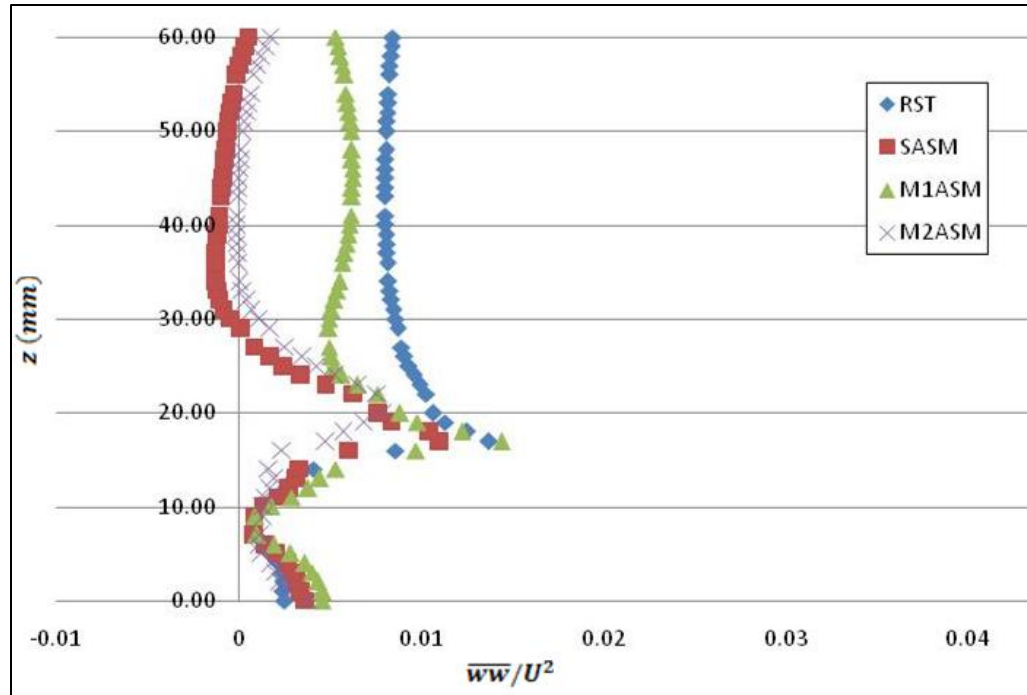


**Figure 8.54** Comparison of Reynolds stress  $\overline{w}w$  computed using various ASM models with RST model for line 6.

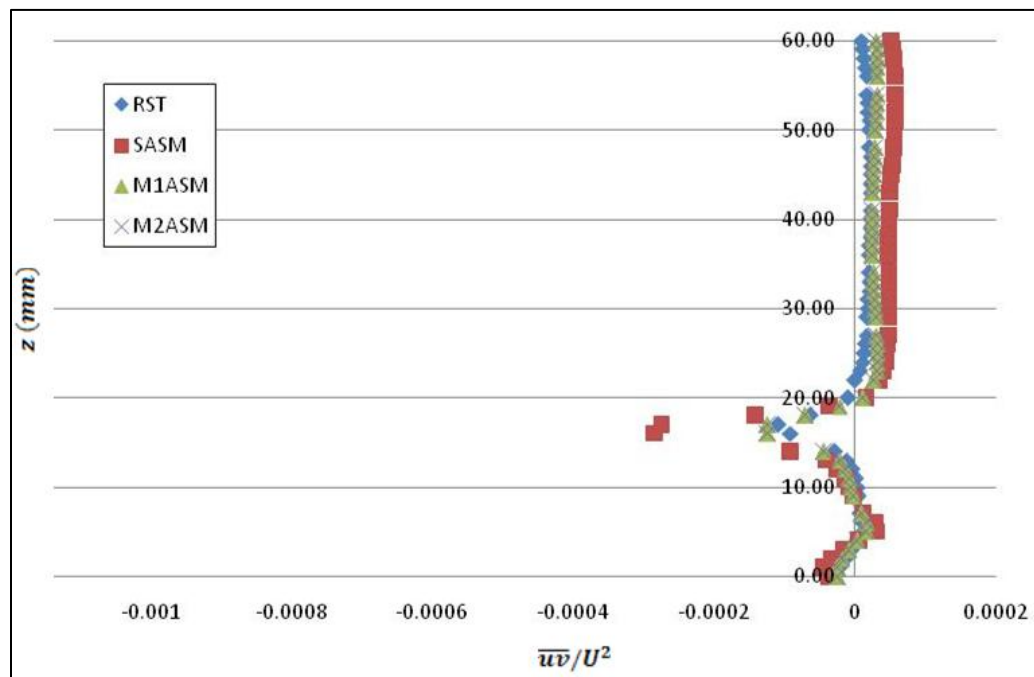


**Figure 8.55** Comparison of Reynolds stress  $\overline{u}v$  computed using various ASM models with RST model for line 6.

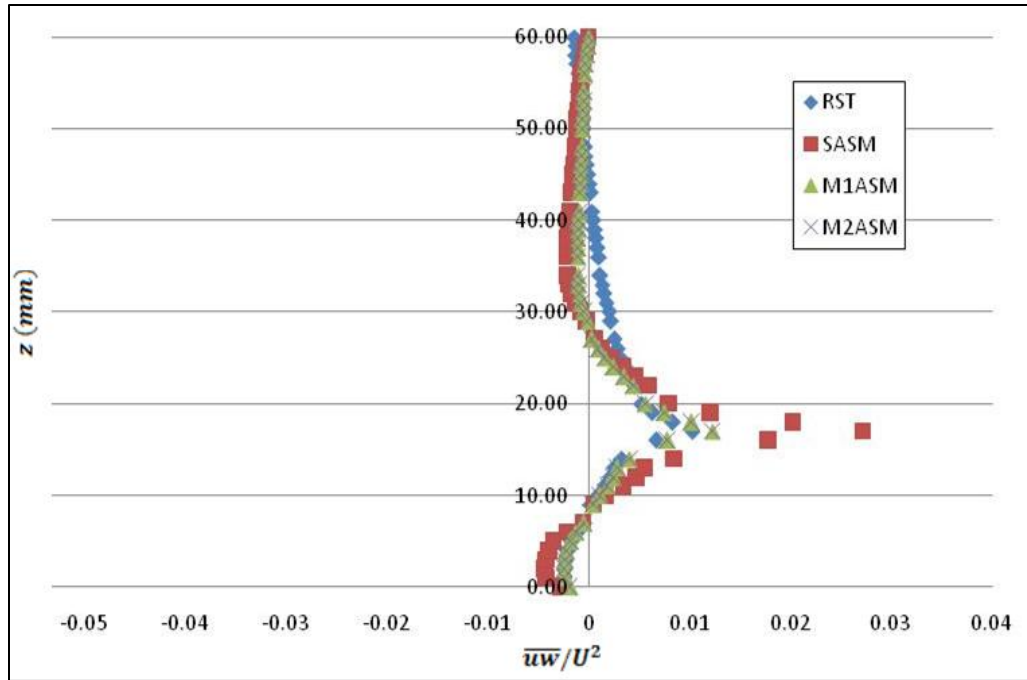


**Figure 8.56** Comparison of Reynolds stress  $\bar{u}\bar{w}$  computed using various ASM models with RST model for line 6.

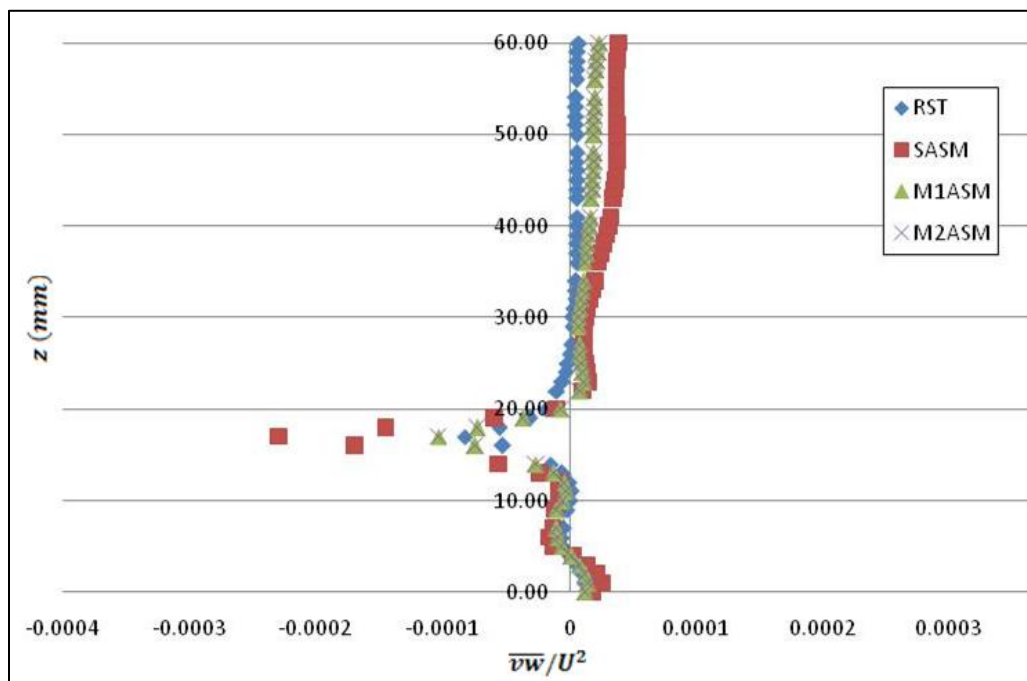


**Figure 8.57** Comparison of Reynolds stress  $\bar{v}\bar{w}$  computed using various ASM models with RST model for line 6.

For stresses along line 7 in the wake region a little farther away from the Ahmed body the comparison of various ASM model is shown in Figs. 8.58 - 8.63. From Fig. 8.58, it can be observed that the  $\overline{uu}$  stresses predicted using M1ASM model is in closest agreement with the RST model stresses as compared to M2ASM and SASM models. The SASM model over-predicts the stresses for regions within 20 mm distance away from the wall where as M2ASM models under-predicts the stresses.

For the  $\overline{vv}$  stresses (refer Fig. 8.59) the only stresses that closely follow the RST model stresses are the one using the M1ASM while the other two models M2ASM and SASM perform poorly with under-predicting the stresses in most of the region. Same goes for the case of  $\overline{ww}$  stresses as well as can be seen in Fig. 8.60.

Figure 8.61 shows the comparison of the Reynolds shear stress  $\overline{uv}$  for various models. It can be noted from the figure that the prediction of stresses using M1ASM and M2ASM are in better agreement with the RST models stresses as compared with the SASM stresses which over-predicts the stresses in most of the region.

From Fig. 8.62 it can be observed that the Reynolds shear stress  $\overline{uw}$  is predicted quite well using the M1ASM and M2ASM model as compared with the SASM model stresses. For the  $\overline{vw}$  stresses from Fig. 8.63 it can be seen that the closest stresses are the one from the M1ASM and M2ASM models for most of the regions. All the models give excellent agreement with the RST model stresses for region within 10 mm away from the wall.

In general, the performance of the M1ASM and M2ASM model is found to be better than the SASM model in the wake region as well giving stresses that are in good agreement with the RST model stresses.

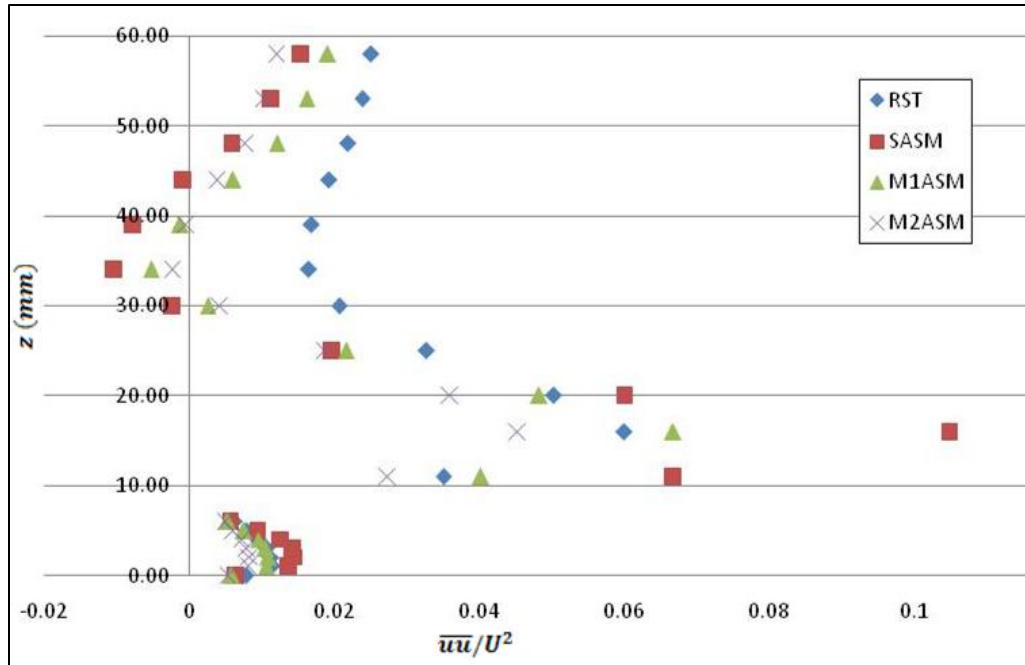


**Figure 8.58** Comparison of Reynolds stress  $\overline{uu}$  computed using various ASM models with RST model for line 7.

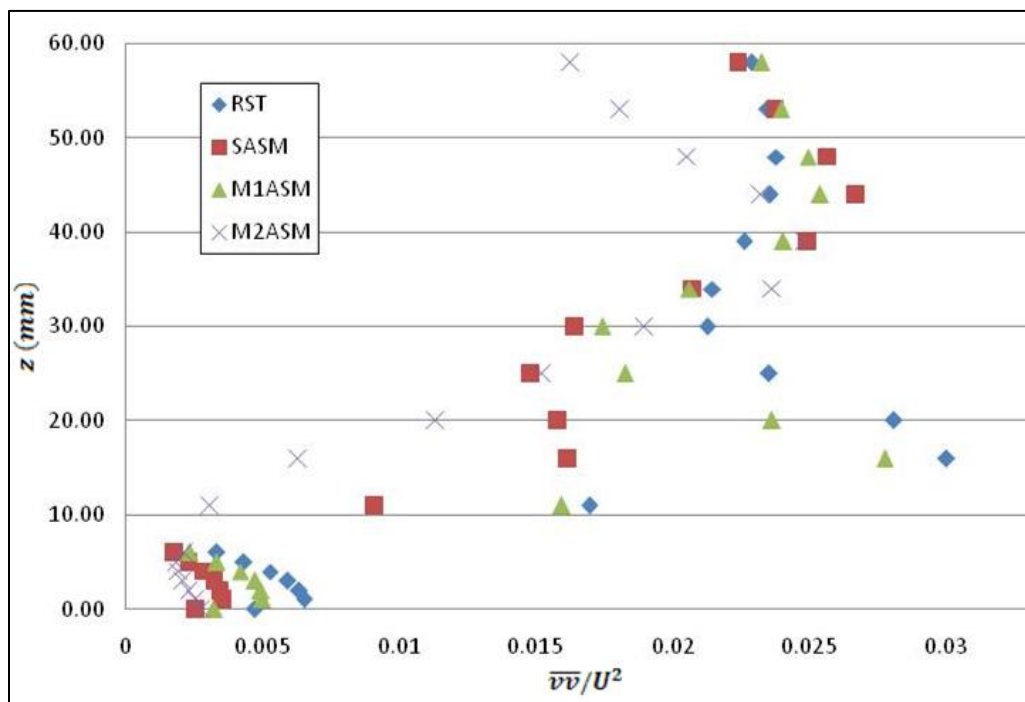


**Figure 8.59** Comparison of Reynolds stress  $\overline{vv}$  computed using various ASM models with RST model for line 7.

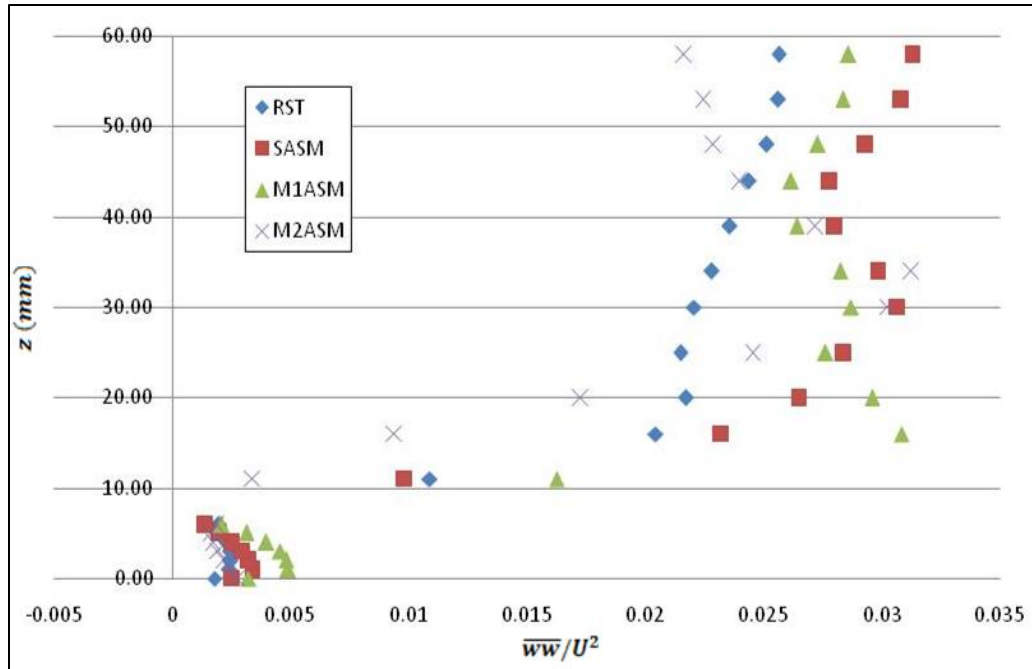


**Figure 8.60** Comparison of Reynolds stress  $\overline{w}w$  computed using various ASM models with RST model for line 7.

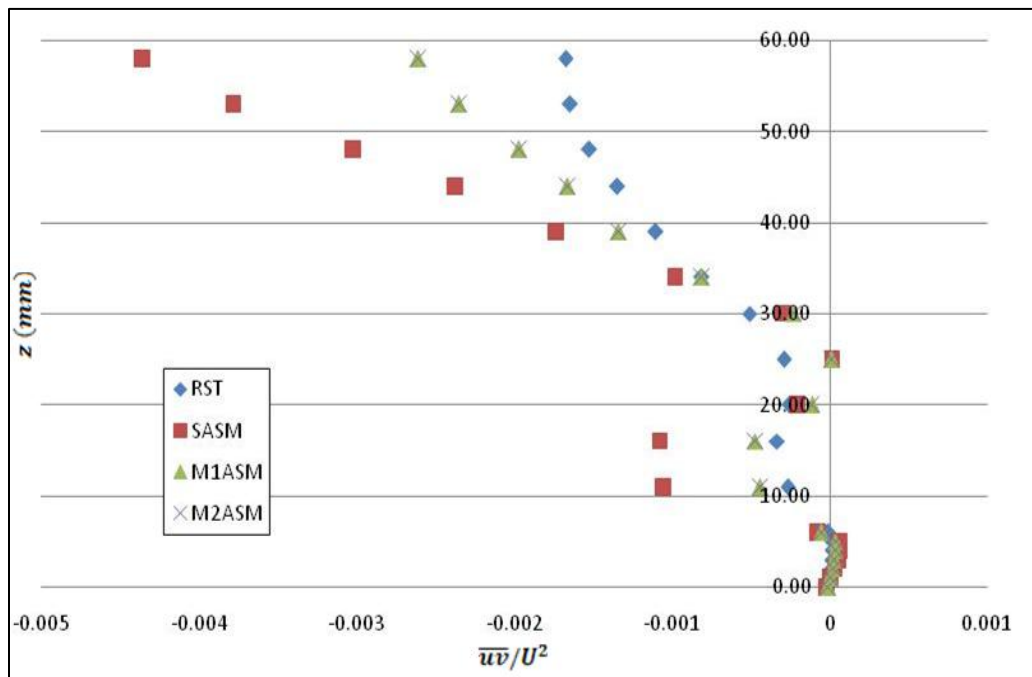


**Figure 8.61** Comparison of Reynolds stress  $\overline{u}v$  computed using various ASM models with RST model for line 7.



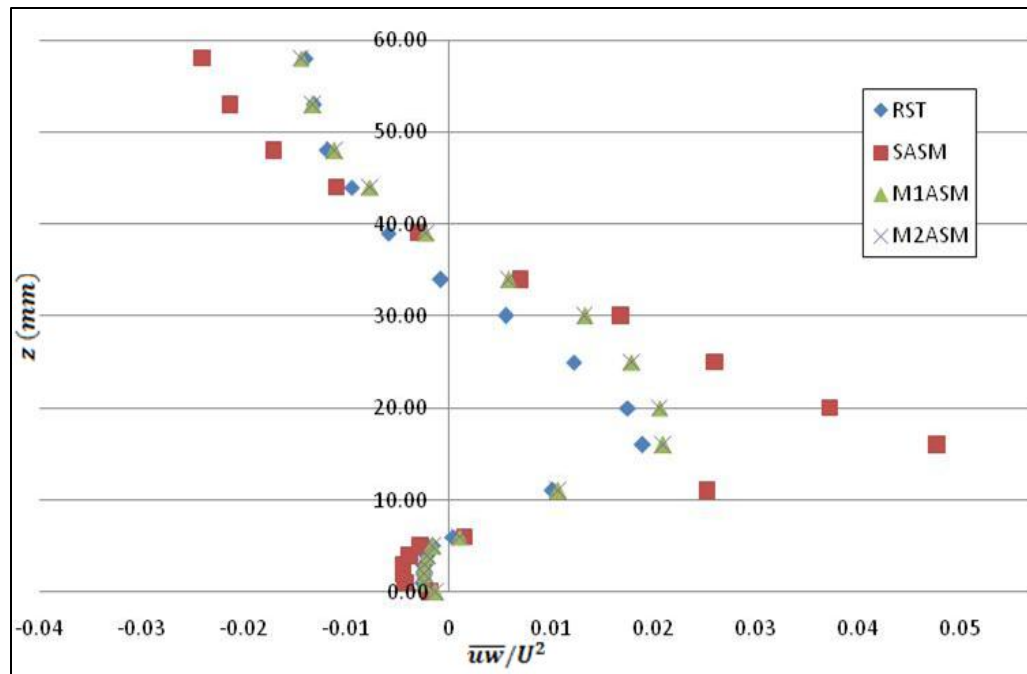


**Figure 8.62** Comparison of Reynolds stress  $\overline{uw}$  computed using various ASM models with RST model for line 7.

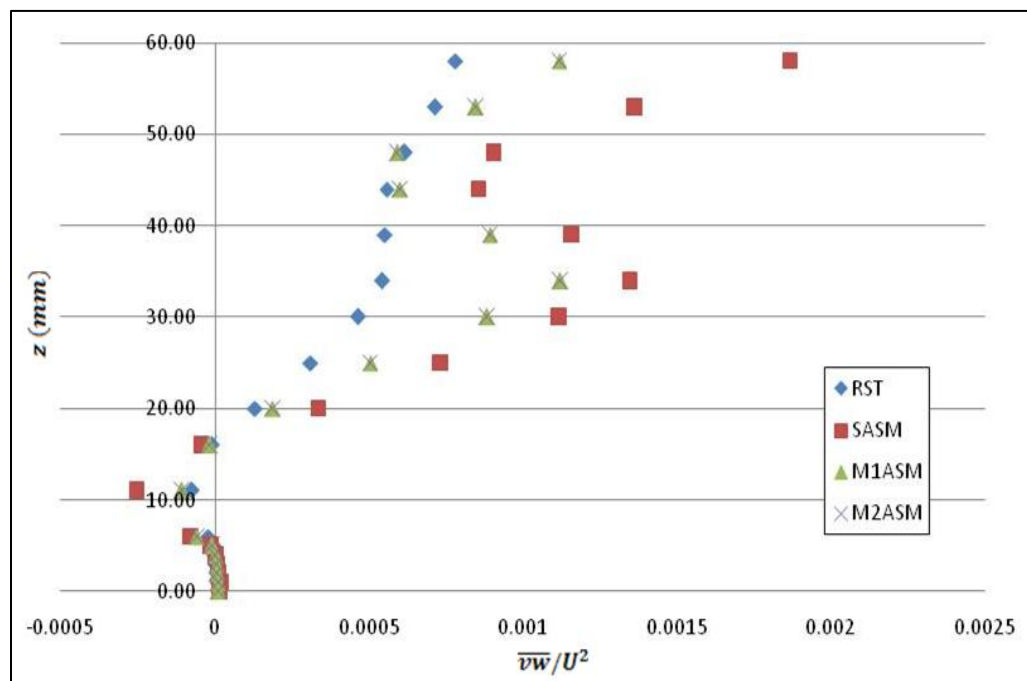


**Figure 8.63** Comparison of Reynolds stress  $\overline{vw}$  computed using various ASM models with RST model for line 7.

From the results and discussion on the stresses obtained using the ASM models for various flow regimes which include boundary layer flow (line 3), flow near an obstruction (line 5), flow right behind the Ahmed body where recirculation occurs (line 6) and flow farther in the wake of the Ahmed body (line 6), a good and diversified validation of the ASM was achieved. In general, both M1ASM and M2ASM models were found to perform better than the SASM model for all the above mentioned flow regimes, giving stresses that were in good agreement with the stresses from the RST model. The most probable reason for this superior performance of the M1ASM and M2ASM can be attributed to the extra terms considered in these models than the SASM model which neglects the production of turbulent kinetic energy ( $G_k$ ) entirely. For regions close to a wall, recirculation, wake, etc., the turbulence level is relatively high and neglecting the production of turbulent kinetic energy can introduce significant errors in the Reynolds stress determination as can be seen in the comparison of the Reynolds stresses for various ASM models above. The ASM models developed provided Reynolds stresses that vary slightly from the RST model stresses at lesser expense since the process involved solving simple algebraic equations rather than complex partial differential equations of the RST model. Also, the anisotropy present in the flow is taken care of in the ASM model unlike the eddy viscosity models which are based on Boussinesq hypothesis and model the momentum transfer caused by turbulent eddies with an eddy viscosity, which is not a fluid property rather it depends on the state of turbulence in the flow. Therefore, the ASM model approach to determine the Reynolds stresses with good accuracy at a lesser cost is a valuable option that can be adopted for various flow regimes.

### 8.3 Summary

The main focus of this chapter was the validation and verification of the ASM model developed in Chapter 7. Two flow scenarios were used to test the ASM model for its Reynolds stresses predictive quality – a simple two-dimensional flow over a flat plate and a complex three dimensional flow around Ahmed body. To model the turbulent flow over a flat plate of length  $L = 10$  at free stream velocity of  $U_\infty = 10\text{m/s}$ , realizable  $k - \varepsilon$  turbulence model was used. In addition to  $k - \varepsilon$  model,  $RST$  model was also used to get the Reynolds stresses in the near-wall regions since the  $k - \varepsilon$  model is incapable of providing the Reynolds stresses data. These simulations were validated with the theoretical solution using the one-seventh power law to obtain the velocity profiles at the mid-length and full length of the plate. These validated simulations provided all the flow properties, turbulent quantities, Reynolds stresses, which were used in the developed ASM model to obtain the modified Reynolds stresses. A hybrid technique which involved the use of data from both  $k - \varepsilon$  model and  $RST$  models was adopted to determine modified Reynolds stresses from the ASM model. Two variations of the ASM model were tested and the modified ASM stresses were compared with the  $RST$  model stresses. In general, a very good agreement was observed for the M1ASM and M2ASM models with the  $RST$  model stresses as compared to the SASM model, thus proving the superiority of M1ASM and M2ASM models over the SASM model. The most likely reason for this advantage of the developed model over SASM was the consideration of the production of turbulent kinetic energy ( $G_k$ ) term which was neglected in the SASM model. This term plays a very crucial role in regions of high turbulence and affects the

Reynolds stress distribution significantly, thus neglecting this term leads to error in the Reynolds stress determination using ASM models.

This validation is followed with a more rigorous testing of the developed ASM model. A three dimensional complex flow around Ahmed body is numerically simulated and verified with the available experimental data. Performance of various turbulence models ( $k - \varepsilon$  and  $k - \omega - SST$  and  $LES$ ) is compared with the experimental velocity data. From the velocity profiles, it was inferred that the  $LES$  model performed the best giving velocity profiles that were within 7% error as well for the forced coefficient the error was approximately 4% which is lower than the other models tested. Details of the computational set-up and numerical method used are presented for a full-scale Ahmed body. Later the same CFD methodology is implemented on a small-scale Ahmed body which was tested in the Wind Tunnel Facility at the University of Wisconsin - Milwaukee.

A complete description of the Wind Tunnel Facility used for the experiments and the test-section where the scaled-down Ahmed body is mounted for measurements is also presented. The hot-wire anemometry is dealt in detail in the chapter. The specifications of the miniature X-probe used, the hot-wire calibration equipment and procedure is outlined. A thorough representation of the data conversion from acquired voltages to velocity components ( $U$  and  $V$ ) with all the relevant equations involved is also presented. For the time-averaged analysis involved in the flow measurements, a sampling rate of 2000 and number of samples 20000 was used which gives the sampling time as 10 s. A detailed error analysis for the hot-wire measurements performed estimated error of at most  $\Delta u = \pm 0.00041 \text{ m/s}$  and  $\Delta v = \pm 0.00044 \text{ m/s}$  for the

velocity components  $U$  and  $V$  respectively. Other sources of errors included temperature, pressure variations, composition, etc. which were quite small (1% - 2 %).

The wind tunnel measurements were conducted at a inlet velocity of 12 m/s with turbulence intensity of 0.01%. The Reynolds number based on the Ahmed body scaled down prototype length was  $3.3 \times 10^5$ . The hot-wire measurements were performed at the mid-plane ( $y = 0$ ) along 8 vertical lines capturing the flow in front and behind the Ahmed body. This experimental data was then used to validate the *LES* and *RST* simulations performed on the scaled-down model. In general, a good agreement was observed for the streamwise velocity profiles obtained from experiment and simulations except in the recirculation zone behind the Ahmed body. This discrepancy in the velocity profiles in the wake of the Ahmed body was due to the limited capability of the hot-wire to measure recirculation and resolve flow direction. Other factor which resulted in erroneous measurements in the wake region was the potential interference between the thermal wake of the two sensors which alters the voltages recorded for the two probes resulting in incorrect velocities.

Next, the validated *RST* simulations were used to collect all the user inputs required for the ASM model. The modified stresses determined using the M1ASM and M2ASM models were then compared with the *RST* model stresses and SASM stresses. These comparison were made in the regions such that a variety of flow regimes is covered like boundary layer region, region in front of an obstruction, zone right behind the Ahmed body and farther in the wake region. The validation of the ASM models in all these flow regimes provided extensive data to evaluate the performance of the ASM model under different flow conditions. In general, both M1ASM and M2ASM models

were found to perform better than the SASM model for all the above mentioned flow regimes, giving stresses that were in good agreement with the stresses from the RST model. The most probable reason for this superior performance of the M1ASM and M2ASM can be attributed to the extra terms considered in these models than the SASM model which neglects the production of turbulent kinetic energy ( $G_k$ ) entirely.

The ASM models developed provided Reynolds stresses that vary slightly from the RST model stresses at lesser expense since the process involved solving simple algebraic equations rather than complex partial differential equations of the RST model. Additionally, it is shown that the ASM model can predict unequal normal stresses and leads to anisotropic eddy viscosity. Thus, the anisotropy present in the flow is taken care of in the ASM model unlike the eddy viscosity models which assumes isotropic eddy viscosity to model the turbulence flow. Furthermore, the ASM model captured the wall blockage effect (which damps the velocity fluctuations normal to the solid surface) without the use of distance from the wall or scaling with the local friction velocity that can vanish in separation or reattachment points, thus it can be applied to complex geometries. Therefore, the ASM model approach to determine the Reynolds stresses at lower cost can be sought for a variety of flow regimes as demonstrated in the chapter. In addition to the ASM model adopted for Reynolds stresses in the near-wall regions, the *LES* model can be used for regions away from the wall for its better predictive quality of the flow away from the wall. Thus, a hybrid approach combining two or more turbulence models can be adopted for a more detailed insight in to the flow structures and turbulent quantities.

## **Chapter 9 - Conclusions and Future Research**

This work provides a variety of mixing flow results in the dilution zone of a combustor simulator for non-reacting flows. Furthermore, an Algebraic Stress Model approach is devised for better understanding of the flow structures. The main conclusions of the study can be summarized as in Sec. 9.1 followed by some future recommendations for research in Sec. 9.2.

### **9.1 Conclusions**

It has been the primary endeavor of this dissertation to develop and test novel passive control techniques which enhance mixing between primary and dilution streams and give better temperature uniformity at the combustor exit with minimum pressure loss. More uniform temperature flow leads to lesser damage to turbine blades, reducing its maintenance cost and extending its life-span. Thus, making the complete gas turbine system more cost efficient. These techniques are chiefly motivated from the observation that the quality of mixing of two streams is sensitive to the entrance of the dilution jets as well as their penetration into the primary stream. A combustor simulator is designed to perform experiments to test the effectiveness of the techniques developed to enhance mixing in order to produce more uniform temperature flow field. Both two and three dimensional computational fluid dynamic (CFD) analysis is taken up to narrow down the design decisions for the combustor simulator and perform parametric studies for in-depth exploration of the mixing process. Various parameters are defined to judge the

temperature uniformity of the flow such as mixture fraction, pattern factor, mixture uniformity, etc.

The two dimensional CFD analysis proved that the introduction of the dilution cooling air through larger dilution holes results in better mixing and temperature uniformity with lower pressure loss as compared to the case of introduction of air at the same flow rate having the same total surface area, but from smaller dilution holes. Further, based on the three dimensional CFD analysis performed on in-line and staggered dilution holes geometry as well as on its variant with the streamlined body inside the test-section, it was observed that the staggered dilution holes resulted in better mixing as compared to the in-line counter parts. Additionally, the use of a streamlined body inside the test section with the staggered dilution holes improved the mixing of the primary and dilution (or secondary) air by pushing the primary air towards the cooler dilution jets, which resulted in more uniform exit temperature flow field. Almost 91% of the equilibrium mixture fraction value was achieved for the case of staggered dilution holes with streamlined body.

The effect of jet-to-mainstream momentum flux ratio on the exit temperature uniformity was investigated with the help of numerical simulations. To realize this study, CFD analysis was performed for the basic staggered dilution holes geometry and validated with the experimental data obtained by running tests on the combustor simulator. The validated CFD model was then used to generate various cases with different flux ratio and simulations were performed. Comparison of the velocity vectors for different flux ratios demonstrated that the dilution jets penetrated deeper into the flow at higher flux ratio causing enhanced mixing and improved temperature uniformity.



Nearly 85% of the equilibrium mixture fraction was achieved at the flux ratio of 0.85. Also, it was observed that further increasing the flux ratio did not give any improvement in the temperature uniformity rather resulted in increased pressure loss. The exergy analysis showed that there is an exponential increase in the exergy loss with the increase in the flux ratio. Thus, there is an optimum flux ratio associated with particular flow conditions at which any combustor should be run. To locate the regions of high temperature gradients within the mixing zone which may result in cold regions, a new parameter 'Cooling Rate Number (CRN)' was defined. A higher cooling rate number was observed at the vicinity of the dilution holes indicating higher temperature gradients in these regions and possible sites for the gas composition becoming frozen resulting in more unburned CO in the exhaust. Special attention should be given to the design of these regions to avoid the rapid change in temperature gradients and the potential discharge of unburned CO in the exhaust associated with rapid cooling.

Extensive experimentation was conducted to compare the proposed dilution techniques – staggered dilution holes, staggered dilution holes with streamlined body and staggered dilution holes with guide vanes at various orientations ( $0^\circ$ ,  $30^\circ$ ,  $60^\circ$  and  $90^\circ$ ). These guide vanes orientations were tested to evaluate the effect of varying the injection angle of the dilution jets on the temperature uniformity. These experiments were performed at three Reynolds Numbers – 100000, 80000 and 30000. Another weighted parameter was defined called 'uniformity factor ( $\chi'$ )' to compare how close the mixture fraction is to the equilibrium value. On the basis of the variation of the uniformity factor for various techniques tested at different Reynolds Numbers, it was found that the mixing improved at the lower Reynolds Number in general. A plausible reason could be the more

residence time available inside the dilution zone due to lower flow rate conditions, which provided sufficient time for the mixing of the primary hot air and the cooler dilution air, thus, resulting in a better mixed flow and more uniform temperature profile at the combustor exit. For the majority of the flow conditions tested, the 30° guide vanes gave the most uniform temperature flow with just about 1% higher pressure loss as compared to the staggered dilution holes geometry. The average uniformity factor for 30° guide vanes  $\chi_{avg} = 0.22$ , which was found to be about 15% more uniform than the staggered holes ( $\chi_{avg} = 0.26$ ). The fact that the use of 30° guide vanes can provide the turbine blade with 15% more uniform temperature flow than the staggered dilution holes design with merely 1% more pressure drop, has a very important implementation in order to reduce the damage of the turbine blades due to non-uniform temperature flow and extend its life-span. This would result in an overall reduction in the maintenance cost of the gas turbine systems which is quite significant. Furthermore, it was found that the introduction of the streamlined body not only improved the mixing in some cases but also helped decrease the pressure drop from inlet to exit of the experimental set-up. This is expected to increase the overall system efficiency and decrease the operating cost of a gas turbine system.

The other significant part of this dissertation comprised of development of an Algebraic Stress Model (ASM) in order to estimate the turbulence via Reynolds stresses prediction. There exists class of turbulence flow problems which is mainly governed by the Reynolds stresses such as flow separation, recirculation, near-wall region flows, etc. There are various approaches to acquire these stresses - some include modeling while other includes solving independent equations for the six Reynolds stress components or a

combination of both - modeling and solving. The incapability of the eddy viscosity models to accurately predict the turbulent quantities in anisotropic turbulent flows such as flow separation, recirculation or near-wall region flows, restricts the use of these models and calls for a more sophisticated higher-order model which can solve for all the six components of Reynolds stresses.

Although the Direct Numerical Simulation (DNS) and Large Eddy Simulation (LES) are capable of giving closer insight to the turbulence structures in a fluid flow, their use is still restricted to primarily simpler problems due to the high computational resource, time and grid resolution requirements. Thus, the focus is brought back to the Reynolds Stress Model (RSM) which resolves all the components of the Reynolds stress tensor at lesser resource requirements than the DNS and LES. To further reduce the task of solving the complex transport equations for Reynolds stresses, algebraic approach is adopted. The Reynolds stress transport equation is converted into simpler algebraic form by a combination of solving and/or modeling the contributor to the Reynolds stress transport process which include - generation of stresses, dissipation of stresses due to molecular viscous action, pressure-strain interaction and lastly, diffusion of stresses due to velocity fluctuations, pressure fluctuations and molecular transport.

The ASM model developed is validated for a simple two-dimensional turbulent flow over a flat plate and a complex three dimensional flow around Ahmed body. Various flow regimes covered for validation included - boundary layer flow, flow in front of an obstruction, flow behind the Ahmed body in the recirculation zone, wake region of the Ahmed body. The developed model provided Reynolds stresses that vary slightly from the RST model stresses for all the above mentioned flow regimes at lesser expense

since the ASM model involved solving simple algebraic equations unlike complex partial differential equations of the RST model. The model is capable of predicting Reynolds stresses for a variety of flow regimes. The model can predict unequal normal stresses and thus, takes care of the anisotropy present in the flow in contrast to the eddy viscosity models which are based on Boussinesq hypothesis and assume isotropic eddy viscosity. Additionally, the ASM model captured the wall blockage effect without using the distance from the wall or scaling with the local friction velocity that can vanish in separation or reattachment points, thus making it suitable for use on complex geometries. Adopting a hybrid approach which combines the advantages of the ASM model with other turbulence models can be sought after for a more in-depth analysis of the flow structures and turbulent quantities both near-wall and away from the boundary for any fluid flow problem. The accurate prediction of the turbulent quantities plays a significant role in not just the fluid motion/transfer phenomenon rather it governs the heat exchange process as well especially in regions close to the wall.

## 9.2 Recommendations

The improved temperature uniformity observed with the use of streamlined body and guide vanes clearly indicates prospective use of these novel techniques in practical applications. Implementation of these techniques in real combustors, optimization of the design parameters and more experimentation with a combination of various guide vane angles and streamlined body, forms another potential area of research.

Optimization of the ASM model constants  $C_{\phi 1}$  and  $C_{\phi 2}$  according to the fluid flow problem can be attempted in future to further improve the predictive quality of the ASM

model. The inversion of the implicit ASM model developed to an explicit form is suggested further for future work.

## References

- [1] Ahmed, M. R., & Sharma, S. D. (2006). Turbulent Mixing Enhancement with a 20 Degree Chute Mixer. *Experimental Thermal and Fluid Science* , 161-174.
- [2] Ahmed, M. R., Sharma, S. D., & Kohama, Y. (2000). Experimental Investigation on Turbulent Mixing Enhancement in Confined, Co-axial Jets Using Chute Mixer Configuration. *JSME International Journal Series B* , 414-426.
- [3] Ahmed, S. R., Ramm, G., & Faltin, G. (1984). Some Salient Features of the Time-Averaged Ground Vehicle Wake. *International Congress & Exposition*. Detroit.
- [4] Andreopoulos, J. (1983). Heat Transfer Measurements in a Heated Jet-pipe Flow issuing into a Cold Cross Stream. *Physics of Fluid* , 3201-3210.
- [5] Andreopoulos, J., & Rodi, W. (1984). Experimental Investigation of Jets in a Crossflow. *Journal of Fluid Mechanics* , 93-127.
- [6] Barringer, M. D., Richard, O. T., Walter, J. P., Stitzel, S. M., & Thole, K. A. (2002). Flow Field Simulations of a Gas Turbine Combustor. *Journal of Turbomachinery* , 508-516.
- [7] Boyce, M. P. (2006). *Gas turbine Engineering Handbook* (3rd ed.). Boston: Gulf Professional Publishing.
- [8] Bradshaw, P., & Pankhurst, R. C. (1964). The Design of Low-Speed Wind Tunnels. *Progress in Aerospace Sciences* , 1-69.
- [9] Channwala, S. A., & Kulshreshtha, D. (2010). Numerical Simulation Approach as Design Optimization for Micro Combustion Chamber. *Tenth International Congree of Fluid Dynamics*, (pp. 1-31). Ain Soukhna.
- [10] Chen, C.-J., & Jaw, S.-Y. (1998). *Fundamentals of Turbulence Modeling*. Washington, DC: Taylor & Francis.
- [11] Chen, Y., Aung, K., Glezer, A., & Jagoda, J. (1999). Enhanced Mixing in a simulated Combustor Using Synthetic Jet Actuators. *37th AIAA Aerospace Sciences Meeting and Exhibit*. Reno.
- [12] Crocker, D. S., & Smith, C. E. (1995). Numerical Investigation of Enhanced Dilution Zone Mixing in a Reverse Flow Gas Turbine Combustor. *Journal of Engineering for Gas Turbines and Power* , 272-281.

- [13] Daly, B. J., & Harlow, F. H. (1970). Transport Equations of Turbulence. *Physics of Fluids* , 2634-2649.
- [14] Doerr, T., Blomeyer, M., & Hennecke, D. K. (1997). Optimization of Multiple Jets Mixing with a Confined Crossflow. *Journal of Engineering for Gas Turbines and Power* , 119 (2), 315-321.
- [15] El-Behery, S. M., & Hamed, M. H. (2009). A Comparative Study of Turbulence Models Performance for Turbulent Flow in a Planar Asymmetric Diffuser. *World Academy of Science: Engineering & Technology* , 769-780.
- [16] Gobbato, P., Lazzaretto, A., & Masi, M. (2012). Improvement of the Outlet Temperature Distribution of a Dual-Fuel Gas Turbine Combustor by a Simplified CFD Model. *ASME Turbo Expo*. Copenhagen.
- [17] Greiner, C. M. (1990). *Unsteady Hot-Wire and Hot-Film Wake Measurements of Automobile-Like Bluff Bodies*. Cambridge: Massachusetts Institute of Technology.
- [18] Gulati, A., Tolpadi, A., & VanDeusen, G. (1995). Effect of Dilution Air on the Scalar Flowfield at Combustor Sector Exit. *Journal of Propulsion and Power* , 1162-1169.
- [19] Gupta, A., Ibrahim, M. S., & Amano, R. S. (2012). Computational Analysis of Mixing in a Gas Turbine Combustor. *Proceedings of the ASME IMECE Conference*. Houston.
- [20] Gupta, A., Ibrahim, M. S., & Amano, R. S. (2013). Numerical and Experimental Study of the Effect of Momentum-flux Ratio on Temperature Uniformity at the Combustor Exit. *49th AIAA/ASME/SAE/ASEE Joint Propulsion Conference & Exhibit and 11th International Energy Conversion Engineering Conference*. San Jose.
- [21] Hanjalic, K. (2005). Turbulence and Transport Phenomena - Modeling and Simulation. *Lecture Note* .
- [22] Hanjalic, K., & Launder, B. E. (1972). A Reynolds Stress Model of Turbulence and its Application to Thin Shear Flows. *Journal of Fluid Mechanics* , 609-638.
- [23] Hatch, M. S., Sowa, W. A., & Samuelson, G. S. (1995). Geometry and Flow Influences on Jet Mixing in a Cylindrical Duct. *Journal of Propulsion and Power*, 393-402.
- [24] Holdeman, J. D. (1993). Mixing of Multiple Jets with a Confined Subsonic Crossflow. *Progress in Energy and Combustion Science* , 19 (1), 31-70.

- [25] Holdeman, J. D., Walker, R. E., & Kors, D. L. (1973). Mixing of Multiple Dilution Jets with a Hot Primary Airstream for Gas Turbine Combustors. . *AIAA and Society of Engineers Ninth Propulsion Conference*. Las Vegas.
- [26] Ibrahim, M. S., Gupta, A., Rux, A., Lang, M., Moll, T., & Amano, R. S. (2012). Numerical Investigation and Experimental Lab Setting-up for Analysis of Gas Turbine Combustor Dilution Process. *ASME IDETC/CIE Conference*. Chicago.
- [27] Idelchik, I. E. (1994). *Handbook of Hydraulic Resistance* (3rd ed.). CRC Press Inc.
- [28] Iki, N., Gruber, A., & Yoshida, H. (2008). A Numerical and an Experimental Study for Optimization of a Small Annular Combustor. *Journal of Power and Energy Systems* , 2 (3), 921-933.
- [29] Jaafar, M. N., Jusoff, K., Osman, M. S., & Ishak, M. S. (2011). Combustor Aerodynamic Using Radial Swirler. *International Journal of the Physical Sciences* , 6 (13), 3091-3098.
- [30] Jorgensen, F. E. (2002). How to Measure Turbulence with Hot-wire Anemometers - A Practical Guide. DANTEC Dynamics.
- [31] Kotzer, C. E. (2008). *Effects of Combustion Chamber Geometry Upon Exit Temperature Profiles*. Kingston: Royal Military College of Canada.
- [32] Kotzer, C., LaViolette, M., & Allan, W. (2009). Effects of Combustion Chamber Geometry Upon Exit Temperature Profiles. *ASME Turbo Expo*. Orlando.
- [33] Krastev, V., & Bella, G. (2011). On the Steady and Unsteady Turbulence Modeling in Ground Vehicle Aerodynamic Design and Optimization. *10th International Conference on Engines & Vehicles*. Capri.
- [34] Kumar, S. (2012). *Investigation of Heat Transfer and Flow using Ribs within Gas Turbine Blade Cooling Passage: Experimental and Hybrid LES/RANS Modeling*. Milwaukee: University of Wisconsin.
- [35] Langston, L. S., & Opdyke, G. (1997). Introduction to Gas Turbines for Non-Engineers. *Global Gas Turbine Newsletter* , 37 (2).
- [36] Launder, B. E., Reece, G. J., & Rodi, W. (1975). Progress in the Development of a Reynolds-stress Turbulence Closure. *Journal of Fluid Mechanics* , 537-566.
- [37] Lefebvre, A. H., & Ballal, D. R. (2010). *Gas turbine Combustion Alternative Fuels and Emissions* (3rd ed.). Taylor & Francis Group.



- [38] Lefevbre, A. H. (1984). Fuel Effects on Gas Turbine Combustion-liner Temperature, Pattern Factor, and Pollutant Emissions. *Journal of Aircraft* , 887-898.
- [39] Lienhart, H., Stoots, C., & Becker, S. (2002). Flow and Turbulence Structures in the Wake of a Simplified Car Model (Ahmed Modell). *New Results in Numerical and Experimental Fluid Mechanics III* , 323-330.
- [40] Lilley, D. G. (2011). Swirling Flows and Lateral Jet Injection for Improved Mixing and Combustion. *49th AIAA Aerospace Sciences Meeting Including the New Horizons Forum and Aerospace Exposition*. Orlando.
- [41] Liou, T. -M., Hsiao, K. -L., & Tsai, M. -K. (1991). Experimental and Theoretical Studies on Turbulent Mixing of Two Confined Jets. *International Journal of Heat and Fluid Flow* , 210-217.
- [42] Liukai, & Xuli. (2012). Study on Combustor Outlet Temperature Field of Gas Turbine. *Applied Mechanics and Materials* , 962-966.
- [43] Motsamai, O. S., Snyman, J. A., & Meyer, J. P. (2010). Optimization of Gas Turbine Combustor Mixing for Improved Exit Temperature Profile. *Heat Transfer Engineering* , 31 (5), 402-418.
- [44] Motsamai, O. S., Visser, J. A., & Morris, R. M. (2008). Multi-disciplinary Design Optimization of a Combustor. *Engineering Optimization* , 137-156.
- [45] Norgren, C. T., & Humenik, F. M. (1968). *Dilution-Jet Mixing Study for Gas Turbine Combustors*. National Aeronautics and Space Administration. Springfield: Clearinghouse for Fedral Scientific and Technical Information.
- [46] Norihiko, I., Gruber, A., & Yoshida, H. (2008). A Numerical and an Experimental study for Optimization of a Small Annular Combustor. *Journal of Power and Energy Systems* , 921-933.
- [47] Owens, S. F. (1992). *CFD-ACE: Command Language Reference Manual*. Huntsville: CFDRC Report.
- [48] Patankar, S. V. (1980). *Numerical Heat Transfer and Fluid Flow*. New York: McGraw-Hill.
- [49] Patankar, S. V., & Spalding, D. B. (1972). A Calculation Procedure for Heat, Mass and Momentum Transfer in Three-Dimensional Parabolic Flows. *International Journal of Heat and Mass Transfer* , 1787-1806.
- [50] Pope, S. B. (2000). *Turbulent Flows*. New York: Cambridge University Press.

- [51] Pratt, & Whitney. (1988). *The Aircraft Gas Turbine Engine and Its Operation* (3rd ed.).
- [52] Rajaei, M. (1992). *Measurement and Mathematical Analysis of Free Shear Flow*. Providence: Brown University.
- [53] Rodi, W. (2006). DNS and LES of Some Engineering Flows. *Fluid Dynamics Research* , 145-173.
- [54] Sayre, A., Lallemant, N., Dugue, J., & Weber, R. (1996). *Scaling Characteristics of Aerodynamics and Low-NO<sub>x</sub> Properties of Industrial Natural Gas Burners*. The Netherlands: International Flame Research Foundation.
- [55] Sheu, T. S., Chen, S. J., & Chen, J. J. (2012). Mixing of a Split and Recombine Micromixer with Tapered Curved Microchannels. *Chemical Engineering Science*, 321-332.
- [56] Shyy, W., Correa, S. M., & Braaten, M. E. (1988). Computation of Flow in a Gas Turbine Combustor. *Combustion Science and Technology* , 97-117.
- [57] Spalding, D. B. (1972). A Novel Finite-Difference Formulation for Differential Expressions involving both First and Second Derivatives. *International Journal for Numerical Methods in Engineering* , 551-559.
- [58] Stevens, S. J., & Carrotte, J. F. (1988). Experimental Studies of Combustor Dilution Zone Aerodynamics. *AIAA/ASME/SAE/ASEE 24th Joint Propulsion Conference*. Boston.
- [59] Su, K., & Zhou, C. Q. (2000). Numerical Modeling of Gas Turbine Combustor Integrated with Diffuser. *34th National Heat Transfer Conference*, (pp. 1-8). Pittsburgh.
- [60] Talpallikar, M. V., Smith, C. E., Lai, M. C., & Holdeman, J. D. (1992). CFD Analysis of Jet Mixing in Low NO<sub>x</sub> Flametube Combustors. *Journal of Engineering for Gas Turbines and Power* , 417-424.
- [61] Tao, Y., Adler, W., & Specht, E. (2002). Numerical Analysis of Multiple Jets Discharging into a Confined Cylindrical Crossflow. *Journal of Process Mechanical Engineering* , 173-180.
- [62] Vakil, S. S., & Thole, K. A. (2005). Flow and Thermal Field Measurements in a Combustor Simulator Relevant to a Gas Turbine Aeroengine. *Journal of Engineering for Gas Turbines and Power* , 257-267.

- [63] Wang, C.-j., Wang, D.-d., & Wu, Z.-y. (2011). Turbulence Combustion Modeling in the Gas turbine Combustor. *Third International Conference on Measuring Technology and Mechatronics Automation*. Shanghai.
- [64] Wang, T., Chintalapati, S., Bunker, R. S., & Lee, C. P. (2000). Jet Mixig in a Slot. *Experimental Thermal and Fluid Science* , 1-17.
- [65] Wegner, B., Huai, Y., & Sadiki, A. (2004). Comparative Study of Turbulent Mixing in Jet in Cross-flow configurations using LES. *International Journal of Heat and Fluid Flow* , 25 (5), 767-775.
- [66] White, F. M. (2009). *Fluid Mechanics*. New York: McGraw-Hill.
- [67] Wittig, S. L., Elbahar, O. M., & Noll, B. E. (1984). Temperature Profile Development in Turbulent Mixing of Coolant Jets with a Confined Hot Crossflow. *Journal of Engineering for Gas Turbines and Power* , 106 (1), 193-197.
- [68] Yehia A., E., Hossam S., A., Khalid M., S., & Jaafar, M. N. (2011). A Multiple Inlet Swirler for Gas Turbine Combustors. *International Journal of Aerospace and Mechanical Engineering* , 5 (2), 106-109.
- [69] ZhenXun, G., & ChunHian, L. (2011). Numerical Research on Mixing Characteristics of Different Injection Schemes for Supersonic Transverse Jet. *Science China. Technological Sciences* , 883-893.

## Appendix

This section presents another graphical representation of the velocity data for the Ahmed body. Figure A.1 shows the comparison of experimental and simulation velocity data for the scaled-down Ahmed body represented in terms of coordinates. This figure is a consolidated illustration of the data plotted in Figs. 8.30 - 8.37. As observed previously, a good agreement exists between simulation and experimental data in front of the Ahmed body while the experimental data behind the Ahmed body is erroneous due to limitation of hot-wire measurement. The 'PlotZCoordinate' and 'PlotXCoordinate' are given by the following equations:

$$PlotZCoordinate (mm) = Z - coordinate \times 1000 \quad (1.1)$$

$$PlotXCoordinate (mm) = \left[ X - coordinate + 0.0254 \times \frac{VelocityMagnitude}{InletVelocity} \right] \times 1000 \quad (1.2)$$

Figure A.2 shows the streamwise velocity profile obtained in front of the full-scale Ahmed body for various mesh sizes. A grid independent study was performed on full-scale Ahmed body with mesh sizes - 6 million, 10 million and 13 million elements. Although the profile look similar for all the mesh sizes, it was important to go for the higher mesh size to capture the large eddies to perform the large eddy simulations more accurately. Due to the computational resource limitation, a still higher mesh size could not be tested and all the simulations were performed on 13 million elements mesh size.

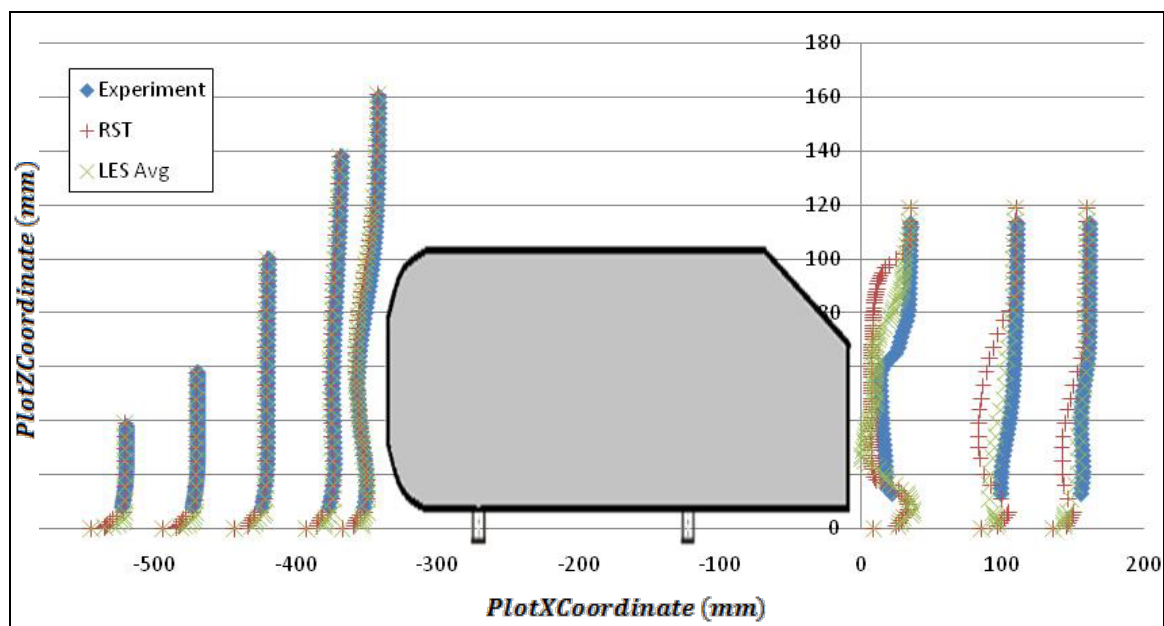


**Figure A.1** Streamwise velocity profile at various locations around scaled-down Ahmed body.

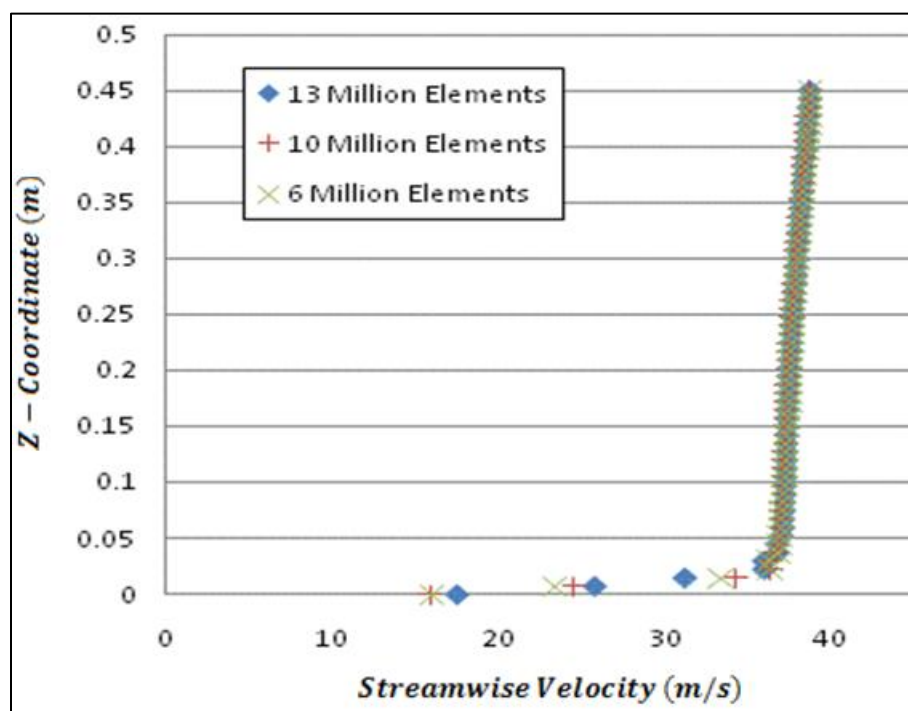


**Figure A.2** Velocity profile for various mesh sizes of full-scale Ahmed body.

## CURRICULUM VITAE

Alka Gupta

**Place of Birth:** Kanpur, Uttar Pradesh, India

### Education

Doctor of Philosophy (Ph.D.) in Engineering, May 2014  
University of Wisconsin – Milwaukee, Wisconsin, US

Master of Technology (M. Tech) in Mechanical Engineering, June 2010  
Indian Institute of Technology (B.H.U.) - Varanasi, Uttar Pradesh, India

Bachelor of Technology (B. Tech.) in Mechanical Engineering, July 2007  
Harcourt Butler Technological Institute, Kanpur, Uttar Pradesh, India

### Industrial Experience

Jan 2013 – Present, CFD Engineer Co-op, Harley-Davidson Motor Company,  
Wauwatosa, Wisconsin, US

Aug 2007 – June 2008, Software Engineer, Infosys Technologies Limited, Hyderabad,  
Andhra Pradesh, India

June 2005 – July 2005, Intern, Hindustan Aeronautics Limited (HAL), Kanpur, Uttar  
Pradesh, India

### Research Experience

Jan 2011 – March 2014, University of Wisconsin – Milwaukee, Wisconsin, US  
Topic: *Development of Novel Passive Control Techniques for More Uniform  
Temperature at Combustor Exit and Hybrid LES/RANS Modeling*

Jan 2012 – Dec 2013, University of Wisconsin – Milwaukee, Wisconsin, US  
Topic: *Design & CFD Analysis of Wind Turbine Blades - Winglet, Tubercle and Slotted*

Jan 2012 – Dec 2013, University of Wisconsin – Milwaukee, Wisconsin, US  
Topic: *Experimental Investigation of Biomass Gasification Using Carbon dioxide*

June 2006 – July 2006, Indian Institute of Technology, Kanpur, Uttar Pradesh, India  
Topic: *Suppression of Cup-burner Flame Using Nitrogen Gas*

## Teaching Experience

Jan 2011 – Dec 2012, Teaching Assistant, Fluid Mechanics Laboratory, Heat Transfer, How Things Work, University of Wisconsin – Milwaukee, Wisconsin, US

July 2010 – Dec 2010, Assistant Professor, Thermal & Hydraulic Machines, Heat Transfer Laboratory, Engineering Graphics, Senior Design Project, Pranveer Singh Institute of Technology – Kanpur, Uttar Pradesh, India

## Papers in Refereed Journals and Peer Reviewed Conference Proceedings

### Journal Publications:

- Gupta, A., Ibrahim, M. S., & Amano, R. S. (2013). Experimental Study of Novel Passive Control Methods to Improve Combustor Exit Temperature Uniformity. *Heat and Mass Transfer*. [Accepted]
- Gupta, A., Prakash, O., & Shukla, S. (2011). Thermodynamic Analysis of Gas - Steam Combined Cycle with Carbon Dioxide (CO<sub>2</sub>) Emissions Saving. *International Journal of Energy and Environment*, 2 (2), 219-230.

### Conference Publications (more than 10):

- Gupta, A., Ibrahim, M. S., Wiegand, B. & Amano, R. S. (2013). Computational and Experimental Study of Enhanced Mixing in a Gas Turbine Combustor Using Guide Vanes. *ASME Summer Heat Transfer Conference*. Minneapolis.
- Gupta, A., Ibrahim, M. S., & Amano, R. S. (2012). Computational Analysis of Mixing in a Gas Turbine Combustor. *Proceedings of the ASME IMECE Conference*. Houston.
- Ibrahim, M. S., Gupta, A., Rux, A., Lang, M., Moll, T., & Amano, R. S. (2012). Numerical Investigation and Experimental Lab Setting-up for Analysis of Gas Turbine Combustor Dilution Process. *ASME IDETC/CIE Conference*. Chicago.

## Awards and Recognition

- Member of American Society of Mechanical Engineers (ASME) and American Institute of Aeronautics and Astronautics (AIAA).
- President of American Institute of Aeronautics and Astronautics (AIAA) Student Organization at University of Wisconsin - Milwaukee.
- Awarded Chancellor's Award by the department of Mechanical Engineering at the University of Wisconsin – Milwaukee for excellent research and academic performance (GPA 4.0/4.0).
- Topper in M. Tech. Mechanical Engineering and honored with a gold medal.
- Undergraduate topper in a batch of 66 students and honored with a silver medal.
- Awarded institute Merit Scholarship throughout undergraduate college.